Structural Trends in Off-stoichiometric $Cu_2ZnGeSe_4$ Kesterite-type Compound Semiconductors

Dissertation zur Erlangung des akademischen Grades
Doktor der Naturwissenschaften
(Dr. rer. nat.)

vorgelegt von
René Gunder

Eingereicht am Fachbereich Geowissenschaften
der Freien Universität Berlin

Angefertigt an der Helmholtz-Zentrum Berlin für Materialien und Energie GmbH
im Rahmen der Graduiertenschule Materials for Energy Conversion
Abteilung Struktur und Dynamik von Energiematerialien

Die Arbeit ist in englischer Sprache verfasst

Berlin, Oktober 2021

Erstgutachterin:	Prof. Dr. Susan Schorr
Zweitgutachter:	PD Dr. Ralf Milke
Tag der Disputation:	04.03.2022

“God made the bulk;

surfaces were invented by the devil”

- Wolfgang Pauli -

Zusammenfassung

Der Klimawandel schreitet unerbittlich voran und ist im Begriff eine unkontrollierbare globale Erwärmung herbeizuführen, was zusätzlich mit sich selbstverstärkenden Rückkopplungsprozessen und verheerenden kaskadierenden Effekten einhergehen wird. Da der globale Energieverbrauch gleichzeitig immer weiter zunimmt, ist entschlossenes Handeln hinsichtlich eines zügigen Ausbaus erneuerbarer Energiequellen nötig um das Eintreten des schlimmsten Falls zu verhindern. Nachhaltige und leistungsstarke PV-Technologien wie c-Si, CdTe und CIGSe sind zwar bereits verfügbar, aber aufgrund kontraproduktiver Energieamortiserungszeiten (c-Si) bzw. giftiger und seltener Bestandteile (CdTe, CIGSe) kommt keine von denen für einen großskaligen Einsatz in Frage. Mit CZTSSe vom Kesterit-Strukturtyp hat sich ein alternatives Material für PV-Anwendung hervorgetan, das prinzipiell aus ungiftigen und ausreichend vorhandenen Elementen zusammengesetzt werden kann, jedoch müssen vor der Anwendungsreife einige leistungsbeschränkende Faktoren angegangen werden. Dabei zielen die Verbesserungen nicht nur auf eine Verringerrung der Lücke zum Shockley-Queisser-Limit [1], sondern beinhalten außerdem eine Diversifizierung der Anwendungen. Das Ersetzen von Zinn durch Germanium führt zu einer Aufweitung der Bandlücke und somit zu neuen Anwendungen, wobei aber bisher nur wenig bekannt ist bezüglich strukureller Trends in CZGSe und wie diese zu dessen Materialeigenschaften in Beziehung stehen. Um die strukturellen Eigenschaften stärker zu beleuchten wurden nicht-stöchiometrische Pulverproben [2-4] von CZGSe mittels Festkörpersynthese hergestellt. Die Zusammensetzung und chemische Homogenität wurde anhand von WDX-Spektroskopie untersucht, und UV-Vis-Spektroskopie wurde eingesetzt um die Bandlückenenergie zu bestimmen [5]. Rietveld-Analyse sowie die Methode der mittleren Neutronenstreulänge wurden für eine eingehende strukurelle Charakterisierung verwendet. In dem Großteil der Proben war die CZGSe-Phase ausreichend chemisch homogen und erlaubte somit eine zielführende Untersuchung, obschon sie häufig mit Nebenphasen koexistiert. Eine sorgfältige Strukturanalyse hat bestätigt, dass CZGSe

die Struktur vom Kesterit-Typ annimmt (Raumgruppe $I\bar{4}$), jedoch mit einer gewissen Cu-Zn-Unordnung auf den 2c- und 2d-Wyckoffpositionen. Für die elektronischen Eigenschaften nachteilige Punktdefekte wurden durchgehend im Cu-reichen Bereich (z.B. Cu_{Ge}^{3-}) sowie für einen großen Teil des Cu-armen Bereichs (z.B. Zn_i^{2+}) gefunden, was hinsichtlich PV-Anwendungen die große Bedeutung für das Erreichen einer Zusammensetzung entsprechend dem A – B-Typ unterstreicht.

Abstract

Climate change is advancing inexorably and is en route to cause uncontrollable global warming that will go along with self-amplifying feedback loops and disastrous cascading effects. At the same time is the global energy consumption further increasing, meaning decisive action to prevent the worst from happening needs to be taken that essentially include a rapid expansion of renewable energy sources. Sustainable and well-performing PV-based technologies like c-Si, CdTe and CIGSe are already existing but none of these are considered a meaningful candidate for substantial large-scale installations owing to virtually counterproductive energy payback times (c-Si), or severe toxicity and scarcity of their constituents (CdTe, CIGSe). With kesterite-type CZTSSe an alternative PV material class did emerge that can essentially be composed of abundantly available and non-toxic elements but several performance limiting factors need to be tackled prior to application maturity. Improvements are not exclusively aiming at reducing the gap towards the Shockley-Queisser limit [1] but also include a diversification of its application. The substitution of tin with germanium leads to a widening of the band gap and thus to new applications, yet little knowledge existed regarding structural trends in CZGSe and how they relate to its material's properties. In order to shed more light on structural characteristics solid-state reaction was applied to synthesize off-stoichiometric CZGSe powder samples [2-4]. The composition and chemical homogeneity were examined by quantitative WDX spectroscopy, and UV-Vis spectroscopy was employed to estimate the band gap energy [5]. Rietveld analysis [6, 7] and the average neutron scattering length method [8, 9] were applied both to p-XRD and p-ND data for a comprehensive structural characterization. The majority of the samples exhibited a sufficient chemical homogeneity of the CZGSe phase allowing for a meaningful investigation, albeit oftentimes co-existing with secondary phases. Careful structure analysis revealed that CZGSe adopts the kesterite-type structure (s.g. $I\bar{4}$) which is subject to a certain degree of Cu-Zn disorder among 2c and 2d Wyckoff positions. Electronically harmful point defects were found throughout the Cu-rich regime (e.g. Cu_{Ge}^{3-}) as well as for a grand portion of the Cu-poor region (e.g. Zn_i^{2+}), thus highlighting the huge relevance in achieving A – B-type composition when aiming at reasonable PV devices.

Contents

List of figures

List of tables

List of abbreviations

2Θ…… recorded diffraction angle

5N…… five “nines” (99.999 %; grade of purity)

α…… absorption coefficient

β…… integral breadth

ε…… maximum microstrain

η……mixing (shape) parameter

λ…… wavelength

ν…… stoichiometric coefficient

ρ_e…… electron density

σ…… cross section

φ…… phase shift

Θ…… angle of the incident beam

Å……Ångström

A_s…… scattering amplitude

AZO…… aluminum zinc oxide

a.u.…… arbitrary units

b……neutron scattering length

BSE…… backscattered electron

CBM…… conduction band minimum

CIGSe…… $Cu(In,Ga)Se_2$

CGSe…… Cu_2GeSe_3

CZGS…… Cu_2ZnGeS_4

CZGSe…… $Cu_2ZnGeSe_4$

CZGSSe…… $Cu_2ZnGe(S,Se)_4$

CZTS…… Cu_2ZnSnS_4

CZTSe …… $Cu_2ZnSnSe_4$

CZTSSe…… $Cu_2ZnSn(S,Se)_4$

d……days

DFT…… density functional theory

d_{hkl}…… lattice plane distance

$D_{\langle V \rangle}$…… volume-averaged domain size

e …… elementary charge

EDX…… energy-dispersive X-ray spectroscopy

E_g…… band gap energy

EPMA…… electron probe microanalyzer

f…… atomic form factor

F…… structure factor

fcc…… face centered cube

FF…… fill factor

FWHM, Γ…… full width at half maximum

GGI…… Ga/(Ga+In)

hcp…… hexagonal close-packed

hν…… photon energy

HR…… high-resolution

I, y…… intensity

IRF…… instrumental resolution function

I_{sc}…… short-circuit current

ITO…… indium tin oxide

J_{sc}…… short-circuit current density

l…… bond length

n…… integer number

N_e…… number of electrons

NIR…… near-infrared

NREL…… National Renewable Energy Laboratory

occ…… site occupancy factor

PCE, η…… power conversion efficiency

p-ND…… powder neutron diffraction

pV…… pseudo-Voigt (function)

PV…… photovoltaic

*p-XR*D…… powder X-ray diffraction

r…… radius

R…… reflectance

RT…… room temperature

S_{hkl}……anisotropic strain coefficient

S_y…… residuum

SEM…… scanning electron microscope

s.g. …… space group

T_c…… critical temperature

TCH…… Thompson-Cox-Hastings (function)

T_m…… melting point

u…….. tetragonal distortion parameter

UV…….. ultra-violet (light spectroscopy)

VBM…….. valence band maximum

Vis…….. visible (light spectroscopy)

V_{oc}…….. open-circuit voltage

WDX…….. wavelength-dispersive X-ray spectroscopy

Z…….. atomic number

1 Introduction

1.1 Retrospective and state of affairs

The capability to induce voltage and electric current in metallic and semi-metallic compounds is a well-known feature of electromagnetic radiation that has for the first time been demonstrated by Edmond Becquerel in 1839 using an electrochemical cell [10]. This phenomenon of electrons being excited by photons to higher-energy orbitals and thereby creating an electric potential is referred to as the Becquerel effect that certainly marked one of the grandest cornerstones in the history of photovoltaics (PV). Although it was far away from being considered for real applications in this human epoch the first solar cell was fabricated by Charles Fritts in 1883 which yet possessed a poor photovoltaic performance [11]. From the phenomenological and descriptive point of view the work from Albert Einstein about the photoelectric effect, published in 1905 [12], represented one of the most important and influential contribution towards understanding the physics behind the characteristics of light and its interaction with matter. This work had a considerable impact on the description of the nature by the concept of quantum theory for which he was eventually honored with the Nobel prize. This period, the 19th and the first decades of the 20th century, was characterized by seminal and fundamental discoveries that led to theories giving rise to a new perception of what is governing the world at very small length scales and how the microcosm translates to the macrocosm. However, the political, societal, and economic climate particularly at that time (and to some extent at any time in general) could not keep up with the scientific achievements as the industrial revolution was still advancing and became increasingly manifest in everyday life.

For a process to happen differences in energy are required, which can only be achieved using energy in a suitable form. Electric energy, for instance, is a form of energy allowing to trigger and keep running many processes very efficiently. However, it is a very ordered form of energy that, in turn, requires a lot of energy

itself in order to be generated. The lowest energy form is heat as it results from every process, readily dissipates and equilibrates and, thus, the poorest ordered one is. The key for the industrial revolution to happen is laid in the utilization of heat originating from combustion of fossil fuels that are abundantly enough available to facilitate the continuous increase in prosperity and technological advancement for some 200 years, even until present. Since then, and in spite of their obvious disadvantages, fossil fuels were and are still the main energy source as its exploitation is technologically rather straightforward and stands like nothing else for economic success. The liberated heat energy upon combustion of fossil fuels is used to transform it into any higher-grade energy form but inevitably goes along with a low efficiency. A considerable amount of heat energy is simply lost as nothing else but heat without contributing to the intended transformation. In addition, fossil fuels are a limited resource that will unavoidably cease to be a major energy carrier once exploration and exploitation of fossil fuel reservoirs become intricately enough to make them more expensive than renewable sources. While it is quite unquestioned that the global energy needs will keep following its trend of increase, no robust prediction regarding the availability of fossil fuels can be made.

Still, on Earth huge amounts of fossil fuels were buried or deposited on continental shelves, and new exploitation technologies (e.g. fracking) along with off-shore exploration sites will make them accessible. And yet, continued focusing on fossil fuels as main energy source is not a foresighted strategy because the fossil fuels buried over hundreds of millions of years act as an important carbon sink. In the period from the industrialization until present the carbon was eventually released into the atmosphere several orders of magnitude faster than it took to become involved in the long-term tectonic carbon cycle [13]. Consequently, the concentration of carbon in the atmosphere rapidly increases, which not only greatly enhances the greenhouse effect but also causes a shift in atmosphere-ocean equilibrium towards lower pH values and thus an acidification of the oceans. Beside imminently less perceptible consequences like uncontrollable global warming and environmental harms, the air polluted with aerosols and respirable fine dust definitely mean a tangible threat for the health of people.

A technology that, at the first glance, is more environmentally-friendly is energy generation by fission of heavy atomic nuclei. After WWII the nuclear fission has also been utilized for civilian worth and nuclear power plants were built to complement the fossil fuel-based energy supply of prosperous and advanced enough countries. However, while nuclear power plants were at first well accepted and even acclaimed for their technological advancement that they represent, their construction and operation is way more expensive and complex as compared with conventional power plants. Apart from this, cataclysmic incidents were indeed few but if it came to happen, a devastating aftermath has always result [14, 15]. And after all, the most urgent question about the fate of the nuclear waste and its final storage could, so far, never been answered satisfactorily. Nevertheless, in light of climate protection regulations many countries still rely on this technology and new nuclear power plants are built or planned to counterbalance the negligence with respect to sustainable energy sources. On the other hand, a growing consensus exists that this technology is already outdated specifically because nuclear fuel is a limited resource as well, which is not even replenished over geological time scales as fossil fuels would be.

Another nuclear energy technology is based on the fusion of light nuclides (deuterium, D, and tritium, T), which is credited to be a comparably clean and potentially enormous energy source. All over the world there are currently only a few field tests attempting to experimentally approach and fathom the constructional, geometrical and physical requirements aiming at a reasonably working fusion reactor. The challenges are huge, and the expenses too. Thus, this technology is mainly studied theoretically including questions of the fundamental and most promising design (e.g. of the reaction chamber and the array of coils). The few experimental fusion reactors so far are devoted as to be a proof of concept through testing different chamber geometries, ranging from rotation-symmetric toroidal [16] to complex asymmetrically twisted shapes [17]. As an attempt to mimic the well-known and massive energy-delivering fusion process taking place in the sun's core the temperature (i.e. kinetic energy) of the D-T plasma has to be around ten times higher in order to get a self-sustaining chain reaction started. It is clearly the utmost challenge to confine the plasma and to sustain the chain reaction, and solutions for these and other problems does not seem to come close at hand very

soon. It is expected that it will still take several decades and plenty of financial efforts before fusion reactors become technologically mature. However, since Earth hosts a huge amount of water even the rather rare isotopes deuterium and tritium are abundant enough to provide fusion fuels for a very long period, and apart from matter-antimatter annihilation nuclear fusion supplies the highest yield in energy. So, some day it may become the key technology for the energy sector.

Meanwhile more immediate solutions are needed to satisfy the global energy demand while respecting the ecological aspect. On Earth's surface one can find energy sources that are powerful and continuously replenished, and that can essentially be climate-neutrally exploited. Those potentially utilizable energy sources are to some extent driven by heat and motions found in the interior of the Earth (endogenic) but solar-driven (exogenic) effects do have the greatest impact. While geothermal energy plays a niche role on a global scale, are the usage of hydropower plants, wind energy and solar energy of larger importance at present as the Earth's surface receives an amount of solar energy multiple orders of magnitude higher than the global demand [18, 19]. Wind power plants, solar fields and hydropower plants hence are a mean to at least indirectly make use of nuclear fusion.

The public energy supply in many prosperous and advanced countries increasingly comprises a mixture of various energy sources to reduce the fraction of climate-damaging energy production. Eco-friendly energy obtained from wind power plants and solar modules is nowadays an important contributor to this energy mix. Paradoxically, eco-friendly energy in general and wind energy in particular is widely accepted and appreciated unless wind power plants are about to be built in the vicinity of settlements, where they run into strong opposition for aesthetic and noise concerns [20]. Of course, abandoning of climate-harming past technologies in favor of such sustainable energy sources goes along with a decentralization of power production, eventually making it omnipresent and many people feel bothered. Apart from that, decentralization of power production, the dependency on weather conditions (wind speed, cloud coverage etc.) as well as the spatial and temporal fluctuations in insolation (day-night cycle, clouds, seasons, latitude etc.) mean a particular challenge for renewable energy. The efficient storage of surplus energy

resulting from periods of strong insolation and high wind speeds as well as the maintenance of the power grid stability are still major issues [21, 22].

In contrast to wind power, usage of solar energy meets a greater general acceptance as it can serve as a noiseless energy supply with a wide range of scalability and shaping that can basically be employed everywhere. After Charles Fritts has produced his solar cell consisting of selenium in 1883 [11] it took some seven decades before the next researchers began to noticeably focus on solar cells again. Beside global disasters and humanitarian tragedies like WWI, WWII and the Great Depression it was the absence of any urging stimulus to overcome the usual forces of inertia regarding changing lifestyle and acceptance of innovations. This is generally true if well-researched technologies are available, commonly established, and that have proven to increase the overall prosperity and quality of life through growing economy. Neither the society nor the industry was longing for alternative energy sources questioning the prevailed fossil fuel industry that has proven to secure prosperity and employment. So, it was up to the just emerging aerospace programs, politically aiming at proofing technological and ideological superiority rather than primarily for the exploration of something new and unknown, for which devices allowing for an independent and long-term power supply were required.

Pioneering work in the field of solar energy conversion was done on Si-based [23] as well as on the prediction of inorganic compound semiconductors [24-26] in the 1950s, which marked the start of a continuous advancement afterwards. However, it took another two decades until the oil crisis made politics and society change their view on fossil fuels as it explicitly illustrated how toxic and destabilizing the strong dependency on a single resource can be for whole economies. Alternative ways for power generation were suddenly of interest, which is reflected by the encouragement particularly of solar energy research aiming at acting as a relevant civilian energy supply that indeed led to a remarkable progression over the last decades (Figure 1-1).

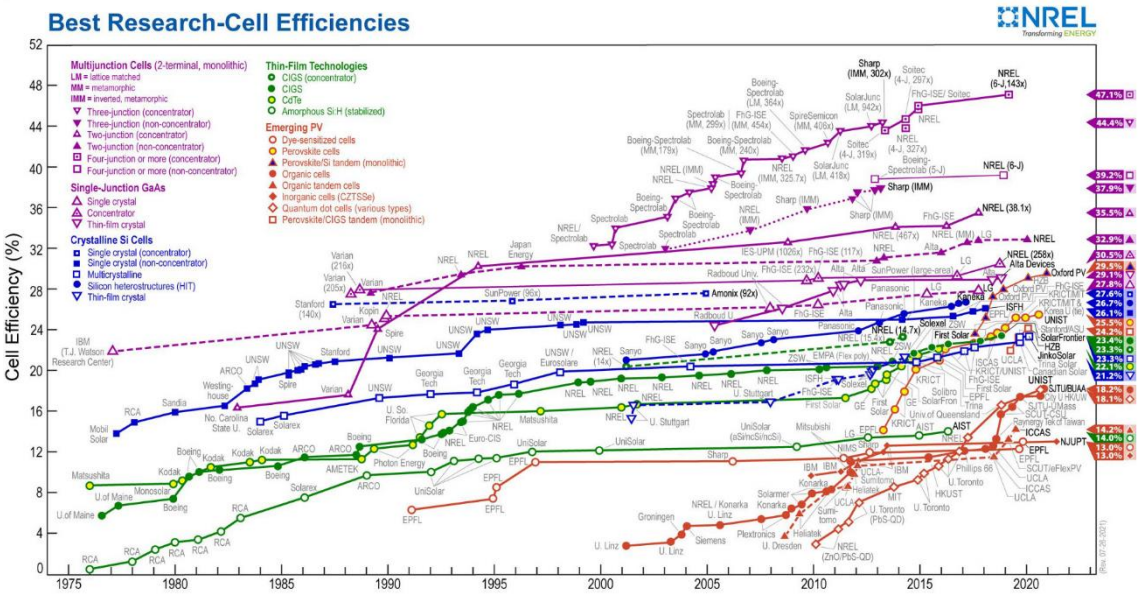

Figure 1-1 NREL (National Renewable Energy Laboratory) chart showing the progress in solar power conversion efficiencies (PCE) of the various material classes used for photovoltaic applications [27].

1.2 Frame conditions and motivation

The terrestrial maximum power conversion efficiency (PCE) of a single p-n junction solar cell is limited by several fundamental factors that were investigated in detail by Shockley & Queisser in 1961, giving rise to the theoretical maximum power conversion efficiency [1]. This well-known Shockley-Queisser limit includes considerations like losses through thermalization, radiative recombination (re-emission), and the (atmospherically modified) spectral distribution of the incoming sun light, and eventually allows to predict the maximum PCE as a function of the band gap energy. In dependence of the applied reference spectrum slightly different values regarding optimal band gap energy and maximum efficiency are obtained. For temperate latitudes the AM1.5G spectrum, implying an air mass corresponding to 1.5 atmospheres and additional standardized parameters like zenithal angle of insolation is typically applied, where the theoretically highest possible efficiency of ~32 % is achieved for a band gap energy of ~1.3 eV [28] (Figure 1-2).

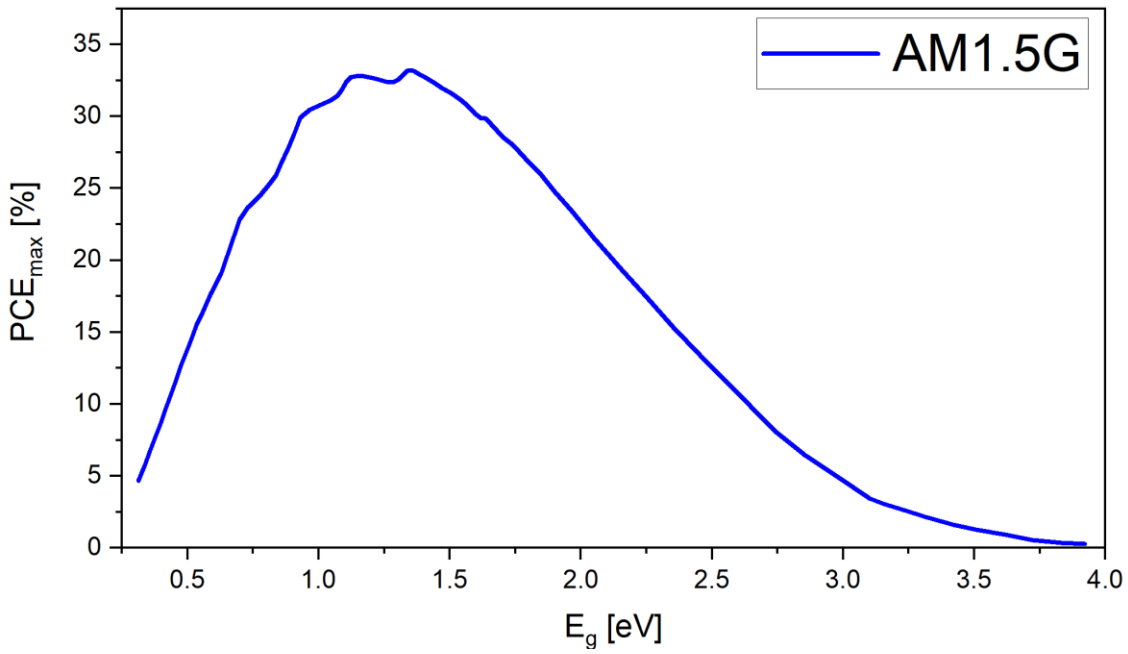

Figure 1-2 The maximum power conversion efficiency in dependence of the band gap energy for a single-junction solar cell irradiated with the AM1.5G spectrum (modified after [28]).

At the end the PCE is by far of paramount relevance eventually determining whether the solar cell is of reasonable quality. There are however additional fundamental parameters [29] being equally important to fully characterize the photovoltaic performance of a solar cell from which the PCE is actually derived from, and each of them may point to specific causes for a possible underperformance [30]:

- Open-circuit voltage (V_{oc}) – is measured in a circuit that is not connected to an external load (current I = 0 A) and thus represents the maximum potential difference (i.e. V_{oc} = V_{max} at I = 0 A).

  Some possible causes for a low V_{oc} are:

  - band gap fluctuations, e.g. by structural disorder
  - various recombination modes
  - secondary phases in the bulk or chemical inhomogeneities
  - too small grain size and poor grain boundary passivation
  - unfavorable band alignment

- Short-circuit current density (J_{sc}) – is the current per area ($J_{sc} = I_{sc}/A$ [mA cm^{-2}]) measured when the device is short-circuited ($V = 0$ V), which for a non-ideal solar cell is the highest current (i.e. $J_{sc} = J_{max}$ at $V = 0$ V).

  Some possible causes for a low J_{sc} are:

  - small diffusion length
  - too thin absorber
  - secondary phases at absorber surface

- Fill factor (FF) – is a quality factor that relates the voltage V_{mp} and current I_{mp} at the maximum power point P_{mp} to V_{oc} and I_{sc}:

$$FF = \frac{V_{mp} \cdot I_{mp}}{V_{oc} \cdot I_{sc}} \tag{1.1}$$

  and since $V_{mp} \cdot I_{mp} = P_{mp}$ the fill factor eventually determines the maximum power P_{max} that can be drawn from a solar cell for a given V_{oc} and I_{sc}, respectively:

$$P_{max} = V_{oc} \cdot I_{sc} \cdot FF. \tag{1.2}$$

  Some possible reasons for a low FF are:

  - voids or resistive secondary phase at the back interface
  - non-radiative recombination
  - secondary phases in the bulk
  - low bulk absorber conductivity
  - small diffusion length
  - secondary phases at absorber surface

- Power conversion efficiency (η, PCE) – is the ratio between maximum power output P_{max} and power input P_{in}:

$$\eta = \frac{P_{max}}{P_{in}} = \frac{V_{oc} \cdot I_{sc} \cdot FF}{P_{in}}. \tag{1.3}$$

By measuring the current-voltage (I-V) curve of a solar cell these basic parameters can be obtained at one stroke (Figure 1-3).

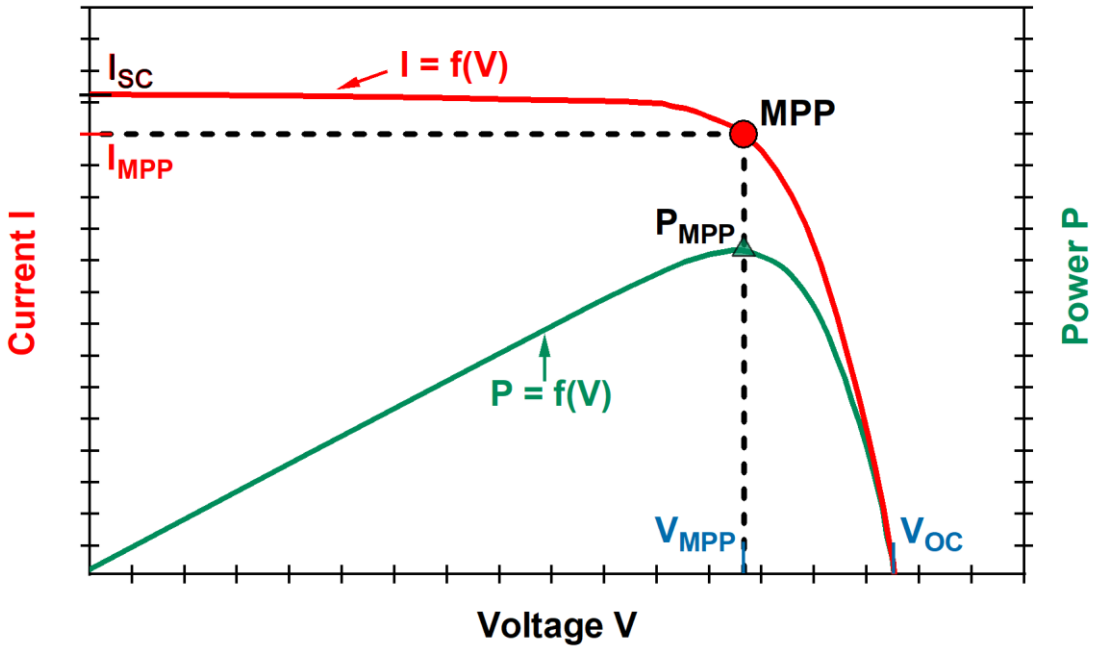

Figure 1-3 Characteristic I(V) and P(V) curve for a solar cell (modified after [31]).

Of course, the suitability of a material class for photovoltaic and related applications is foremostly determined by its optoelectronic properties, specifically by the band gap type and its energy gap. For the photoelectric effect to happen light with sufficient energy needs to be incident on the semiconductor material. In every semiconductor the photon energy $h\nu$ must be equal or higher as the discrete energy gap E_g between valence band maximum (VBM) and conduction band minimum (CBM): $h\nu \geq E_g$. However, in indirect semiconductors an absorbed photon of essentially high enough energy to let the electron overcome the energy gap is an intermediate state of a two-step process (Figure 1-4a). In order to make an electron effectively passing from the VBM to the CBM an additional vector component within the momentum space is necessary for which phonons do account for. This additional

requirement reduces the probability of this event to happen, eventually causing the absorbed energy oftentimes to be re-emitted as the electron excitation to the CBM is instantly followed by de-excitation to the previous ground state in the VBM. Indirect semiconductors like silicon are thus inherently characterized by a low absorption coefficient α of around ~10^2 cm^{-1} [32] at its band gap energy of ~1.15 eV [33, 34]. Consequently, absorber layers as thick as 200 – 300 µm are needed in order to harvest enough light for sufficient charge carrier generation.

For no spatial difference between VBM and CBM location in the momentum space a direct transition is possible which only depends on the photon energy (Figure 1-4b). Direct semiconductors are therefore possessing an absorption coefficient at least two orders of magnitudes higher (>10^4 cm^{-1} [35, 36]) that eventually allows for the fabrication of thin film absorber layers being over a hundred times thinner than in case of indirect semiconductor materials.

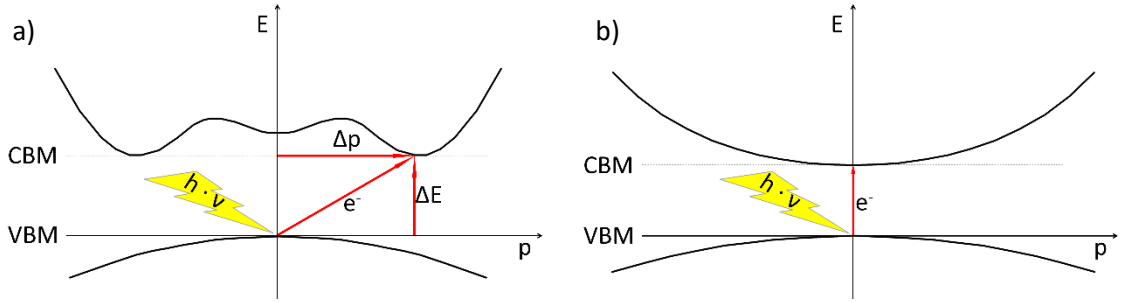

Figure 1-4 Schematic of the electronic structure (density of states – DOS) at the Γ point for a) indirect and b) direct semiconductor (figure taken from [37]).

In spite of its indirect band gap single-crystalline silicon (c-Si) solar cells at first experienced a strong consideration as the raw material is extremely abundant and fundamental insights were already elaborated. In 1977, a c-Si (non-concentrator) solar cell remarkably yielding over 12 % power conversion efficiency (PCE) was reported by Mobil Solar [38]. In the same year a PCE even of around 22 % was achieved for single-crystalline GaAs by IBM [39]. Production of single crystals with high enough quality is however an energy-intensive process that leads to comparably long energy amortization times [40].

Ideally, for a material class to be suitable for large-scale PV application the following criteria should be met:

- direct band gap and high absorption coefficient
- optical band gap as close as possible to the optimum, or at least tunable by composition without compromising other properties
- high PCE, preferentially in close proximity to the Shockley-Queisser limit
- high availability and low costs of constituent raw materials
- low material requisition and low weight
- flexible shaping
- non-hazardous to environment and health
- producibility through facile, fast, low-cost, and low-energy processes
- long-term stability and durability

Even if silicon-based solar cells do very well fulfill some of the aforementioned criteria, it is an indirect semiconductor that needs to be extrinsically doped to induce p-type or n-type conductivity and is inherently suffering from a low absorption coefficient. Absorber layer thicknesses of up to 300 µm are thus required meaning higher material consumption. GaAs, on the other hand, is a direct semiconductor allowing for much thinner layers being on the order of a few microns, but is subject to high material costs and an unfavorable energy amortization time, although much valued for their good performance and specifically employed where the weight-to-performance ratio is a more crucial parameter than expenses (e.g. aerospace).

As an attempt to reduce production costs, material usage, and energy consumption upon manufacturing single-crystalline silicon (and GaAs) solar cells, alternative material classes (CdTe, CIGSe) and concepts (amorphous Si; a-Si) aiming at thin film solar cells were therefore contemporarily researched in the 1970s. With silicon being an overwhelmingly abundant and cheap raw material, the possibility of manufacturing also amorphous thin film solar cells was endeavored whose performance indeed rapidly increases for a decade or so but only little progress was achieved during the past decades (cf. Figure 1-1). Polycrystalline compound semiconductors were instead of higher relevance as they achieved much better PCEs from the beginning. From the family of compound semiconductors two

representatives have to be outlined particularly, namely zincblende-type CdTe and chalcopyrite-type $Cu(In_xGa_{1-x})S_ySe_{2-y}$ (CIGSe). CdTe solar cells are much appreciated not only for their formidable PCE of presently 22.1 % [41] and its optical band gap of ~1.45 eV [25] being close to the optimum of 1.34 eV (for AM1.5G spectrum) [28] but exhibit the shortest energy payback time and lowest carbon footprint among all PV technologies [40]. Despite these qualities a large-scale installation of CdTe PV modules is unlikely to happen owing to strong environmental and health hazards linked to cadmium, which represents a severe issue upon handling and recycling. Besides, in the continental crust tellurium is the least abundant element [42] relevant for the various PV material classes, hence rendering upscaling impossible due to low raw material availability and associated higher costs (Figure 1-5). Replacement of the divalent (and toxic) cation cadmium with monovalent (Cu^+) and trivalent cations (In^{3+}, Ga^{3+}) as well as of the rare (and expensive) tellurium through by size better matching chalcogens (S^{2-}, Se^{2-}) results in the ternary chalcopyrite-type compound referred to as CIGSe. PV technology based on CIGSe experienced a continuous and occasionally even a steep rise in PCE, which so far reached 23.4 % [43] and is hence on route to draw nearer the power conversion efficiency limit. However, it became evident quite early that CIGSe is not a reasonable or exclusive candidate to be considered for large-scale installation. Gallium and indium are rare and expensive elements (Figure 1-5), with indium being even classified a critical raw material [44] that is also required for other key technologies on a grand scale.

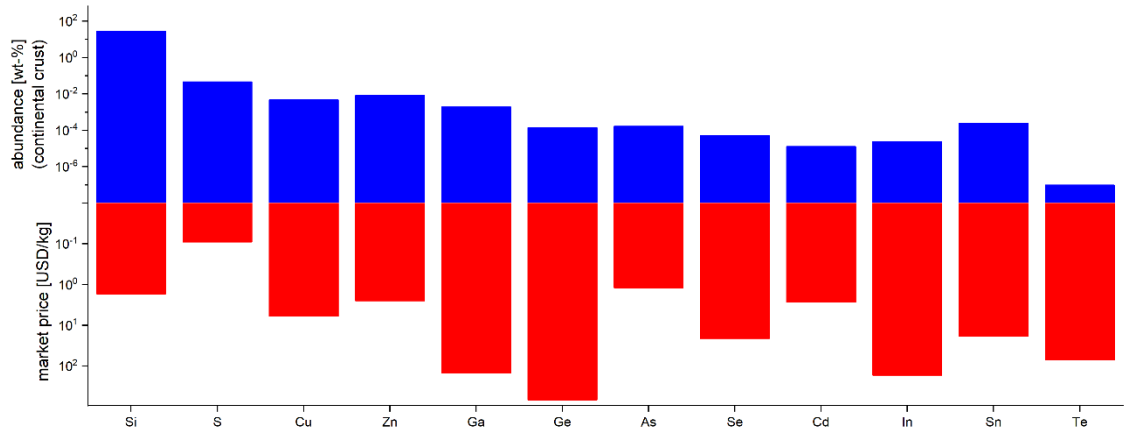

Figure 1-5 Abundance and market prices of chemical elements relevant for the various material classes that come into question for inorganic solar cells (abundances from [42]; market prices from [45-47]).

In search of alternative material classes capable for large-scale installation structural analogy has proven a very powerful tool in systematically and exhaustively predicting inorganic semiconducting compounds [24, 26, 48], which gave rise to a catalogue of potential candidates for PV application. Besides the binary compounds (GaAs, CdTe) and ternary chalcopyrite-type compounds (CIGSe) it has also been the basis for the emerging quaternary kesterite-type compounds (e.g. CZTS). The latter were proposed as an alternative photovoltaic material class possessing a direct [36, 49] and flexibly tunable band gap E_g (between ≈1.0 eV for $Cu_2ZnSnSe_4$, CZTSe [36, 50], and ≈1.5 eV for Cu_2ZnSnS_4, CZTS [51, 52]), intrinsic p-type conductivity [36, 53], and may be constituted by non-hazardous and abundant elements. Structurally, kesterite-type compounds are a derivative of the chalcopyrite-type CIGSe [8, 54]. While the monovalent Cu^+ is preserved are the trivalent cations being replaced by divalent (Zn^{2+}) and tetravalent (Sn^{4+}) ones, thus, rendering the composition economically competitive and readily upscalable through sufficient abundance of the involved elements (c.f. Figure 1-5).

Owing to their structural and optoelectronic similarities, the already existing knowledge gathered for CIGSe can widely be applied for solar cells based on kesterite-type absorber layers. For instance, it was obvious that the general device architecture (both substrate and superstrate structure, respectively) of kesterite-type solar cells could simply be copied from the established device structure of CIGSe solar cells (Figure 1-6), hence made this longsome empirical process needless.

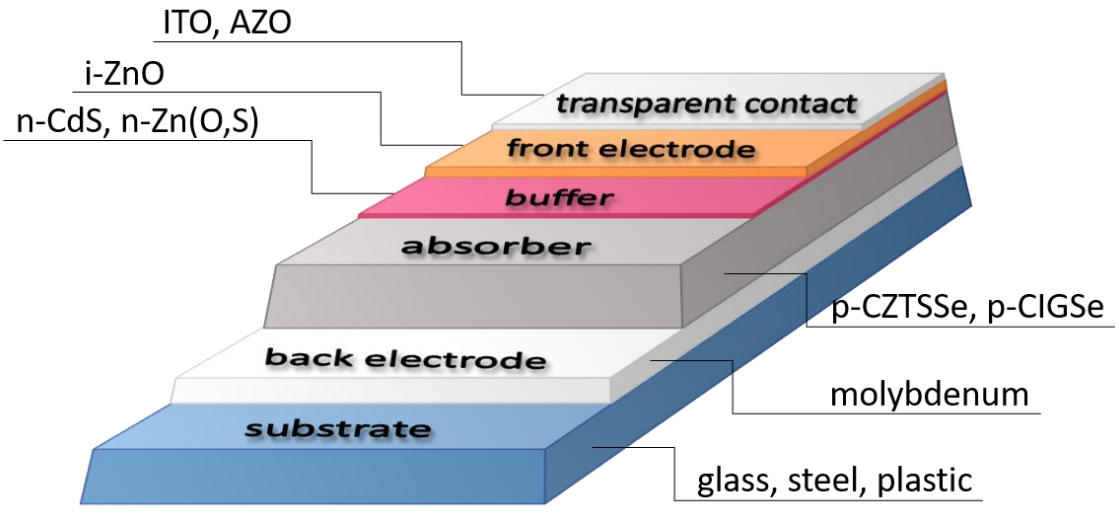

Figure 1-6 General p-n device structure of CIGSe/CZTSSe solar cells in substrate configuration (not to scale).

The first heterodiode comprising a quaternary compound semiconductor (Cu_2CdSnS_4) was reported in 1977 [53]. Its conversion efficiency of 1.6 % was indeed very low but principle information like conductivity type and band gap energy were determined [53]. More than a decade later profound photovoltaic characteristics were reported for Cu_2ZnSnS_4 and Cu_2CdSnS_4 [36]. In 1996 the first spray-deposited kesterite-type Cu_2ZnSnS_4 (CZTS) thin film solar cell was fabricated [55]. However, this study has put emphasis primarily on describing the synthesis route as it has been a facile, non-vacuum process. A more thoroughly investigation of the optical and electronical properties has been done on selenized electron beam evaporated CZTS thin film solar cells in the following year by Katagiri et. al [56], stating on the band gap energy of to be 1.45 eV and the absorption coefficient of to be on the order of 10^4 cm^{-1}. In addition to the basic optical and electronic properties the photovoltaic performance was examined too, reporting however a very low PCE of below 1 % [56]. A few years later, in 2005, the PCE could already be raised beyond 5 % for sequentially vacuum evaporated CZTS thin films [57]. By further process optimization [58, 59] and through other approaches [60, 61] the PCE of kesterite-type solar cells could steadily be improved even close to 10 % [61]. In 2011, eventually, an important milestone was reached as the 10 % threshold has been surpassed by means of a hydrazine-based solution process [62].

This steady improvement however appeared to have reached its (transient) terminus when the longstanding PCE record of 12.6 % [63] has been hit in 2014, again by using the hydrazine approach. For seven years, no further improvements of the photovoltaic performance of (conventional) $Cu_2ZnSnS_xSe_{1-x}$ (CZTSSe) solar cells could been scored. A particular challenge kesterite-based solar cells are subject to is the underperformance of every parameter determining the solar cell's PCE: (1) a too low open-circuit voltage (V_{oc}), (2) a too low short-circuit current (I_{sc}), and (3) a too low fill factor (*FF*) [30]. However, the parameter that allover underperforms the most is the open-circuit voltage (V_{OC}) and addressing the possible causes and mechanisms of failure is the most pressing issue. By the analogy to CIGSe various approaches that have proven successful for CIGSe solar cells are adopted for kesterite-based solar cells, attempting to further improve the photovoltaic performance. For instance, the beneficial impact of compositional grading [64, 65]

on PV performance is well known from the chalcopyrite-type CIGSe, which led to considerable improvements of its PCE. In CIGSe the Ga/(Ga+In) ratio (GGI) is not only a mean to optimize the optical band gap but also leads to a more favorable p-n band alignment for a suitably chosen vertical In/Ga gradient ("V"-type) [64, 65]. Therefore, vertical compositional grading [66-70] also became a more important tool for manufacturing CZTSSe solar cells as it allows optimization of the band alignment between absorber and buffer layer [66, 70]. On the other hand, the CdS buffer layer oftentimes employed in $Cu_2ZnSnS_xSe_{1-x}$ (CZTSSe) solar cells, which was also just adopted from CIGSe solar cells, only yields high efficiencies in case of intermediate values for '*x*' [63, 71]. Apart from that does CdS not only comprise toxic cadmium but also leads to unfavorable band alignment particularly for S-rich CZTSSe absorber layers [71]. For these reasons, also alternative buffer layers are evaluated with Zn(O,S) [72] and $ZnSnO_x$ [73] being so far promising Cd- and In-free candidates.

Besides, it was found rather by accident [74] that marginal incorporation of alkali elements in CIGSe significantly enhances grain growth and passivates grain boundaries [74, 75], which eventually reduces the recombinatorial losses of charge carriers at grain boundaries [76]. Consequently, the impact of alkali metal doping [77-81] on grain size and grain boundary passivation has also been investigated for CZTSSe that have shown great promise for improvements especially in terms of the V_{oc} deficit [77-79]. In 2021, utilization of organic lithium salts in the CZTSSe precursor solution eventually led to a PCE of 12.7 % [82] which made the long-time PCE record, held since 2014, being flimsily outperformed. Virtually at the same time an even higher PCE of 12.8 % [83] has been achieved through deployment of a carbon-rich bottom layer underneath the CZTSSe layer, whereas usage of a tin precursor comprising two differently oxidized tin species (namely Sn^{2+} and Sn^{4+}) resulted in the current world record PCE of 13.0 % [84]. It is particularly worthy to mention that these recent record CZTSSe solar cells have been manufactured applying non-hydrazine (and non-vacuum) solution-based fabrication methods, and thus manufactured by relatively facile, energy-saving and less hazardous processes.

Regardless of the fabrication method applied, it is without any controversial that off-stoichiometric Cu-poor and Zn-rich composition is a universal requirement when

aiming at as high as possible PCEs for CZTSSe solar cells [61-63, 85, 86]. Similarly, best-performing CIGSe solar cells are exclusively achieved for an overall Cu-poor composition because the deviation from stoichiometry towards Cu-poor composition induces electronically benign copper vacancies (V_{Cu}^{-}) that are giving rise to the p-type conductivity [87] while the formation of detrimental binary Cu phases is inhibited. In CZTSSe the Cu deficiency also creates benign intrinsic V_{Cu}^{-} point defects and additionally reduces the probability of detrimental defects like Sn_{Cu}^{3+} to form [85, 86, 88]. Maintenance of charge balance inevitably leads to the formation of additional intrinsic point defects that together constitute the defect complexes [2-4, 89-91] (cf. chapter 1.5.3 for more details). One possible complementary point defect is Sn_{Cu}^{3+}, which however is known to create a deep defect level that heavily deteriorates the solar cell performance [86]. The composition must therefore be chosen such that only benign or harmless point defects do preferentially occur [86] which is achieved for Cu-poor and Zn-rich composition resulting in the $[V_{Cu}^{-} + Zn_{Cu}^{+}]$ defect complex [2].

In addition, it is particularly challenging to synthesize single-phase kesterite due to its very small existence region [92-94]. Even though the kesterite-type structure tolerates huge deviations from stoichiometry, secondary phases are readily formed already for slight deviations from stoichiometry. However, while Zn(S,Se) secondary phase is typically formed upon synthesizing Cu-poor and Zn-rich absorber layers it is still under debate whether or not its presence is generally harmful to the PV performance, but certainly depends on its amount and spatial distribution within the absorber layer [95-100]. Cu-S,Se and Sn-S,Se (Ge-S,Se) binary phases, on the other hand, are known to have a detrimental effect on the overall performance though [72, 101, 102]. While one could argue that these phases are prevented from being formed for the targeted composition it was found that the CZTSSe phase decomposes when in contact with the metallic molybdenum back electrode [103]. In addition to a typically thick $Mo(S,Se)_2$ layer formed upon chalcogenization [103-105] several secondary phases are potentially be introduced leading to parasitic resistances and other loss mechanisms related to detrimental band alignments, which again considerably contributes to the V_{oc} deficit. Spatial band gap fluctuations

induced by Cu-Zn disorder also represents a major source for the low V_{oc} [106, 107] and is a specialty of the kesterite-type material [9, 108-111].

Regarding the V_{oc} deficit promising advancements could also been made by including small amounts of germanium into the CZTSSe absorber layer, leading to an overall enhancement of the performance for the employed process [70, 112, 113]. The solid solution (CZGSSe) between $Cu_2ZnGeSe_4$ (CZGSe) and Cu_2ZnGeS_4 (CZGS) with tin being entirely replaced by germanium is referred to as wide-band gap semiconductor and the selenium end-member CZGSe will eventually be the subject of this thesis. While the subsequent chapter will outline prospective application fields of CZGSe, is the main intention of this thesis a detailed analysis of its crystal structure with particular emphasis on cation distribution and point defects with respect to different off-stoichiometries. Only little or vague knowledge existed about the kind and density of structural point defects in dependency of the various stoichiometric deviations, and no secured statement could even be made regarding the actual crystal structure (space group) of CZGSe. This thesis aims at elucidating the puzzle regarding the crystal structure and at providing comprehensive insights about the cation distribution by means of neutron diffraction from which the density of the existing point defect species is eventually being deduced.

1.3 Beyond fundamental research: prospective applications of CZGSe kesterite-type compound semiconductors

Although it must be noticed that germanium is classified a critical raw material [44] which belongs to the rarer and most expensive elements [42, 45] (cf. Figure 1-5), the usage of Ge is nevertheless deemed tantalizing as it widens the application range beyond the level classical CZTSSe is constrained to. A widening of the application range can mainly be achieved by altering the optoelectronic properties, specifically by widening the band gap. The band gap of $Cu_2ZnGeSe_4$ (CZGSe) is around 1.5 eV [114, 115], the one of the sulfur-counterpart Cu_2ZnGeS_4 (CZGS) is even around 2.2

eV [116, 117] and, thus, each increased by at least 500 meV in comparison with their Sn analogues (Figure 1-7).

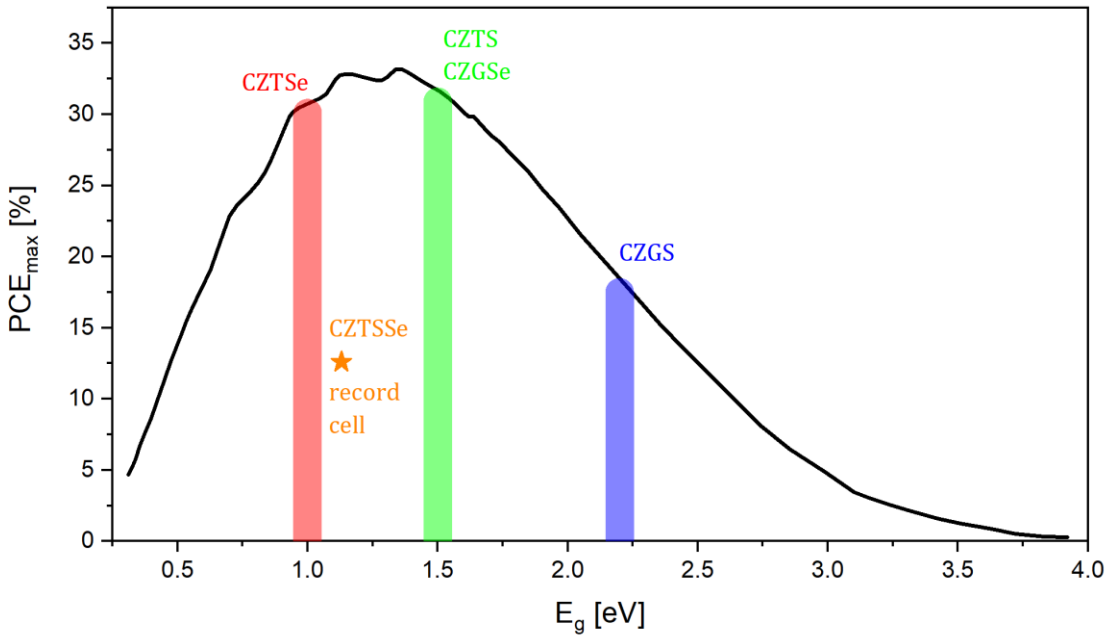

Figure 1-7 PCE vs. E_g curve for an AM1.5G spectrum [28] including the band gap energies of the end-members CZTSe, CZTS, CZGSe and CZGS [36, 50-52, 114-117]. The widths of the colored bars qualitatively reflect the margins of the reported band gap values. In order to achieve efficient solar cells the band gap needs to be in between the CZTSe and CZTS end-members as is the case for the current CZTSSe record solar cell [84] whereas higher band gap energies allow consideration for other applications.

As can be seen in Figure 1-7 a band gap optimally adjusted with respect to the solar spectrum can be obtained for a solid solution between CZTSe and CZTS whereas CZGSe and CZGS are considerably off the highest possible PCE, which naturally further limits the achievable photovoltaic performance. This however only holds for single-junction solar cells for which CZTSSe would clearly be the better choice. A possibility to exceed the Shockley-Queisser limit is given by multi-junction (tandem) solar cells comprising a stack of at least two differently composed solar cells. Self-evidently, the stacking sequence must be chosen such that it facilitates an optimal exploitation of incident photons for a broad spectral distribution. The solar cell with the widest band gap therefore constitutes the upper part and the solar cells underneath have to have band gaps that become successively narrower. This device architecture allows the collection of a large portion of the solar spectrum giving rise to power conversion efficiencies surpassing the Shockley-Queisser limit. For instance, a new PCE world record of 47.1 % was recently reported for a six-junction

solar cell using a stack of differently alloyed GaP/GaAs ($III-V$) layers with light concentrators on top [118]. However, this solar cell design and the high requirements on absorber quality and compositional fine-tuning leads to immense expenses, hence remaining a large-scale installation out of consideration but being of particular value for rather exotic applications like aerospace. With wide-band gap CZGSSe the possibility is given to manufacture tandem solar cells possessing a simpler design with polycrystalline absorber layers, even if the PCE will by far not reach those of epitaxial/single-crystalline $III-V$-based tandem solar cells. As of now, however, no tandem solar cell comprising CZGSSe has been reported.

Apart from the conversion of solar energy to electric power kesterite-type materials are also suggested for the conversion of heat to electric power owing to their promising thermoelectric properties [119-121]. In thermoelectric materials a voltage is created by a temperature difference (Seebeck effect) [122] allowing for instance to partly recover waste heat. Vice versa, if a voltage is applied a change in temperature can be induced (Peltier effect) [123] that allows cooling without refrigerant and mechanical parts and offers thus cooling devices with small sizes, yet showing rather poor efficiencies [124]. Another application specifically for wide-band gap materials again related to solar energy utilization is the production of solar fuels, that is, hydrogen as for instance needed for hydrogen fuel cells. The minimum energy necessary for the dissociation $H_2O \rightleftharpoons 2H^+ + O^{2-}$ is 1.23 eV [125], though, higher band gap energies even of around 2 eV [125] are required for high-efficient photocatalytic water splitting, which is eventually provided by wide-band gap S-rich CZGSSe [114-117]. In fact, there are not many materials existing that offer non-toxic or abundantly available constituents, or a direct band gap with energies suitable for being used as top cell in tandem devices, or that is required for efficient photocatalytic water splitting. Semiconducting materials like Se [126], BP [127], AlAs [128], and GaP [129] do have applicable band gap energies but are indirect semiconductors mostly consisting of rare elements. Suitable direct semiconductors like ZnTe [130], CdZnTe [131], AlGaAs [132], InGaP [133] and AlGaAs [134] do all contain rare and some even toxic elements. Because CZGSSe is mainly composed of abundant and non-toxic elements it potentially becomes a superior alternative featuring better sustainability and cost-efficiency for specific applications.

1.4 The quaternary Cu-Zn-Sn(Ge)-X system: features and phase relations

Quaternary selenide compounds employing different cations were synthesized from melt by Matsushita et al., reporting on the melting point for $Cu_2ZnGeSe_4$ as to be $T_m = 890°$ C [135] which eventually served as reference for the maximum temperature used for the solid-state synthesis as described in chapter 2.1. A thoroughly investigation of the phase diagram of the Cu_2GeSe_3 – ZnSe system was then elaborated by Parasyuk et al. [136] and the phase equilibria in the Cu_2Se – ZnSe – $GeSe_2$ system were investigated by Romanyuk and Parasyuk [94]. Similar work was done for the Sn-containing system by Dudchak and Piskach [92] and by Olekseyuk et al. [137], respectively. The studies about the Sn-containing system are however more detailed regarding the binary sections, thus the $Cu_2(S,Se)$ – Zn(S,Se) – $Sn(S,Se)_2$ system [92, 137] is, in principle, considered applicable for CZGSe too. For generalization purposes the anions S and Se will subsequently be represented by the capital letter 'X'. A graphical representation of a system comprising four chemical elements is achieved using a composition tetrahedron with the respective elements located at the apices (Figure 1-8a). More plain and clearer however is the reduction to a two-dimensional view by projecting the pseudo-ternary section of the binary components Cu_2X – ZnX – GeX_2 (Figure 1-8b).

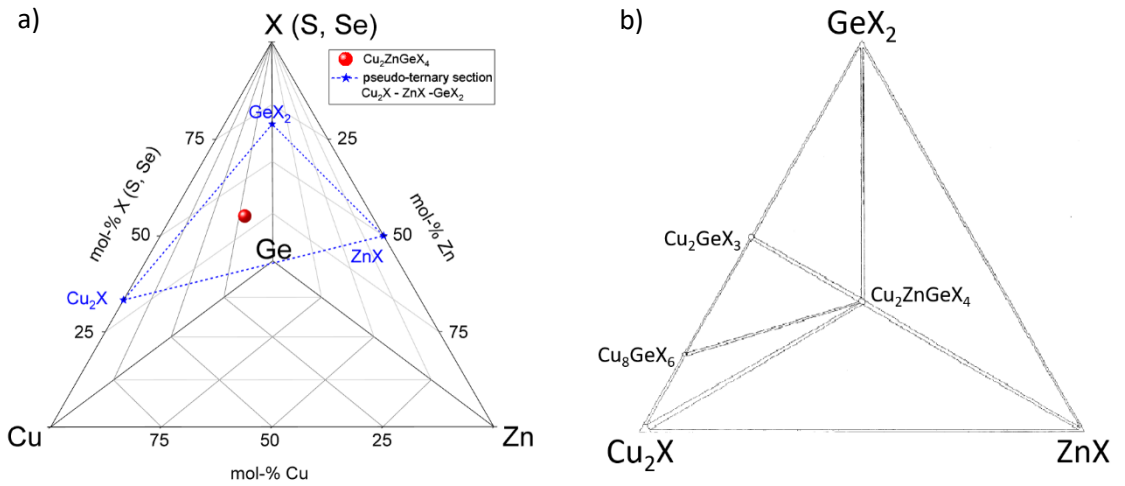

Figure 1-8 a) The quaternary Cu-Zn-Ge-X diagram including the location of stoichiometric CZGX and the pseudo-ternary section given by the binary components. b) Projection of the pseudo-ternary section [94] showing the existence region of CZGX and occurring ternary phases along the Cu_2X – GeX_2 section.

It can be seen from Figure 1-8a that stoichiometric Cu_2ZnGeX_4 contains 25 mol% copper, 12.5 mol% zinc, 12.5 mol% germanium and 50 mol% sulfur/selenium ('X'). In terms of binary components stoichiometric CZGX consists of 33.33 mol% Cu_2X, 33.33 mol% ZnX and 33.33 mol% GeX_2 and is therefore located at the center of the ternary diagram (Figure 1-8). In the solid state the binary components are generally subject to low solubility among each other owing to the different oxidation states of their respective cations. At lower (room temperature) and even moderate temperatures the solubility of ZnX both in Cu_2X and SnX_2 (GeX_2), and vice versa, does not exceed a few mol% giving rise to large miscibility gaps [92, 137]. No thermodynamically stable ternary phases are forming neither along the pseudo-binary section Cu_2X – ZnX [137] nor the pseudo-binary section SnX (GeX) – ZnX [138]. There is indeed no complete solubility in the pseudo-binary section Cu_2X – SnX (GeX) but some ternary phases were found to be stable [94, 137], with Cu_2SnX_3 (Cu_2GeX_3) being most relevant.

Accordingly, single-phase quaternary Cu_2ZnSnX_4 can therefore be obtained from:

- pure elements: 2Cu + Zn + Sn +4X (refer to Figure 1-8a)
- binary compounds: Cu_2X + ZnX + SnX_2
- ternary and binary compounds: Cu_2SnX_3 + ZnX

Although there are additional reaction paths also leading to quaternary Cu_2ZnSnX_4, they all go along with the formation of secondary phases and will not be further considered since single-phase Cu_2ZnSnX_4 is desired. In fact, Cu_2ZnSnX_4 exhibits a rather small existence region [92, 94, 137] which already makes the unintentional formation of secondary phases very probable. In conjunction with the different possible oxidation states specifically of Cu and Sn (Ge) various secondary phases may form upon synthesis (and decomposition) of Cu_2ZnSnX_4. Depending on the partial pressure of X during the synthesis CuX, Cu_9X_5 ($Cu_{1.8}X$) and SnX (GeX) are possibly formed instead of Cu_2X and SnX_2. The complexity of the quaternary system with its numerous secondary phases becomes therefore a particular challenge when aiming at off-stoichiometric and possibly single-phase Cu_2ZnSnX_4.

1.5 Properties of the kesterite-type structure

1.5.1 The crystal structure of kesterite: an example for good crystallographic practice

Kesterite is a naturally occurring mineral denominating the Zn-rich part [8, 139] of the quaternary $Cu_2Zn_xFe_{1-x}SnS_4$ [139, 140] compound and that crystallizes in space group (s.g.) $I\bar{4}$ [139]). Upon a higher iron level [8, 139, 140], the cations will change their arrangement with the resulting crystal structure being in accordance with space group $I\bar{4}2m$ [140] and the mineral being named stannite. Both minerals are eponym for the respective structure-type, referring compounds being isostructural with kesterite to as kesterite-type (or 'kesterites') and those being isostructural with stannite to as stannite-type (or 'stannites'). The stannite-type structure also appears to be the favored structure if either cadmium or mercury [141, 142]) is the dominant divalent cation. An X-ray diffraction study conducted in 1967 [143] on differently composed single crystals revealed the basic structural information of the various quaternary compounds but the crystal structure could not be unraveled for every end-member, or was mistakenly reported to be stannite-type. For a long period, the actual space group of kesterites was under debate, though often stated to be $I\bar{4}2m$ [141, 143] owing to the differentiation problem in X-ray diffraction connected with isoelectronic Cu^+ and Zn^{2+}. However, both minerals are commonly found as two-phase intergrowths [139] indicating a preference of being segregated as Zn-rich kesterite and Fe-rich stannite. The compositional discontinuity in the Fe/Zn ratio found for natural kesterite and stannite specimens led to the assumption of a structural break between them, which along with unreasonable thermal parameters obtained from structure refinements using the $I\bar{4}2m$ structural model made the space group $I\bar{4}$ appearing more plausible [139]. This has further been confirmed through an observable difference between *hkl* and *khl* intensities ($I_{hkl} \neq I_{khl}$), thus, pointing once more to space group $I\bar{4}$ [139] because these intensities would be equal for space group $I\bar{4}2m$: $I_{hkl} = I_{khl}$. However, since lattice plane distances d_{hkl} and d_{khl} are equal in a tetragonal crystal system a difference in intensity can only be observed in case of single-crystal XRD [139]. Hall et al. assumed that Cu and Zn

(and/or Fe) are orderly distributed on structural sites 2c and 2d [139], respectively, while neutron diffraction experiments indeed confirmed that kesterite crystallizes in space group $I\bar{4}$ [8, 9, 144] but revealed a disordered distribution of Cu and Zn between 2c and 2d Wyckoff positions [8, 9, 144]. Probable reasons for this discrepancy are both the different methods (X-ray vs. neutron diffraction) applied with X-ray diffraction being incapable of discriminating isoelectronic ions and the different kind of investigated specimens (natural vs. synthetic) [8]. First principle calculations predicted the kesterite-type structure (s.g. $I\bar{4}$) to be the most stable one, however, with the stannite-structure (s.g. $I\bar{4}2m$) being only slightly higher in energy [52, 145]. This is due to the almost equal cation radii of tetrahedrally coordinated Cu^{+} and Zn^{2+} [146] in conjunction with the similar local structural environment of the 2c and 2d Wyckoff positions, which eventually allows them to easily interchange between these positions already at moderate temperatures [109, 110, 147, 148]. Above the critical temperature T_c (~200° C < T_c < 260° C [109, 110, 147]) the copper and zinc atoms are randomly distributed among 2c and 2d Wyckoff positions, hence giving rise to the order-disorder transition leading to higher symmetry (s.g. $I\bar{4}2m$) [8, 109, 110, 149]. It was pointed out that the extent of Cu-Zn disorder present in kesterite very much depends on its cooling history and cation ordering is indeed subject to a long equilibration time [109, 110, 147]. Differences between natural kesterite and its synthetic analogues can thus be expected. Beside the order-disorder transition which is restricted to Cu and Zn exchanging between 2c and 2d sites a complete random distribution of all cations over every position will result once the temperature becomes high enough to even out the energy barrier given by ionic radii, valence state and binding energy. In-situ synchrotron measurements performed on CZTS demonstrated the occurrence of a phase transition at ~865° C from Cu-Zn (2c-2d) disordered kesterite (s.g. $I\bar{4}2m$) to the zincblende-type structure (s.g. $F\bar{4}3m$) with all cations being randomly distributed over every cation position. Consequently, the new Wyckoff position 4a is created as 2a, 2b, 2c and 2d become indistinguishable that coevally leads to the 4b position for the anion [149]. The relation between kesterite-type structure and zincblende-type structure will eventually be subject of the next section.

1.5.2 The adamantine compound family: the roots of the kesterite-type structure

The term quaternary compound does actually not directly refer to the composition stating on the number of different elements involved but originates from the number of structural sites hosting different ion species, which in turn feedbacks on the symmetry. For generalization purposes and to account for chemical substitutions a generic notation using capital letters and Roman numerals representing equivalent ion species and the valence state of the ions was established that replaces the element symbols used in sum formulas. The general formula of binary compounds is therefore be expressed as $A^N X^{8-N}$ which for zincblende-type compounds is written as $A^{II}X^{VI}$ (with A = divalent cations, X = chalcogen) [150]. For ternary chalcopyrite-type compounds the general notation is given by $A^I B^{III} X_2^{VI}$ [150] (with A = monovalent cation, B = trivalent cation, X = chalcogen). A stannite-type or kesterite-type quaternary compound eventually results if a third aliovalent cation species is added, which is represented by $A_2^I B^{II} C^{IV} X_4^{VI}$ (with A = monovalent cation, B = divalent cation, C = tetravalent cation, X = chalcogen).

Raising the number of constituting ion species differing in terms of, respectively, valence state and/or considerably in ionic radius (i.e. mainly for differing groups of elements) typically causes them to arrange in an increasingly ordered manner, and the symmetry to decrease. The adamantine family [48, 54] (Figure 1-9) comprises compounds that are structural derivatives of the parental diamond-type structure (s.g. $Fd\bar{3}m$) [151] which is adopted by a number of chemical elements (C, Si, Ge, Sn) as well as of some compounds and alloys. The diamond-type structure is characterized by a face-centered cube (fcc) Bravais lattice that can be viewed as two interpenetrating fcc lattices offset by $\left(\frac{1}{4},\frac{1}{4},\frac{1}{4}\right)$ fractional multiples of the unit cell edge length along all three dimensions. The general motif is given by atoms occupying half of the tetrahedral voids that constitutes a network of regular corner-shared tetrahedra. Every atom in the structure is characterized by the same Wyckoff position (8a), which conventionally is equal to the origin of the unit cell (0,0,0) and that also implies the number of formula units per unit cell, Z = 8, when fully occupied.

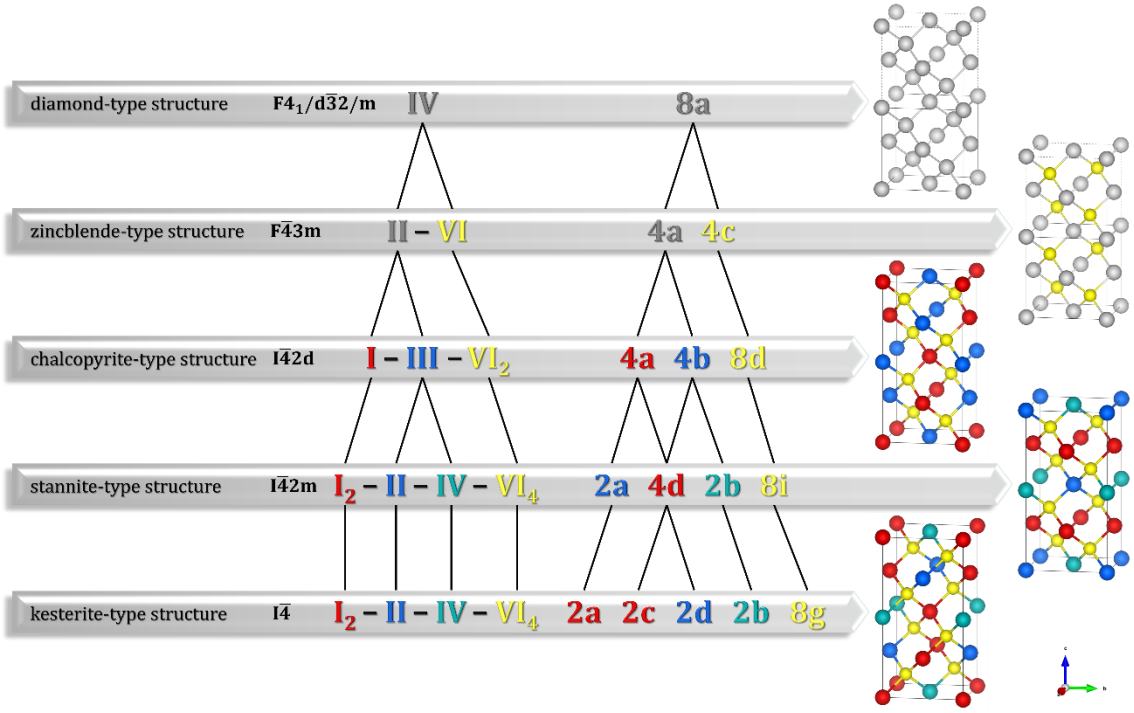

Figure 1-9 Scheme of part of the adamantine family [8, 54] of crystal structures referring to the evolution towards the kesterite-type structure. For the sake of better comparability two unit cells are shown for the cubic structures of diamond-type and zincblende-type, respectively.

Replacing the single chemical element (e.g. C) by two elements each affiliated to different groups other than the carbon group (i.e. ≠ group 14) involves the constitution of cations and anions. The previously covalent bond type therefore becomes then dominated by the ionic component and the compounds are referred to as ionic crystals. Zincblende and wurtzite (ZnS), for instance, are such ionic crystals and eponym, respectively, for the zincblende-type structure (s.g. $F\bar{4}3m$) [152] and wurtzite-type structure (s.g. $P6_3mc$) [153]. The latter is a derivative of the high-pressure hexagonal (hcp) modification of carbon (lonsdaleite) whereas the cubic zincblende-type structure is the direct successor of the (fcc) diamond-type structure. In zincblende-type ZnS the position (0,0,0) is normally assigned to the Zn^{2+} cations and the position $\left(\frac{1}{4},\frac{1}{4},\frac{1}{4}\right)$ to the S^{2-} anions, giving rise to identical fcc cation-anion sublattices but each with a different basis. As a consequence, the Wyckoff position 8a of the diamond-type structure degenerates to 4a (0,0,0) and 4c $\left(\frac{1}{4},\frac{1}{4},\frac{1}{4}\right)$ in the zincblende-type structure which corresponds with the lowering in symmetry and is referred to as binary compound.

Through incorporation of a second cation species belonging to a different group of elements the symmetry will further be reduced because the cations will energetically be forced to arrange in an increasingly ordered manner on the structural sites owing to their different valence states and/or ionic radii. This ordered distribution of the cations leads to different electrostatic interactions which eventually results in varying bond distances and bond angles. Consequently, the coordination tetrahedra become irregular and the unit cell dimensions are changing allometrically. Hence, the identity period of a cubic unit cell does not anymore apply but can instead be obtained when being duplicated along the c-axis, thereby yielding a tetragonal crystal system. In ternary compounds adopting tetragonal chalcopyrite-type structure (s.g. $I\bar{4}2d$) [150] the anion is therefore shifted off its ideal position $\left(\frac{1}{4},\frac{1}{4},\frac{1}{4}\right)$ with the *x*-coordinate becoming an independent parameter. The *y*- and *z*-coordinates basically preserve whose ideal values, though, the latter is being bisected due to the unit cell doubling along the crystallographic z-axis. The anion position 4c $\left(\frac{1}{4},\frac{1}{4},\frac{1}{4}\right)$ of the zincblende-type structure thus degenerates to the 8d $\left(x,\frac{1}{4},\frac{1}{8}\right)$ Wyckoff position and the anions thereby become coordinated by a distorted tetrahedron with a given tetragonal distortion $u = |0.25 - x|$. The 4a position (0,0,0) degenerates to 4a (0,0,0) and 4b $\left(0,0,\frac{1}{2}\right)$, respectively, giving rise to $I - III$ (e.g. Cu^{+} – In^{3+}) (001) cation planes at *z* = 0, ¼, ½, and ¾.

Finally, for the coupled substitution of the trivalent cation with a divalent and tetravalent cation, e.g. $2In^{3+} \rightarrow Zn^{2+} + Sn^{4+}$, either the stannite-type structure or kesterite-type structure will result. As outlined in chapter 1.5.1 the actual crystal structure being adopted by a quaternary chalcogenide compound $A_2^I B^{II} C^{IV} X_4^{VI}$ depends on the Zn content among the divalent cations [8, 139]. A low Zn/*II* ratio (*II* = Fe; possibly also Mn, Cd, Hg, Co [141, 154, 155], but are to be taken with caution as the stannite-type structure might have been confused with the kesterite-type structure which was a longstanding problem for CZTS too) favors the stannite-type structure (s.g. $I\bar{4}2m$) [140]. With now three different cation species involved, the cations will arrange in an even more ordered manner and the symmetry is slightly lowered from $I\bar{4}2d$ to $I\bar{4}2m$. The 4a Wyckoff position degenerates to the 2a and 4d position, the 4b Wyckoff position degenerates to the 4d and 2b position, which is

accompanied by the introduction of additional independent anion coordinates and eventually yields the corresponding anion position 8i (x, x, z). The cations again are arranged in (001) planes comprising, respectively, layers of $II - IV$ (e.g. Zn^{2+} – Sn^{4+}) at z = 0 and ½ as well as $I - I$ (e.g. Cu^{+} – Cu^{+}) at z = ¼ and ¾.

For a Zn/Fe ratio >2.3 [8] it was demonstrated that the quaternary compound tends to adopt the kesterite-type structure (s.g. $I\bar{4}$) which by DFT calculations was also shown to be the ground state configuration for the Zn end-member [52, 145] (CZTS and CZTSe). Owing to a different distribution as well as partial ordering of Cu^{+} and Zn^{2+} the symmetry decreases from $I\bar{4}2m$ to $I\bar{4}$ with the 4d Wyckoff position degenerating to 2c and 2d position, respectively. This ordering scheme leads to layers of $I - IV$ (e.g. Cu^{+} – Sn^{4+}) cations at z = 0 and ½, and $I - II$ (e.g. Cu^{+} – Zn^{2+}) cations at z = ¼ and ¾ in the (001) plane. As a result, the anion becomes shifted off the ideal position along any direction, thus, all anion coordinates are then independent parameters which eventually constitute the 8g position (x, y, z). However, such a complete ordering is typically not realized as the ionic radii of Cu^{+} and Zn^{2+} as well as the local environment of their corresponding positions 2c and 2d are too similar [146], which allows them to readily interchange between these two positions. Above the critical temperature T_c for the order-disorder transition a dynamic equilibrium is reached [156] with an equal amount of both Cu^{+} and Zn^{2+} swapping between 2c and 2d position that ultimately creates the 4d Wyckoff position instead. This configuration is referred to as disordered kesterite which is then described by space group $I\bar{4}2m$. Once the temperature falls below T_c the partial ordering of Cu^{+} and Zn^{2+} start to happen and the space group $I\bar{4}2m$ does not hold anymore regardless of the extent of ordering. Nevertheless, their similar radii and comparable positions effectuate only little energy differences for Cu^{+} and Zn^{2+} both for 2c and 2d position, which still facilitates the interchange of Cu^{+} and Zn^{2+} between the 2c and 2d positions. This results in a long-lasting Cu-Zn disorder that tends to approach the ordered state as temperature decreases over long equilibrations times.

1.5.3 Implications of the off-stoichiometry towards intrinsic point defects and defect complexes

Structural defects directly affect the generation, separation and recombination of charge carriers (electron-hole pairs) and have thus a great impact on the electronic properties of solar cells. As mentioned in section 1.2 solar cell performance considerably benefits from off-stoichiometric Cu-poor and Zn-rich absorber composition [61-63]. In general, any deviation from stoichiometry is equivalent to intrinsic doping that gives rise to a specific conductivity type. It could be shown that the crystal structures of ternary [157] and quaternary [2-4, 89-91] chalcogenides tolerate even huge deviations from stoichiometry while still keeping their respective structures, which eventually allows to host a large population of electronically benign point defects like V_{Cu}^{-} and Cu_{Zn}^{-} [85, 86]. In terms of the conceptual off-stoichiometry types such intrinsic point defects can however not be considered alone but always require at least another associated point defect to maintain charge neutrality.

In terms of quaternary chalcogenides one can imagine the composition either to be poor, rich, or stoichiometric (or constant), each for I, II, IV (e.g. Cu, Zn, Ge) cations with the anion being normalized to them, which results in $3^3 = 27$ combinations for no constraints. However, not all of the cation substitution processes are allowed as the majority violates the necessary boundary condition of achieving charge balance (e.g. Cu-poor, Zn-poor, and Ge-poor), which reduces the number of possible cation substitution reactions to 12 different combinations for off-stoichiometric trends [2-4, 89-91] (comprising six pairs of complementary reactions) that enables self-passivation through corresponding defect complexes. Figure 1-10a shows the ternary diagram of the binary components that includes the paths for the 12 off-stoichiometry types A – L [2-4, 89-91]. However, a clearer depiction with only two axes can be chosen since the anion is always normalized to the summed cations and the composition of thin films typically refers to cation ratios (Figure 1-10b) unless different anions are included. Hence, cation ratio plots will hereinafter be shown instead of ternary diagrams.

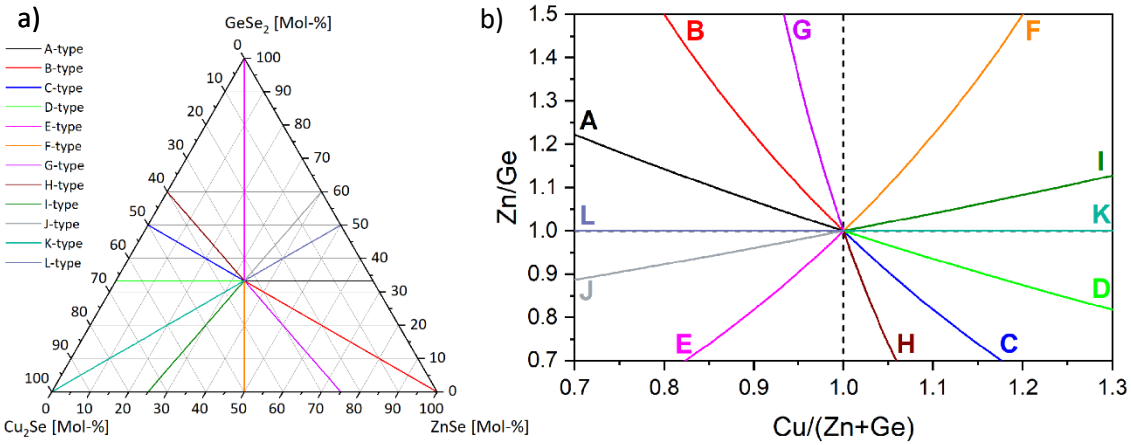

Figure 1-10 The 12 off-stoichiometry (defect) type lines included in a) ternary diagram and b) cation ratio plot.

The off-stoichiometry types A – D were proposed by Lafond et al. [2] which were considered to be the most realistic ones but not claimed to be exhaustive. As this work had a strong reference to PV application the focus was mainly put on the Cu-poor/Zn-rich quadrant of the cation ratio plot where the A- and B-type can be found (Figure 1-10b). The reverse reactions of the corresponding A- and B-type cation substitution processes directly deliver the D- and C-type, respectively, which plot in the diametrical Cu-rich/Zn-poor quadrant (Figure 1-10b).

Subsequent studies on synthesized kesterite-type powder specimens suggested the existence of additional cation substitution reactions: The E-type [4] and its counterpart F-type [3] for which two different defect complexes are proposed each, the G-type [90] and its complementary H-type [90], as well as the each opposing I- and J-type [89] and K- and L-type [91]. A compilation of the 12 off-stoichiometry types with their corresponding compositions, cation substitution reactions, and resulting defect complexes is given in Table 1-1 and schematically portrayed in Figure 1-11.

Table 1-1 Overview of the off-stoichiometry types A – L.

Type	Composition	Cation substitution reaction	Defect complex	Chemical formula
A	Cu-poor Zn-rich Ge-const.	$2Cu^{+} \rightarrow Zn^{2+}$	$V_{Cu}^{-} + Zn_{Cu}^{+}$	$Cu_{2-2a}Zn_{1+a}GeSe_4$
B	Cu-poor Zn-rich Ge-poor	$2Cu^{+} + Ge^{4+} \rightarrow 3Zn^{2+}$	$2Zn_{Cu}^{+} + Zn_{Ge}^{2-}$	$Cu_{2-2b}Zn_{1+3b}Ge_{1-b}Se_4$
C	Cu-rich Zn-poor Ge-rich	$3Zn^{2+} \rightarrow 2Cu^{+} + Ge^{4+}$	$2Cu_{Zn}^{-} + Ge_{Zn}^{2+}$	$Cu_{2+2c}Zn_{1-3c}Ge_{1+c}Se_4$
D	Cu-rich Zn-poor Ge-const.	$Zn^{2+} \rightarrow 2Cu^{+}$	$Cu_{Zn}^{-} + Cu_{i}^{+}$	$Cu_{2+2d}Zn_{1-d}GeSe_4$
E	Cu-poor Zn-poor Ge-rich	$2Cu^{+} + Zn^{2+} \rightarrow Ge^{4+}$	(1) $V_{Cu}^{-} + Ge_{Zn}^{2+}$ (2) $Ge_{Cu}^{3+} + V_{Cu}^{-} + V_{Zn}^{2-}$	$Cu_{2-2e}Zn_{1-e}Ge_{1+e}Se_4$
F	Cu-rich Zn-rich Ge-poor	$Ge^{4+} \rightarrow Zn^{2+} + 2Cu^{+}$	(1) $Zn_{Ge}^{2-} + 2Cu_{i}^{+}$ (2) $Cu_{Ge}^{3-} + Cu_{i}^{+} + Zn_{i}^{2+}$	$Cu_{2+2f}Zn_{1+f}Ge_{1-f}Se_4$
G	Cu-const. Zn-rich Ge-poor	$Ge^{4+} \rightarrow 2Zn^{2+}$	$Zn_{Ge}^{2-} + Zn_{i}^{2+}$	$Cu_2Zn_{1+2g}Ge_{1-g}Se_4$
H	Cu-const. Zn-poor Ge-rich	$2Zn^{2+} \rightarrow Ge^{4+}$	$Ge_{Zn}^{2+} + V_{Zn}^{2-}$	$Cu_2Zn_{1-h}Ge_{1+1/2h}Se_4$
I	Cu-rich Zn-const. Ge-poor	$Ge^{4+} \rightarrow 4Cu^{+}$	$Cu_{Ge}^{3-} + 3Cu_{i}^{+}$	$Cu_{2(1+2i)}ZnGe_{1-i}Se_4$
J	Cu-poor Zn-const. Ge-rich	$4Cu^{+} \rightarrow Ge^{4+}$	$Ge_{Cu}^{3+} + 3V_{Cu}^{-}$	$Cu_{2-2j}ZnGe_{1+1/2j}Se_4$
K	Cu-rich Zn/Ge = 1= const.	$Zn^{2+} + Ge^{4+} \rightarrow 6Cu^{+}$	$Cu_{Zn}^{-} + Cu_{Ge}^{3-} + 4Cu_{i}^{+}$	$Cu_{2+6k}Zn_{1-k}Ge_{1-k}Se_4$
L	Cu-poor Zn/Ge = 1 = const.	$6Cu^{+} \rightarrow Ge^{4+} + Zn^{2+}$	$Zn_{Cu}^{+} + Ge_{Cu}^{3+} + 4V_{Cu}^{-}$	$Cu_{2-2l}Zn_{1+1/3l}Ge_{1+1/3l}Se_4$

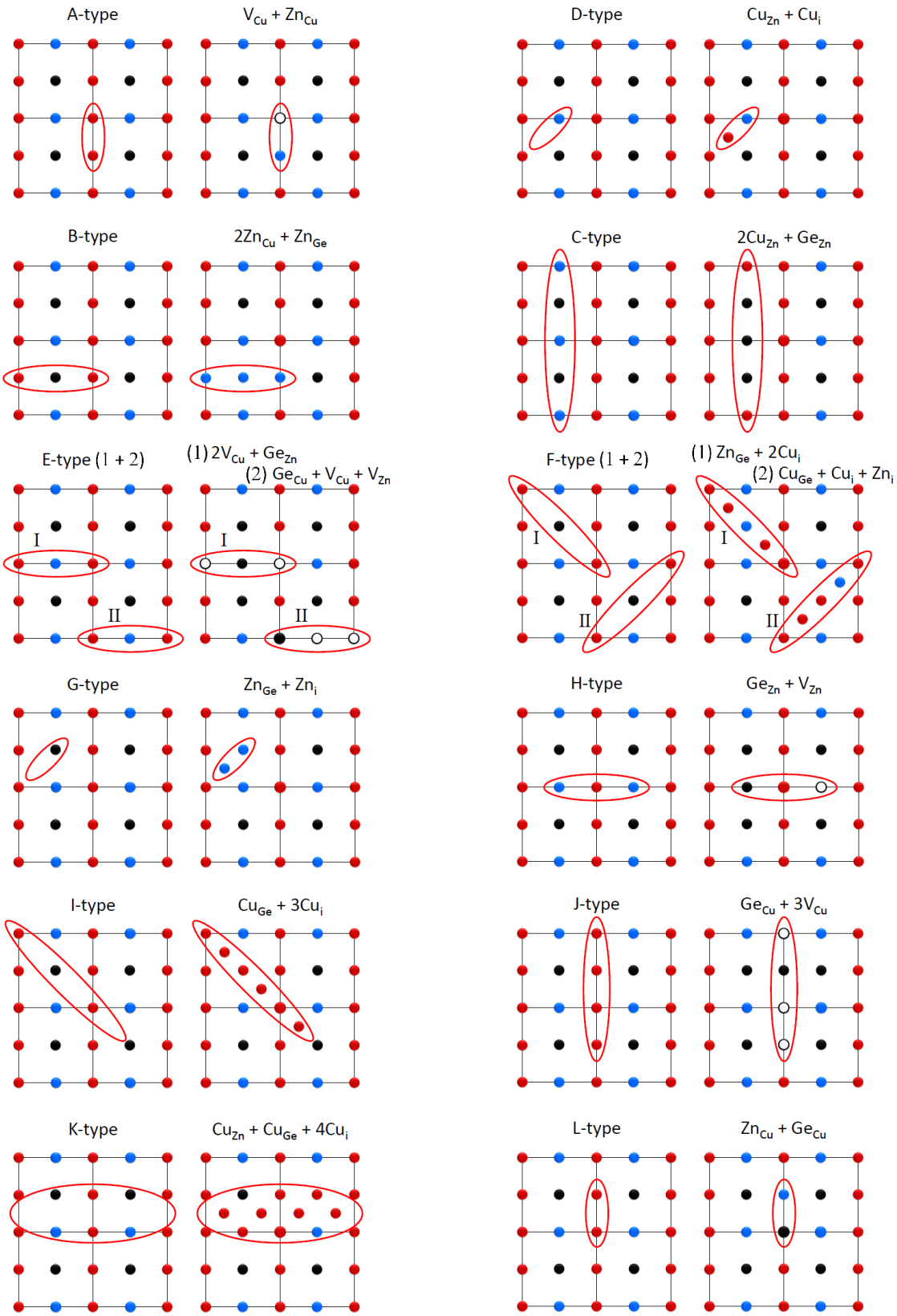

Figure 1-11 The 12 off-stoichiometry types illustrated by a composite of the cation planes, respectively, at z = 0 and 0.25 within two-dimensional representations of the CZGSe unit cell projected along [001] direction. Red ovals do highlight the stylized cation substitution processes. Each row comprises the respective complementary reactions. For better visibility four unit cells are shown in each case and anions are excluded (red = copper, blue = zinc, black = germanium). (Modified after [3])

First principle calculations performed for CZTS and CZTSe demonstrate that certain point defects have an overall low formation energy for various chemical potentials of the cations and are likely be present even for stoichiometric composition [85, 86]. The intrinsic p-type conductivity of kesterite-type semiconductors is for instance attributed to a high population of copper vacancies V_{Cu}^{-} and particularly to the Cu_{Zn}^{-} antisite defect [85], with the latter being the lowest-energy acceptor defect for any chemical potential (Figure 1-12a). In addition, the ionization levels of V_{Cu}^{-} and Cu_{Zn}^{-} in the band gap are very shallow and are thus resulting in a weak impact on the electronic structure [85, 86] (Figure 1-12b). Seen like this, their low formation energy in conjunction with their benign electronic behavior is ultimately key for this material class to be considered for PV applications at all. Another fortunate instant is the rather high formation energy for most of the detrimental point defects creating deep donor levels like Sn_{Cu}^{3+} (Ge_{Cu}^{3+})and Sn_{Zn}^{2+} (Ge_{Zn}^{2+}) or deep acceptor levels like V_{Sn}^{4-} (V_{Ge}^{4-}) [85]. On the other hand, the acceptor antisite defect Cu_{Sn}^{3-} shows the lowest formation energy among the defects creating deep states in the band gap [85] acting as recombination centers and can at least partly be credited responsible for deteriorated electronic properties (Figure 1-12a & b). To date, however, only few and less detailed calculations were done for CZGSe [158] and, as for the phase relations discussed in section 1.4, the results available for CZTSe are considered reasonably comparable for CZGSe.

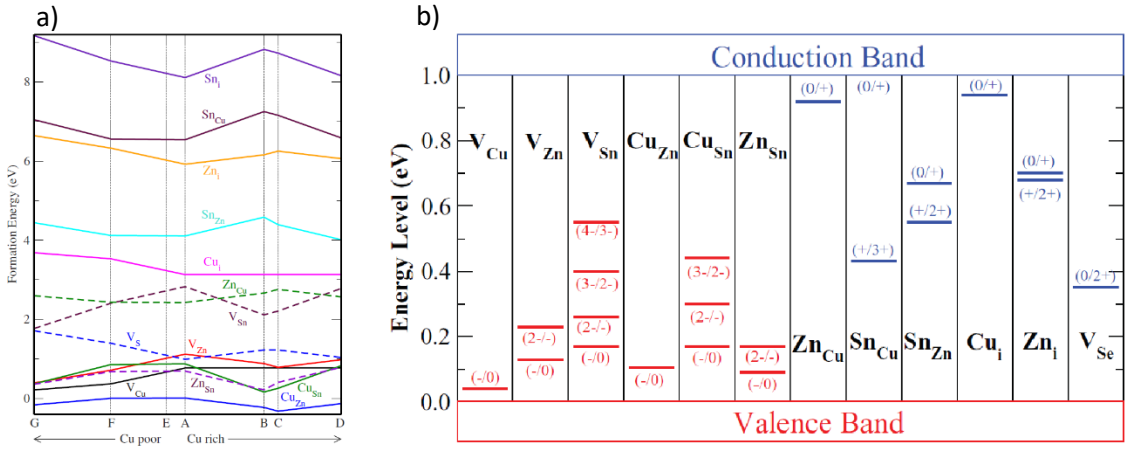

Figure 1-12 a) Formation energy of intrinsic point defects (for CZTS) in dependence of the chemical potential (taken from [85]) and b) ionization levels of intrinsic point defects in the band gap of CZTSe (taken from [86]).

Isolated acceptor and donor defects can however attract and compensate each other, giving rise to defect clusters which are charge-neutral and do therefore not contribute to the overall charge carrier concentration [86]. Since every physical system tends to achieve charge-neutrality the overall formation energy of defect clusters is considerably lower than the summed formation energy of the respective isolated point defects [86]. Hence, a distinction can be made between structural defects that are charge-compensated and those that are electronically active with the latter being generally lower populated. The lowest overall formation energy is obtained for the $[Cu_{Zn}^{-} + Zn_{Cu}^{+}]$ defect cluster [86] owing to their similar ionic radii [146] and the small difference in their respective (and favored) valence state (Figure 1-13a). This defect cluster represents the Cu-Zn disorder, and its small formation energy over a number of chemical potentials explains its facile generation as well as its long persistence. Furthermore, the similarities between Cu^{+} and Zn^{2+} cause this defect cluster to only have a minor impact on the electronic structure whereas the $[Sn_{Cu}^{3+} + Cu_{Sn}^{3-}]$ and $[Zn_{i}^{2+} + Zn_{Sn}^{2-}]$ defect clusters are significantly narrowing the fundamental band gap [86] and are particularly harmful to the optoelectronic properties (Figure 1-13b).

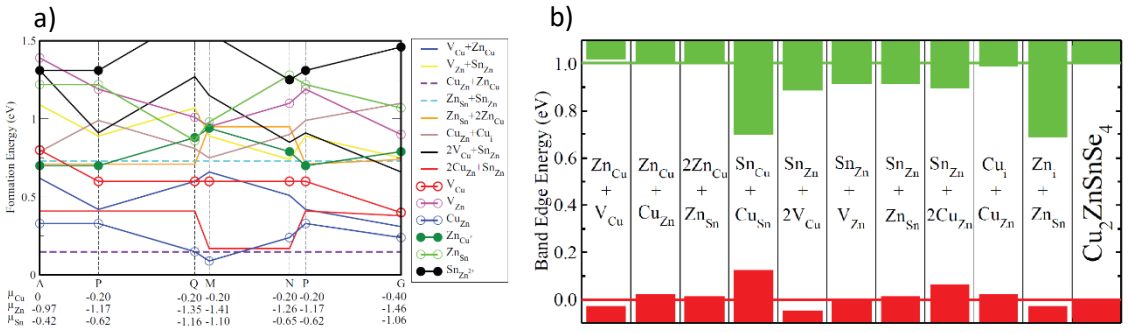

Figure 1-13 a) Formation energy of defect clusters and low-energy point defects in CZTSe as a function of the chemical potential and b) the calculated shifts of VBM and CBM caused by different defect cluster (Figure a) & b) taken from [86]).

2 Experimental

2.1 Material: synthesis by solid-state reaction

A detailed structural analysis can best be achieved using single crystals. However, the synthesis of single crystals is quite intricated and their analysis specifically by means of neutron diffraction somewhat more complex, while single crystal diffractometers at neutron sources are generally fewer available. Apart from that, potential applications are based on polycrystalline kesterite-type compounds rendering bulky powder samples possibly including secondary phases and inhomogeneities more valuable in terms of phase and structure-property relations, respectively. Moreover, powder samples may serve as a better reference providing insights into some materials properties that cannot directly be obtained from the functional layers in devices itself owing to their small scattering volumes that are inappropriate for neutron diffraction. Synthesis of powder specimens by solid-state reaction enables enough sample material as well as reasonable sample and grain statistics to better reflect the wide variations in off-stoichiometric compositions in the quaternary CZGSe compound. For the analytical methods to be applied aiming at accessing robust information about chemical composition as well as the crystal structure with particular emphasis on cation distribution and point defect species the synthesis of powder specimens is therefore considered most fruitful.

In total eight sample series are synthesized comprising 40 powder samples with a predefined deviation from stoichiometry according to the off-stoichiometry types A, B, C, D, E, and F [2-4] as well as another seven samples intentionally targeting the stoichiometric composition. As an attempt to test a different approach upon synthesis two series of A-type (A-1 and A-2) and C-type (C-1 and C-2) samples are synthesized, each with the same stoichiometric deviational steps but with different pre-treatment of the germanium metal pieces used to synthesize the CZGSe samples. In order to enhance the reactivity, the germanium pieces are pre-milled in case of the A-2 and the C-2 series. At the time of materials preparation, the off-stoichiometry types G to L were not established and are thus not considered for

synthesis. Figure 2-1 depicts the cation ratio plot with the off-stoichiometry type lines A to F and the targeted composition of the powder specimens.

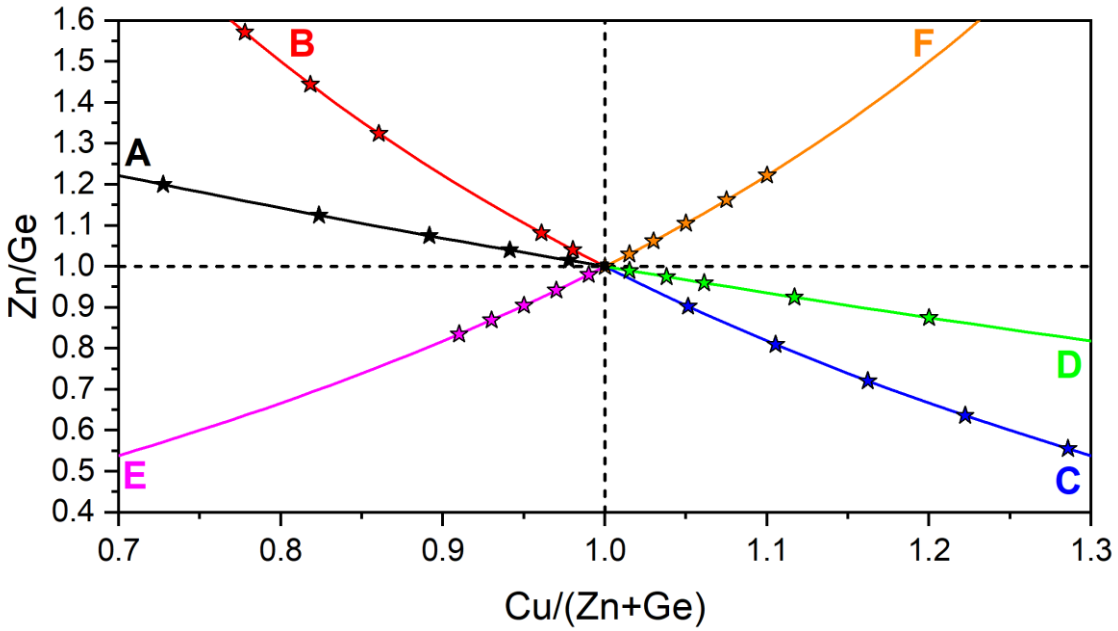

Figure 2-1 Cation ratio plot showing the successive increase in off-stoichiometry for each sample series. A total of 47 powder samples are synthesized with seven samples located at the stoichiometric point and the A- and C-type series each being synthesized in two batches.

The preparation of the samples is done employing pieces of high-purity elements (99.999 %; 5N) of copper, zinc, germanium and selenium which are weighed in using a high-precision balance with selenium however being provided slightly in excess in order to facilitate the complete reaction of the cations. The excess selenium at most amounts for 3 wt.-% as the elevated temperatures required for the elements to react will render the selenium partial pressure critical for the sealed glass ampoules. Depending on the sample series the total weight of each sample is between 4 g and 8 g. After the weighing the elements are filled into a pyrolytic carbon vessel which is then placed into a glass ampoule. For the intended reaction to happen it is of crucial importance to reduce the oxygen partial pressure as oxygen would compete against the reaction of the metals with selenium. Hence the glass ampoules are connected to a high-performance pumping station and evacuated down to 10^{-5} mbar. The glass ampoule is then sealed using an oxyhydrogen torch which however necessitates simultaneous cooling of the ampoule's tip with liquid nitrogen to prevent selenium from being sublimated and to be ultimately drawn off by the

pumping station. After the sealing is tested using a vacuum indicator the silica tubes are placed in a tubular furnace and stepwisely heated up to 700° C. In order to avoid destructive overpressure exerted by selenium the temperature is slowly raised with 10 K/h and two intermediate temperature ramps are introduced. The entire heat treatment of the first reaction step takes about 24 days but typically still results in a reaction product with insufficient compositional homogeneity. Thus, a second heat treatment is required. For this purpose, the preliminary sample from the first reaction step is ground using an agate ball mill with the resulting powder being pressed into pellets. Each pellet is then placed in a silica ampoule which again is evacuated and sealed for the second heat treatment. A faster increase in temperature is now less critical as only little amounts of elemental selenium are present. After the second reaction step the pellets are ground once more to obtain the final powder specimens as being necessary for the various analysis techniques employed, which are described in chapter 2.2. Figure 2-2 depicts the essential steps of the solid-state synthesis applied. The details of the heat treatment are provided in Table 2-1.

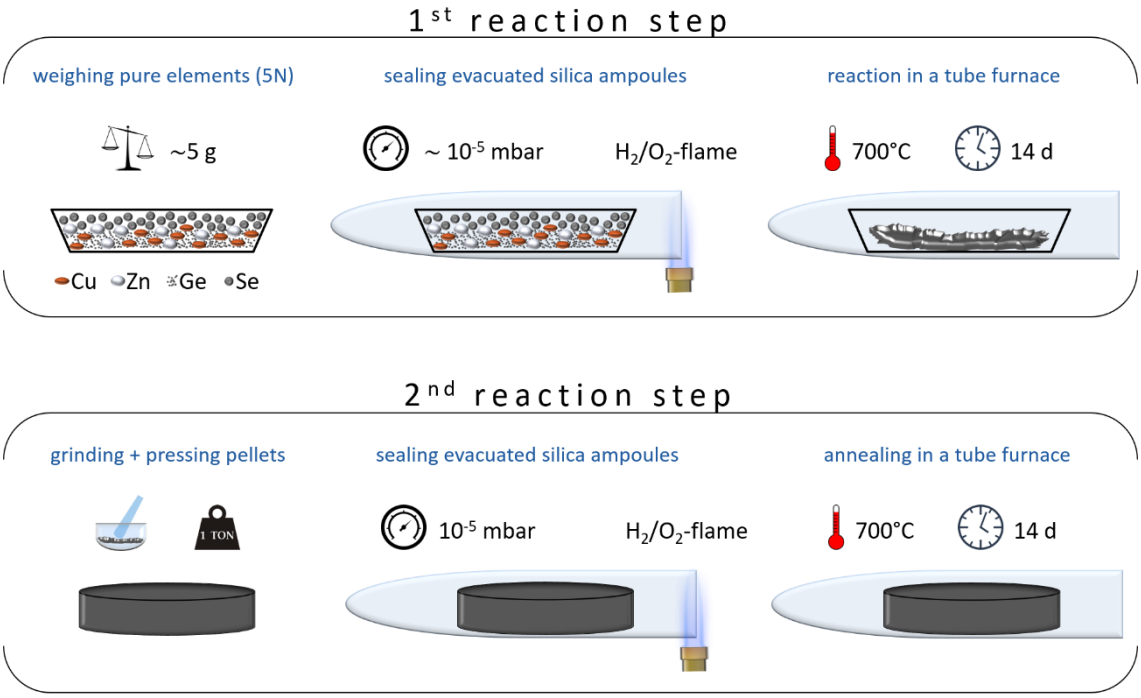

Figure 2-2 Schematic of the applied synthesis route that comprises two major steps: In the first step the reaction of the pure elements to a mixture of numerous compounds and poor homogeneity is facilitated. The second step is crucial to obtain a reasonably homogeneous and possibly single-phase quaternary compound. Thus, this second step is also referred to as homogenization step.

Table 2-1 Overview of the thermal treatment applied during the solid-state reaction.

Reaction step	Thermal treatment	Temperature [° C]	dT/dt [K h^{-1}]	Duration [d]
1st reaction step	start	RT	—	—
			10	~1
	1st heating stage	250	—	2
			10	~1
	2nd heating stage	450	—	2
			10	~1
	final heating stage	700	—	14
			10	~3
	cooling	RT	—	—
2nd reaction step	start	RT	—	—
			50	~0.5
	final heating stage	700	—	14
			10	~3
	cooling	RT	—	—
Total				~41.5

2.2 Methods: analysis of composition, crystal structure and band gap energies

2.2.1 Chemical analysis and survey of compositional homogeneity

Precise knowledge of the chemical phase composition and certainty about the chemical homogeneity of the quaternary kesterite phase is of crucial importance specifically to take full advantage of neutron diffraction data. In order to retrieve the chemical composition quantitatively an electron probe microanalyzer (EPMA; JEOL-JXA 8200 Superprobe) equipped with a wavelength-dispersive X-ray spectroscopy (WDX) unit is employed. Quantitative results with a relative error of less than ±1 % are enabled at least for the main elements through calibration with elemental standards, provided the specimens are reasonably well prepared and the EPMA instrument is properly adjusted. In fact, only a small fraction of the synthesized

material is required for the preparation of specimens being suitable for EPMA. For the preparation the powder material is epoxy-embedded into the cavities of acrylic sample carriers and subsequently polished until a smooth surface is attained and the superficial grains are not anymore covered with epoxy. Prior to the measurements the sample carriers are coated with a thin layer of conductive carbon in order to drain off electric charges that are steadily supplied by the probing electron beam.

The measurements are performed using a focused electron beam with a diameter of 1 µm employing an acceleration voltage of 15 kV and a beam current of 20 nA. Only grains considerably larger than 10 µm are chosen for measurements to account for the electron trajectories and corresponding X-ray emission beyond the beam diameter of 1 µm. In order to achieve a robust statistic and to detect possible inhomogeneities line scans each comprising 10 points are performed for every sample on at least 20 grains. The measured data obtained for each spot from a line scan are averaged unless their spread becomes larger than the error or if a too large discrepancy exists regarding the total weight percentages. From the average composition of each grain the average composition of the entire sample is eventually obtained. However, deviations in composition among the grains of more than 2 % are indicative of the presence of at least two kesterite phases. In such a case the sample is either discarded for further analysis or re-annealed to improve the homogeneity.

Among the various interactions happening between the electrons incident on the specimen and its constituents [159] only the backscattered electrons and the characteristic X-rays are purposefully utilized. The backscattering coefficient is a function of the atomic number and, thus, a mean to visualize and spatially assign compositional variations. The quantification of the chemical composition j^{WDX} is eventually based on the characteristic X-rays emitted by atoms constituting the sample. Indeed, the WDX analysis is more time-consuming as compared with energy-dispersive spectroscopy (EDX) owing to the limitation of separately measuring each element but possesses a much higher spectral resolution which makes peak overlap or ambiguities less probable and hence the results reliably quantifiable. On the other hand, WDX will only find the elements one is looking for

and that are actually preset in the measurement conditions. For this reason it is generally a good strategy to perform an EDX analysis for a qualitative survey of the elements actually present in a specimen before a WDX analysis is carried out. However, since the samples investigated in this thesis are artificially synthesized with high confidence about the constituent elements an EDX analysis is not taken into consideration, which is proven justified by a summed weight percentage being typically close to 100 %.

2.2.2 Phase identification, structural characterization and data evaluation

2.2.2.1 X-ray diffraction

In order to determine the phase content quantitatively as well as basic structural parameters of the kesterite phase Rietveld analysis [6, 7] (see section 2.2.2.3) of powder X-ray diffraction (p-XRD) data is performed. The measurements are conducted at a PANalytical MPD Pro X-ray diffractometer (Cu K_α radiation: $\lambda_{\alpha 1}$ = 1.54056 Å) equipped with fixed divergence slit and PIXcel strip detector in scanning line mode. The samples are prepared on an obliquely cut (9 1 1) single-crystal silicon carrier which considerably suppresses the background level and does not contribute accessible Bragg reflections at any diffraction angle for the given wavelength. A spinning sample stage with a preset revolution time of 1 s is chosen to reduce effects originating from preferred grain orientation. The measurements are carried out in parafocusing reflection geometry covering a 2Θ range from 10° to 150° with a step size of 0.01313°. For the parafocusing condition to be fulfilled a symmetric scan geometry is required, which is referred to as Θ–2Θ or Bragg-Brentano geometry [160], respectively. The divergent X-ray beam emitted from the X-ray tube is diffracted (‘reflected’) by the horizontally and sub-horizontally oriented lattice planes of the sample and all diffracted X-rays ideally intersect the goniometer circle and the active detector window at a single point, which is giving rise to high angular resolutions (Figure 2-3a).

The diffraction condition has first been described for the reciprocal space by M. von Laue, W. Friedrich and P. Knipping in 1912 [161]. A year later L. Bragg and W. H. Bragg developed a plainer explanation for the diffraction phenomenon that applies to real space and is based on the consideration of X-ray beams being reflected at lattice planes [162] (Figure 2-3b). Either of the concepts are fully equivalent to each other, but for the sake of convenience the Bragg formulation will be used in the following.

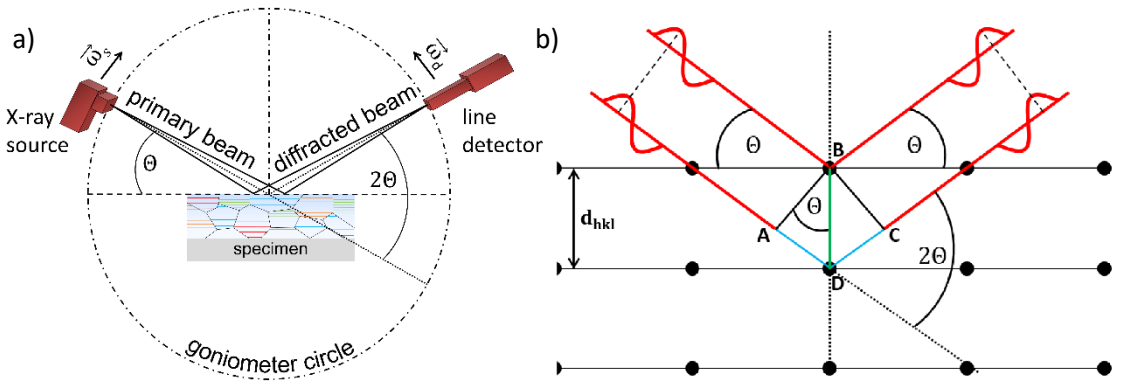

Figure 2-3 a) Schematic of the Bragg-Brentano reflection geometry (not to scale). The X-ray source and the detector are moving along the goniometer circle each at the same angular velocity, $\omega_s = \omega_d$ (symmetric scan). b) Geometrical representation of the diffraction condition in real space giving rise to the Bragg equation (not to scale).

Figure 2-3b shows how the Bragg condition of achieving constructive interference is geometrically derived, which is satisfied if the additional path length $\overline{ADC}$ equals an integer multiple n of the wavelength λ of the X-rays. Given by the trigonometric relations the angle Θ at which constructive interference and thus a diffraction signal occurs is therefore a function of the lattice plane distance d_{hkl} and the wavelength λ of the incident electromagnetic wave:

$$n\lambda = 2d_{hkl} \cdot sin\Theta \tag{2.1}$$

Consequently, slight deviations of the angle Θ from the position leading to constructive interference cause the diffracted waves to be phase shifted relative to each other ($\varphi \neq g\pi, g = \pm 2\mathbb{Z}$) and the diffracted intensity to drop. For a single array of point scatterers and no further geometrical effects convoluted a normal

distribution of the intensity will result with the complete destructive case being realized for $g = \pm 2\mathbb{Z} + 1$ (or for $n = \mathbb{Z} \pm 0.5$ in Equation 2.1). On the other hand, for an infinite and perfect crystal all waves diffracted from the various lattice plane positions will interfere with each other that eventually creates the sharpest possible Bragg reflection (δ function). In reality however non-ideal (finite) crystals are dealt with, resulting in intensity distributions of the Bragg reflections being in between the two limit cases as it is affected by the finite instrumental resolution and the crystal's long-range (but finite) periodicity that is additionally perturbated by structural defects. The latter induces strains in the lattice and locally changes the spacing between atoms (lattice planes) giving rise to a number of slightly different diffraction angles for which the Bragg condition (Equation 2.1) holds. This effect will further be discussed in section 2.2.2.3.

While the distribution of the scattered intensity is determined by the lattice type and the resulting interference of the waves, is the scattering power (intensity) given by the basis (atoms, ions, molecules), namely the electron density distribution $\rho_e(\vec{r})$ since the scattering amplitude A_s is proportional to the number of electrons N_e for a given volume element $d^3\vec{r}$ [163]:

$$A_s \propto N_e(\vec{r}) = \int_V \rho_e(\vec{r})\, d^3\vec{r} \tag{2.2}$$

The Fourier transform of the spatial electron density distribution for a discrete scattering center yields the atomic form factor (or atomic scattering factor) f in reciprocal (momentum) space $\vec{r}^*$ [163]:

$$T[\rho_e(\vec{r})] = f(\vec{r}^*) = \int_V \rho_e(\vec{r}) e^{2\pi \cdot i \cdot (\vec{r}^* \cdot \vec{r})} d^3\vec{r} \tag{2.3}$$

with $\vec{r}^* \cdot \vec{r} = hx + ky + lz$ when applied to a unit cell.

The resulting scattering power of all atoms *j* being situated on the same lattice plane *hkl* and located on the positions $(x, y, z)_j$ in the unit cell is obtained from the structure amplitude *F(hkl)* [163]:

$$F(hkl) = \sum_{j=1}^{N} f_j e^{2\pi \cdot i \cdot (hx_j + ky_j + lz_j)} \tag{2.4}$$

The observable (measured) intensity *I(hkl)* is proportional to the squared absolute quantity of the structure amplitude *F(hkl)*:

$$I(hkl) \propto |F(hkl)|^2 \tag{2.5}$$

The atomic form factor *f* can also be defined by the ratio of the amplitude of the wave scattered by an atom and the amplitude of the wave scattered by an electron. However, the volume element $d^3\vec{r}$ around an atomic nucleus with a non-zero electron probability density is quite large compared to the wavelength of the X-rays and only for an atom for which scattering occurs in forward direction (Θ = 0°) the atomic form factor is equal to the atomic number: $f = Z$. As the angle Θ increases a phase difference is introduced between the waves scattered at the electron shell that increasingly leads to more destructive interference. Therefore the scattered amplitude generally decreases with increasing scattering angle. This effect is even enhanced by heavier atoms owing to the larger cross-section of their electron shell. The thermal displacement of the atoms also increases the effective cross-section of the electron shell and, thus, contributes to the decay of intensity which is referred to as Debye-Waller factor [164, 165]. In case of CZGSe an additional limitation connected to the too similar cationic scattering factors (Figure 2-4) exists that does not allow to discriminate between Cu^+, Zn^{2+} and Ge^{4+} as they exhibit the same electron configuration [Ar] $3d^{10}$. The determination of the cation distribution will eventually be made accessible by using neutron diffraction, as described in the subsequent section.

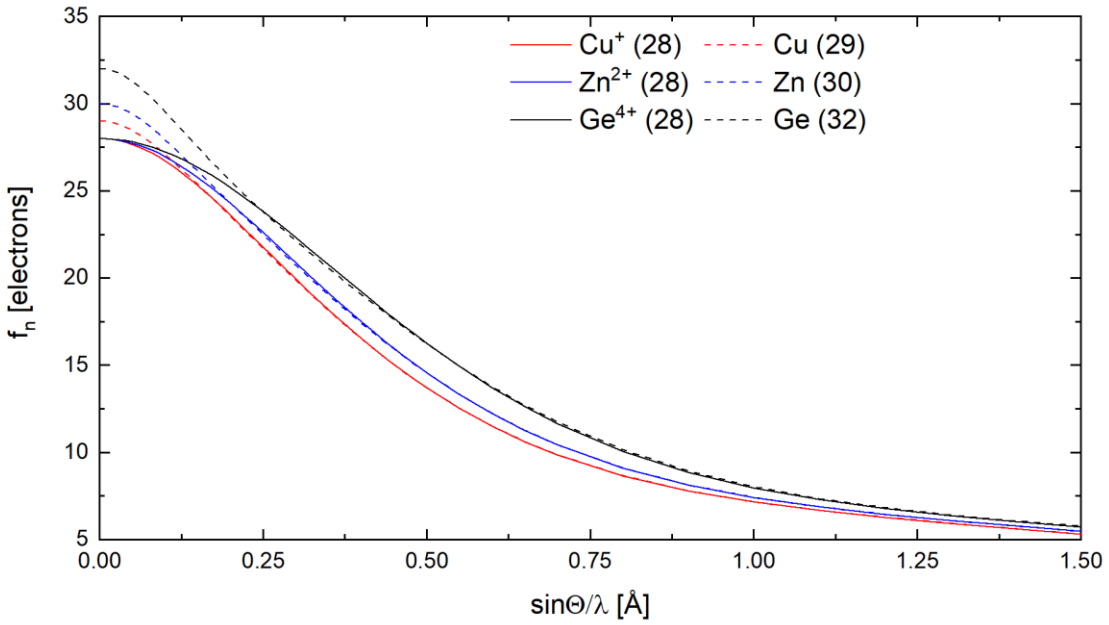

Figure 2-4 Atomic form factors (values tabulated in[166]) for the metals contained in CZGSe, both in atomic and cationic form, respectively. In general the atomic form factors are very similar for elements adjacent in the periodic table. Cations with the same electron configuration render a discrimination using conventional X-ray diffraction techniques impossible.

2.2.2.2 Neutron diffraction

As aforementioned, conventional X-ray diffraction is incapable in reliably obtaining the cation distribution on the Wyckoff positions owing to the isoelectronic cations in CZGSe and the inherent decay in intensity as the scattering angle Θ becomes larger. In contrast to X-rays, however, neutrons do interact with the nucleus of atoms. The effective cross section, σ, of a nucleus is magnitudes smaller compared both with the typical wavelengths of neutrons used as well as to the electron shells X-rays do interact with, making atomic nuclei approaching what can be considered an ideal point scatterer. Hence the analogue of the atomic form factor for neutrons, the neutron scattering length b_j, is independent of the scattering angle Θ which overall provides increased peak intensities. The structure factor *F(hkl)* determining the intensity in case of neutron diffraction follows a similar expression as for X-rays (Equation 2.4) with the atomic form factor f being substituted with the neutron scattering length b:

$$F(hkl) = \sum_{j=1}^{N} b_j e^{2\pi \cdot i \cdot (hx_j + ky_j + lz_j)} \qquad (2.6)$$

While the atomic form factor generally increases as atoms become heavier, is the neutron scattering length non-proportionally dependent on the number and constitution of nucleons which may lead to considerable differences in neutron scattering lengths [167] for chemical elements of similar mass number *Z* and even for isotopes. The differentiation problem regarding isoelectronic ions like Cu^{+}, Zn^{2+} an Ge^{4+} that exists for X-ray diffraction can therefore be circumvented by means of neutron diffraction since their contrast in neutron scattering lengths is large enough to be adequately distinguishable (Figure 2-5).

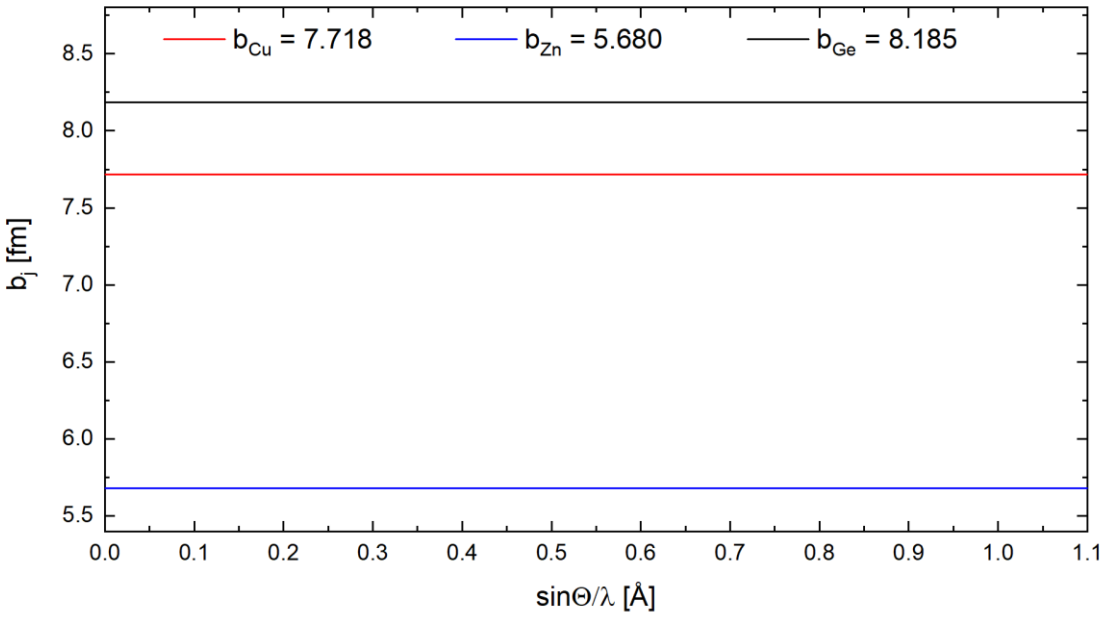

Figure 2-5 The neutron scattering lengths *b* (given in units of fm) of copper, zinc and germanium [167].

Powder neutron diffraction (p-ND) diffraction experiments are conducted at the E9 fine resolution powder diffractometer (FIREPOD) [168] at the BER II research reactor operated by the Helmholtz-Zentrum Berlin (HZB). In order to counterbalance the small effective cross sections and the generally low neutron flux a large scattering volume (i.e. several grams of powder material) is required. The powder material is filled into sample containers of 6 mm diameter and ~40 mm height to provide a large enough scattering volume. Vanadium is chosen as container

material as it scatters neutrons weakly and thus only little contributes to the diffraction pattern. The measurements are performed using a wavelength of 1.7982 Å [168] over a 2Θ range of 10° to 140° and a step size of 0.075°. An overall integration time of ~4 hours is employed assuring a reasonable counting statistic larger than 10^4 counts for the strongest peak.

2.2.2.3 The Rietveld method

Both p-XRD and p-ND data are evaluated using the Rietveld method [6, 7] implemented in the Fullprof suite software package [169, 170] aiming at refining the crystal structure of CZGSe. The intensity I recorded upon a diffraction experiment is, apart from energy-dispersive or time-of-flight mode, a function of the diffraction angle 2Θ: $I = f(2\Theta)$, with the intensity and its angular distribution being a direct result of the crystal structure and the instrumental parameters. The total profile h, thus, is a convolution of the sample profile f and the instrumental profile g: $h = f \otimes g$. The Rietveld method enables a whole-pattern deconvolution using a least-squares weighting scheme minimizing the difference (residual) S_y between observed intensity y_i and calculated intensity y_{ci} for ith steps:

$$S_y = \sum_i w_i (y_i - y_{ci})^2 \tag{2.7}$$

with $w_i = 1/y_i$ = weighting factor and the residual being the sum over i data points. The intensity y_{ci} is calculated according to the $|F(hkl)|^2$ values given by the applied structural model at each data point i. The integral intensity and the angular distribution of a measured peak is however always modified by several parameters, or might additionally be affected by overlapping Bragg reflections, which is accounted for by the Rietveld decomposition formula and that eventually addresses the limitations arising from overlapping peaks when integrated intensities are taken to obtain structural parameters [6] as it was done prior to the Rietveld method (and

before the advent of computers on which the refinement of such data sets was performable):

$$y_{ci} = s \sum_K H_K L_K P_K S_R E_X A \, |F_K|^2 \Phi(2\Theta_i - 2\Theta_K) + y_{bi} \qquad (2.8)$$

where the subscripted K refers to the Miller indices hkl of a Bragg reflection. The observed peak profile is determined by various physical and geometrical effects which can be approached by modeling the contributions from the crystal structure (sample dependent, f) and the instrument (instrument dependent, g), with the meaning of the parameters in Equation 2.8 being as follows:

- s: scale factor ($f + g$)
- H_K: multiplicity factor (f)
- L_K: Lorentz and polarization factor (g)
- P_K: preferred orientation factor (f)
- S_R: surface roughness factor (f)
- E_X: extinction factor (f)
- A: absorption factor ($f + g$ (by wavelength))
- F_K: structure factor (f)
- Φ: peak profile function ($f + g$)
- $2\Theta_i$: measured Bragg reflection position ($f + g$ (by wavelength))
- $2\Theta_K$: calculated Bragg reflection position ($f + g$ (by wavelength))
- y_{bi}: background intensity ($f + g$)

During the structure refinement the parameters are varied cyclically under the condition $S_y \rightarrow 0$. The refined parameters are updated after each cycle and applied for the subsequent cycle until the convergence criterion is reached. In general, such fitting routines allow both a reasonable deconvolution of the peak profile as well as robust refinement of the crystal structure(s). However, for an as far as possible self-stabilizing refinement a large 2Θ range, a decent angular resolution (given by instrument optics and X-ray wavelength), a good counting statistic, an appropriate starting model and a meaningful refinement strategy are necessary. For instance, the simultaneous refinement particularly of strongly correlated parameters likely

leads to instabilities or to convergence onto false (local) minima, and the resulting crystal structure refinement will probably be in poor agreement with the actual crystal structure, which may not become obvious from the refinement's quality factors. Apart from this the quality factors [7, 169, 171] are nevertheless important to evaluate the results obtained from a structure refinement, most notably by means of the R-Bragg factor

$$R_{Bragg} = 100 \cdot \left(\frac{\sum_K \left| I_{i,K} - I_{ci,K} \right|}{\sum_K I_{i,K}} \right) \tag{2.9}$$

and the goodness-of-fit criterion, χ^2 (chi-square)

$$\chi^2 = \left(\frac{R_{wp}}{R_{exp}} \right)^2 \tag{2.10}$$

with

$$R_{wp} = 100 \cdot \left(\frac{\sum_i w_i |y_i - y_{ci}|^2}{\sum_i w_i y_i^2} \right)^{\frac{1}{2}} \tag{2.11}$$

and

$$R_{exp} = 100 \cdot \left(\frac{n - p}{\sum_i w_i y_i^2} \right)^{\frac{1}{2}} \tag{2.12}$$

where n = total number of points used in the refinement and p = number refined parameters [169]. The highest possible agreement of a fit is realized for $R_{Bragg} = 0$ and for $\chi^2 = 1$. In practice however, an R_{Bragg} value below six is typically considered

satisfactorily while the χ^2 is very sensitive to the absolute intensity and, thus, can be a lot larger than one already through relatively little differences between measured pattern and calculated profile.

For a decent fit of a measured profile the selection of an appropriate profile function Φ (cf. Equation 2.8) is important. Relevant parameters used to describe the peak profile are the full width at half maximum parameter Γ (often abbreviated as FWHM) and the integral breadth β, which might be computed using a Gaussian (Caglioti) function [172]

$$\Gamma_G^2(\Theta) = U\ tan^2\Theta + V\ tan\Theta + W \tag{2.13}$$

$$\beta_G = \frac{\Gamma_G}{2}\sqrt{\frac{\pi}{ln2}} \tag{2.14}$$

or a Lorentzian function

$$\Gamma_L(\Theta) = X\ tan\Theta + \frac{Y}{cos\Theta} \tag{2.15}$$

$$\beta_L = \frac{\pi\Gamma_L}{2} \tag{2.16}$$

with U, V, W, X, and Y being refinable profile parameters. The experimentally obtained profile is typically a convolution of the Gaussian (G) and Lorentzian (L) function, respectively, which results in the Voigt profile

$$V = G \otimes L \tag{2.17}$$

This however is a mathematically complex procedure that requires sufficient computational capabilities specifically when used in a structure refinement routine. At present the computational performance even of personal computers is indeed sufficient, but the Voigt function is not implemented in Fullprof (yet). Instead, a pseudo-Voigt approach based on linear combination and an empirically deduced internal parametrizations of Γ and shape parameter η suggested by Thompson, Cox, and Hastings [173] are applied to mimic the Voigt profile, which in fact approximates it sufficiently. The Thompson-Cox-Hastings pseudo-Voigt (TCH-pV) profile function is an extension of the pseudo-Voigt function

$$\beta_{pV} = \eta \frac{\pi \Gamma_L}{2} + (1 - \eta) \frac{\Gamma_G}{2} \sqrt{\frac{\pi}{ln2}} \tag{2.18}$$

where Equations 2.14 and 2.16 are linked via the refinable shape parameter η ($0 \leq \eta \leq 1$). In the TCH-pV function the FWHM parameter (Γ_G and Γ_L) obtained from Equations 2.13 and 2.15 as well as the shape parameter η are approximated by series expansions, yielding Γ_{TCH} and η_{TCH}. Their detailed numerical formulations can be found in [173].

For the structure refinements an instrumental resolution function (IRF) determined using appropriate standard reference materials (LaB_6 in case of XRD, Y_2O_3 in case of ND) is employed and, in doing so, two advantages go along with: (1) enabling of a more stable refinement of the profile parameters as only U, X, and Y are sample-dependent and (2) calculation of the microstructure parameters through automatic subtraction of the instrument function. Since the instrumental resolution is higher for p-XRD and the employed standard reference material (LaB_6) is specifically dedicated for line profile analysis the microstructure is evaluated for p-XRD data only. Microstructure parameters include microstrain, ε, and the size of the volume-averaged coherently scattering domains, $D_{\langle V \rangle}$, which each are causing a broadening of the integral peak breadths, $\beta_{\mu,K}$. A separation of the two effects is enabled by the different shape of the broadening and a different angular dependency. Microstrain might be induced by any structural defects (1-D, 2-D, and 3-D) as they locally perturbate atomic distances which creates a strained lattice. Such defects can

normally be assumed to be statistically distributed in the sample and the various, slightly differing lattice distances in the vicinity of a distortion center lead to a normal (Gaussian) distribution of scattering angles over a certain angular range. Since the Fourier transform of a Gaussian is another Gaussian, this type of broadening can typically be attributed to microstrain, which exhibits a tanΘ dependency. The microstrain is calculated using the Stokes-Wilson equation [174]:

$$\beta_{strain} = 4\varepsilon tan\Theta \tag{2.19}$$

For a possibly precise approach of the microstrain the anisotropic broadening is refined using the broadening model for the Laue class 4/m that applies for space group $I\bar{4}$ and includes four strain coefficients S_{hkl} to treat the broadening of h00, 00l, hh0, and h0h reflections independently. A discussion of the phenomenological and mathematical background of this quartic description of microstrain can be found elsewhere [175, 176]. Owing to the rather weak anisotropy and in favor of a more robust refinement of the microstrain the diagonal directions are not refined though.

Broadening caused by small domain sizes can essentially be assumed to be of Lorentzian-type (Cauchy distribution) due to the resulting box function created both by a steep increase and decrease in intensity of the X-rays coherently scattered within the domain's boundaries, and the Fourier transform of a box function is a Lorentzian function. The domain size broadening exhibits a $1/\cos\Theta$ dependency and is calculated using the Scherrer equation [177]:

$$\beta_{size} = \frac{\lambda}{D_{\langle V \rangle} cos\Theta} \tag{2.20}$$

Additional functions are used to improve the overall refinement results, such as the Finger-Cox-Jephcoat asymmetry function [178] for axial divergence treatment that is convoluted with the TCH-pV function. A multi-axial model employing the March-Dollase [179] preferred orientation function is applied in case of p-XRD data to

account for the preferred orientation typically present along multiple directions, which could not be avoided in spite of carefully prepared specimens. Contrarily, the preferred orientation is virtually absent for p-ND data owing to a looser sample preparation enabled by the employed sample containers and the applied transmission geometry.

The Rietveld method also allows for quantification of the weight fractions (wt%) present in a multi-phase sample but may be prone to severe uncertainties due to typically few and low-intensity peaks, preferred orientation, micro-absorption effects etc. However, in spite of the possibly poor accuracy regarding quantification of phase fractions the weight percentages will nevertheless be included to at least provide an order of magnitude for their abundance. According to the respective advantages and reliabilities of p-XRD and p-ND the refinement results will selectively be reported. The main purpose of p-XRD data acquisition and their structure refinements is to retrieve precise lattice parameters, quantitative phase content and microstructure information. From the structure refinements of the p-ND data the anion coordinates (x,y,z), bond angles and distances, and site occupancy factors (occ) are taken.

2.2.2.4 The average neutron scattering length method

In general, one possibility to retrieve the site occupancy factors ($occ_{j,w}$) of the cations j (j = Cu, Zn, Ge) for the 'cationic' Wyckoff positions w (w = 2a, 2b, 2c, 2d) is given by tripling each Wyckoff position in the structural starting model. An arbitrary (but preferentially reasonable) fraction for each $occ_{j,w}$ may be chosen to start with, provided that $\sum_j occ_{j,w} = 1$ for each Wyckoff position (and for no vacancies). This strategy however is highly susceptible to instabilities and unreliably determined site occupancy factors owing to the implementation of more correlated and poorly constrainable parameters which strongly deteriorate the robustness of the refinement. Apart from that, the fraction of possible vacancies V_w can hardly be estimated neither.

Therefore a method allowing for a much more straightforward access to the site occupancy factors will instead be applied, namely the average neutron scattering length method [8, 9] for which as precise as possible information about the chemical composition is required. This method is based on each Wyckoff position occ_w being included one-time only, to which the theoretically present cation *j* is assigned and to which its neutron scattering length b_j is exclusively applied. As a result, the refined site occupancy factor may be either smaller, equal, or larger than one, giving rise to the experimentally deduced average neutron scattering length $\bar{b}_w^{exp}$ for each Wyckoff position

$$\bar{b}_w^{exp} = occ_w^{exp} \cdot b_{j,w} \tag{2.21}$$

and may point to a mixed occupation of different species and/or a certain fraction of vacancies. In consideration of the distinctively different neutron scattering lengths (c.f Figure 2-5) which for vacancies, self-evidently, is zero the fractional contribution of each species to any Wyckoff position in question can be approached, yielding the modeled average neutron scattering length

$$\bar{b}_w^{mod} = \sum_j occ_{j,w}^{mod} \cdot b_{j,w} \tag{2.22}$$

that meets the conditions

$$occ_w^{mod} = \sum_j occ_{j,w}^{mod} + V_w^{mod} = 1 \tag{2.23}$$

and

$$\bar{b}_w^{mod} \cong \bar{b}_w^{exp} \tag{2.24}$$

Cations potentially being yet left over are attributed to interstitial positions i_j to fulfill the requirement

$$\sum_w occ_{j,w}^{mod} + i_j^{mod} = j^{WDX} \tag{2.25}$$

The 'allowed' defect complexes given by the off-stoichiometry type is an additional condition to be met which highlights the importance of the defect type concept as it reasonably constrains the degrees of freedom. The error bars of the refined site occupancy factors serve as another boundary condition for the cation distribution model and should therefore be as small as possible for a meaningful outcome. Too large error bars may result in case of compositionally inhomogeneous samples, a poor counting statistic of the neutron diffraction patterns, or an inappropriate refinement strategy.

Since the F-type is characterized by two possible defect complexes including interstitial cations yet another constrain is applied in that case to provide a more reliable basis for the modeled cation distribution. On the Ge(2b) position either antisite zinc (F-type 1) which is coupled with two copper interstitials ($2Cu_i^+$) or antisite copper (F-type 2) coupled with one copper interstitial and one zinc interstitial ($Cu_i^+ + Zn_i^{2+}$) can be distributed on (cf. Table 1-1 and Figure 1-11). The fraction of each sub-type is determined by considering the Cu_i^+/Zn_i^{2+}ratios resulting, respectively, from the cation distribution model and from what is dictated by the fraction of the respective defect complex. Self-evidently, the highest confidence about the model is achieved when both ratios are equal.

2.2.2.5 UV-Vis spectroscopy

Diffuse reflectance measurements are carried out with an UV/Vis/NIR spectrometer (PerkinElmer Lambda 750 S) in high-resolution (HR) mode. The instrument is equipped with an InGaAs integrating sphere (100 mm) to recover as much as possible of the diffusely reflected light. Prior to the measurement the reflectance is calibrated using a standard made of the same material as the integrating sphere (InGaAs) to obtain the reference values of the reflected intensities for any wavelength increment $I_0(\lambda)$ along the selected wavelength range. The ratio between the intensity reflected by the sample $I_s(\lambda)$ and those reflected by the reference material $I_0(\lambda)$ yields the reflectance $R(\lambda)$.

For the reflectance measurements the powder samples are filled into glass cuvettes that are light-transmissive for the wavelength range applied. Reflectance spectra $R(\lambda)$ for each sample are taken from 700 nm to 1200 nm in steps of 1 nm that are subsequently converted to pseudo-absorption spectra $F(R)$ using the Kubelka-Munk function [5]

$$R(\lambda) \rightarrow F(R) = \frac{(1-R)^2}{2R} \tag{2.26}$$

By means of a Tauc plot [180] in which $(F(R)\cdot h\nu)^2$ is plotted versus energy ($h\nu$) an estimation of the optical band gap energy is eventually given through the intercept of the extrapolated linear region with the abscissa.

3 Results and discussion

3.1 Proof of chemical homogeneity of the CZGSe phase

Quantitative chemical analysis using an electron probe microanalyzer (EPMA) system equipped with an WDX unit (cf. Section 2.2.1) is employed to obtain both precise knowledge about the chemical composition as well as certainty about the chemical homogeneity, which is key for the whole methodical routine to be applied subsequently. For every sample the averaged composition of each measured grain must not differ from the averaged composition of all grains by more than the assumed EPMA error of ±1 % (Figure 3-1).

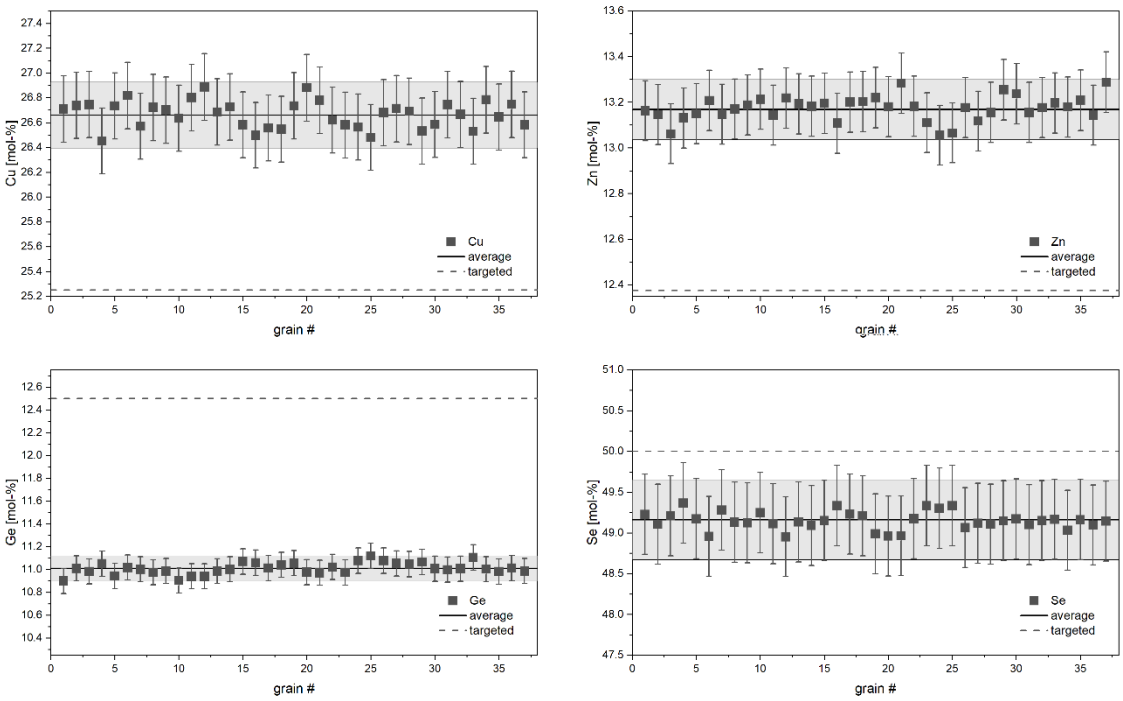

Figure 3-1 Example of a specimen considered sufficiently homogeneous that, consequently, contains one CZGSe phase only. The shaded area represents the 'allowed' range of compositional variation given by the error of the WDX analysis. The targeted (as-weighed) composition is indicated by dashed lines showing a considerable discrepancy with the measured composition particularly for the cations.

A too large compositional spread indicates the presence of several differently composed kesterite phases that would render the affected sample inappropriate for further analysis. A repetition of the 2nd reaction step (cf. Figure 2-2 & Table 2-1) is

then required to improve the homogeneity. The samples in the majority of the various off-stoichiometry type series show throughout a satisfying homogeneity with the exception of the two C-type series. Apart from one C-type sample for which a reasonable homogeneity is attained already after the regular synthesis route, the entire C(1)-type as well as C(2)-type series exhibit considerable inhomogeneities. As an attempt to improve the homogeneity the 2nd reaction step (including milling and pressing new pellets) is repeated which however led to success in case of only three out of ten samples (Figure 3-2). Those samples containing several CZGSe phases will be excluded from further discussion as the considerable chemical inhomogeneity renders a sufficiently reliable establishment of the cation distribution impossible. Consequently, only samples exhibiting a satisfactorily homogeneity of the contained CZGSe phase, and what can thus be considered to be consisting of a single CZGSe phase, will be presented and discussed in the following sections.

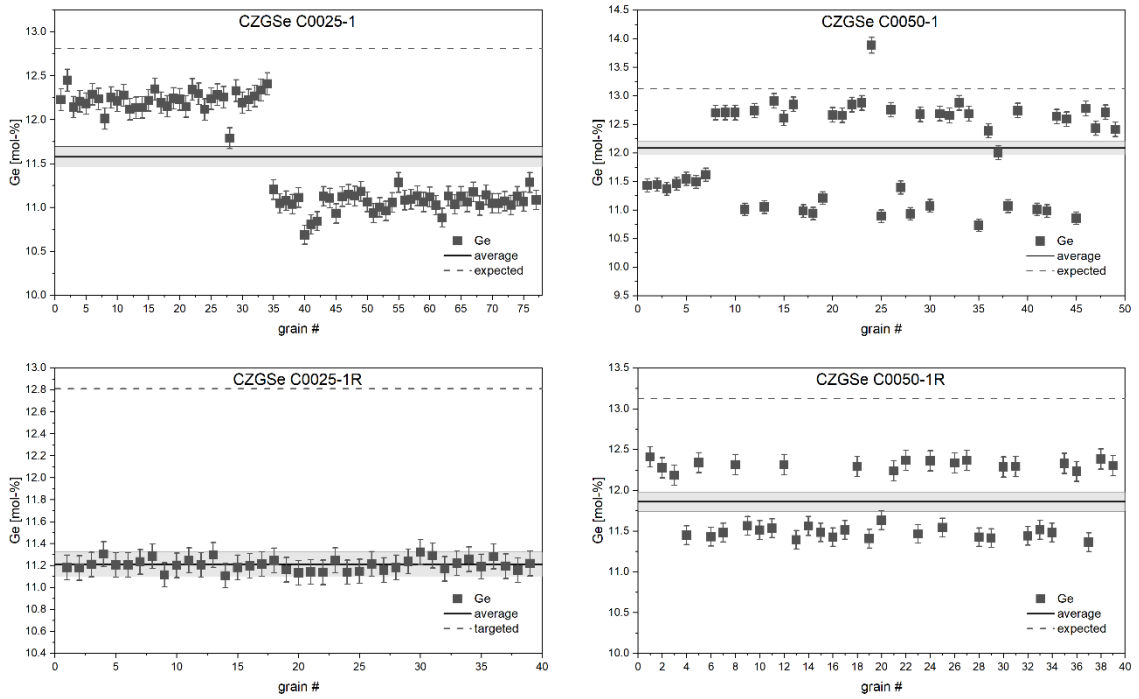

Figure 3-2 Among all synthesized sample series the C-type samples (with one exception only) are exclusively and widely subject to inhomogeneities regarding the cations, albeit most pronounced for germanium (upper graphs). The repetition of the 2nd reaction step satisfactorily homogenized only three out of ten affected samples (bottom left). Seven samples still show a strong inhomogeneity after the repetition of the 2nd reaction step and are thus excluded from further analysis and discussion (bottom right).

3.2 Comparison of targeted and obtained composition: where does germanium go?

Even though CZGSe is overall the main phase and sufficient compositional homogeneity is achieved for most of the samples a considerable discrepancy always exists between averaged measured composition and targeted (as-weighed) composition. This result is in common for all samples with germanium being virtually always deficient and copper and zinc being relatively enriched (cf. Figure 3-1). For most of the samples dark-gray, roundish patches condensed on the inner ampule wall are macroscopically visible. Qualitative EDX spectroscopy performed on a scanning electron microscope (SEM) reveals that the patches are composed of germanium and selenium (Figure 3-3).

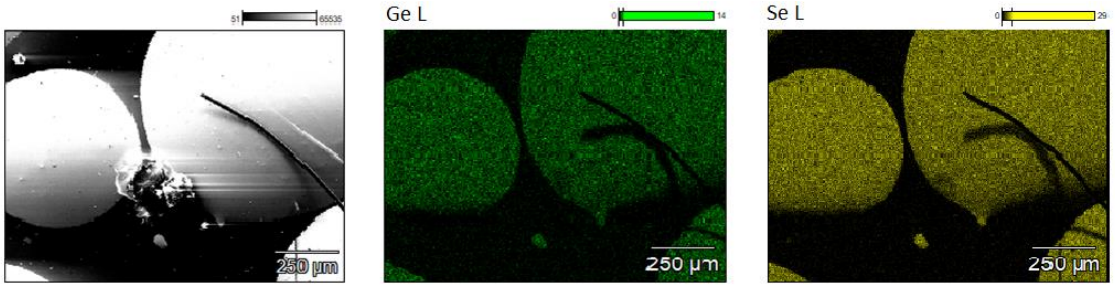

Figure 3-3 SEM (EDX) micrographs (magnification x225) of dark-gray patches condensed on the inner ampule walls, which are found to be composed of germanium and selenium.

The melting point of selenium is at 218° C (at 1 bar) [181], hence, the partial pressure of selenium in the ampule will be significant at elevated temperatures. Considering the melting point of germanium at one atmospheric pressure (T_M = 941° C [181]) its existence as gaseous phase appears unlikely for the applied maximum temperature of 700° C even at lowered pressure in the ampule. However, GeSe that may have formed in an early stage of the solid-state reaction sublimes at around 425° C (at 1 bar) [181], which may varies somewhat depending on the summed partial pressures in the ampule, especially those of selenium. Upon cooling the gaseous $GeSe_{(g)}$ preferentially condenses at the cooler glass ampule where it forms patches of solid $GeSe_{(s)}$. Consequently, this phase is spatially separated from the actual specimen and can therefore not be addressed in the quantitative phase analysis. This Ge-loss mechanism is after all facilitated by the low sublimation

temperature and rather high vapor pressure of GeSe, which is in analogy to the loss in Sn upon fabricating CZTSSe absorber layers as pointed out, for instance, by Redinger et. al [182] and Scragg et. al [183].

A comparison between the molar quantity of germanium that corresponds with its weighed-in amount and its deviation in the CZGSe phase after the synthesis reveals a remarkable behavior; the deviation of germanium (ΔGe) follows a fairly linear dependency with respect to the relative amount of germanium deployed in the synthesis process (as-weighed). Zinc likewise shows a quite linear but inverse dependency tending to Zn depletion for intended Ge-poor composition and a Zn surplus towards intended Ge-rich composition. While copper follows a similar trend as zinc does it is however always relatively enriched with respect to its intended molar amount and exhibits an additional opposing trend that is created by the B-type sample series (Figure 3-4a). At least for the given synthesis parameters it can be concluded that the extent of compositional deviation in germanium is a function of the initial amount of germanium itself. On average, the molar amount of germanium (Ge^{WDX}) eventually incorporated in the various CZGSe phases can be stated to be around 0.9 no matter how much germanium is deployed in the synthesis process. The F-type sample series, however, clearly represents an exception from this behavior (Figure 3-4b).

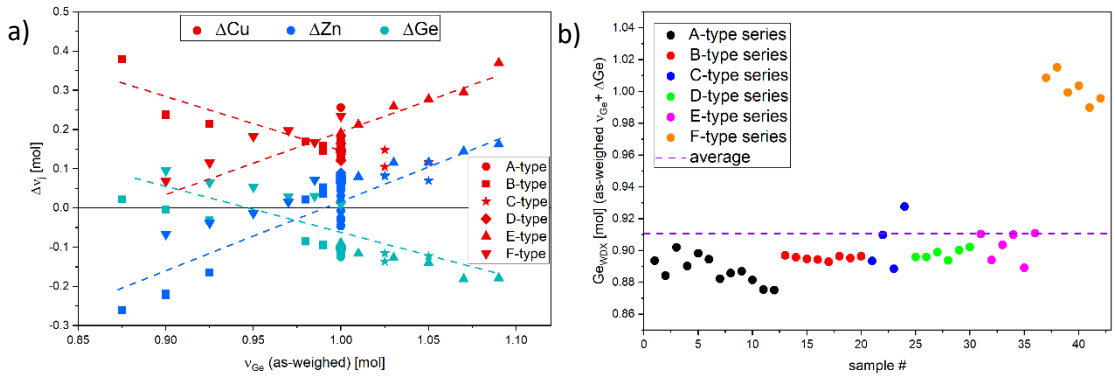

Figure 3-4 a) Difference between measured and weighed molar amounts of the cations ($\nu_{j(WDX)} - \nu_{j(weighed)}$) in dependence of the weighed amount of germanium. Intended off-stoichiometry types are indicated by differently shaped symbols. b) Molar amounts of germanium in each sample as obtained from WDX measurements showing a systematic depletion for all sample series except for the F-type series.

3.3 Mixtures of off-stoichiometry types

Owing to the likely formation of secondary phases and through the loss in volatile components during the heat treatment it can be expected that the composition of the synthesized products will differ from the targeted composition and, thus, may not coincide with a specific type-line anymore. The sample will then comprise a mixture of two off-stoichiometry types each with a certain fraction. The fraction is determined by interpolating linearly between the two type lines adjoining the measured composition of the CZGSe phase in the cation ratio plot. For practical reasons this approach is based on the simplification that the interpolation is done parallel either to the ordinate or the abscissa, respectively, which is subsequently demonstrated exemplarily by means of a hypothetical A – B-type CZGSe sample (Figure 3-5).

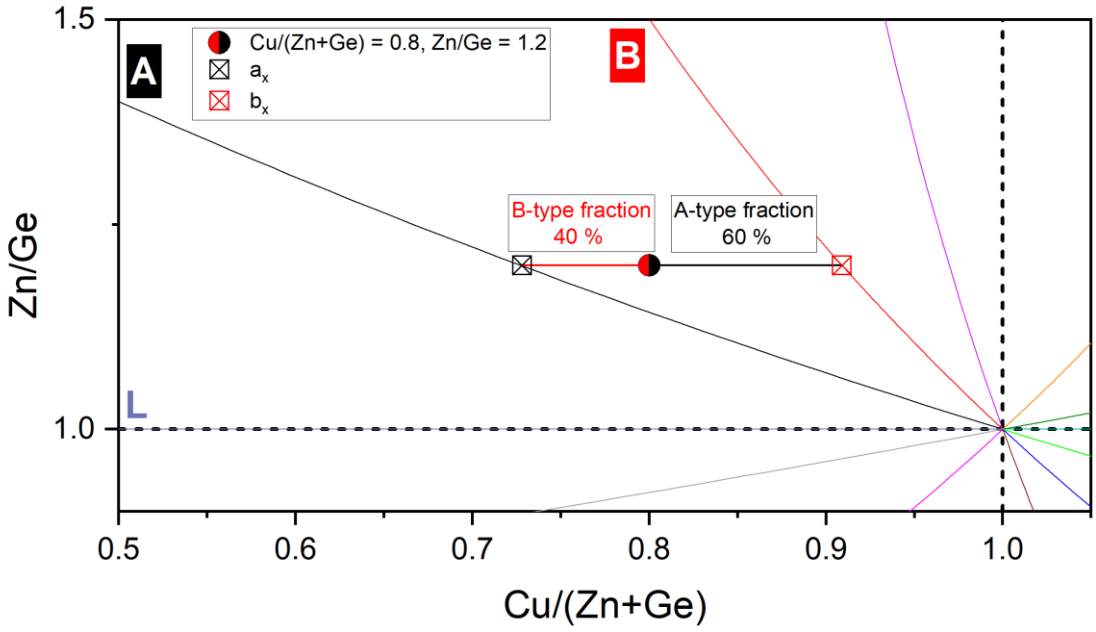

Figure 3-5 Graphical determination of the off-stoichiometry type fractions for a hypothetical CZGSe sample.

Figure 3-5 shows how the off-stoichiometry type fractions of a mixed A – B-type sample can graphically be represented ('lever' rule). In this example (and for any other A – B-type composition) the interpolation is conventionally done parallel to the abscissa. In general, a different A-to-B ratio will result for an interpolation parallel to the ordinate. Hence, a higher confidence about the type fractions might

be reachable if the average of the interpolations parallel both to the abscissa and ordinate is taken. Nevertheless, the interpolation parallel to the ordinate is performed only either when the L- or the K-type is involved since those lines are straight parallel to the abscissa themselves. In order to calculate the resulting sum formula with respect to the off-stoichiometry type fractions (again demonstrated on an A – B-type mixture) a system of linear equations based on the cation ratios is used to obtain the type-specific stoichiometric coefficients ν_a and ν_b (cf. Table 1-1) and, eventually, the contribution of each off-stoichiometry type. The type-specific sum formulae of the A-type and B-type, respectively, are

A-type: $$Cu_{2-2a}Zn_{1+a}GeSe_4 \tag{3.1a}$$

B-type: $$Cu_{2-2b}Zn_{1+3b}Ge_{1-b}Se_4 \tag{3.1b}$$

with

A-type: $$\frac{Zn}{Ge} = \frac{(1+a)}{1} = 1 + a \tag{3.2a}$$

B-type: $$\frac{Zn}{Ge} = \frac{(1+3b)}{(1-b)} \tag{3.2b}$$

Solving for a and b, respectively, delivers

A-type: $$a = \frac{Zn}{Ge} - 1 \tag{3.3a}$$

B-type: $$b = \frac{\left(\frac{Zn}{Ge} - 1\right)}{\left(\frac{Zn}{Ge} + 3\right)} \quad (3.3b)$$

The intersection with the A-type and B-type line is each obtained as follows

A-type: $$a_x = \left(\frac{Cu}{(Zn + Ge)}\right)_A = \frac{(2 - 2a)}{(1 + a + 1)} = \frac{(2 - 2a)}{(2 + a)} \quad (3.4a)$$

B-type: $$b_x = \left(\frac{Cu}{(Zn + Ge)}\right)_B = \frac{(2 - 2b)}{(1 + 3b + 1 - b)} \quad (3.4b)$$

which allows to obtain the type fraction f_j by interpolating Cu/(Zn+Ge) between a_x and b_x

A-type: $$f_A[\%] = \frac{\left(b_x - \frac{Cu}{(Zn + Ge)}\right)}{(b_x - a_x)} \cdot 100 \quad (3.5a)$$

B-type: $$f_B[\%] = \frac{\left(\frac{Cu}{(Zn + Ge)} - a_x\right)}{(b_x - a_x)} \cdot 100 \quad (3.5b)$$

3.4 Chemical composition and phase content of the synthesized powder specimens

Beside compositional analysis EPMA is additionally used as an assisting tool for the phase identification by means of the differing contrasts (different levels of grey) exhibited by backscattered electrons (BSE) micrographs, and through the quantitative results itself. The latter can provide important information about

phases that might be hidden in p-XRD and p-ND patterns due to strongly superposing peaks, specifically as in case of $Cu_2ZnGeSe_4$ (CZGSe) and Cu_2GeSe_3 (CGSe). However, in none of the samples this ternary phase is detected. Its presence would otherwise lead to severe limitations from the structure refinement point of view. The majority of the phase identification is however based upon p-XRD data, but to a minor extent also on p-ND data that have particularly proven useful in detecting remnants of pure germanium due to its large neutron scattering length (cf. Figure 2-5). In the following sections the composition of each CZGSe phase with the corresponding type fractions as well as the phase content found in every sample will be presented in detail. In favor of a better clearness the sample series are grouped according to their targeted location in the cation ratio plot.

3.4.1 The Cu-poor and Zn-rich quadrant

Three synthesized sample series originally following the A-type line and the B-type line, respectively, are characterized in terms of post-synthesis composition and phase content. As outlined in Section 2.1 two A-type series of equal off-stoichiometric progression are prepared that are differing regarding the treatment of the pure germanium metal pieces, which are pre-milled prior to the 1st reaction step in case of the A(2) sample series. Every sample series consists of a set of six samples each comprising one stoichiometrically weighed sample and five samples with an incrementally increasing off-stoichiometry, giving rise to 15 powder samples with a targeted Cu-poor and Zn-rich composition and three samples with intended stoichiometric composition (star-shaped symbols in Figure 3-6). The total number of synthesized samples has however increased to 20 because cracks in the pellets of two B-type samples (B0010-1, B0100-1) made them fell apart into two fragments each that were spatially separated in their respective glass ampules. The pellet fragments are treated as independent samples and labeled using suffixes ‘A’, ‘B’, respectively.

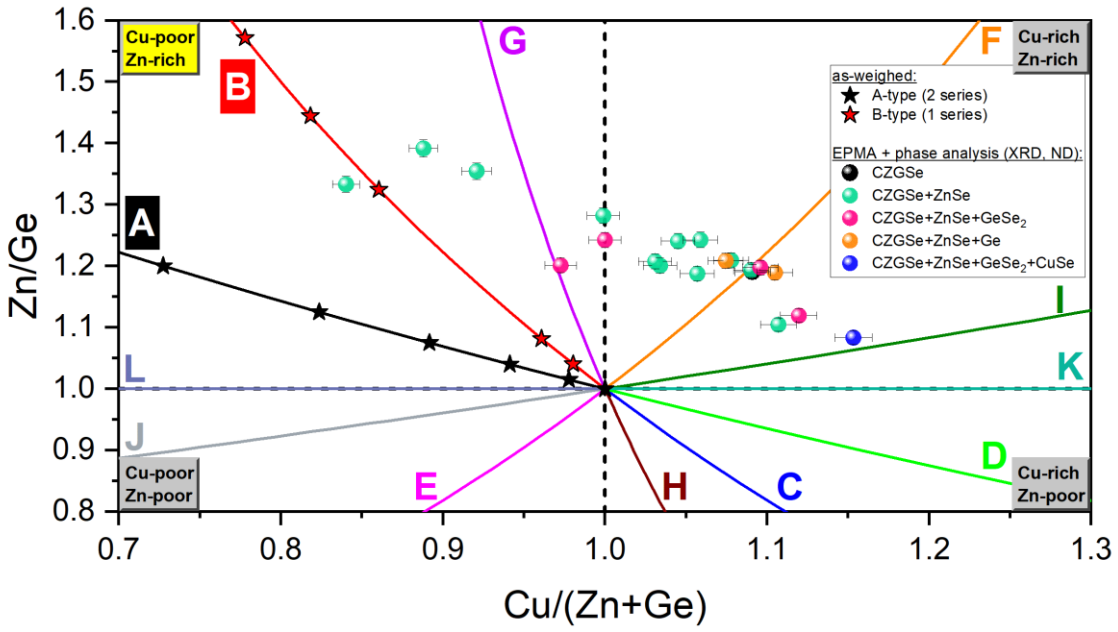

Figure 3-6 Cation ratio plot showing the as-weighed composition of the A-type and B-type series (star-shaped symbols) as well as their chemical and phase composition after the solid-state synthesis (spheres).

The compositions of the CZGSe phases in the intended A- and B-type samples do actually differ significantly from the targeted compositions which to a great extent can be attributed to the loss in germanium as described previously. The formation of secondary phases and the corresponding partial consumption of specific reactants does not seem to have a major impact on the compositional deviations, which becomes evident for two reasons: (1) the amount of any secondary phase determined by quantitative phase analysis is typically well below 10 wt% and (2) even the single-phase sample is subject to a similarly strong compositional deviation (Figure 3-6).

Apart from one sample containing the CZGSe phase only, secondary phases are found in the remaining 19 samples with ZnSe being always present which is also the only secondary phase in the vast majority of the samples. A few samples additionally contain either $GeSe_2$ or pure germanium while for one sample three secondary phases are identified (ZnSe, $GeSe_2$, CuSe). An overview of the targeted and obtained off-stoichiometry types as well as of the identified secondary phases is presented in Table 3-1.

Table 3-1 Overview of the obtained off-stoichiometry type mixtures and identified secondary phases in intended Cu-poor/Zn-rich samples.

Sample labeling (pre-synthesis)	Sample labeling (post-synthesis)	Intended off-stoichiometry type	Obtained off-stoichiometry type mixture	Secondary phases (in wt%)
A0000-1	A0000-1	A	F – I	ZnSe (5), CuSe (5), $GeSe_2$ (3)
A0015-1	A0015-1	A	F – I	ZnSe (3), $GeSe_2$ (1)
A0040-1	A0040-1	A	F – I	ZnSe (1)
A0075-1	A0075-1	A	F – G	ZnSe (2), $GeSe_2$ (2)
A0125-1	A0125-1	A	F – G	ZnSe (1), $GeSe_2$ (1)
A0200-1	A0200-1	A	A – B	ZnSe (2)
A0000-2	A0000-2	A	F – I	ZnSe (2), Ge (9)
A0015-2	A0015-2	A	F – I	ZnSe (1), $GeSe_2$ (1)
A0040-2	A0040-2	A	F – G	ZnSe (2)
A0075-2	A0075-2	A	F – G	ZnSe (2)
A0125-2	A0125-2	A	B – G	ZnSe (3)
A0200-2	A0200-2	A	B – G	ZnSe (10)
B0000-1	B0000-1	B	F – I	ZnSe (1)
B0010-1	B0010-1A	B	G – F	ZnSe (2), Ge (12)
	B0010-1B	B	F – I	none
B0020-1	B0020-1	B	F – G	ZnSe (3)
B0075-1	B0075-1	B	F – G	ZnSe (9)
B0100-1	B0100-1A	B	F – G	ZnSe (11)
	B0100-1B	B	F – G	ZnSe (11)
B0125-1	B0125-1	B	F – G	ZnSe (16)

3.4.1.1 A-type series 1

A total of six A(1)-type samples are prepared according to the corresponding off-stoichiometry type (cf. Table 1-1 & Formula 3.1a), comprising one stoichiometrically and five off-stoichiometrically weighed specimens. The off-stoichiometry parameter *a* is varied at unequal steps (*a* = 0,…,0.2) with the weights of the elements being in proper proportions but normalized to achieve a cumulated weight of 4 g for each sample. All element pieces taken for the synthesis are of >millimeter size. Figure 3-7 shows the as-weighed and obtained composition of the A(1) series. The data points belonging to the same sample are indicated with dash-dotted tie lines, highlighting the fairly systematic compositional shift towards more Cu-rich and Zn-rich (Ge-poor) conditions mainly due to the loss in germanium. Consequently, mostly F – I-type and G – F-type samples are obtained with only one sample being of A – B-type composition.

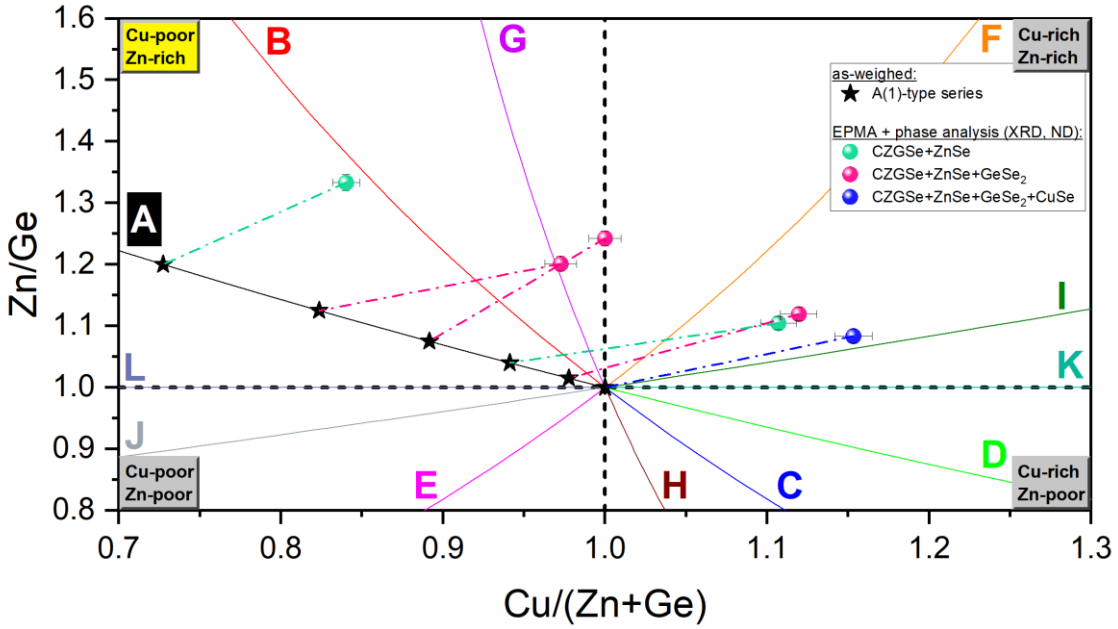

Figure 3-7 As-weighed and obtained composition of the CZGSe phases within the A(1)-type series. Data points stemming from the same sample are connected with dash-dotted tie lines. The phase content is represented by different colors.

Secondary phases are found in all samples with ZnSe being pervasively present. $GeSe_2$ is identified in four samples, though, its abundance does not exceed 3 wt% and might even be present in the remaining samples but is then below the detection limit. In the most Cu-rich sample, which was prepared in stoichiometric proportions

of the weighed elements, additionally contains CuSe as secondary phase. A summary of the composition results is given in Table 3-2 with the presented sum formulae resulting from the EPMA measurements and accounting for the off-stoichiometry type mixture (cf. Equations 3.3a,b & 3.5a,b).

Table 3-2 Overview of the post-synthesis composition and type fractions determined for the A(1)-type sample series.

Sample labeling	*a* (as-weighed)	Sum formula ($Cu_{2-a}Zn_{1+a}GeSe_4$)	Cu/(Zn+Ge)	Zn/Ge	Type fractions (%)
A0000-1	0.000	$Cu_{2.24}Zn_{1.01}Ge_{0.93}Se_4$	1.153	1.083	F (29) – I (71)
A0015-1	0.015	$Cu_{2.20}Zn_{1.04}Ge_{0.93}Se_4$	1.120	1.119	F (71) – I (29)
A0040-1	0.040	$Cu_{2.18}Zn_{1.04}Ge_{0.94}Se_4$	1.107	1.105	F (72) – I (28)
A0075-1	0.075	$Cu_{2.05}Zn_{1.14}Ge_{0.92}Se_4$	1.000	1.242	F (25) – G (75)
A0125-1	0.125	$Cu_{2.01}Zn_{1.13}Ge_{0.94}Se_4$	0.973	1.201	F (2) – G (98)
A0200-1	0.200	$Cu_{1.82}Zn_{1.24}Ge_{0.93}Se_4$	0.840	1.333	A (6) – B (94)

3.4.1.2 A-type series 2

The preparation of the A(2)-type series is identical to the A(1)-type series with the exception of the size of the germanium pieces utilized for the synthesis as well as the total weight being now doubled to 8 g. The germanium pieces of originally >millimeter size are pre-milled to examine the effect on compositional deviation between as-weighed and obtained composition.

On the other hand, the larger amounts of elements, particular of selenium, will cause the partial pressures to be around twice as high as in case of the A(1)-type series (the ampule volume is kept constant). However, the discrepancy in composition persists at a similar magnitude, yet more systematically and evenly shifted towards Cu-rich and Zn-rich composition that results in F – I-, F – G-, and B – G-type mixtures. (Figure 3-8). An overview about the obtained compositions and type fractions is given in Table 3-3.

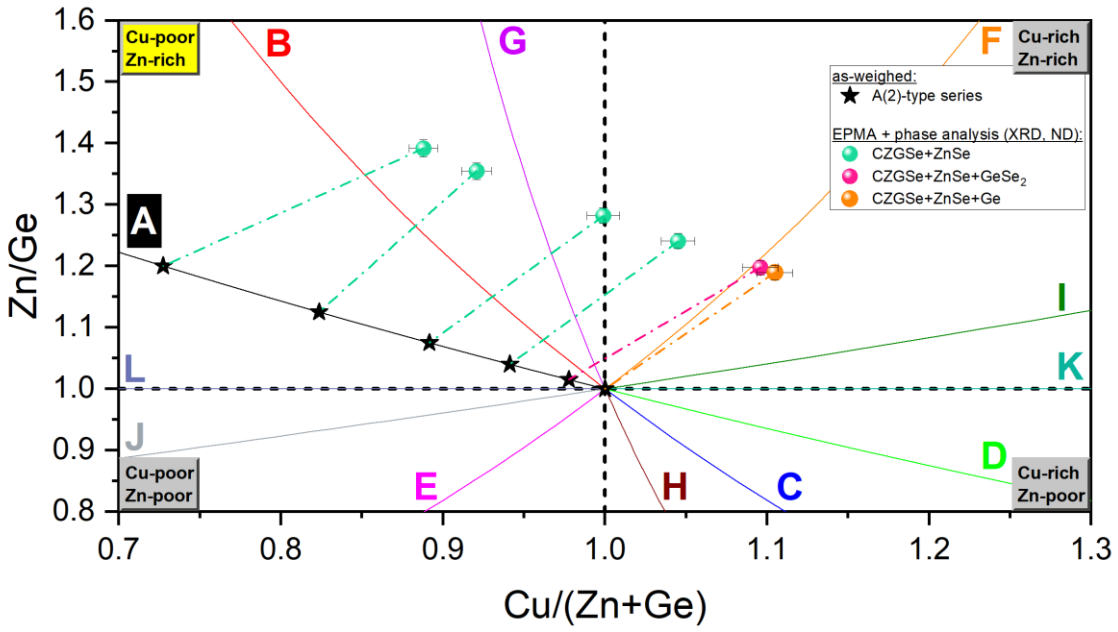

Figure 3-8 As-weighed and obtained composition of the CZGSe phases within the A(2)-type series. Data points stemming from the same sample are connected with dash-dotted tie lines. The phase content is represented by different colors.

Table 3-3 Overview of the post-synthesis composition and type fractions determined for the A(2)-type sample series.

Sample labeling	*a* (as-weighed)	Sum formula ($Cu_{2-a}Zn_{1+a}GeSe_4$)	Cu/(Zn+Ge)	Zn/Ge	Type fractions (%)
A0000-2	0.000	$Cu_{2.20}Zn_{1.08}Ge_{0.91}Se_4$	1.105	1.189	F (95) – I (5)
A0015-2	0.015	$Cu_{2.19}Zn_{1.09}Ge_{0.91}Se_4$	1.096	1.197	F (98) – I (2)
A0040-2	0.040	$Cu_{2.12}Zn_{1.13}Ge_{0.91}Se_4$	1.045	1.240	F (56) – G (44)
A0075-2	0.075	$Cu_{2.06}Zn_{1.16}Ge_{0.91}Se_4$	0.999	1.282	F (24) – G (76)
A0125-2	0.125	$Cu_{1.95}Zn_{1.22}Ge_{0.90}Se_4$	0.921	1.354	B (29) – G (71)
A0200-2	0.200	$Cu_{1.91}Zn_{1.25}Ge_{0.90}Se_4$	0.888	1.392	B (53) – G (47)

In all samples ZnSe is found as secondary phase, and one sample additionally contains $GeSe_2$. Furthermore, pure germanium remnants are identified in the most Cu-rich and Zn-rich (least Ge-rich) sample by means of the p-ND pattern. Its weight fraction of almost 9 % should however be also visible in the p-XRD pattern. This absence of germanium peaks in the p-XRD data might be explainable by too few but potentially larger germanium pieces in the entire powder specimen that are by

chance not present in the sample prepared for the p-XRD measurement. The larger sample volume required for p-ND can be considered more representative for a sample and the entirety of containing phases therein.

3.4.1.3 B-type series

Six powder samples of B-type composition (cf. Table 1-1) are weighed in with the sample series beginning again at the stoichiometric point. The weight of each sample amounts for 6 g and the off-stoichiometry parameter *b* ranges between 0 and 0.125. Upon the 2nd reaction step two pellets with pre-existing cracks fell apart into two pieces each and are treated as independent samples (A, B). The number of samples belonging to this series is therefore increasing to eight. As for the previously described Cu-poor and Zn-rich A(1,2)-series a strong deviation between as-weighed and obtained composition is found for the B-type series too. Contrarily, the B-type series is originally characterized by Ge-poor composition whereas germanium is kept constant in the A-type case. This peculiarity of the B-type series might be responsible for the different mode of compositional shifts which is not a nearly parallel translation of the as-weighed composition leading to a relative systematic enrichment of Cu and Zn (cf. Figure 3-7 & Figure 3-8). Instead, the composition strongly tends to the Cu-rich regime and the magnitude of compositional deviation differs significantly among the synthesized B-type samples, of which only the least Ge-poor samples show a similar shift in composition as observed for the A-type series. Initially most Zn-rich samples are relatively depleted in zinc while slightly and moderately Zn-rich samples become enriched in zinc. This trend complies with the sum formula of the B-type with copper decreasing (ν_{Cu} = 2-2*b*) and zinc increasing (ν_{Zn} = 1+3*b*) as the off-stoichiometry increases. Unlike for the other type series germanium is generally depleted to a fewer extent. The initially most Ge-poor sample even experiences a slight relative enrichment in germanium (larger ν_{Ge}) which is unique among all samples synthesized under Cu-poor and Zn-rich conditions but nevertheless complies with the trend elaborated in section 3.2 (cf. Figure 3-4). In consequence the measured compositions are not lining up anymore

but do plot in a quite confined region in the cation ratio plot, comprising two F – I- and six F – G-type mixtures of approximately similar compositions (Figure 3-9).

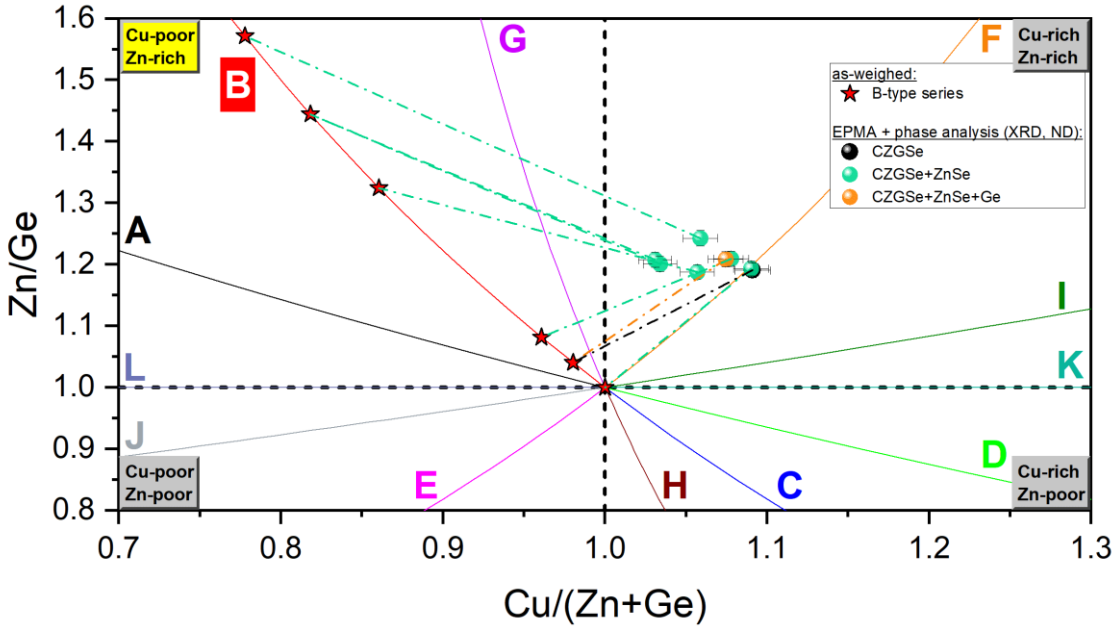

Figure 3-9 As-weighed and obtained composition of the CZGSe phases within the B-type series. Data points stemming from the same sample are connected with dash-dotted tie lines. The phase content is represented by different colors.

With the exception of one sample exclusively consisting of CZGSe, ZnSe is found to be present in the remaining seven samples of which one sample additionally contains pure germanium. Remarkably, the single-phase sample (B0010-1B) and the sample showing the two secondary phases ZnSe and Ge (B0010-1A) are originally descending from the same sample (B0010-1) indicating a segregation of the secondary phases. This segregation is probably due to a pre-existing inhomogeneity that persisted after the 1st reaction step rather than a phase segregation happening during the 2nd reaction step. For instance, an unreacted piece of germanium may still have been present in the sample but, by chance, ended up in the 'A' piece. A segregation during the 2nd reaction step facilitated for example by small but probable temperature gradients in the glass ampule appears further unlikely when considering the phase content and fractions of the other sample separated into two pellets (B0100-1A,B), each with almost the same weight fraction of ZnSe (~11 %). In general, the weight fractions of secondary phases determined for the B-type samples are, if present, comparably large and very often around or

above 10 % (cf. Table 3-1). A summary of the obtained compositions and corresponding type fractions is presented in Table 3-4.

Table 3-4 Overview of the post-synthesis composition and type fractions determined for the B-type sample series.

Sample labeling	*b* (as-weighed)	Sum formula ($Cu_{2-2b}Zn_{1+3b}Ge_{1-b}Se_4$)	Cu/(Zn+Ge)	Zn/Ge	Type fractions (%)
B0000-1	0.000	$Cu_{2.18}Zn_{1.09}Ge_{0.91}Se_4$	1.090	1.193	F (99) – I (1)
B0010-1A	0.010	$Cu_{2.16}Zn_{1.10}Ge_{0.91}Se_4$	1.074	1.208	F (84) – G (16)
B0010-1B	0.010	$Cu_{2.18}Zn_{1.09}Ge_{0.91}Se_4$	1.091	1.191	F (99) – I (1)
B0020-1	0.020	$Cu_{2.16}Zn_{1.10}Ge_{0.91}Se_4$	1.078	1.209	F (87) – G (13)
B0075-1	0.075	$Cu_{2.13}Zn_{1.09}Ge_{0.92}Se_4$	1.057	1.188	F (75) – G (25)
B0100-1A	0.100	$Cu_{2.10}Zn_{1.11}Ge_{0.92}Se_4$	1.034	1.200	F (53) – G (47)
B0100-1B	0.100	$Cu_{2.09}Zn_{1.11}Ge_{0.92}Se_4$	1.031	1.208	F (50) – G (50)
B0125-1	0.125	$Cu_{2.14}Zn_{1.12}Ge_{0.90}Se_4$	1.059	1.243	F (66) – G (34)

3.4.2 The Cu-rich and Zn-poor quadrant

Similar to the complementary compositional regime discussed in the previous sections again three sample series are prepared aiming at Cu-rich and Zn-poor conditions. This compositional regime is indeed of minor relevance from the application point of view but its investigation may provide deeper insights in this material class in general. Therefore, two C-type and one D-type sample series are prepared which represent the opposing off-stoichiometric trends of the B- and A-type, respectively. The difference between both C-type series again is the deployment of pre-milled germanium pieces for the C(2)-type series prior to the 1st reaction step as analogous to the A(2)-type series described in section 3.4.1.2. The C(2)- and D-type series, respectively, are consisting of six samples each. The C(1)-type series is synthesized at identical off-stoichiometric steps as the C(2)-type series but the stoichiometric specimen is omitted, eventually yielding a total of 15 off-

stoichiometrically and two stoichiometrically weighed samples (star-shaped symbols in Figure 3-10). In case of the C(1)-type series the calculation of the targeted composition is normalized to a total weight of 5 g per sample whereas the samples of the C(2)- and D-type series are normalized to 6 g each.

After the solid-state reaction both C-type series exhibit strong compositional inhomogeneities and, thus, several CZGSe phases (c.f Figure 3-2 in section 3.1) with only one out of 11 samples being sufficiently homogeneous. The inhomogeneous samples are therefore milled and pressed to pellets again and subsequently underwent a repetition of the 2nd reaction step (indicated with suffix 'R'). A satisfying homogeneity is however achieved for three samples only, meaning that eventually four C-type samples suitable for further analysis are overall obtained. Unlike both C-type series the six samples belonging to the D-type series are sufficiently homogeneous already after the regular solid-state reaction so that the total number of successfully synthesized samples in this compositional regime becomes 10 (Figure 3-10).

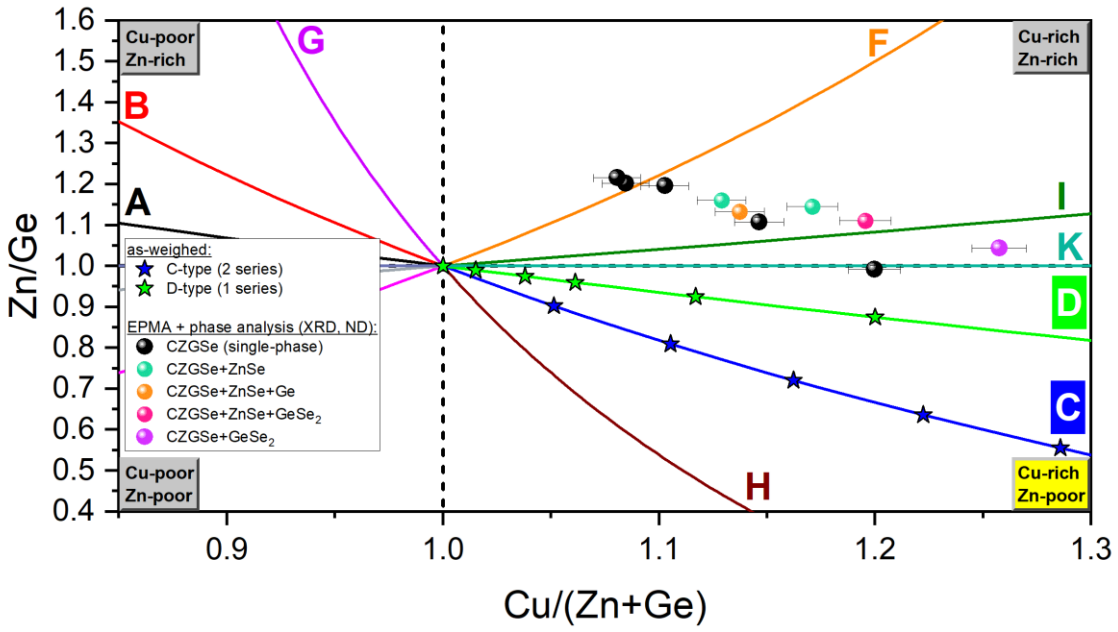

Figure 3-10 Cation ratio plot showing the as-weighed composition of the C-type and D-type series (star-shaped symbols) as well as their chemical and phase composition after the solid-state synthesis (spheres).

As can be seen in Figure 3-10 the obtained compositions are considerably off the as-weighed ones. The compositional shift again heavily tends to Ge-poor conditions

implying the same germanium loss mechanism which is observed in the Cu-poor and Zn-rich sample series and as outlined in section 3.2. The resulting type mixtures do not involve any C-type and only one D-type contribution, though, the latter is characterized by a much stronger K-type component. Most of the samples consist of an F – I-type mixture, two are showing F – G-type and one shows I – K-type composition, respectively. Table 3-5 summarizes the results on obtained type composition and detected secondary phases.

Table 3-5 Overview of the obtained off-stoichiometry type mixtures and identified secondary phases in intended Cu-rich/Zn-poor samples.

Sample labeling (pre-synthesis)	Sample labeling (post-synthesis)	Intended off-stoichiometry type	Obtained off-stoichiometry type mixture	Secondary phases (in wt%)
C0025-1	C0025-1R	C	F – I	none
C0050-1	C0050-1R	C	n/a	$GeSe_2$ (1)
C0075-1	C0075-1R	C	n/a	ZnSe (1)
C0100-1	C0100-1R	C	n/a	none
C0125-1	C0125-1R	C	n/a	ZnSe (n/a)
C0000-2	C0000-2R	C	F – G	none
C0025-2	C0025-2	C	F – I	ZnSe (1), Ge (8)
C0050-2	C0050-2R	C	D – K	none
C0075-2	C0075-2R	C	n/a	none
C0100-2	C0100-2R	C	n/a	none
C0125-2	C0125-2R	C	n/a	none
D0000-1	D0000-1	D	F – G	none
D0010-1	D0010-1	D	F – I	none
D0025-1	D0025-1	D	F – I	ZnSe (1)
D0040-1	D0040-1	D	F – I	ZnSe (1)
D0075-1	D0075-1	D	F – I	ZnSe (1), $GeSe_2$ (1)
D0125-1	D0125-1	D	I – K	$GeSe_2$ (2)

Samples that are too inhomogeneous cannot reasonably be characterized neither in terms of type mixtures nor regarding quantitative phase content owing to strong compositional variations and/or poor-quality p-XRD and p-ND patterns (indicated by 'n/a' in Table 3-5). The majority of the samples do actually not contain secondary phases or only very little amounts of ZnSe and/or $GeSe_2$. The only C-type sample that did not require a repetition of the 2nd reaction step additionally shows germanium peaks in the p-ND pattern.

3.4.2.1 C-type series 1 & 2

Two C-type sample series each with equal incremental changes of the off-stoichiometry parameter c (c = 0,…,0.125) are synthesized by solid-state reaction and subsequently characterized with respect to composition and phase content. The C-type off-stoichiometric composition is Cu-rich, Zn-poor and Ge-rich and hence the counterpart of the B-type. The weight of each sample in the C(1)-type series is 5 g, while 6 g are prepared in case of the C(2)-type series. As aforementioned, pre-milled germanium is employed for the latter, and yet only one out of six samples is homogeneous enough which does not point to a beneficial impact of pre-milled germanium on homogeneity. On the other hand, three out of four succesfully homogenized samples do eventually belong to the C(2)-type series, thus subtly suggesting a potential benefit.

It is remarkable that of all things both the C-type series as well as the B-type series, each with a non-stoichiometric germanium content exhibit distinctively different behavior when compared with the other off-stoichiometry types under investigation. The B-type samples indeed achieved a satisfying homogeneity, yet their mode of compositional shift is not an approximately parallel translation from targeted to obtained composition but rather concentrates onto a fairly constricted area in the cation ratio plot (cf. Figure 3-9). This is also reflected by the strong relative enrichment in copper which however is decreasing with the weighed-in amount of germanium and roughly follows the trend shown by germanium while the opposite is true for the other type series (cf. Figure 3-4).

The peculiarity of the originally Ge-rich C-type series is its obvious susceptibility to inhomogeneities at least for the synthesis conditions applied. It remains however unclear why the targeted stoichiometric sample is subject to severe inhomogeneities too, although it is the least inhomogeneous one among the samples that required a repetition of the 2nd reaction step. The mode of compositional shift is comparable with the one observed for the A-type and D-type (see subsequent section) as well as for the originally least Ge-poor B-type samples, respectively. The resulting composition of the four C-type samples comprises three different off-stoichiometry type mixtures: one F – G-, two F – I-, and one D – K-type (Figure 3-11).

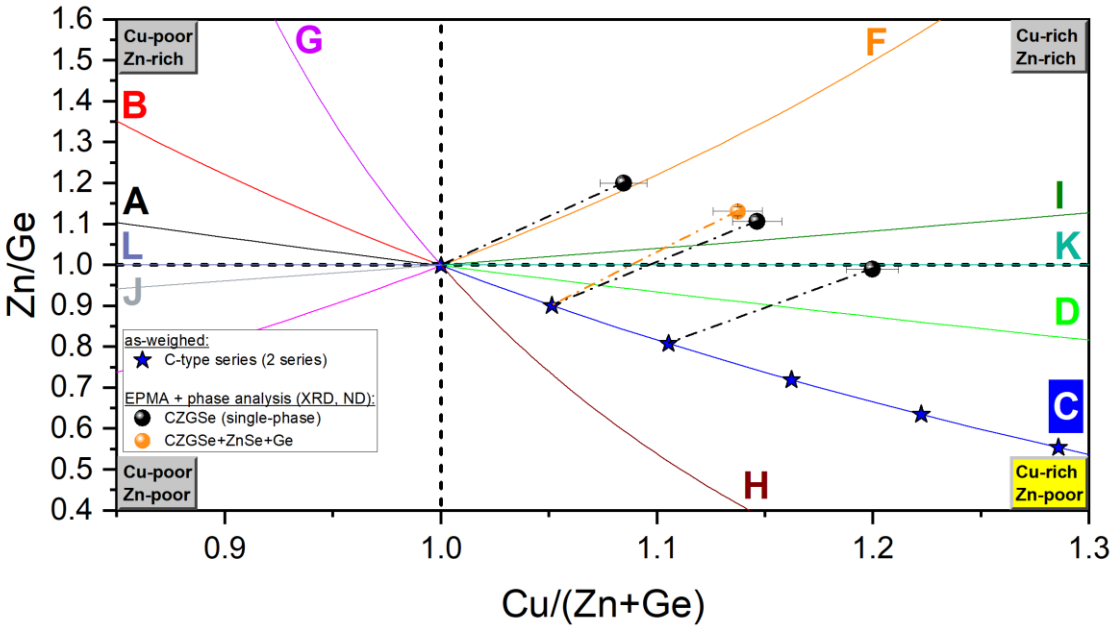

Figure 3-11 As-weighed and obtained composition of the CZGSe phases within the C-type series. Data points stemming from the same sample are connected with dash-dotted tie lines. The phase content is represented by different colors.

Most of the C-type samples exclusively show the CZGSe phase(s), including also the disregarded samples and, thus, even in spite of the vast inhomogeneities present therein (cf. Table 3-5). Three out of four samples of sufficient homogeneity resulted in the formation of the CZGSe phase without indications of secondary phases. The only sample showing secondary phases (ZnSe, Ge) is the one that did not undergo a repetition of the 2nd reaction step (cf. Table 3-5 & Figure 3-11). A summary of the measured compositions and corresponding type mixtures is presented in Table 3-6.

Table 3-6 Overview of the post-synthesis composition and type fractions determined for the C-type sample series (inhomogeneous samples are excluded).

Sample labeling	*c* (as-weighed)	Sum formula ($Cu_{2+2c}Zn_{1-3c}Ge_{1+c}Se_4$)	Cu/(Zn+Ge)	Zn/Ge	Type fractions (%)
C0025-1R	0.025	$Cu_{2.24}Zn_{1.03}Ge_{0.93}Se_4$	1.146	1.108	F (54) – I (46)
C0000-2R	0.000	$Cu_{2.17}Zn_{1.09}Ge_{0.91}Se_4$	1.085	1.202	F (94) – G (6)
C0025-2	0.025	$Cu_{2.23}Zn_{1.04}Ge_{0.92}Se_4$	1.137	1.132	F (70) – I (30)
C0050-2R	0.050	$Cu_{2.28}Zn_{0.95}Ge_{0.96}Se_4$	1.200	0.992	D (7) – K (93)

3.4.2.2 D-type series

The synthesis of the D-type sample series comprises five off-stoichiometrically weighed samples with the off-stoichiometry parameter *d* ranging from 0.010 to 0.125 and once more includes one intended stoichiometric sample (*d* = 0), each having 6 g. Every sample achieves sufficient compositional homogeneity. A considerable and very systematic shift between targeted and obtained composition persists that again follows a similar pattern as the A- and C-type samples, that is, towards relative enrichment in copper and zinc as well as depletion in germanium (Figure 3-12). The sample with targeted stoichiometric composition yields an F – G-type mixture while the samples with *d* = 0.010 to 0.075 are shifted into the F – I-type field. An I – K-type mixture is obtained for the most off-stoichiometric specimen (*d* = 0.125).

This sample series is charcterized by little amounts of secondary phases. The two least off-stoichiometric samples actually do not show any indication of secondary phases. For samples with intermediate values of the off-stoichiometry parameter minor amounts of around 1 wt% ZnSe are found. The fraction of $GeSe_2$ in the two samples with the largest off-stoichiometry is of similar abundance (Figure 3-12). The results on composition and type fractions are shown in Table 3-7.

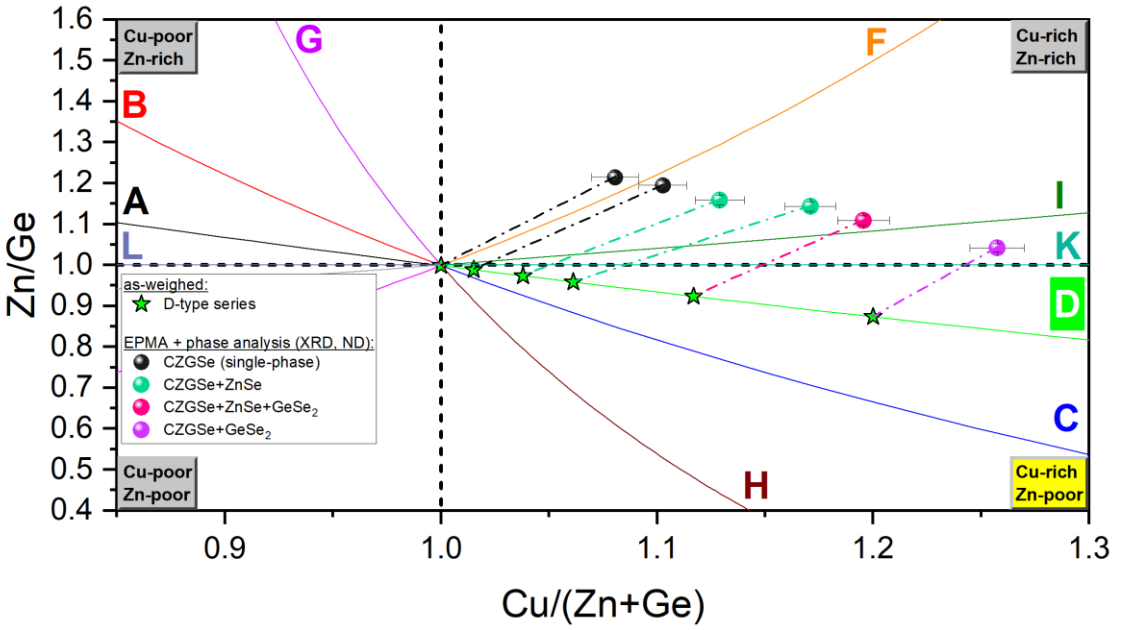

Figure 3-12 As-weighed and obtained composition of the CZGSe phases within the D-type series. Data points stemming from the same sample are connected with dash-dotted tie lines. The phase content is represented by different colors.

Table 3-7 Overview of the post-synthesis composition and type fractions determined for the D-type sample series.

Sample labeling	*d* (as-weighed)	Sum formula ($Cu_{2+2d}Zn_{1-d}GeSe_4$)	Cu/(Zn+Ge)	Zn/Ge	Type fractions (%)
D0000-1	0.000	$Cu_{2.17}Zn_{1.10}Ge_{0.91}Se_4$	1.081	1.216	F (87) – G (13)
D0010-1	0.010	$Cu_{2.20}Zn_{1.09}Ge_{0.91}Se_4$	1.103	1.196	F (96) – I (4)
D0025-1	0.025	$Cu_{2.22}Zn_{1.06}Ge_{0.91}Se_4$	1.129	1.160	F (82) – I (18)
D0040-1	0.040	$Cu_{2.28}Zn_{1.04}Ge_{0.91}Se_4$	1.171	1.145	F (62) – I (38)
D0075-1	0.075	$Cu_{2.31}Zn_{1.02}Ge_{0.92}Se_4$	1.196	1.110	F (32) – I (68)
D0125-1	0.125	$Cu_{2.37}Zn_{0.96}Ge_{0.92}Se_4$	1.257	1.044	I (40) – K (60)

3.4.3 The Cu-poor and Zn-poor quadrant

3.4.3.1 E-type series

The Cu-poor and Zn-poor quadrant only comprises one synthesized sample series (E-type). Like the Cu-rich and Zn-poor quadrant (e.g. C- and D-type), this composition is not of high interest for any application but is nevertheless also investigated for the sake of completeness. This E-type series again starts with a stoichiometrically weighed sample (e = 0). The actual off-stoichiometric series begins at e = 0.010, which is incrementally increased by Δe = 0.020 until 0.090 for the subsequent samples. Each of the six weighed-in samples is normalized to 5 g. The mode of compositional deviation between as-weighed and post-synthesis samples is different to all sample series previously described. Indeed, the compositional shift very consistently points to Ge-poor conditions once again but the absolute deviations are differing in a way such that the measured compositions are in close proximity in the cation ratio plot and is in this regard comparable with the B-type series (cf. section 3.4.1.3).

However, copper and zinc are just following the opposite trend as in the B-type series with copper and zinc being both generally enriched and increasing with the as-weighed amount of germanium (cf. Figure 3-4). In addition, copper and zinc do deviate in a similar manner (cf. Figure 3-4) which agrees with their off-stoichiometric coefficients (i.e. 2-2e for Cu and 1-e for Zn). The mechanism mainly governing the compositional evolution of the CZGSe phase is the behavior of germanium that heavily tends to achieve a molar amount of around 90 % not only in the E-type series but in every sample except for the F-type series, and is thus irrespective of the type series and the as-weighed amount of germanium. Therefore, and because the compositional deviations of copper and zinc do fairly cancel out each other, the obtained compositions are more or less a projection along the E-type line towards the F – I-type region in the Cu-rich and Zn-rich quadrant (Figure 3-13). In spite of the strong compositional shifts no indication of secondary phases in any of the samples is found (Figure 3-13). The relative depletion in germanium is again attributable to the formation of GeSe which however condenses at the ampule wall and is therefore spatially separated from the investigated specimen. The post-

synthesis compositions accounting for the type mixtures and the corresponding calculated type fractions are shown in Table 3-8.

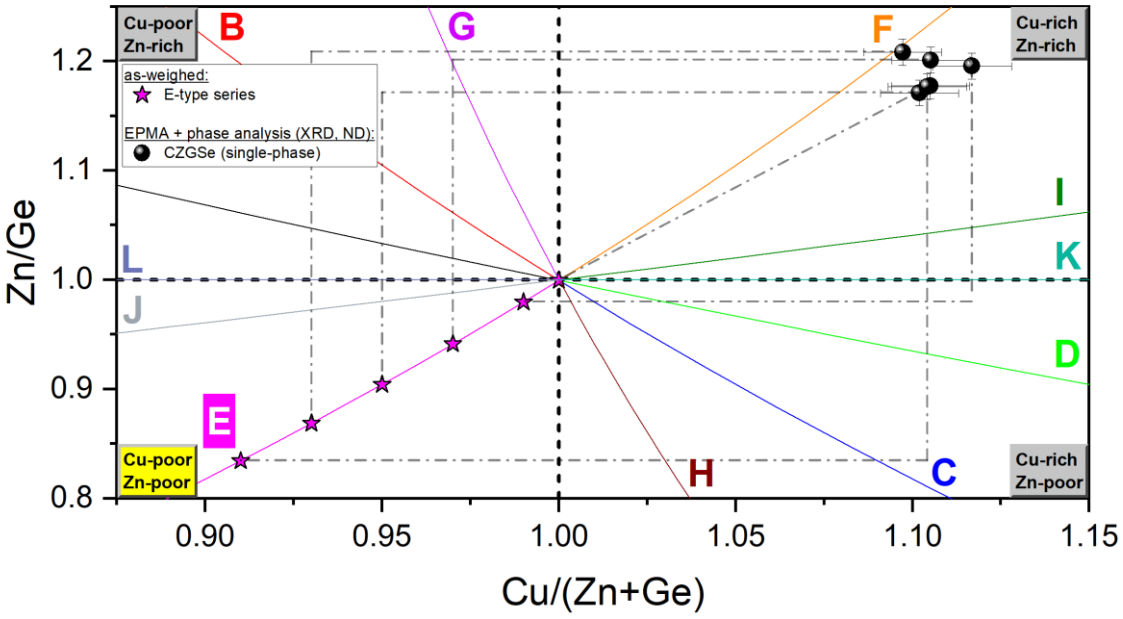

Figure 3-13 As-weighed and obtained composition of the CZGSe phases within the E-type series. Data points stemming from the same sample are connected with dash-dotted tie lines. All synthesized samples solely consist of the CZGSe phase.

Table 3-8 Overview of the post-synthesis composition and type fractions determined for the E-type sample series.

Sample labeling	*e* (as-weighed)	Sum formula ($Cu_{2-2e}Zn_{1-e}Ge_{1+e}Se_4$)	Cu/(Zn+Ge)	Zn/Ge	Type fractions (%)
E0000-1	0.000	$Cu_{2.20}Zn_{1.08}Ge_{0.91}Se_4$	1.105	1.178	F (93) – I (7)
E0010-1	0.010	$Cu_{2.22}Zn_{1.08}Ge_{0.91}Se_4$	1.117	1.196	F (92) – I (8)
E0030-1	0.030	$Cu_{2.20}Zn_{1.09}Ge_{0.91}Se_4$	1.105	1.202	F (96) – I (4)
E0050-1	0.050	$Cu_{2.19}Zn_{1.07}Ge_{0.92}Se_4$	1.102	1.172	F (93) – I (7)
E0070-1	0.070	$Cu_{2.19}Zn_{1.09}Ge_{0.91}Se_4$	1.097	1.209	F (99) – I (1)
E0090-1	0.090	$Cu_{2.19}Zn_{1.08}Ge_{0.91}Se_4$	1.104	1.177	F (93) – I (7)

3.4.4 The Cu-rich and Zn-rich quadrant

3.4.4.1 F-type series

Reversing the cation substitution reaction defining the E-type series leads to the Cu-rich and Zn-rich F-type series. Five off-stoichiometrically samples and one stoichiometrically weighed sample of 5 g each are synthesized to eventually finish the survey of all compositional quadrants – at least regarding the as-weighed compositions. In fact, most of the samples previously discussed experienced a compositional shift tending towards the Cu-rich and Zn-rich regime after the thermal treatment and thus make them clustering around the F-type line anyway. Consequentially and in spite of yet another considerable discrepancy between as-weighed and obtained composition, the samples of original F-type composition represent the only sample series whose post-synthesis compositions remain entirely in the same compositional regime, that is, the Cu-rich and Zn-rich quadrant.

The mode of the compositional shift reminisces about the one shown by the Cu-poor B-type sample series (cf. Figure 3-9) which is also Zn-rich and Ge-poor and, thus, compositionally 'mirrored' with respect to the Cu-rich F-type; the least off-stoichiometric samples are rather following the path that is generally exhibited by the A-, C-, D- and E-type series while samples originally characterized by stronger off-stoichiometries are becoming relatively depleted in zinc or enriched in germanium. This compositional shift therefore results in F – I- and I – K-type mixtures mainly plotting around the I-type line. Secondary phases have formed in the majority of the samples with only the stoichiometrically weighed sample being exclusively composed of the CZGSe phase. In the remaining samples ZnSe again is present, and CuSe has additionally formed in the most off-stoichiometric samples (Figure 3-14). The weight fraction of secondary phases steadily increases as the targeted off-stoichiometry becomes larger. The quantified amounts of secondary phases as well as the actual type mixtures are presented in Table 3-9.

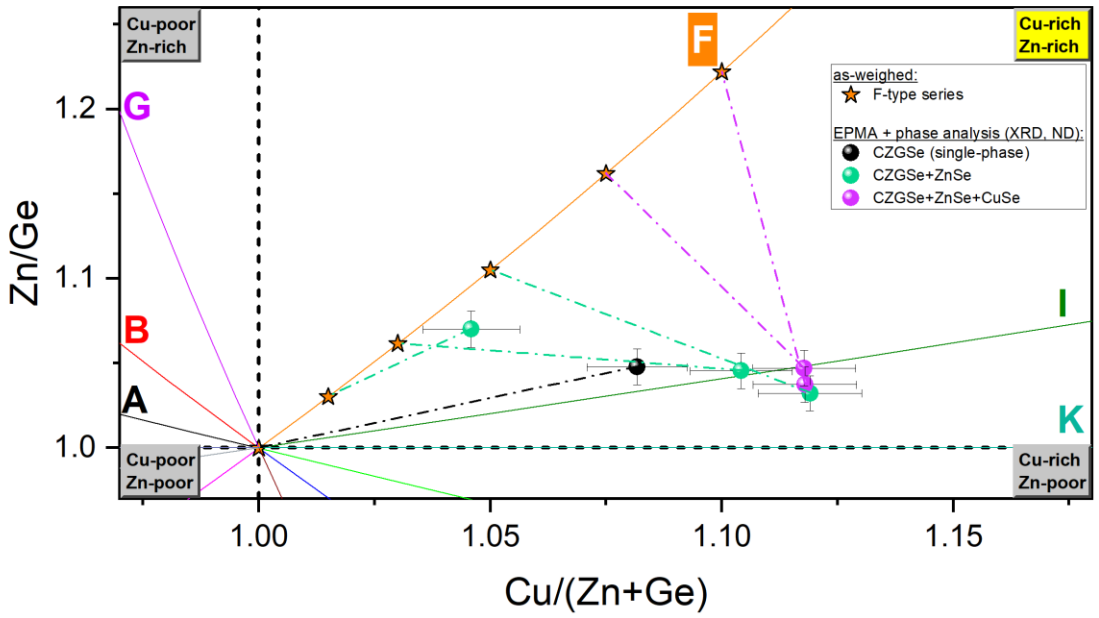

Figure 3-14 As-weighed and obtained composition of the CZGSe phases within the F-type series. Data points stemming from the same sample are connected with dash-dotted tie lines. The phase content is represented by different colors.

Table 3-9 Overview of the obtained off-stoichiometry type mixtures and identified secondary phases in intended Cu-rich/Zn-rich F-type samples.

Sample labeling (pre-synthesis)	Sample labeling (post-synthesis)	Intended off-stoichiometry type	Obtained off-stoichiometry type mixture	Secondary phases (in wt%)
F0000-1	F0000-1	F	F – I	none
F0015-1	F0015-1	F	F – I	ZnSe (2)
F0030-1	F0030-1	F	F – I	ZnSe (3)
F0050-1	F0050-1	F	I – K	ZnSe (6)
F0075-1	F0075-1	F	I – K	ZnSe (8), CuSe (5)
F0100-1	F0100-1	f	I – K	ZnSe (7), CuSe (8)

The amount of germanium incorporated in the F-type samples is remarkably different compared to the others as all F-type samples are relatively enriched in germanium (cf. Figure 3-4) and are also characterized by generally higher molar quantities of germanium. The samples from the A- to the E-type series very consistently show 0.92 mole of germanium on average while the F-type series

averagely contains 0.96 mole of germanium. The compositional shift observable in Figure 3-14 is governed by an overall relative enrichment both in copper and germanium, and a relative depletion in zinc with increasing off-stoichiometry (i.e. with larger amounts of zinc employed in the synthesis) eventually leading to a dominating I-type contribution (Table 3-10).

Table 3-10 Overview of the post-synthesis composition and type fractions determined for the F-type sample series.

Sample labeling	*f* (as-weighed)	Sum formula ($Cu_{2+2f}Zn_{1+f}Ge_{1-f}Se_4$)	Cu/(Zn+Ge)	Zn/Ge	Type fractions (%)
F0000-1	0.000	$Cu_{2.13}Zn_{1.01}Ge_{0.96}Se_4$	1.082	1.048	F (38) – I (62)
F0015-1	0.015	$Cu_{2.09}Zn_{1.03}Ge_{0.96}Se_4$	1.046	1.070	F (91) – I (9)
F0030-1	0.030	$Cu_{2.16}Zn_{1.00}Ge_{0.96}Se_4$	1.104	1.046	F (9) – I (91)
F0050-1	0.050	$Cu_{2.18}Zn_{0.99}Ge_{0.96}Se_4$	1.119	1.033	I (67) – K (33)
F0075-1	0.075	$Cu_{2.18}Zn_{1.00}Ge_{0.95}Se_4$	1.118	1.047	I (98) – K (2)
F0100-1	0.100	$Cu_{2.18}Zn_{0.99}Ge_{0.96}Se_4$	1.118	1.038	I (78) – K (22)

3.4.5 Hot spots of secondary phases and the role of germanium

The chemical composition and the phase content obtained after the synthesis are discussed in the previous sections where emphasis is clearly put on the composition and its mode of deviation. In addition, secondary phases are identified in the majority of the samples with cumulated weight fractions ranging between ~1 and 16 %. When plotted in the cation ratio graph localized regions with larger quantities of secondary phases become apparent. The most pronounced 'hot spot' is located around the I-type line at Cu/(Zn+Ge) ~1.15 (Zn/Ge ~1.05) and a second one between the G- and F-type line at Cu/(Zn+Ge) ~1.03 (Zn/Ge ~1.2). A third region of increased fractions of secondary phases potentially emerges in the Cu-poor regime between the B- and G-type line at Cu/(Zn+Ge) <0.90 (Zn/Ge >1.4) but data basis is too sparse around there (Figure 3-15a). Like for the compositional outcome, the initial germanium content apparently very much influences the quantity of

secondary phases formed. As previously mentioned, gaseous GeSe preferentially condenses at the ampule walls and, thus, is separated from the actual specimen such that no traces of this phase are observable in any of the samples. The secondary phases identified in the samples therefore includes ZnSe, CuSe, $GeSe_2$, and even unreacted Ge. Among these secondary phases ZnSe is by far the most abundant representative. Like Figure 3-4a in section 3.2, Figure 3-15b shows once again the deviation between as-weighed pre-synthesis and post-synthesis CZGSe composition related to the as-weighed amount of germanium, but now with emphasis on the total weight fractions of the secondary phases.

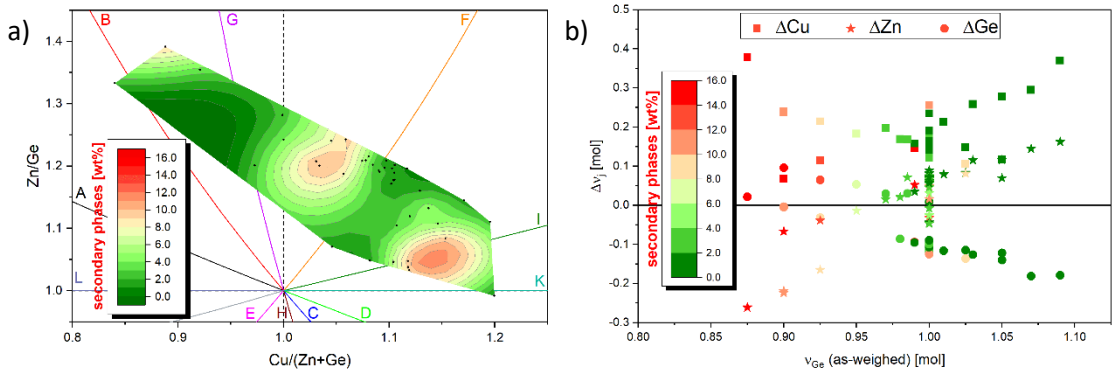

Figure 3-15 a) Contour plot showing the weight fractions of secondary phases (mainly ZnSe). At least two regions where samples with strongly raised weight fractions of secondary phases are concentrated at can be identified. b) Difference between measured and weighed molar amounts of the cations ($\nu_{j(WDX)} - \nu_{j(weighed)}$) in dependence of the weighed amount of germanium with the fractions of detectable secondary phases being color-coded.

The largest amounts of aforementioned secondary phases (particularly ZnSe) have formed under Ge-poor start conditions as well as for samples with an initially stoichiometric Ge content and Zn-rich conditions. Consequently, the A- (Zn-rich, Ge = 1 = constant), B- (Zn-rich, Ge-poor) and F-type (Zn-rich, Ge-poor) samples do contain the largest weight fractions of (quantifiable) secondary phases. From that point of view, it can be hypothesized that Ge-rich (and Zn-poor) start conditions lead to the formation of a similar quantity of secondary phases but it is then mainly a matter of volatile GeSe (rather than $GeSe_2$). This may also explain the susceptibility of the C-type samples to become chemically inhomogeneous as they are Ge-rich and the Zn-poorest ones; the enhanced formation and removal of the GeSe component may negatively affects the homogenization process. The B-type series, which is Ge-poor and the most Zn-rich type series and thus the C-type's counterpart, contains

the largest amounts of secondary phases (mainly ZnSe) but is chemically homogeneous. So, Ge-poor and Zn-rich conditions particularly facilitate the formation of ZnSe but seems not to hinder the homogenization considerably whereas any chemical potential promoting the formation of (more) volatile GeSe appears to have a detrimental impact on chemical homogeneity.

3.4.6 Conclusions of chemical and phase characterization

Solid-state synthesis was employed to prepare CZGSe powder specimens at sufficient amounts as specifically required for powder neutron diffraction. In total eight sample series comprising, respectively, 42 off-stoichiometrically and seven stoichiometrically weighed samples were synthesized aiming at addressing all compositional regimes. Upon synthesis every sample is however subject to processes that alter the composition of the final product. Of course, the solid-state reaction provides a closed system meaning the integral composition of the as-weighed educts and the entirety of the post-synthesis products will remain the same. The integral compositions, however, were not determined and hence the chemical balancing was restricted to a comparison both between the well-known composition of the educts and the obtained CZGSe phases.

Probably the biggest weakness of the solid-state reaction is related to the large reaction volume compared to the dimensions of the carbon crucible or the specimen itself that eventually facilitates more GeSe to sublime. Because the reaction volume was kept constant for every ampule, compositional shifts of similar extent as well as the tendency of the investigated CZGSe phases to consistently incorporate around 90 mol% of germanium might be explainable. Despite, for the majority of the samples the chemical homogeneity achieved after the synthesis turns out to be adequate enough for a reasonable characterization with respect to cation distribution and point defect concentration, albeit the two C-type series represent a great exception. Most of the C-type samples developed strong chemical inhomogeneities that even remain after a second homogenization step, although slightly rectified. Once a synthesis results in such inhomogeneities an improvement

towards a more satisfying compositional spread seems demanding at least for the applied heat treatment. In contrast to the pure elements the syntheses were started with, higher temperatures (i.e. >700° C) will probably be required for the produced compounds to facilitate better mobilization and redistribution of the atoms. In addition, germanium has partly been driven off the sample crucible upon formation and sublimation of gaseous GeSe. The $GeSe_{(g)}$ did mainly condense at the ampule walls and was not (fully) recoverable to restore the initial sample's composition. The specimens retrieved after the solid-state synthesis were therefore subject to germanium deficiency that likely further impeded a successful homogenization.

Owing to the small existence region of the CZGSe phase (cf. Figure 1-8b) secondary phases do readily form with ZnSe being by far the most frequent one, occasionally along with CuSe and $GeSe_2$ which are present to a much lesser extent. The formation and persistence of secondary phases as well as unreacted educts lead to a selective removal of certain chemical constituents which are then not available for the desired CZGSe phase, what cannot easily (and accurately) be quantified and hence not precisely accounted for. The weight fractions of secondary phases very often only amounted for a few weight percent and rarely reached >10 wt%. The largest amounts of secondary phases (mainly ZnSe) are found in samples that were originally Zn-rich and Ge-poor (B-type). An obvious correlation between the fraction of secondary phases formed and the compositional deviation is found for initially Ge-poor samples (cf. Figure 3-15b). Samples originally being Ge-rich (C- and E-type) appear to contain, if any, considerably fewer secondary phases, yet might still be of similar extent through a more pronounced formation of $GeSe_{(g)}$ which seems to form preferentially as compared to $GeSe_2$ for the given synthesis conditions. In fact, the 13 single-phase samples mostly originate from Ge-rich samples. However, they experienced virtually the same compositional shifts as the multi-phase samples did, indicating that the discrepancy between as-weighed and obtained CZGSe composition is mostly governed by the formation and volatilization of GeSe. In this regard, the ‘hot spots’ of secondary phases shown in Figure 3-15a misleadingly indicate high concentrations of secondary phases for certain compositions, though, rather similar amounts along all compositions can be assumed instead.

3.5 The crystal structure of CZGSe and its structural response to off-stoichiometry

3.5.1 Applicability of the kesterite-type structure and stannite-type structure for CZGSe

In section 1.5.1 the longstanding uncertainty about the actual crystal structure of kesterite and its synthetic analogues is discussed which at first was believed to adopt the stannite-type structure (s.g. $I\bar{4}2m$ [140]) [143]. Although this assumption could be proven incorrect by careful structure refinements on a natural specimen [139] as well as by neutron diffraction experiments [8, 9, 144] the stannite-type structure became widely be accepted and used to describe the crystal structure of kesterite and its synthetic analogues over some decades. In spite of the differences between the kesterite-type and stannite-type structure, respectively, an unambiguous distinction is difficult when conventional X-ray diffraction is used. The latter structure additionally possesses a two-fold rotation axis and a mirror plane, and copper and zinc are distributed differently. Indeed, these additional symmetry elements render intensities of *hkl* and *khl* reflections equivalent and thus reduces the number of Bragg peaks, yet still lead to the exact same set of Bragg peak positions.

Since the stannite-type and kesterite-type structures are each characterized by a tetragonal body-centered Bravais lattice, whose Bragg peaks for which $h + k + l = n$ (n = odd integer number) holds are subject to complete extinction. In addition, the face-centered cubic (fcc) Bravais lattice of the parental diamond-type structure is essentially inherited in both structures, albeit without the ideal cubic metric. As discussed in section 1.5.2 the tetragonal representatives within the adamantine compound family [48, 54] can be viewed as a stack of two face-centered cubic Bravais lattices with an aspect ratio typically close to one but still slightly differing from it: $\frac{c}{2a}$ = tetragonal deformation = $\eta \neq 1$. The displacement vector of the anion affects each of the associated peak intensities by diminishment or enhancement of destructive interference; the *x*- and *y*-coordinates do decisively

govern the h0h and hh0 peak intensities whereas the *z*-component strongly influences the 00l peak intensities. Hence the tetragonal deformation and the anion position eventually determine how strong the X-rays interfere destructively that are scattered from lattice planes to which the fcc extinction rules would apply. The closer the tetragonal deformation approaches one and the smaller the anion's displacement from the 'ideal' position the lower those intensities become.

Because the tetragonal deformation is always pretty close to one and the anion's displacement is small the Bragg peaks of the stannite-type and kesterite-type structure that are corresponding to those being extinguished in case of an fcc lattice are generally subject to low relative intensities. This is additionally strengthened by too similar atomic form factors as is particularly the case for CZGSe, but nevertheless also depends on the occupation scheme of the cations as it changes the small but yet existing contrast in atomic form factors among those planes and thus the resulting net amplitude of the scattered X-rays. In principle, differences in the respective diffraction patterns should therefore be observable that are produced by the anion position, dissimilar tetragonal deformation and the different occupation specifically of the (00l) and (hh0) planes. However, the differences caused by the tetragonal deformation as well as of the anion positions (x,y,z) ($I\bar{4}$), (x,x,z) ($I\bar{4}2m$), and even the 'ideal' $\left(\frac{1}{4},\frac{1}{4},\frac{1}{8}\right)$ anion position, respectively, are quite small and complicates an unambiguous distinction in an experimental XRD pattern. The strongest impact on intensity is after all created by the contrast in atomic form factors of the cations and their different occupation of the layers in the (001) and (110) planes. Accordingly, the 00l and hh0 peak intensities are responding the most on the cation arrangement and are therefore a mean to basically allow differentiation between kesterite-type and stannite-type structure, respectively.

In CZTSe, for instance, the isoelectronic cations Cu^{+} and Zn^{2+} cannot be distinguished and thus their site location not assigned by conventional XRD. Different distributions of Sn^{4+} would indeed cause noticeable changes in the relative peak intensities as its atomic form factor is considerably differing from the ones of copper and zinc. Tin is however occupying the same Wyckoff position (2b) both in the kesterite-type and stannite-type structure, respectively, but generally provides an increased contrast in atomic form factors. In case of CZGSe all cations are

characterized by virtually identical atomic form factors which lead to an overall diminishment of scattering amplitude contrast in between certain lattice planes like (00l), (h0h) and (hh0). The corresponding relative peak intensities are therefore significantly differing between CZTSe and CZGSe as well as between kesterite-type and stannite-type structure but with the exception of the h0h peak intensity (Figure 3-17a & b).

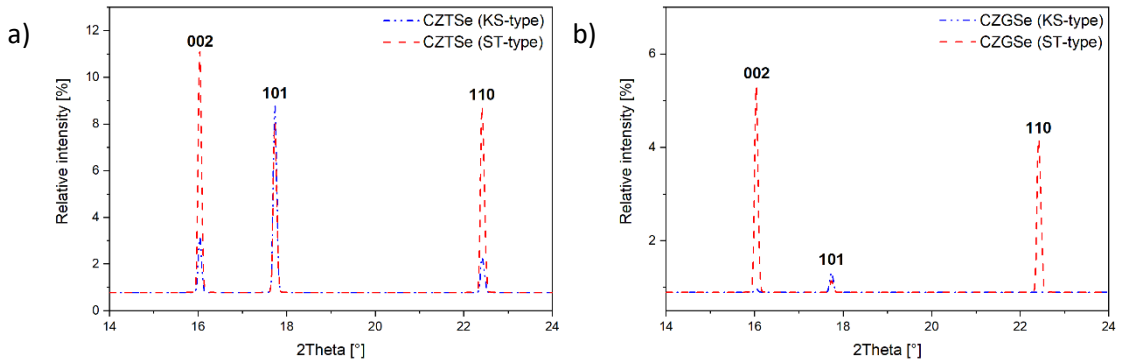

Figure 3-16 Comparison between the calculated relative intensities of the 002, 101 and 110 Bragg peaks of the kesterite-type (KS) and stannite-type (ST) structure for a) CZTSe and b) CZGSe. The different cation arrangement in both structures creates noticeable differences in 002 and 110 peak intensities. The (101) lattice planes are occupied by the same cations which thus not affect the 101 peak intensity. Instead the slight deviation is caused by the different anion position and dissimilar tetragonal deformation.

The (h0h) lattice planes are occupied with the same cations either way and the h0h peak intensity is only subtly influenced both by different tetragonal deformations and anion positions. A perceptible difference only arises from the different occupation of the (00l) and (hh0) planes: In the stannite-type structure Cu – Cu and Zn – Sn (Zn – Ge) layers are forming the (001) and (110) plane, respectively, whereas the kesterite-type structure is characterized by Cu – Zn and Zn – Sn (Zn – Ge) layers along these planes (Figure 3-17a & b). Owing to this different cation arrangement the contrast in atomic form factor is enhanced in the stannite-type structure, hence giving rise to more pronounced relative intensities of the 00l and hh0 peaks. In general, the mixed occupation in the kesterite-type structure leads to an enhanced cancellation in contrast of the atomic form factors and the resulting scattering amplitude, hence to decreasing 002 and 110 Bragg peaks intensities. In case of CZGSe the contrast in atomic form factors is even nearly neutralized and those Bragg peaks are almost vanished completely.

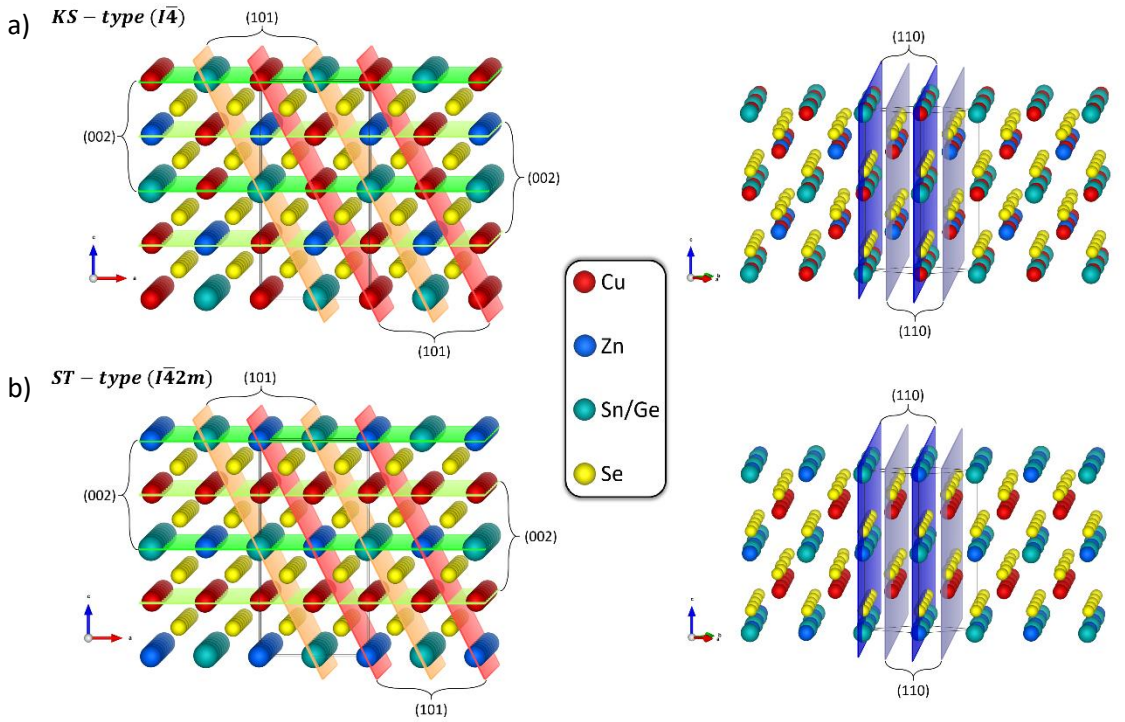

Figure 3-17 Representation of a) kesterite-type (KS) and b) stannite-type structure (ST) along [010] (left panels) and [1$\bar{1}$0] (right panels) direction, portraying the lattice planes contributing to the 002, 101 and 110 peak intensities. For each of these lattice planes an equivalent exists that is occupied differently and offset by ½ (the (101) plane offset by ¼ is omitted in favor of better clarity). The occupation scheme determines the magnitude of the resulting net amplitudes scattered from equivalent lattice planes.

While it is unquestioned that isoelectronic atoms represent a huge obstacle for conventional XRD because they render site allocation of the concerning atoms impossible, it can actually also be advantageous as specifically in case of CZGSe with all cations being isoelectronic that at least allows a more reliable differentiation between stannite-type and kesterite-type structure. Here, the difference in relative intensities is basically large enough but it must however be considered that the 002, 101, and 110 Bragg peaks are comparably low in intensity and subject to a poor signal-to-noise ratio that still can make an unambiguous discrimination a difficult affair. And yet, a Rietveld refinement even of ordinary p-XRD patterns with a sufficiently good counting statistic will nonetheless allow to make a reliable decision on the actual crystal structure. The refinements of the p-XRD patterns recorded for the CZGSe samples examined in this thesis are clearly pointing to the kesterite-type structure as the refinement's quality factors are considerably increased when the stannite-type structure is used as starting model (Figure 3-18a & b).

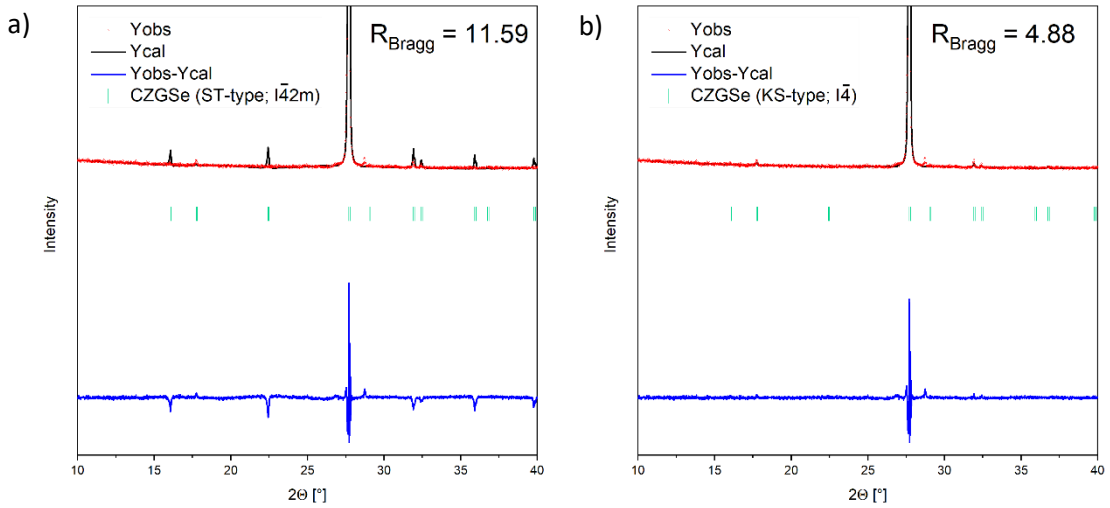

Figure 3-18 Detail view of a refined p-XRD pattern recorded for an off-stoichiometric single-phase CZGSe sample employing a) the stannite-type (ST-type) structure and b) the kesterite-type (KS-type) structure as structural starting model.

That CZGSe adopts the stannite-type structure can also be disproven when this model is applied in the refinements of p-ND data. The respective neutron scattering lengths of the cations are sufficiently different (cf. Figure 2-5 in section 2.2.2.2) to state about the actual crystal structure with higher confidence. Among the 'cationic' Wyckoff positions only the one hosting germanium (i.e. 2b) delivers reasonable site occupancy factors as this position is occupied with germanium in both cases. On the other hand, the 2a position for instance is either occupied with zinc (ST-type) or copper (KS-type). Using the stannite-type structure leads to strongly increased site occupancy factors for this position, resulting in average neutron scattering lengths that cannot be achieved when zinc is occupying this position completely. In fact, already small amounts of zinc would require a large fraction of copper and even of germanium to compensate for its small neutron scattering length and to eventually reduce the huge discrepancy with respect to the average neutron scattering length determined for the 2a site.

3.5.2 Unit cell metrics

With 0.510 Å [146] the ionic radius of tetrahedrally coordinated Ge^{4+} is considerably different from those of Cu^{+} and Zn^{2+}. Its radius accounts for ~80 % of the radii of Cu^{+} and Zn^{2+}, respectively, and the amount of germanium and the way it is distributed in the structure will therefore cause noticeable changes in the dimensions of the unit cell. On the other hand, the effective ionic radii of tetrahedrally coordinated Cu^{+} (0.635 Å) and Zn^{2+} (0.640 Å) [146] are differing by ~0.8 % only, and different distributions of them can thus be expected to affect the unit cell metrics in a much more subtle manner. Nonetheless will the different valence state of Cu^{+} and Zn^{2+} affect the electrostatic interactions in their proximate vicinity and by that bond angles and bond distances do change. Likewise, a significant population of point defects, specifically those involving antisite defects on the Ge (2b) position, may affect the (average) metrics of the unit cell. The subsequent sections will shed some light on the impact the various deviations from stoichiometry and corresponding point defects may have on structural parameters. The structural characterization is based both on p-ND and p-XRD, respectively. In either case the recorded data are treated applying the Rietveld method [6, 7] with the kesterite-type structure (s.g. $I\bar{4}$) being included as structural starting model for the CZGSe phase.

3.5.2.1 Lattice parameters

From neutron diffraction data valuable information can be gathered that are either not reliably or not at all accessible using p-XRD, yet the latter represents a more suitable tool when seeking for more precise lattice parameters. The wavelength of the neutrons is determined experimentally by refining the wavelength upon a measured standard material with well-known lattice parameters while the wavelength of the Cu Kα radiation as employed for p-XRD is determinable more precisely. Apart from that the parafocusing geometry used for p-XRD possesses a ~10 times higher angular resolution making determination of lattice parameters more accurate due to sharper Bragg peaks. Therefore the lattice parameters

determined by Rietveld refinements [6, 7] of p-XRD data will be taken into account only.

The lattice parameters are discussed with respect to the cation ratios Cu/(Zn+Ge) and Zn/Ge, respectively, to reflect the impact of composition and implicated point defects (subject of section 3.5.4) on unit cell dimensions. From a more general perspective each point defect species can be considered to cause either shrinkage or enlargement of the unit cell. For instance, any kind of vacant Wyckoff position will definitely make the unit cell dimensions decreasing as such gaps between atoms are energetically unfavorable and the surrounding atoms are forced to achieve a more densely packed arrangement. Regardless of the very similar ionic radii of Cu^{+} and Zn^{2+} a shrinking influence can also be assumed for the Zn_{Cu}^{+} antisite defect owing to the excessive positive charge that leads to a stronger attraction of the neighboring anions, and the shortened bond distances will eventually be reflected by reduced unit cell volumes.

Intuitively, atoms occupying interstitial positions may generally be credited responsible for an enlargement in unit cell dimensions. However, the actual effect will be determined by the size of the ion and its valence state. In the kesterite-type structure 50% of the tetrahedra voids are nominally unoccupied, hence leaving plenty of space for interstitial cations provided excess charges are compensated. Consequentially, cations on those positions (e.g. Cu_{i}^{+}, Zn_{i}^{2+}) cannot be expected to stretch the local structural environment but the opposite is true instead. Again, the excessive positive charges cause an enhanced attraction of the nearby anions and therefore a decrease in unit cell dimension. Contrarily, due to both its larger size as well as its negative charge and the resulting repulsion of the surrounding anions will the unit cell dimensions increase if an anion is occupying the interstitial position. While defects involving the anion are out of consideration here, do cation-related antisite defects effectively leading to a decrease in positive charges play a major role for the expansion in unit cell dimensions (except for vacancies), and vice versa. Such cation-related antisite defects that result in a deficiency in positive charges, as for instance Cu_{Zn}^{-}, Zn_{Ge}^{2-} and Cu_{Ge}^{3-}, do exert fewer attractive forces on their neighboring anions which eventually cause an enlargement in unit cell dimensions.

As a rough approximation to evaluate how the defect types do correlate with the unit cell volume the difference between the total number defects per unit cell causing enlargement ($\delta^{>} = Cu_{Zn}^{-} + Zn_{Ge}^{2-} + Cu_{Ge}^{3-}$) and those causing shrinkage ($\delta^{<} = V_{Cu}^{-} + Zn_{Cu}^{+} + Zn_{i}^{2+} + Cu_{i}^{+}$) is plotted against Cu/(Zn+Ge) (Figure 3-19a). The unit cell volume (Figure 3-19b) is chosen as it is a more suitable parameter to describe the general response of the unit cell on changing composition as well as on the kind and abundance of point defects. The experimentally deduced point defect species and densities taken for this approach will be the subject of section 3.5.4.

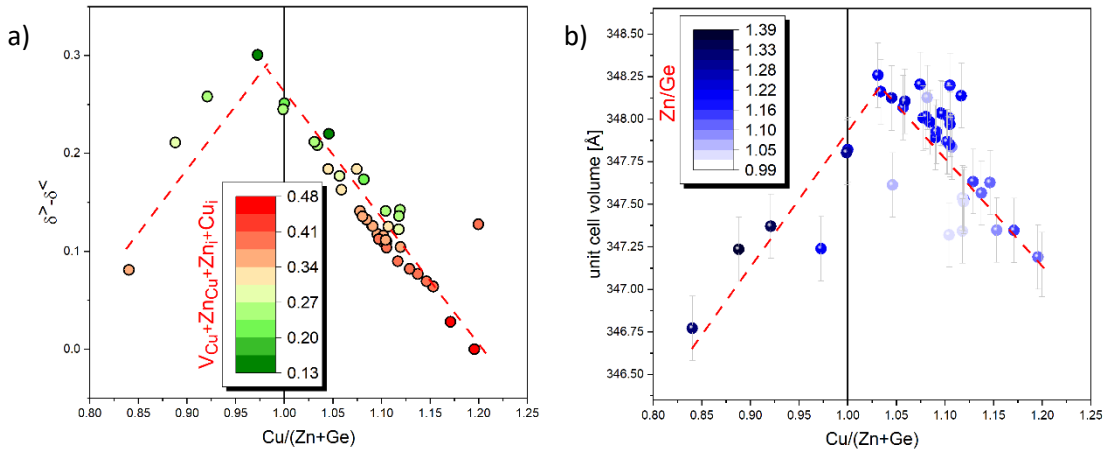

Figure 3-19 Even with the simplistic assumption of equally weighted defects (i.e. without weighting according to the valence number and resulting different Coulomb interaction) the trend exhibited by a) the 'net' amount of defects leading to enlargement, in general, agrees fairly well with the one obtained for b) the unit cell volume. The largest unit cell volumes do correspond with the lowest densities of defect species causing shrinkage of the unit cell volume, and vice versa. The red dashed lines are a guide to the eye.

Although solid trends are also observed for the respective lattice parameters, their behavior is more complex as the various defects induce different changes in *a* and *c*, respectively. Close to the stoichiometric point the lattice parameters *a* and *c* are in good agreement with the values reported in literature [111, 136]. Once the stoichiometric point is left, however, each of them do respond differently with pretty much opposing trends both exhibited by *a* and *c* as well as with respect to Cu/(Zn+Ge) and Zn/Ge (Figure 3-20 to Figure 3-23).

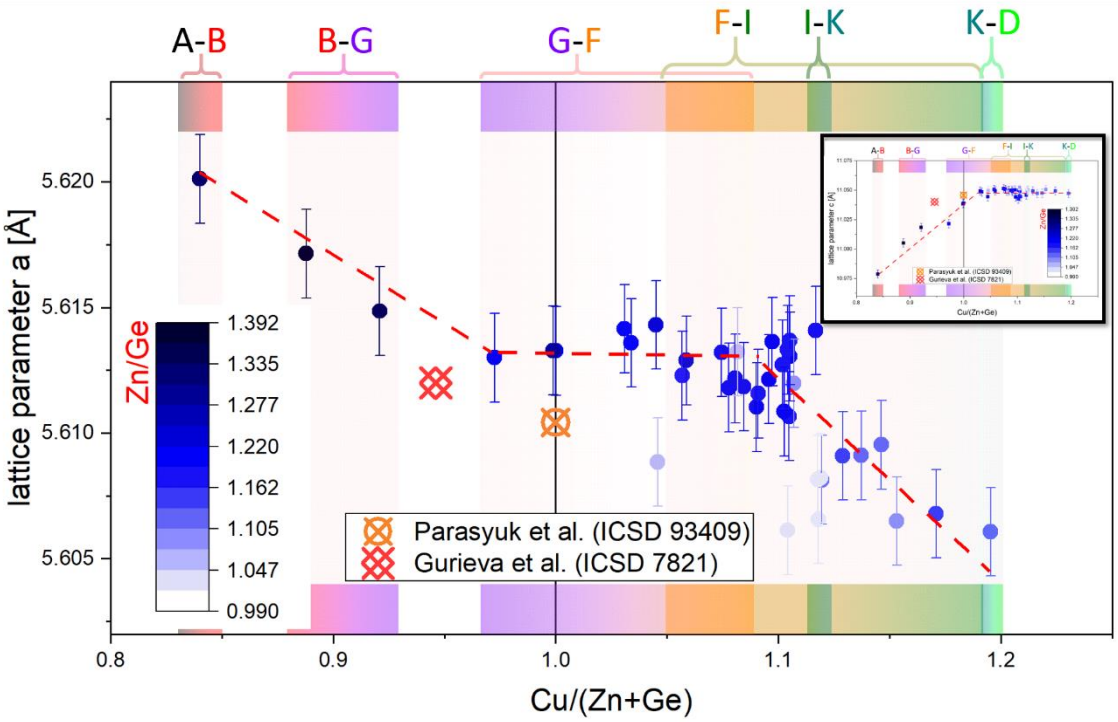

Figure 3-20 Lattice parameter *a* in dependence of Cu/(Zn+Ge). The value for stoichiometric CZGSe taken from the database (ICSD) is included as reference. The Zn/Ge is given by color-coded data points and the type mixture regions are indicated. An inset showing the trend of the *c* parameter is added to allow direct comparison. The red dashed line is a guide to the eye.

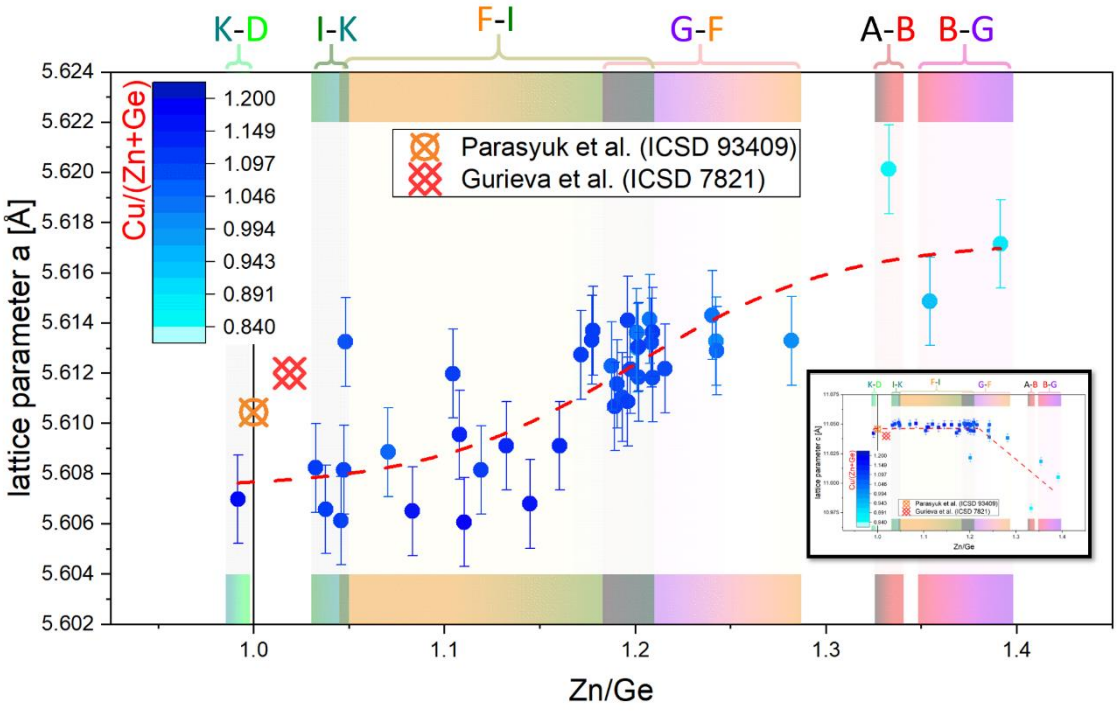

Figure 3-21 Lattice parameter *a* in dependence of Zn/Ge. The value for stoichiometric CZGSe taken from the database (ICSD) is included as reference. The Cu/(Zn+Ge) is given by color-coded data points and the type mixture regions are indicated. An inset showing the trend of the *c* parameter is added to allow direct comparison. The red dashed line is a guide to the eye.

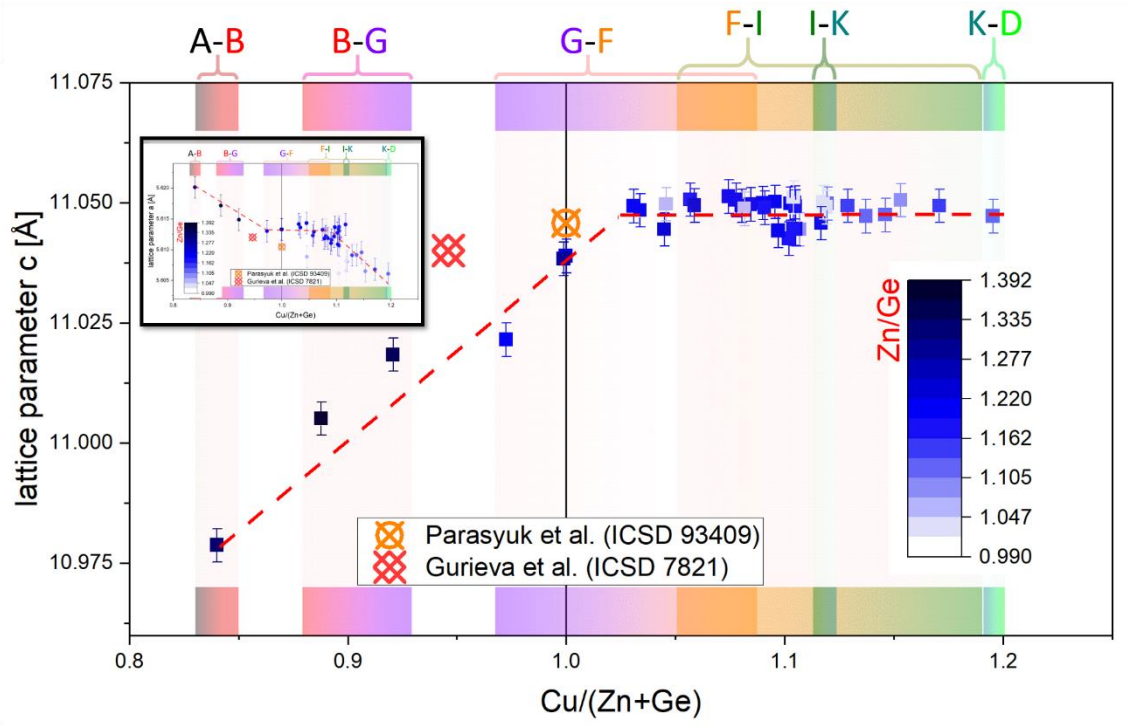

Figure 3-22 Lattice parameter *c* in dependence of Cu/(Zn+Ge). The value for stoichiometric CZGSe taken from the database (ICSD) is included as reference. The Zn/Ge is given by color-coded data points and the type mixture regions are indicated. An inset showing the trend of the *a* parameter is added to allow direct comparison. The red dashed line is a guide to the eye.

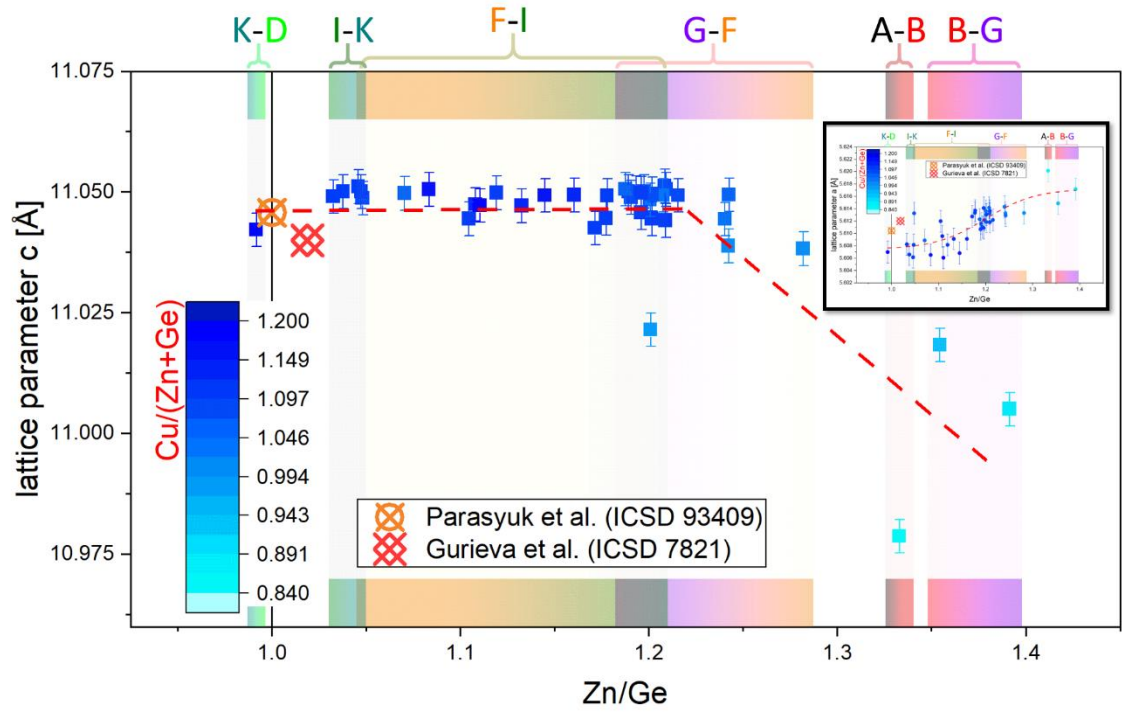

Figure 3-23 Lattice parameter *c* in dependence of Zn/Ge. The value for stoichiometric CZGSe taken from the database (ICSD) is included as reference. The Cu/(Zn+Ge) is given by color-coded data points and the type mixture regions are indicated. An inset showing the trend of the *a* parameter is added to allow direct comparison. The red dashed line is a guide to the eye.

With the exception of a plateau-like trend within the G – F-type region bounded by the stoichiometric point and slightly Cu-rich conditions (~ 1.0 < Cu/(Zn+Ge) < 1.1) lattice parameter *a* generally tends to decrease quite linearly as the copper content increases (cf. Figure 3-20). The first decrease from the most Cu-poor composition to the stoichiometric point is attributed to V_{Cu}^{-} and Zn_{Cu}^{+} whereas the plateau-like region of stagnating *a* parameter coincides with the appearance of unit cell enlarging Cu_{Ge}^{3-} defects that obviously counteract the continued shrinkage of lattice parameter *a* provoked by the V_{Cu}^{-}, Zn_{Cu}^{+} and, in particular, Zn_{i}^{2+} defects (c.f section 3.5.4 for densities of point defect species). With increasing I-, K-, and D-type contribution the unit cell enlarging Zn_{Ge}^{2-} defect disappears while Cu_{i}^{+} defect concentration resides on a high level which eventually makes lattice parameter *a* again decreasing towards highest Cu/(Zn+Ge). A rise in Zn/Ge goes along with an increasing *a* parameter, although the values are more dithering and the trend is best described using a sigmoidal curve (cf. Figure 3-21). Despite of the high density of unit cell enlarging Cu_{Ge}^{3-} (and partly Cu_{Zn}^{-}) antisite defects in the region between Zn/Ge ≈ 1.0 and slightly Zn-rich conditions is the *a* parameter more dominated by a high population particularly of Cu_{i}^{+} and, to a lesser extent, of Zn_{i}^{2+}. Hence, the *a* parameter tends to lower values for lower Zn/Ge. At moderately Zn-rich conditions (Zn/Ge ≈ 1.2) the density both of Cu_{Ge}^{3-} and Cu_{i}^{+} is declining whereas Zn_{Ge}^{2-} starts to rise which all in all increases lattice parameter *a*. In the most Zn-rich regime the Cu_{i}^{+} defect disappears and the unit cell enlarging Zn_{Ge}^{2-} antisite defect competes only with the unit cell shrinking Zn_{Cu}^{+} and Zn_{i}^{2+} defects. As a net effect, lattice parameter *a* tends to result in larger values.

Lattice parameter *c*, on the other hand, shows fairly linear slopes and plateaus both in dependence of Cu/(Zn+Ge) and Zn/Ge, but in which the respective trends are distinctively opposing each other. Between most Cu-poor and slightly Cu-rich conditions the *c* parameter steadily increases until it turns into a wide-stretched plateau (cf. Figure 3-22). When plotted against Zn/Ge this plateau ranges from Zn/Ge ≈ 1.0 to moderately Zn-rich conditions before lattice parameter *c* starts to decrease approximately linearly (cf. Figure 3-23), though, data basis is pretty sparse in this region.

The lowest value of lattice parameter *c* is observed for the lowest Cu/(Zn+Ge) and, thus, governed by V_{Cu}^{-} and Zn_{Cu}^{+} defects. The following two B – G-type samples do not contain normative V_{Cu}^{-} but Zn_i^{2+} and a higher population of Zn_{Ge}^{2-}, with Zn_i^{2+} defects being assumed to cause fewer unit cell shrinkage which is reflected by the increasing *c* parameter. Once the G – F-type region close to the stoichiometric point is reached, Cu_i^{+} defects are introduced to an increasing degree, whose shrinking impact on unit cell dimension (specifically on lattice parameter *c*) is however compensated by the emerging Cu_{Ge}^{3-} antisite defects which show a comparable trend as Cu_i^{+}. This might be explaining those little variations of lattice parameter *c* over a wide compositional range in dependence both of Cu/(Zn+Ge) as well as Zn/Ge.

The tetragonal deformation remains smaller than one for all samples, and whose trends exhibited (Figure 3-24) are mainly coined by lattice parameter *c* as it is subject to larger absolute changes than lattice parameter *a*. Consequently, the tetragonal deformation is strongest (lowest by figure) for low Cu/(Zn+Ge) from where it fairly steeply and linearly decreases (i.e. increases numerably) until Cu/(Zn+Ge) ≈ 1. Following, the tetragonal deformation turns into a gentler slope towards highest Cu/(Zn+Ge). When plotted against Zn/Ge it gently increases (i.e. decreases numerably) from Zn/Ge ≈ 1 to Zn/Ge ≈ 1.2 and shows then a steeper slope towards highest Zn/Ge.

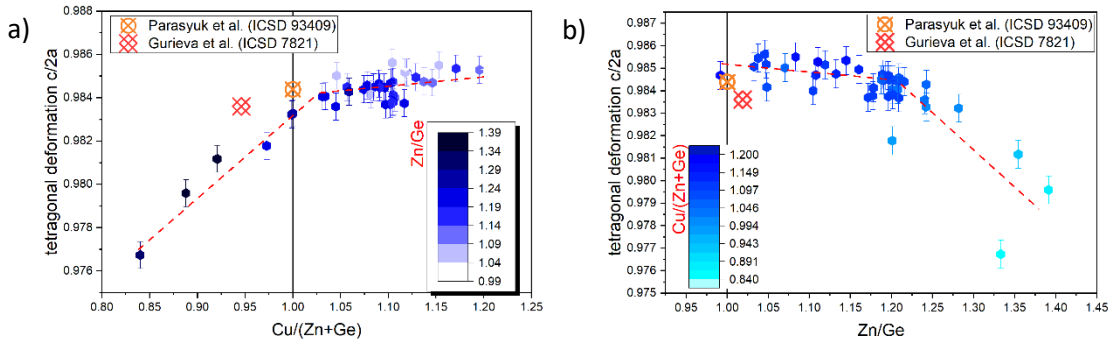

Figure 3-24 Tetragonal deformation in dependence of a) Cu/(Zn+Ge) and b) Zn/Ge. The red dashed lines are a guide to the eye.

3.5.2.2 Anion position and tetragonal distortion

In the kesterite-type structure one can choose between 16 different sets of equivalent coordinates for the anion position (8g) that result from the two possible origins in the parental zincblende-type structure (Figure 3-25) and when the transformations allowed by symmetry are applied.

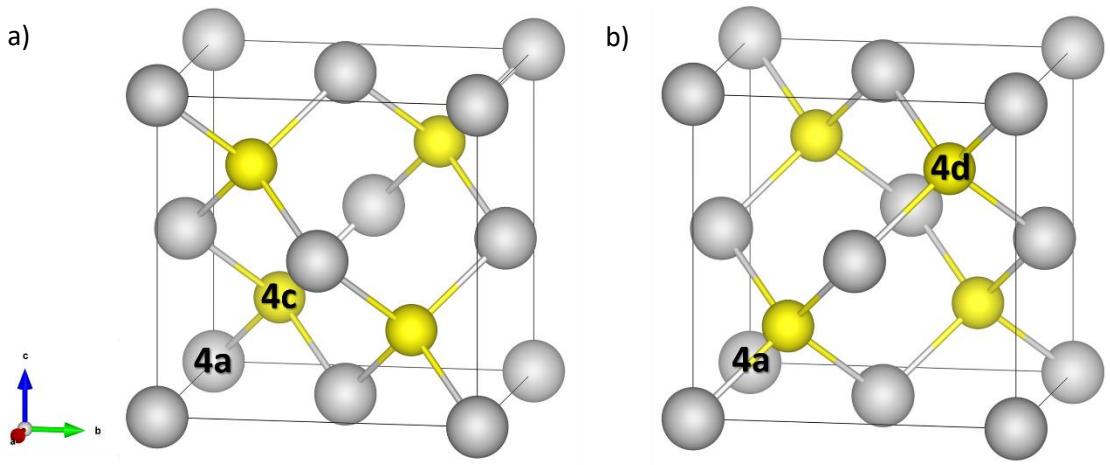

Figure 3-25 Representation of the zincblende-type structure showing its two different but fully equivalent settings with the anion either occupying a) the 4c position or b) the 4d position, respectively.

For the structural model used in the Rietveld analysis the 4c position of the zincblende-type structure is chosen as origin with no transformation applied (i.e. 8g = $x, y, z = \frac{1}{4} \pm \delta_x, \frac{1}{4} \pm \delta_y, \frac{1}{8} \pm \delta_z$). The amount the actual coordinates do differ from the special position $\left(\frac{1}{4}, \frac{1}{4}, \frac{1}{8}\right)$ depends on the size and valence state of the cation species as well as their distribution in the structure and is eventually referred to as tetragonal distortion $u_{x,y,z}$ (with $u_x = \left|\frac{1}{4} - x\right|, u_y = \left|\frac{1}{4} - y\right|, u_z = \left|\frac{1}{8} - z\right|$. In fact, the obtained anion parameters should be in accordance with what can be expected from the change in effective charges and sizes for the respective Wyckoff position that result from the mixed occupation, interstitial defects, or from vacancies. For example, the Cu-poor A – B-type sample is characterized by V_{Cu}^{-}, Zn_{Cu}^{+}, Zn_{Ge}^{2-} defects as well as by a certain amount of Cu-Zn disorder among the 2c and 2d position. The effect those defects do have on the anion position can (naively) be estimated by evaluating the impact on resulting charge and effective size for the respective Wyckoff position (Figure 3-26).

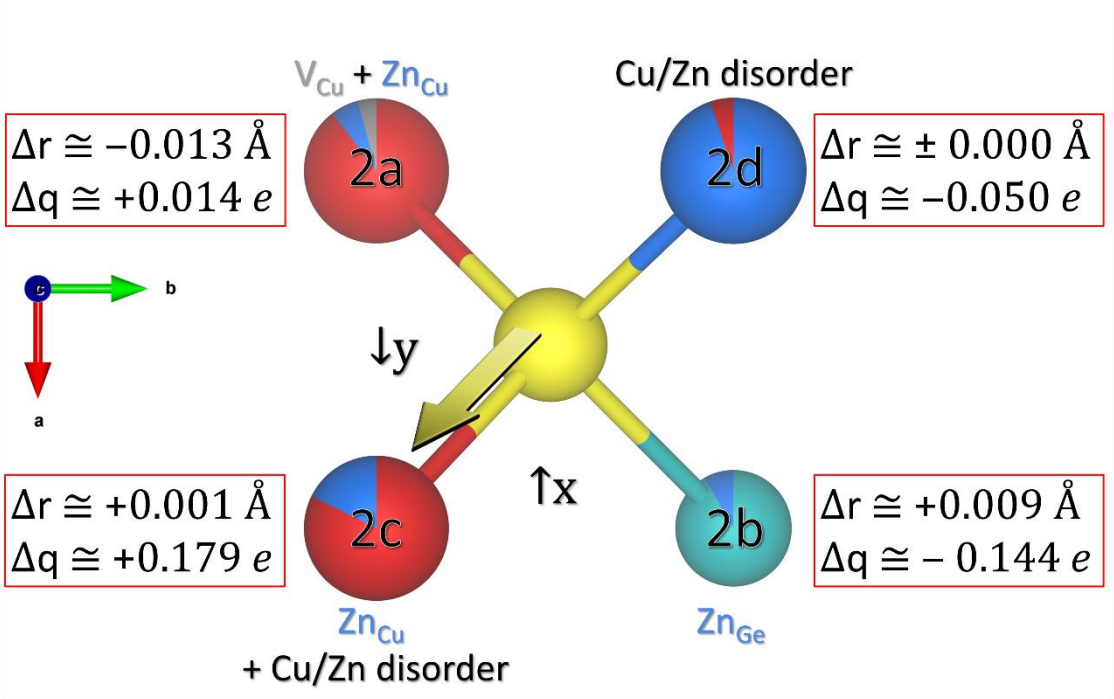

Figure 3-26 Representation of the anion tetrahedron in off-stoichiometric kesterite-type CZGSe. The mixed occupation of the cation positions (as determined for the A – B-type sample) do affect the average radius as well as the Coulomb interaction that eventually result in corresponding displacement of the central anion.

From the cation distribution obtained for the A – B-type sample, the strongest impact on the anion position can be assumed to be exerted by the Cu(2c) position as this is the one being subject to the largest increase in positive charge. The averaged radius, on the other hand, remains pretty much unchanged due to the similar radii of Cu^{+} and Zn^{2+}. Consequently, the anion will likely be shifted closer to the Cu(2c) position which would, relative to the anion coordinates for the hypothetical defect-free and fully ordered case, lead to a positive displacement of the *x*- and *z*-coordinates, respectively, and to a negative displacement of the *y*-coordinate. The resulting percentual change both in charge and radius is eventually determined for every sample in order to roughly evaluate the impact of mixed site occupations on anion parameters. Figure 3-27 compiles the trends of all anion parameters as they could generally expected to be for the cation distributions deduced in section 3.5.3. The anion positions obtained from the refinements of the p-ND data are shown in Figure 3-28.

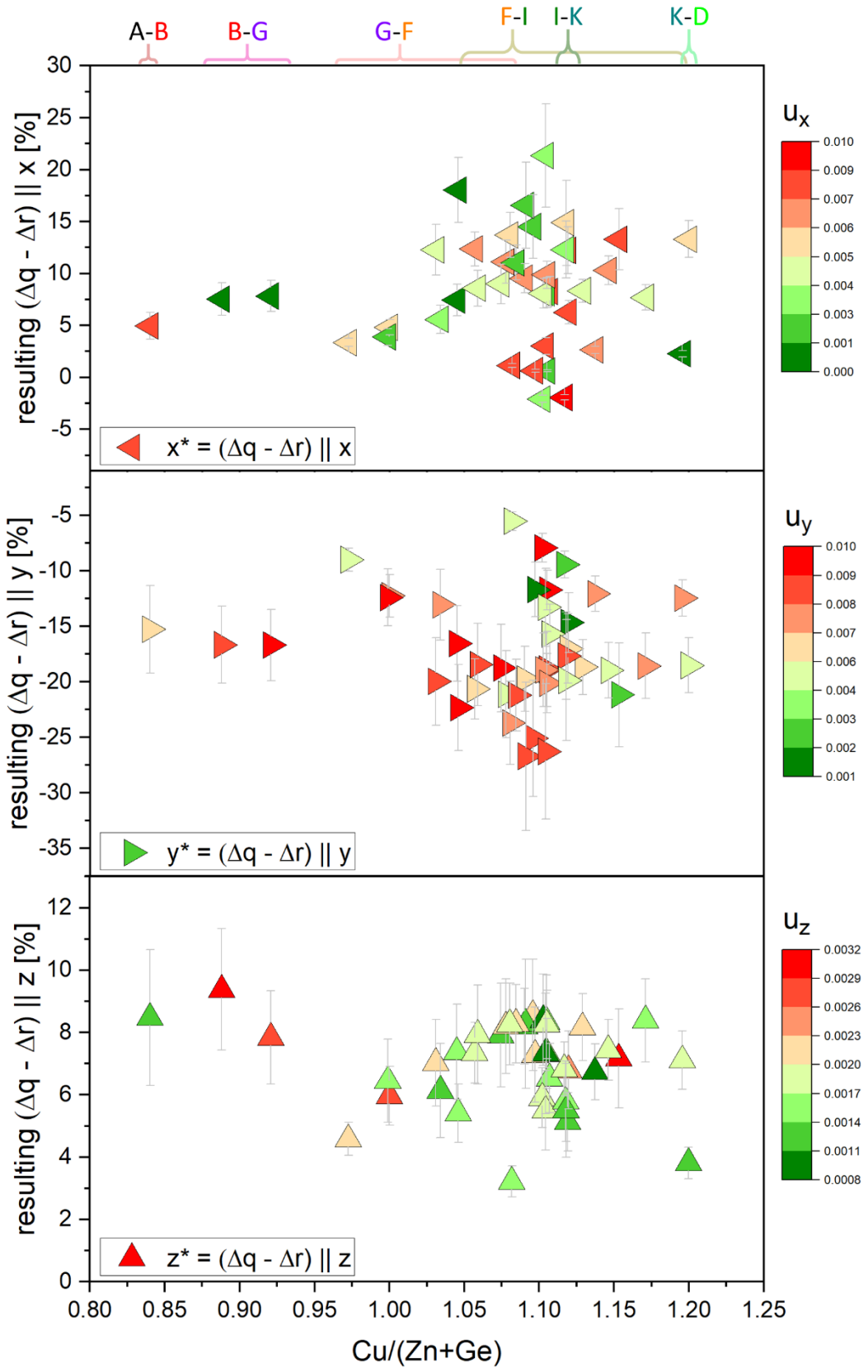

Figure 3-27 Direction and 'magnitude' of anion displacement deduced from the mixed occupation of the Wyckoff positions. The color map represents the tetragonal distortion with reference to the refined anion positions shown in the subsequent figure.

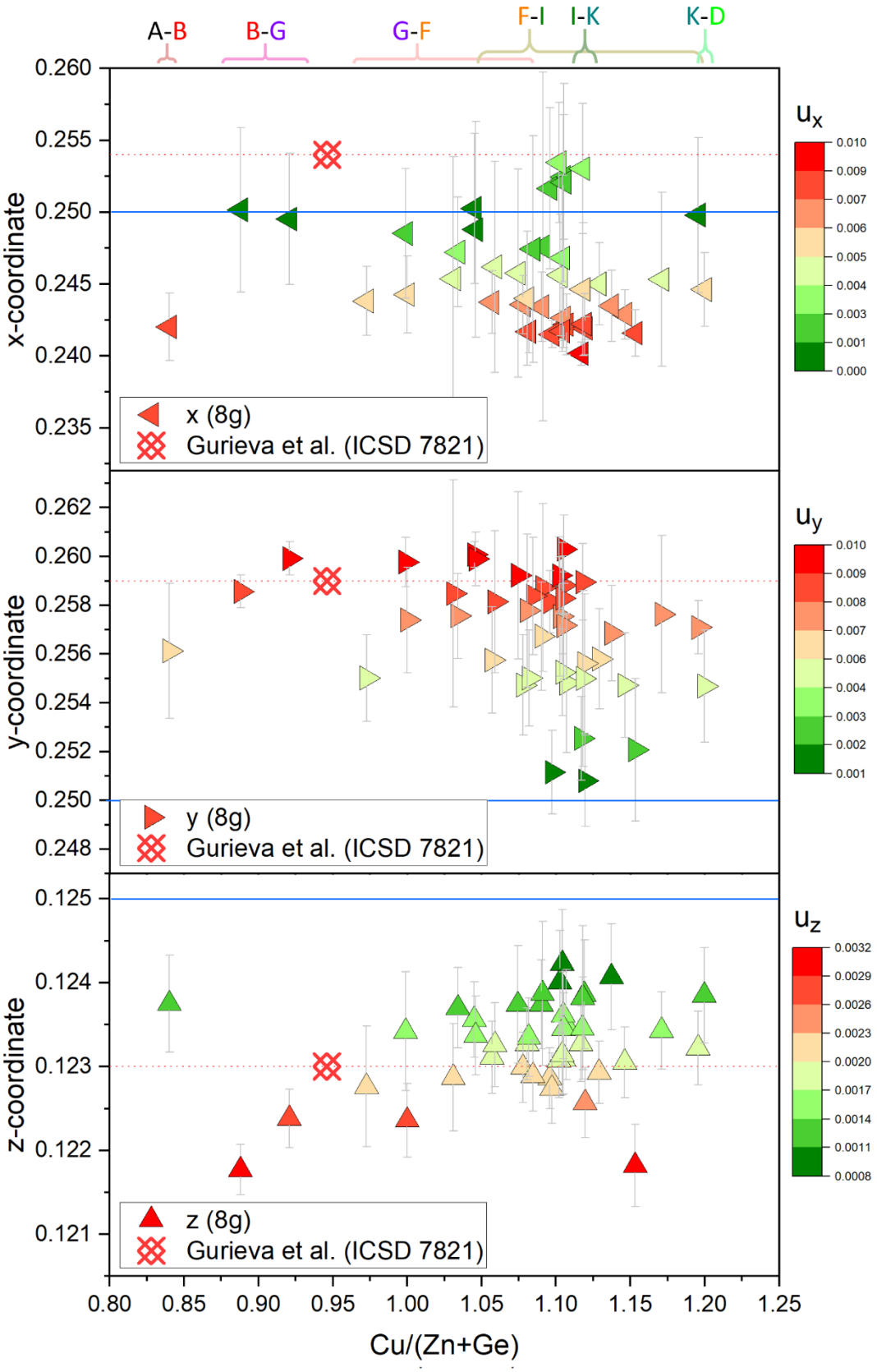

Figure 3-28 Anion parameters of CZGSe in dependence of Cu/(Zn+Ge) as obtained from Rietveld refinements of the neutron diffraction data (triangles). A literature value for each coordinate is included for the sake of comparison. The 'ideal` anion coordinates are indicated by solid blue lines. The corresponding tetragonal distortion $u_{x,y,z}$ is represented by a color map.

In spite of some resemblance does the rather hypothetical trend derived from the cation distribution (Figure 3-27) only remotely agree with whose obtained from the structure refinements (Figure 3-28). Theoretically, a significantly improved congruence should already be attainable if no interstitial defects are involved as they do alter the local structural and electrostatic environment while being tough to consider owing to a multitude of possible distributions on interstitial positions. In reality, thus, are the anion parameters subject to a complex interplay between (1) varying electrostatic forces that are also influenced beyond the neighboring atoms (including ions on intertitial positions), (2) the effective size of a given Wyckoff position, and (3) the dissimilar dependencies of ionic radius r (effects are linearly dependent) and charge q (effects are r^{-2}-dependent and diametrical to changing ionic radius) which are not accounted for. A straight prediction of how the anion position does respond to a certain cation distribution is therefore hardly viable. In addition is the refinement of the anion parameter a difficult affair due to the similarity in particular between x- and y-coordinate, respectively, that results in overall large uncertainties and less robust values. Nonetheless are the results obtained both for the anion parameter and the tetragonal distortion in good agreement with the ones found in literature [111] (Figure 3-28), though, solid trends are not obtained owing to the complex interactions mentioned before. However, faint trends may become obvious if the A – B-type sample is taken out of consideration; whose normative vacancies are unique among all investigated specimens (in addition to a significant portion of Zn_{Cu}^{+} antisite defects) which is eventually reflected by a distinctively different behavior of the anion parameters (cf. Figure 3-28). As a rough approximation do the x- and y-coordinate of the remaining samples tend to lower values as the Cu/(Zn+Ge) ratio increases whereas the z-parameter behaves oppositely. In this regard is the rising concentration particularly in Cu_{Ge}^{3-} antisite defects with increasing Cu/(Zn+Ge) likely the most influential agent as this defect species greatly weakens the attraction of the anion towards the Ge(2b) position. And yet, it should clearly be pointed out that the interactions between the various defect species and their individual impact on the anion position are too complex to allow an exhaustive interpretation of the data, which are additionally subject to relatively large errors.

3.5.2.3 Bond angles and bond distances

For a central atom being coordinated by four atoms of the same kind, a regular tetrahedron results with each of the six tetrahedral bond angles being equal to arccos(-1/3) ≅ 109.5°. In multinary compounds like CZGSe, however, at least two dissimilar atomic species are constituting the apices of the coordination tetrahedron, which makes the bond angles eventually differing from that 'ideal' tetrahedral angle. Both different ionic radii and repulsive forces among the cations do alter the bond angles and are thus depending on the average occupation of each structural site (Figure 3-29a). In a similar way does the cation distribution affect the bond distances; a larger average ionic radius will naturally lead to longer bond distances whereas an average increase in positive charges of the cation position does enhance the attractive forces towards the anion and leads to a shortening of bond distances, and vice versa (Figure 3-29b).

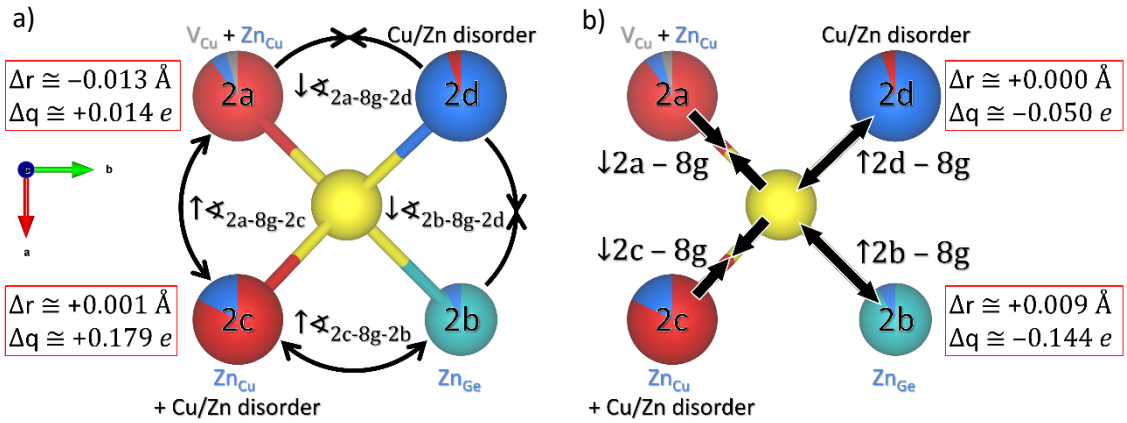

Figure 3-29 The mixed occupation of the cation sites does affect a) the bond angles and b) bond distances both through varying ionic radii as well as changing electrostatic interactions.

It can be noted that the parameters influencing the bond angles and, in particularly, the bond distances (namely ionic radii and electrostatic conditions) are identical to those having impact on the anion position and whose trends are therefore roughly resembling each other. At first glance, a straightforward approach for estimating expectable bond distances seems to be given by the cation distribution model through consideration of the anion radius and the weighted average radii of the cation position [146]: $l_{w-Se}^{mod} = r_{Se_{[IV]}^{2-}} + \sum_j occ_{j,w} \cdot r_j \quad (j = Cu_{[IV]}^{+}, Zn_{[IV]}^{2+}, Ge_{[IV]}^{4+};\ w = 2a, 2b, 2c, 2d)$. However, as in case of the anion parameter a reliable prediction of

trends is difficult to realize owing to the virtually indeterminable impact of interstitials and, last but not least, the inherent uncertainties the cation distribution model is subject to. In addition do all occupied Wyckoff positions mutually influence each other which creates a complex feedback system with poorly predictable behavior, especially if the possible feedbacks are considered between only two atoms isolatedly, as is done here. The results obtained from structure refinements indeed seem to reflect this complexity as an unambiguous dependency on Cu/(Zn+Ge) can neither be observed for the bond angles (Figure 3-30) nor for the bond distances (Figure 3-31).

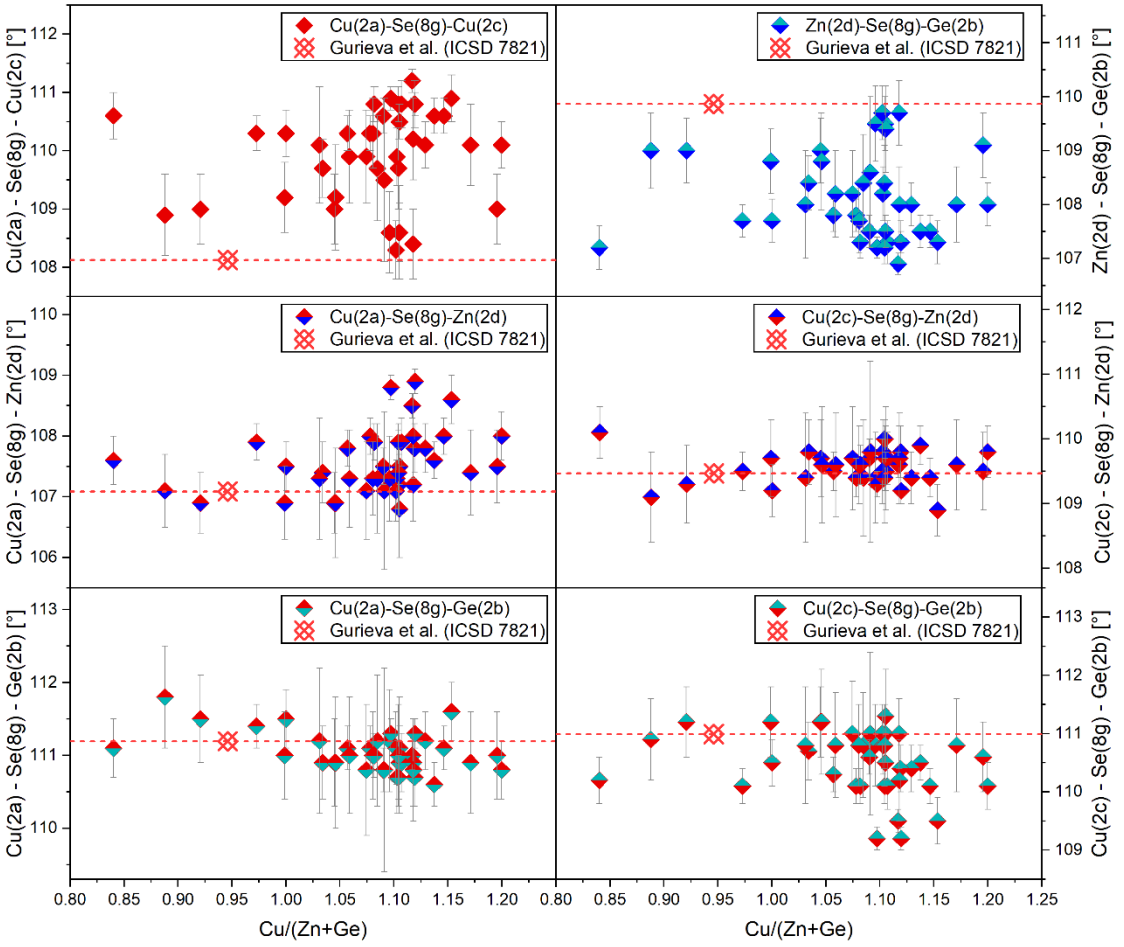

Figure 3-30 The six (obtuse) bond angles of each CZGSe sample determined by structure refinement of p-ND data. In case of a single cation species and negligible point defect density, all angles would be equally having the value of around 109.5° and a regular tetrahedron results. In CZGSe, however, three cation species differing in terms of radius and valence state are involved that cause the actual angles to be deviating from the 'ideal' one. The various modes of cation distribution and associated defect species eventually induce additional deviations. For each bond angle a reference value is included [111].

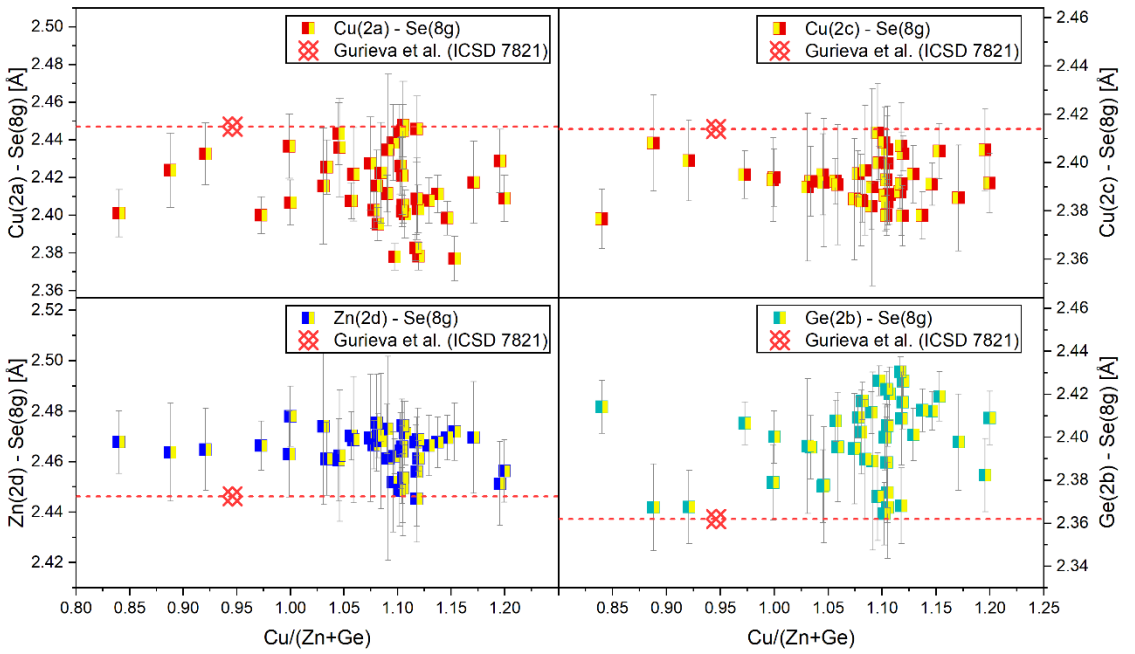

Figure 3-31 Bond distances between the respective 'cationic' Wyckoff position (2a, 2b, 2c, 2d) and anion position (8g) as obtained from structure refinement of p-ND data. For each bond distance a reference value is included [111].

The results for bond angles and bond distances obtained from the structure refinements, each, are in good agreement with reference values derived from crystal structure information published by Gurieva et al. [111]. A pretty pronounced discontinuity in data progression where values vary strongest can be found at around Cu/(Zn+Ge) = 1.1 which coincides with a steep decrease in the concentration of Zn_{Ge}^{2-} antisite defects and the emergence of Cu_{Zn}^{-} antise defects in the K – D-type samples (c.f. Figure 3-38 in section 3.5.4). The noticeably different behavior of the most Cu-poor (A – B-type) sample can be explained by its density in Zn_{Cu}^{+} antisite defects, which is the highest among all samples, and by V_{Cu}^{-} defects that are exclusively found in this sample.

3.5.3 Structural cation distribution

The cation distribution is examined for all samples for which a sufficiently homogeneous composition is achieved and which can therefore be considered to consist of a single CZGSe phase only. Owing to the differentiation problem arising from isoelectronic ions conventional XRD is subject to (as discussed in section 2.2.2.1), powder neutron diffraction patterns are recorded to make information on cation distribution accessible. The Rietveld method [6, 7] including the kesterite-type structure (s.g. $I\bar{4}$) as structural starting model is used to evaluate the patterns with particular emphasis on site occupancy factors (occ) of the cation positions. From the refined values of each site occupancy factor the experimental average neutron scattering length ($\bar{b}_w^{exp}$) is obtained, eventually allowing to draw conclusions about the actual occupation present on each Wyckoff positions. The modeled average neutron scattering length ($\bar{b}_w^{mod}$) resulting from a modeled cation distribution needs to be equal or as close as possible to the experimental one ($\bar{b}_w^{mod} \cong \bar{b}_w^{exp}$). However, relying on refinement of neutron diffraction data only is subject to a severe lack in compositional constraints that is even further exacerbated by a considerable degree of freedom involved by the error of each refined occ (which applies to $\bar{b}_w^{mod}$).

For the average neutron scattering length method [8, 9] to be applicable a comprehensive and precise compositional analysis is necessary, which is provided by quantitative WDX measurements (cf. section 2.2.1). In addition, knowledge about the chemical composition allows prediction of point defects that are most probably existing for the given chemical potential [184]. Here the assessment of the cation distribution and the derivation of the kind and concentration of point defects from it is however based on cation substitution reactions and resulting defect complexes established for the possible off-stoichiometry paths possessing charge neutrality (cf. Table 1-1 & Figure 1-11) [2-4, 89-91]. Combining the average neutron scattering length method both with chemical composition and related defect complexes enables a robust and reliable modeling of the cation distribution which is also of crucial importance for an indirect estimation of vacancy and interstitial defects, respectively.

For the cation distribution model, the cations are not distributed arbitrarily within the range provided by the error bars. Instead, simple linear equations including the proper proportions of the respective point defect species are used to enable a better self-consistency. In case of F – I-type samples, for instance, the amount of the respective interstitial defects (i.e. Zn_i^{2+} and Cu_i^{+}) is taken to evaluate the validity of the cation distribution model. It is also useful to estimate the respective contribution of the two possible F-types. The F(1)-type involves Zn_{Ge}^{2-} and Cu_i^{+} point defects which result in the charge-neutral defect complex $Zn_{Ge}^{2-} + 2Cu_i^{+}$. The F(2)-type, on the other hand, comprises Cu_{Ge}^{3-}, Cu_i^{+} and Zn_i^{2+}, and the corresponding defect complex is constituted just by summing whose isolated point defects without multiplicands: $Cu_{Ge}^{3-} + Cu_i^{+} + Zn_i^{2+}$. From the I-type contribution the defect complex $Cu_{Ge}^{3-} + 3Cu_i^{+}$ will additionally be introduced. Owing to the different proportionalities exhibited by those defect complexes a more robust cation distribution model becomes achievable.

The amount of germanium obtained from WDX measurements is entirely allocated onto the Ge(2b) position with the missing portion to attain complete occupation being attributed to Zn_{Ge}^{2-} (F(1)-type) and Cu_{Ge}^{3-} (F(2)- and I-type), respectively. According to the above definition of the F(1)-type, the introduction of a Zn_{Ge}^{2-} antisite defect dictates the introduction of two Cu_i^{+} defects. On the other hand, with every Cu_{Ge}^{3-} defect either one Cu_i^{+} and one Zn_i^{2+} (F(2)-type) or three Cu_i^{+} (I-type) go along with. Upon applying the corresponding cation substitution reactions to the WDX results (cf. section 3.3) the portions of F- and I-type (as well as of any other type mixture) are determined but the sub fractions of F(1)- and F(2)-type remain unknown at first, hence making the modeled cation distribution pretty much a matter of personal sensation. In order to achieve a stronger constraint on that, the F(1)- and F(2)-type sub fractions are chosen such that the resulting quantities of Cu_i^{+} and Zn_i^{2+} defects are in closest agreement with those yielded by the cation distribution model. Similar approaches are applied to the other type mixtures in order to enhance the robustness of the modeled cation distribution. The obtained cation distribution models are discussed in the following while the resulting point defect concentrations will be subject of the subsequent section.

3.5.3.1 A – B-/B – G-/ I – K-/ K – D-type mixtures

Only a small number of samples are obtained for the A – B-, B – G-, I – K- and K – D-type mixture regions, respectively. These samples will hence be co-presented in the same graphs. Figure 3-32 depicts the experimentally deduced average neutron scattering length for each 'cationic' Wyckoff position together with the modeled cation distribution ($\bar{b}_w^{exp}, \bar{b}_w^{mod}$).

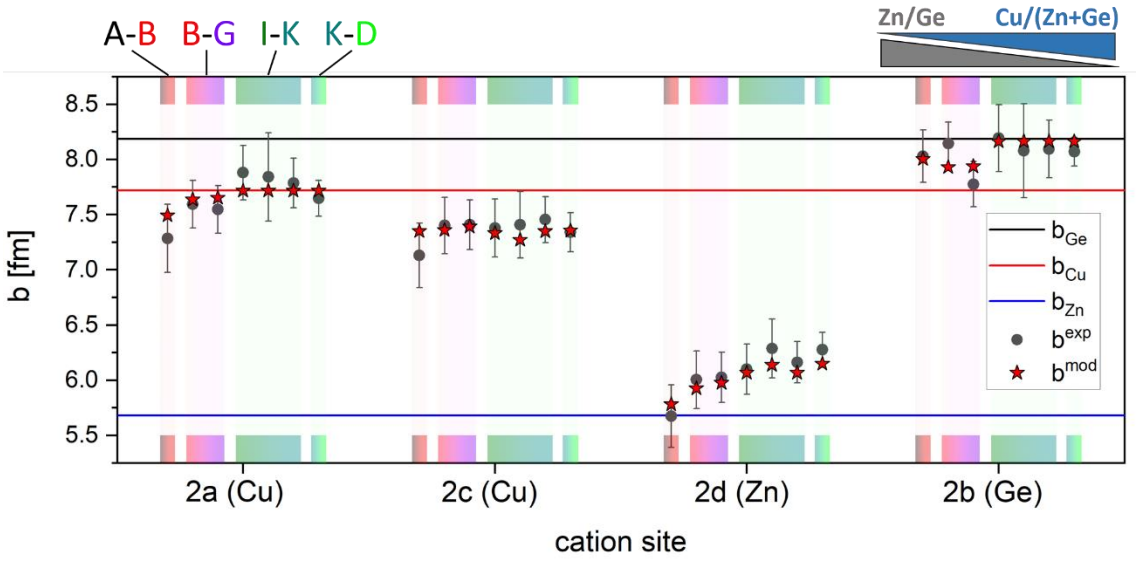

Figure 3-32 Experimentally deduced average neutron scattering length ($\bar{b}_w^{exp}$; black symbols) and modeled average neutron scattering length ($\bar{b}_w^{mod}$; red symbols) for the A – B-, B – G-, I – K- and K – D-type samples. The results are ordered with respect to decreasing Zn/Ge and increasing Cu/(Zn+Ge), respectively.

Even though the error bars of the average neutron scattering lengths obtained from the Rietveld refinements of neutron diffraction data are reasonably small a yet quite large degree of freedom in modeling the cation distribution (red symbols in Figure 3-32) is still possible, which is considerably restricted by applying the procedure mentioned before. The resulting cation distribution given in units of percent is shown in Figure 3-33.

The model applied both for the Cu(2a) and Cu(2c) position of the Cu-poor and Zn-rich A – B-type sample results in average neutron scattering lengths ($\bar{b}_{2a,2c}^{mod}$) that are smaller than the neutron scattering length of copper ($\bar{b}_{2a}^{mod} = 7.494\ fm < b_{Cu} = 7.718\ fm$ and $\bar{b}_{2c}^{mod} = 7.351\ fm < b_{Cu} = 7.718\ fm$). Such a decrease in $\bar{b}$ can be achieved by a mixed occupation that involves a cation having a smaller neutron scattering length (i.e. zinc) and/or by incomplete occupation of those atomic sites

(i.e. vacancies). Here both situations are realized, which is also in accordance with the definitions known for the A- and B-type, respectively.

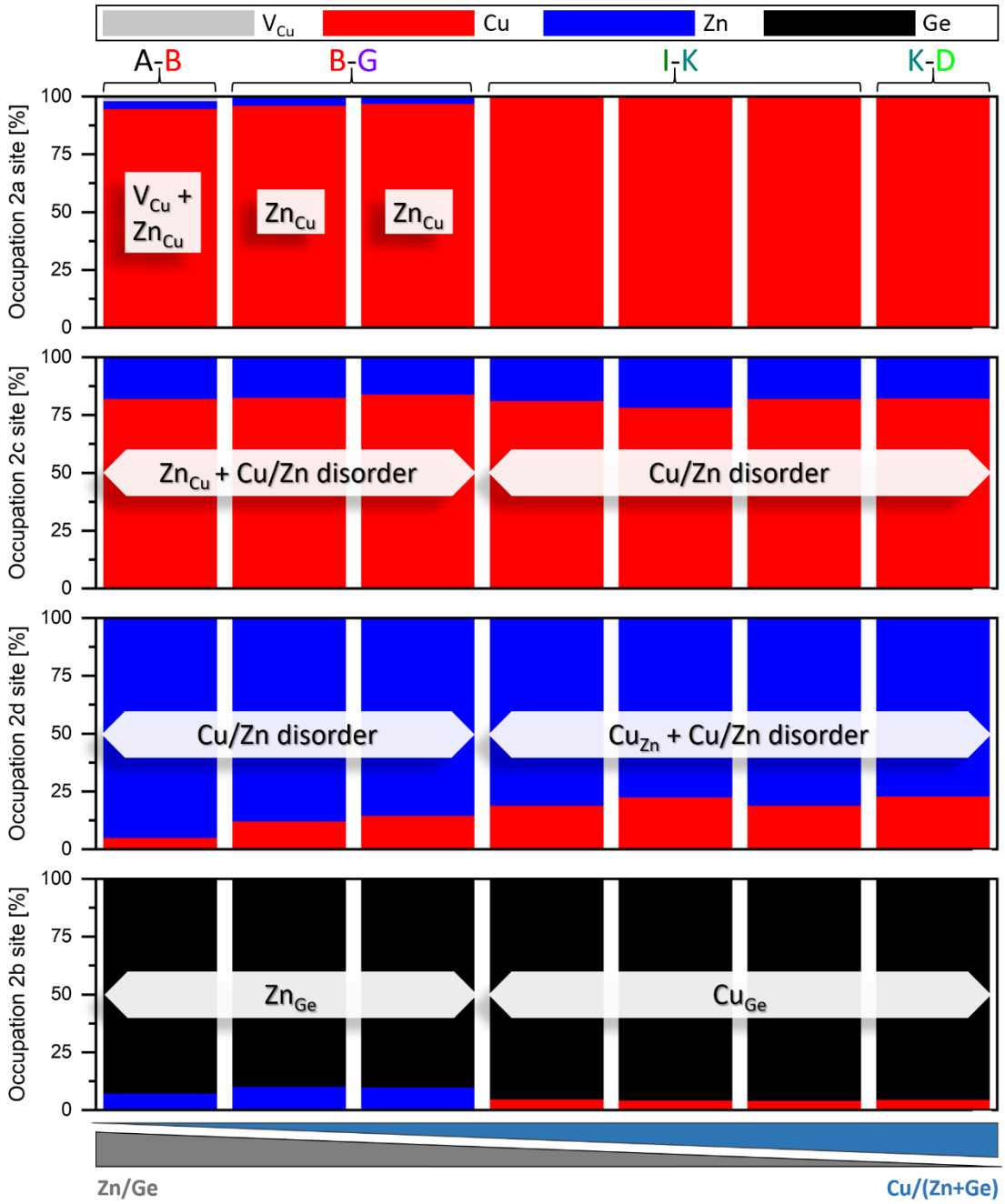

Figure 3-33 Occupation of the 'cationic' Wyckoff positions of the A – B-, B – G-, I – K- and K – D-type samples as derived from $\bar{b}_w^{mod}$ shown in Figure 3-32.

The amount of copper vacancies to be included is simply yielded by the difference between the total number of cations given by stoichiometric composition (or likewise by the number of structural sites to be occupied) and the actual number of cations as obtained by WDX spectroscopy. The copper vacancies are (arbitrarily)

attributed to the 2a position, although they could also be assigned to the 2c site, or to both sites. The resulting point defect concentration will however not be affected in either case. In addition, a certain amount of Zn_{Cu}^{+} antisite defects are required to eventually achieve a distribution model that is in closest agreement with the experimental results. After all, the remaining amount of copper is attributed to the Zn(2c) position, which directly reflects the Cu-Zn disorder, and which is being subtracted from the amount of zinc on the copper position(s) in order to obtain the actual quantity of Zn_{Cu}^{+} antisite defects (and vice versa for the actual amount of Cu_{Zn}^{-} in Cu-rich samples).

The Ge(2b) position is filled up with Zn_{Ge}^{2-} antisite defects, and from whose amount the portion of Zn_{Cu}^{+} antisite defects introduced by the B-type contribution can eventually be derived by respecting the proportionalities (B-type: $2Zn_{Cu}^{+} + Zn_{Ge}^{2-}$ → 2:1). The amount of Zn_{Cu}^{+} related to the A-type contribution is obtained from the amount of copper vacancies (A-type: $V_{Cu}^{-} + Zn_{Cu}^{+}$ → 1:1). The two B – G-type samples also exhibit a $\bar{b}_{2a,2c}^{exp}$ that is smaller than b_{Cu} as can be expected owing to the partly B-type character which leads to the formation of Zn_{Cu}^{+} antisite defects in addition to Cu-Zn disorder. On the other hand, Cu_{Zn}^{-} antisite defects are formally excluded, meaning the increased $\bar{b}_{2d}^{exp}$ over b_{Zn} is solely attributable to the Cu-Zn disorder. The missing germanium on the 2b position is complemented by Zn_{Ge}^{2-} antisite defects. Zinc that is still remaining after complete occupation of the Wyckoff positions is assigned to interstitial positions for which the cation distribution model indeed cannot account for, but can eventually be deduced from the composition to address whose point defect density. While Zn_{Cu}^{+} and Zn_{Ge}^{2-} antisite defects are dominating for the Cu-poor and Zn-rich A – B- and B – G-type samples, are the I – K- and K – D-type samples characterized by Cu_{Zn}^{-} and Cu_{Ge}^{3-} antisite defects due to the Cu-rich composition and a Zn/Ge being relatively close to one. Also, copper interstitial defects (Cu_{i}^{+}) are now formed instead of (normative) Zn_{i}^{2+}.

3.5.3.2 G – F-type mixture

Due to the mode of compositional deviation described in section 3.2 & 3.4, a larger number of samples ended up in the G – F-type region and are thus characterized by Zn-rich and mainly Cu-rich composition. Defects that are formally permitted by those off-stoichiometry types include Zn_{Ge}^{2-}, Cu_{Ge}^{3-}, Zn_{i}^{2+} and Cu_{i}^{+}. The absence of normative Cu_{Zn}^{-} and Zn_{Cu}^{+} antisite defects is particularly advantageous as only one Wyckoff position needs to be dealt with in terms of a free parameter while with additional Zn_{Cu}^{+}, for instance, three Wyckoff positions have to be treated independently.

As previously mentioned, however, the F-type can comprise two different sub types with the F(1)-type being related to Zn_{Ge}^{2-} (and two Cu_{i}^{+}) and the F(2)-type being related to Cu_{Ge}^{3-} (and one Cu_{i}^{+} and Zn_{i}^{2+} each) antisite defects, respectively. Depending on whether the F(1)-type is involved, the Zn_{Ge}^{2-} antisite defect may result both from the F(1)- and the G-type, respectively. By considering the proportionalities of the interstitial defects and by adjusting the sub fractions of the F(1)- and (F(2)-type appropriately, a more robust decision about the fractional occupancies on the Ge(2b) position can be made, which eventually enables a more constraint estimation of the copper and zinc interstitial defect densities, respectively. The average neutron scattering lengths of the G – F-type samples obtained both from experiment ($\bar{b}_w^{exp}$) and model ($\bar{b}_w^{mod}$) are shown in Figure 3-34.

Within the error bars, the values for $\bar{b}_{2a}^{exp}$ are matching well with b_{Cu}. Neither vacancies nor antisite defects concerning the copper position are expected to form for the off-stoichiometry types involved and, hence, the Cu(2a) position is considered fully occupied with copper. On the other hand, both $\bar{b}_{2c}^{exp}$ and $\bar{b}_{2d}^{exp}$ allow a model in which the amount of zinc occupying the Cu(2c) position equals the amount of copper occupying the Zn(2d) position, with the necessity of actual (and formally prohibited) antisite defects on them being avoided.

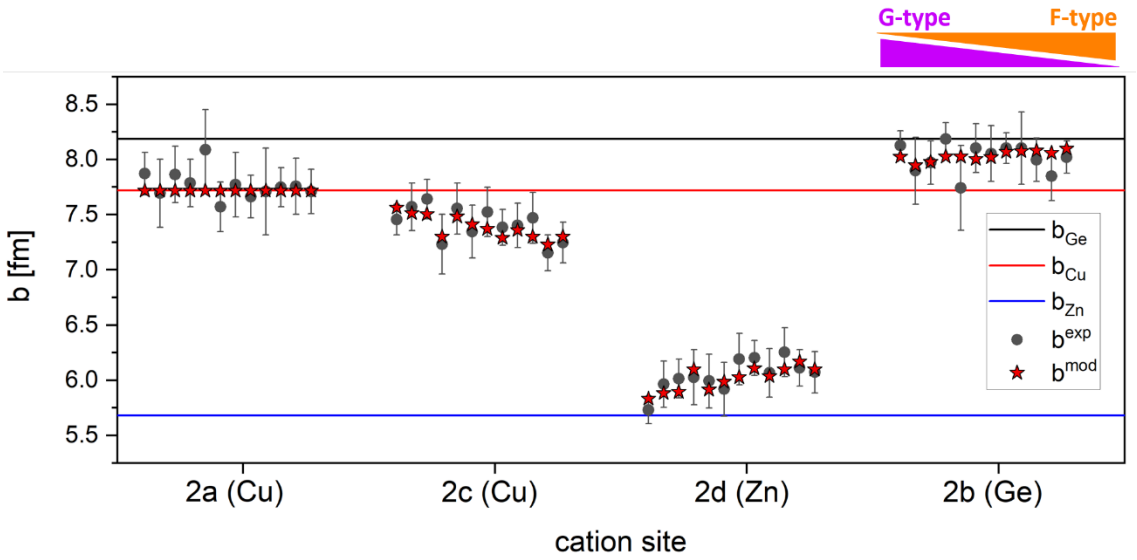

Figure 3-34 Experimentally deduced average neutron scattering length ($\bar{b}_w^{exp}$; black symbols) and modeled average neutron scattering length ($\bar{b}_w^{mod}$; red symbols) for the G – F-type samples. The results are ordered with respect to decreasing G-type and increasing F-type contribution, respectively.

The Cu(2c) and Zn(2d) positions are therefore exclusively subject to Cu-Zn disorder that is partly preserved after the heat treatment and explains the lowered $\bar{b}_{2c}^{exp}$ over b_{Cu} and the increased $\bar{b}_{2d}^{exp}$ over b_{Zn}. The Cu-Zn disorder indeed seems to increase with higher copper content (i.e. stronger F-type contribution) but is assumed to be more impacted by the cooling history, with the latter may differing as the samples are partly stemming from different synthesis runs (i.e. various total weights) which might additionally be subject to slightly different natural cooling.

The Ge(2b) position is complemented by Zn_{Ge}^{2-} antisite defects for the three samples that are slightly Cu-poor (i.e. strongest G-type contribution). Once Cu/(Zn+Ge) becomes larger than one (or rather for the ratio Cu/(Zn+Ge) : Zn/Ge > 0.85), Cu_{Ge}^{3-} defects start to emerge which tend to increasingly compete against the formation of Zn_{Ge}^{2-} defects, yet remain present even up to highest F-type character. The percental cation distribution modeled for the G – F-type samples is shown in Figure 3-35.

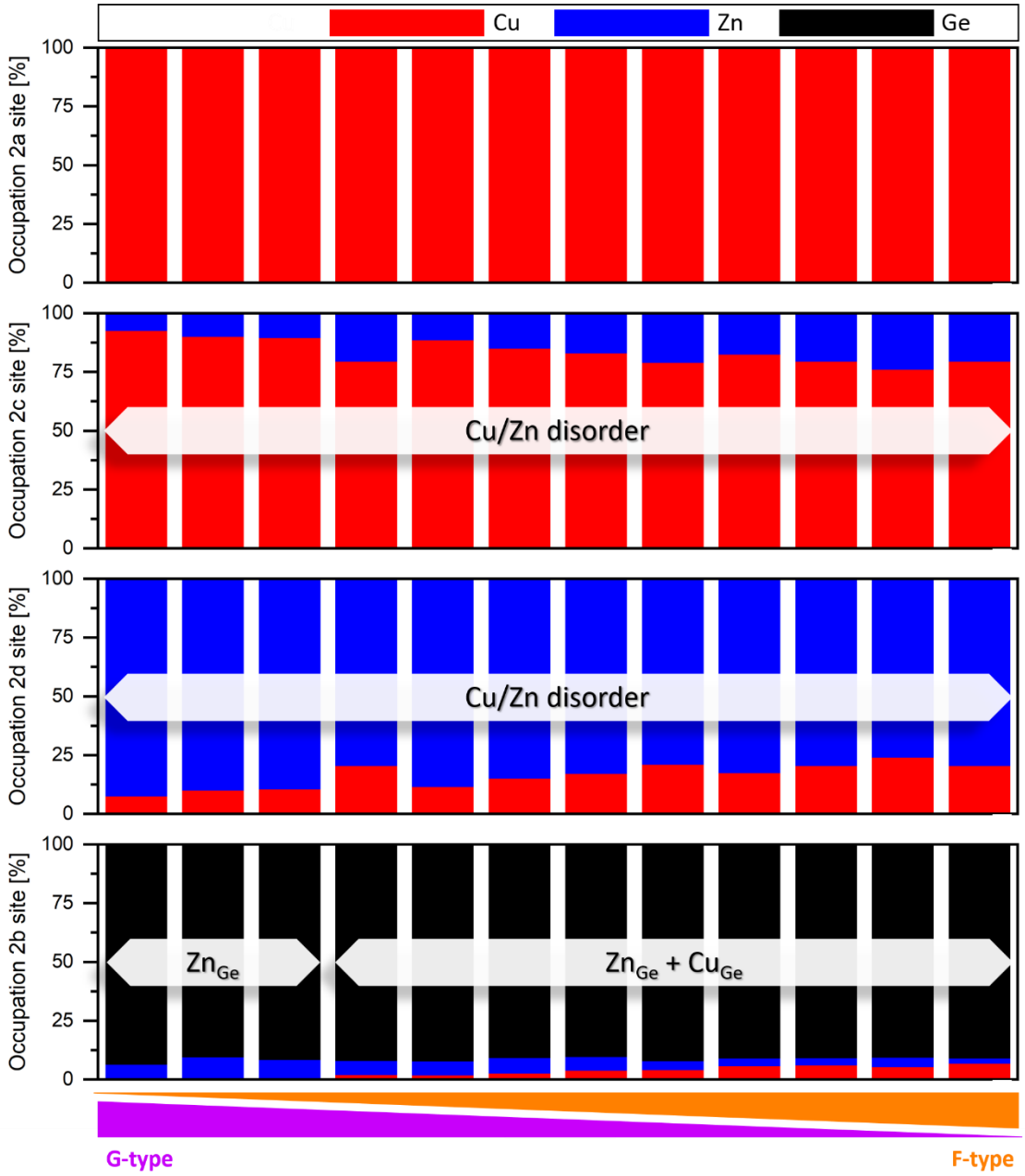

Figure 3-35 Occupation of the 'cationic' Wyckoff positions of the G – F-type samples as derived from $\bar{b}_w^{mod}$ shown in Figure 3-34.

3.5.3.3 F – I-type mixture

The relative enrichment in copper and the loss in germanium during the thermal treatment (c.f. Section 3.2) lead to a favored formation of samples showing F – I-type composition. Figure 3-36 shows the modeled average neutron scattering length and how it compares to the results obtained for the experimental one.

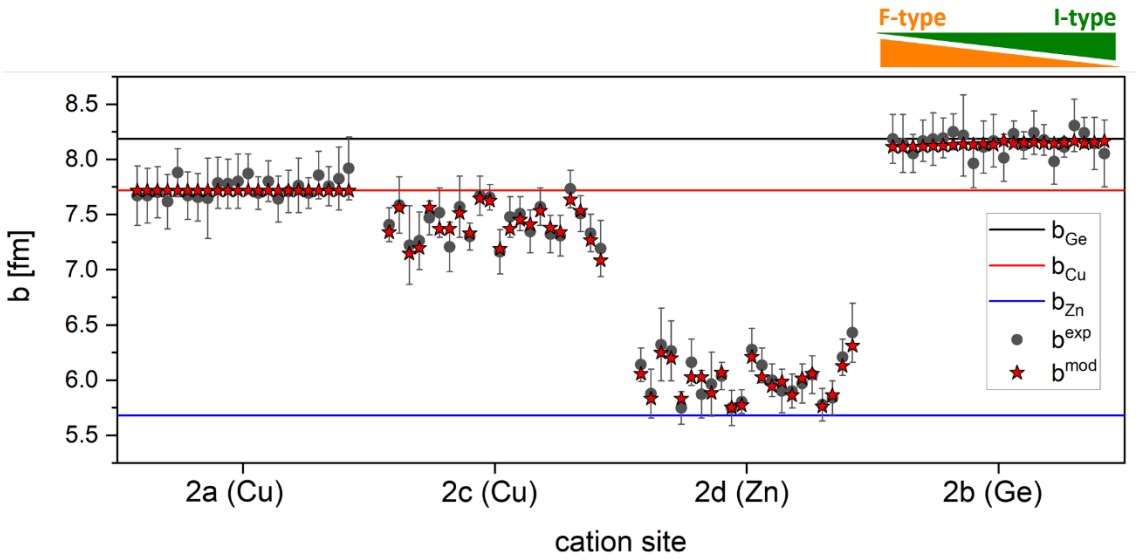

Figure 3-36 Experimentally deduced average neutron scattering length ($\bar{b}_w^{exp}$; black symbols) and modeled average neutron scattering length ($\bar{b}_w^{mod}$; red symbols) for the F – I-type samples. The results are ordered with respect to decreasing F-type and increasing I-type contribution, respectively.

Like for the G – F-type the only issue to be solved is related to the share in Cu_{Ge}^{3-} and Zn_{Ge}^{2-} antisite defects, which once more is achieved by finding the adequate sub fractions of the F(1)- and F(2)-type leading to a minimization of the difference between the number of copper and zinc interstitial defects resulting from the model and those required to maintain the proportionalities of the corresponding defect complexes. All values obtained for $\bar{b}_{2a}^{exp}$ are very close to b_{Cu}, self-explanatorily allowing a full occupation with copper as can be expected for a Cu-rich composition and for the defect species formally given by F- and I-type, respectively. The values for $\bar{b}_{2c}^{exp}$ and $\bar{b}_{2d}^{exp}$ again allow parity between modeled zinc on Cu(2c) and copper on Zn(2d), respectively, and which is thus related to Cu-Zn disorder only. Although $\bar{b}_{2b}^{exp}$ is dithering around b_{Ge} a modeling of the occupation consistent with the above conditions is still performable. Each F – I-type sample is depleted in germanium, and its position is topped up both with Cu_{Ge}^{3-} and Zn_{Ge}^{2-} antisite defects for those samples being closer to the F-type line, which generally show higher zinc content. With increasing copper and decreasing zinc content (i.e. stronger I-type contribution), respectively, the amount of Zn_{Ge}^{2-} antisite defects diminishes and eventually disappears once the ratio Cu/(Zn+Ge) : Zn/Ge has surpassed ~0.97. The occupation scheme of all F – I-type samples resulting from $\bar{b}_w^{mod}$ is depicted in Figure 3-37.

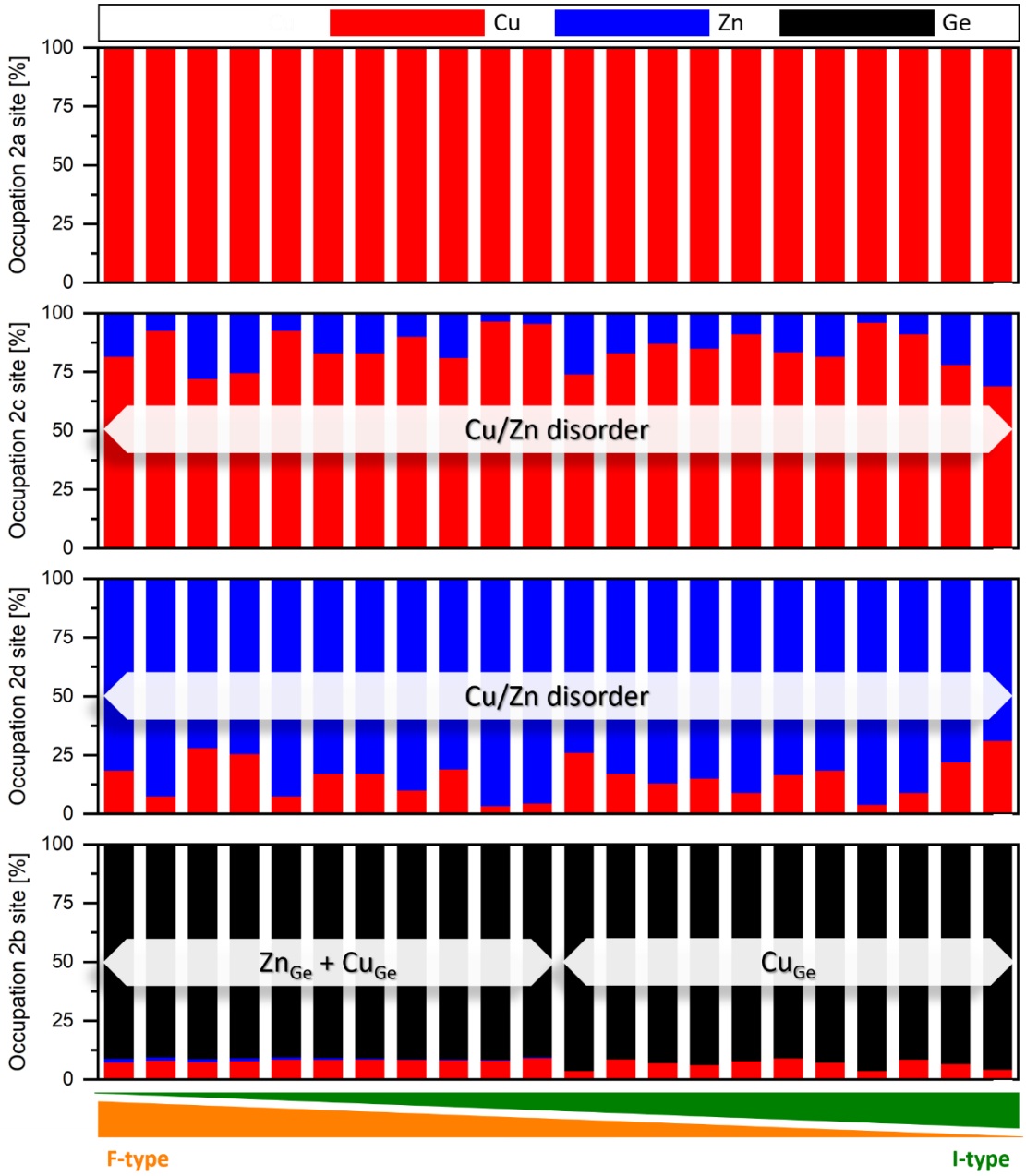

Figure 3-37 Occupation of the 'cationic' Wyckoff positions of the F – I-type samples as derived from $\bar{b}_w^{mod}$ shown in Figure 3-36.

3.5.4 Population of type-specific defects

By means of the modeled cation distribution previously elaborated the point defect species and their densities can be concluded from. In order to calculate the point defect densities in units of cm^{-3} the inverse of the unit cell volume is taken. However, the unit cell of the kesterite-type structure contains two formula units of $Cu_2ZnGeSe_4$

and the number of defects derived from the cation distribution model has therefore to be doubled. The upper and the lower error bars, respectively, are resulting from those of the experimentally deduced neutron scattering length by respecting the positions of the modeled neutron scattering length on them (cf. Figures Figure 3-32, Figure 3-34 & Figure 3-36). In accordance with the off-stoichiometry types, the Cu-poor region is dominated by Zn_{Cu}^{+}, Zn_{Ge}^{2-} and Zn_{i}^{2+} defects while the Cu-rich region shows high densities in Cu_{i}^{+} and Cu_{Ge}^{3-} defects, yet a significant population of Zn_{i}^{2+}defects persists far into the Cu-rich regime. An overview of the type-specific point defects determined for the whole set of samples is presented in Figure 3-38.

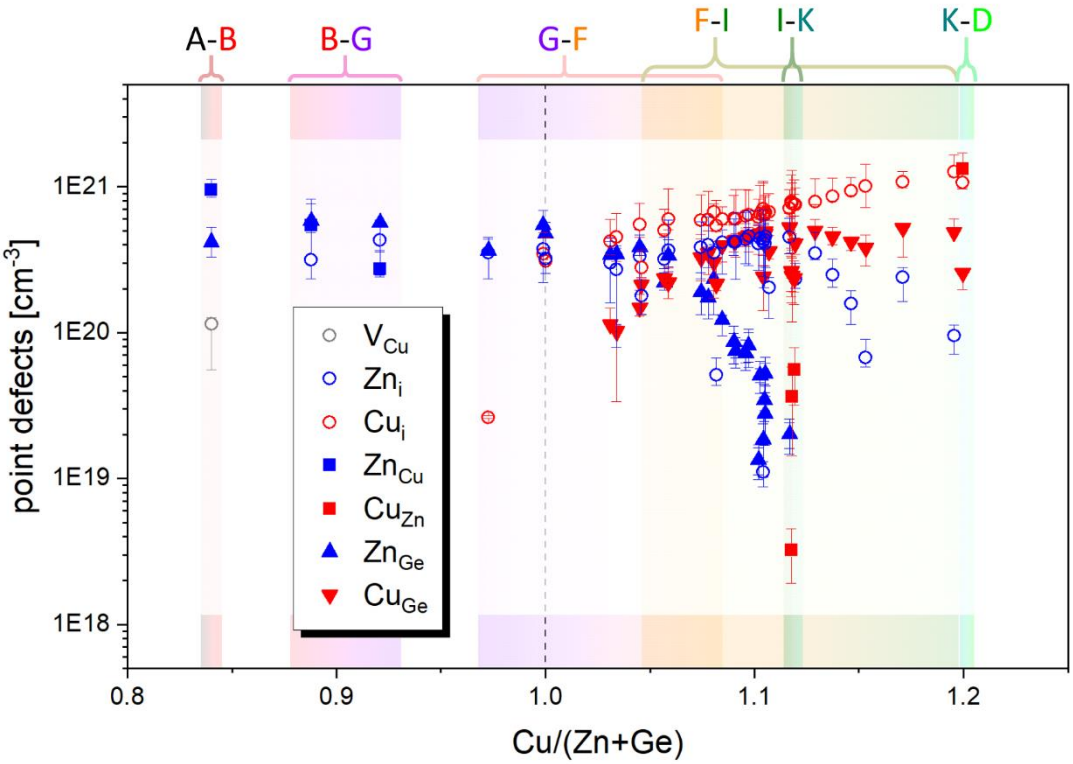

Figure 3-38 Established point defect concentrations in all investigated samples as a function of Cu/(Zn+Ge).

An inspection of the summed defect concentration with regard to the cation ratio plot reveals a dependency of total point defect density not only on the extent of off-stoichiometry but also on the copper content, with the total defect population tending to be higher for Cu-rich samples (Figure 3-39). The defect concentration of the most Cu-rich sample is nearly three times higher as compared to the sample being closest to the stoichiometric point and that features the least defect

concentration. In the cation ration plot two samples do actually offer compositions that allow direct comparison (denoted 'comparable samples' in Figure 3-39).

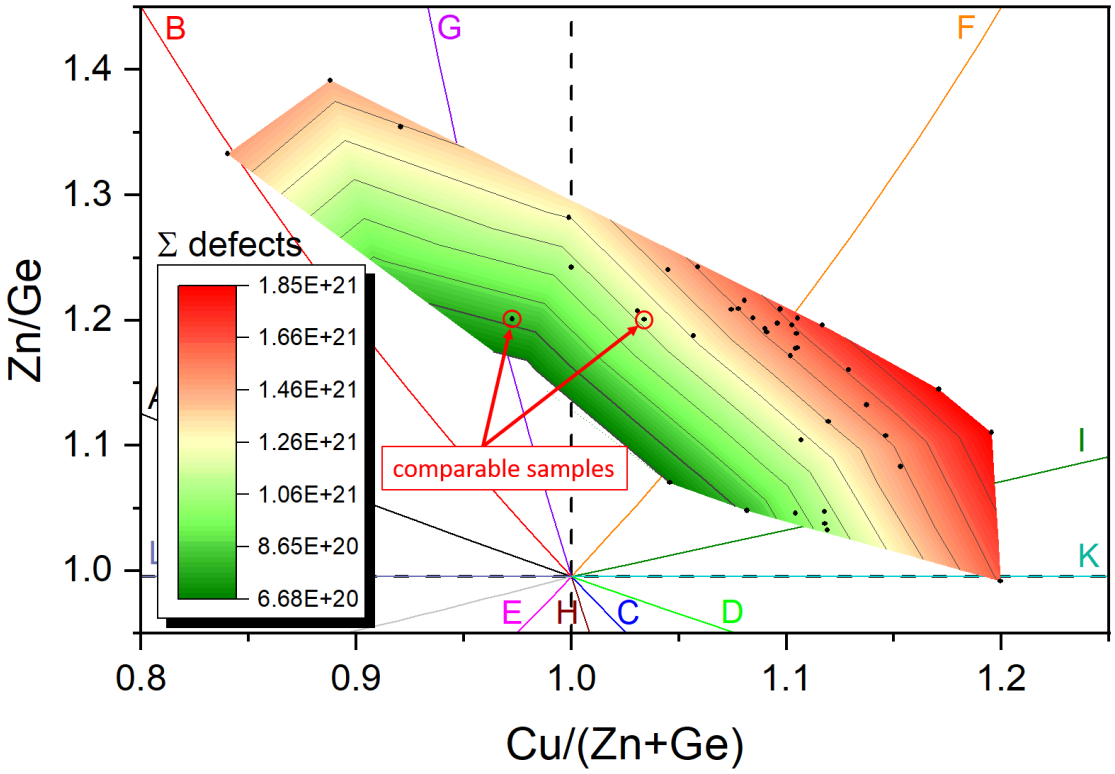

Figure 3-39 Total point defect concentration of each sample depicted as contours in the cation ratio plot. The point defect concentration generally increases with stronger off-stoichiometry, yet even more pronounced towards higher copper content. In spite of their similar deviation from stoichiometry, two comparable representatives ('comparable samples') from the Cu-poor and Cu-rich regime, respectively, clearly differ in terms of defect concentration, with the point defect population being significantly higher in the Cu-rich counterpart.

Those comparable samples are characterized by virtually identical Zn/Ge and a similar but opposite deviation from the stoichiometric line Cu/(Zn+Ge) = 1. The defect concentration in the Cu-rich sample is more than 50% higher than in the Cu-poor counterpart which can be explained by the favored monovalent state of copper. The high population particularly of Cu_{Ge}^{3-} antisite defects present in the Cu-rich region likewise requires a higher population mainly of interstitial defects to compensate for the negative excess charges. Up to moderate Cu-rich conditions one Cu_{Ge}^{3-} may be compensated by one Zn_i^{2+} and Cu_i^{+} whereas at more Cu-rich conditions three Cu_i^{+} defects will be required, which would already lead to a rise in defect concentration by 33%. In the following the defect concentrations and the elaborated trends of the respective defect species will be discussed in more detail.

The small number of occurrences of samples formally permitting, respectively, V_{Cu}^{-}, Zn_{Cu}^{+} and Cu_{Zn}^{-} defects renders individual graphs unreasonable. Hence, these defects solely occurring in A – B-, B – G-, I – K- and K – D-type samples will be presented (Figure 3-40) and evaluated together.

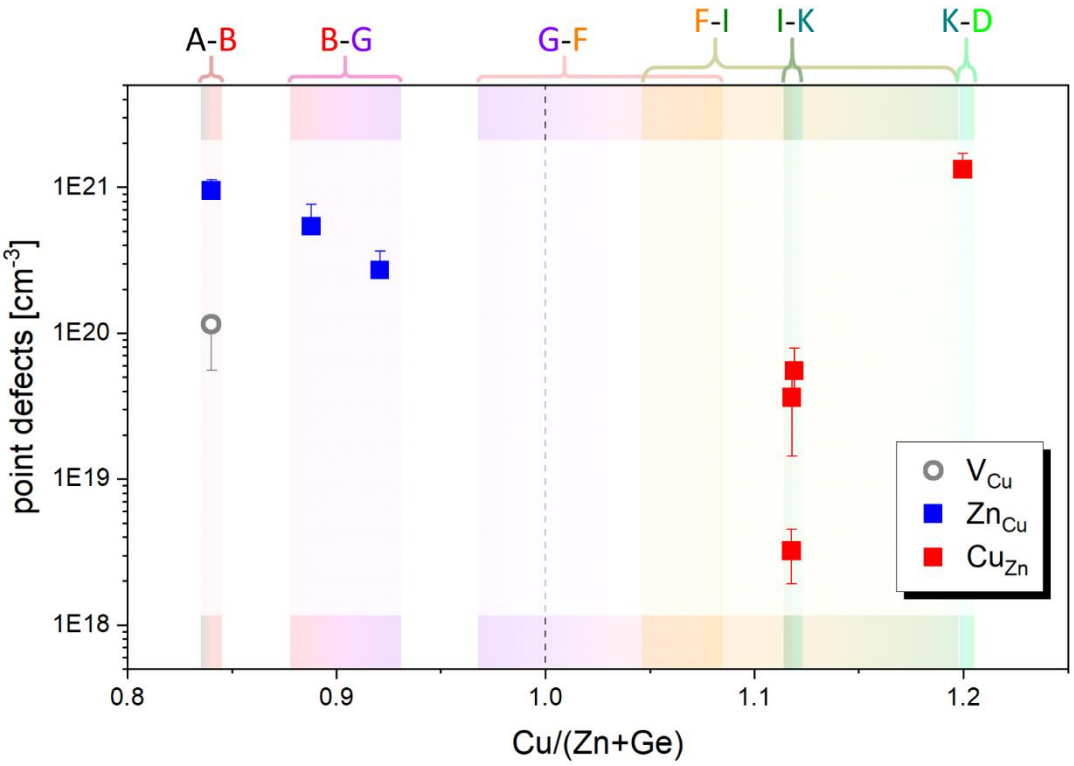

Figure 3-40 Point defect concentration of V_{Cu}^{-}, Zn_{Cu}^{+} and Cu_{Zn}^{-} in dependence of Cu/(Zn+Ge).

The V_{Cu}^{-} defect is detected only in the A – B-type sample which is also in accordance with the definition of the A-type. Although the composition of this sample is the most Cu-poor (Cu/(Zn+Ge) = 0.84) is the concentration of A-type specific V_{Cu}^{-} defects almost one magnitude smaller as compared to the Zn_{Cu}^{+} antisite defect. This can be related to the stronger impact of the B-type defect complex [$2Zn_{Cu}^{+}$ + Zn_{Ge}^{2-}] and to the high zinc content in general (Zn/Ge = 1.33), with zinc eventually topping up the copper positions until zinc is entirely distributed. The yet unoccupied fraction remaining is then making up the V_{Cu}^{-} defects. The formation energy of the resulting A-type defect complex [V_{Cu}^{-} + Zn_{Cu}^{+}], in fact, is lower than those of the isolated defects and its presence is therefore in agreement with first-principle calculations [86] and the A-type formalism [2]. Kesterite-type absorber layers in thin film solar cells are typically showing best performances when being close to A-type composition (cf.

section 1.5.3) as the corresponding defect complex [V_{Cu}^{-} + Zn_{Cu}^{+}] consists of shallow and thus rather benign defects that only little affects the electronic structure.

Strictly speaking, however, does the conception of charge-balanced defect complexes ideally result in an equal concentration of both types of charge carriers (i.e. electrons and holes) and which therefore would not induce any conductivity type (i.e. neither n-type nor p-type). Although the V_{Cu}^{-} acceptor defect is credited partly responsible for the p-type conductivity in kesterite-type compounds was the Cu_{Zn}^{-} acceptor defect found to be the most relevant one [85] which, however, is formally not intended by the A – B-type. Anyhow, the formation energy of the Cu_{Zn}^{-} defect (cf. Figure 1-12 & Figure 1-13) is the lowest among all intrinsic point defects regardless of the chemical potential and is thus readily formed which eventually induces the p-type character. The concentration of this electronically active defect is magnitudes smaller as compared to the self-passivating defects and, hence, far below the sensitivity of the average neutron scattering length method. The concentration of the A- and B-type Zn_{Cu}^{+} defect moderately decreases with increasing Cu/(Zn+Ge) and eventually vanishes together with the B-type contribution. Its counterpart, the Cu_{Zn}^{-} antisite defect, is introduced when D- and/or K-type is involved and thus formally appears at Cu-rich and Zn-poor to only slightly Zn-rich conditions. The concentration of this defect steeply increases as the Cu-content does.

Compositions including B-, G- and F-type contributions do imply the presence of Zn_{Ge}^{2-} defects. The formation energy as an isolated point defect and its impact on the electronic structure is assumed to be comparably low (based on the formation energy and ionization level of Zn_{Sn}^{2-}; cf. Figure 1-12). The concentration of this defect is nearly unchanging over a wide compositional range and only starts to drop significantly at the transition zone between G – F- and F – I-type, respectively, and finally (formally) disappears once the I-type contribution starts to dominate (Figure 3-41) which corresponds to a ratio Cu/(Zn+Ge) : Zn/Ge > 0.97.

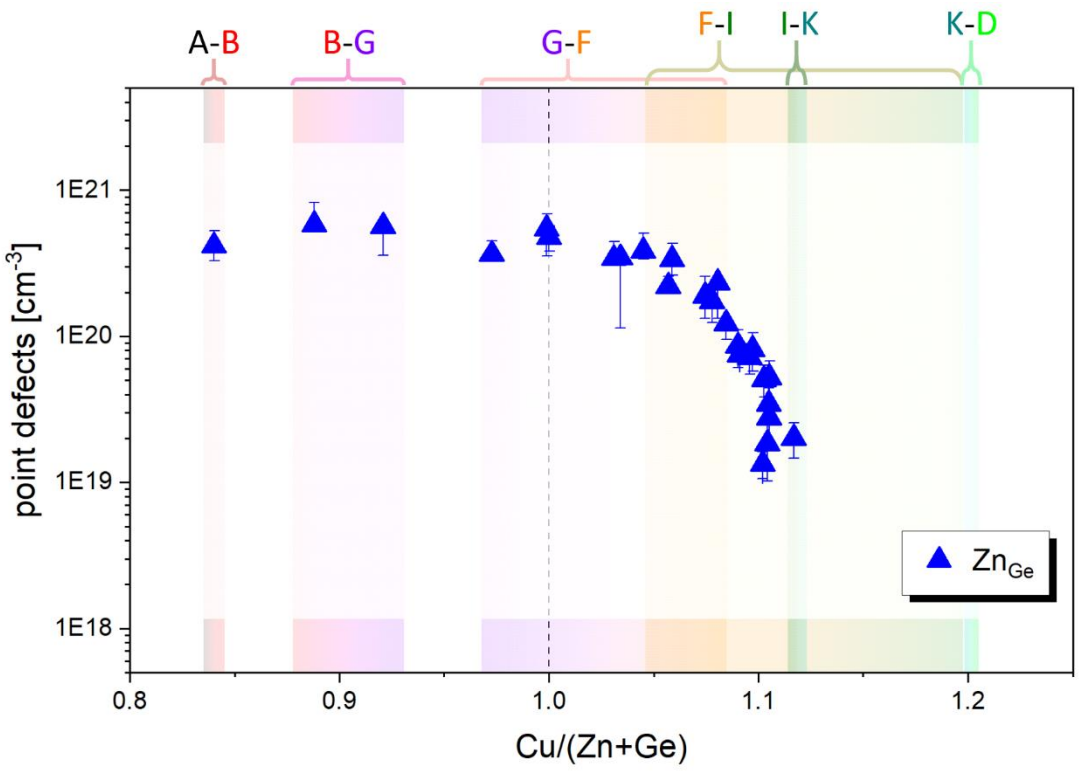

Figure 3-41 Point defect concentration of Zn_{Ge}^{2-} in dependence of Cu/(Zn+Ge).

The decrease in Zn_{Ge}^{2-} defects is accompanied by the onset of Cu_{Ge}^{3-} defects which is exclusively forming under Cu-rich conditions. While the formation energies of the respective point defects are comparable is the Cu_{Ge}^{3-} (or rather Cu_{Sn}^{3-}) defect known to create deep acceptor states that are acting as recombination sites for the majority charge carriers (electron holes) and which are effectively narrowing the band gap. A high population of Cu_{Ge}^{3-} defects will therefore greatly deteriorate the electronic properties. According to the formalisms of the off-stoichiometry types such a high population is unlikely to happen in the compositional regime relevant for PV and related applications. And yet can its low formation energy in conjunction with Ge-poor conditions potentially facilitate an amount of those defects capable to limit the PV performance noticeably. However, in consistence with the definitions of the off-stoichiometry types and within the sensitivity offered by the average neutron scattering length method is the detection of Cu_{Ge}^{3-} defects only viable for the Cu-rich regime. Here, whose concentration steadily rises until reaching a plateau-like region of saturation where the Zn_{Ge}^{2-} defects (cf. Figure 3-41) have entirely been replaced

by Cu_{Ge}^{3-}, hence, leaving no more space remaining on the Ge(2b) position (Figure 3-42).

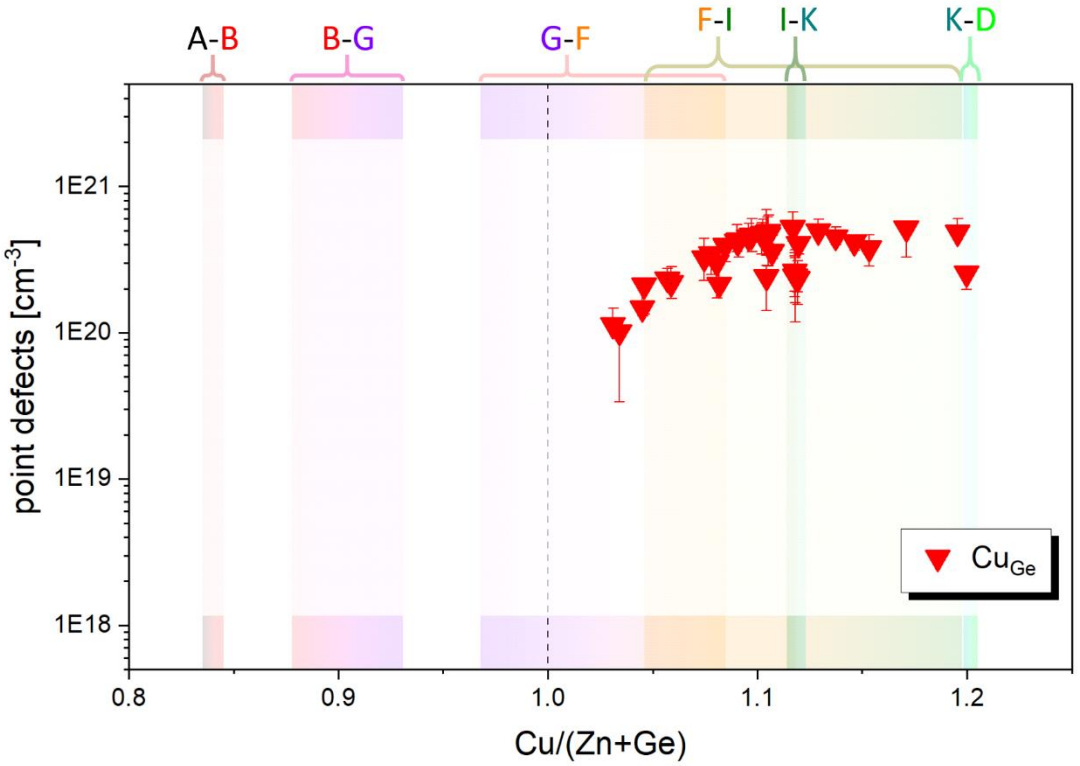

Figure 3-42 Point defect concentration of Cu_{Ge}^{3-} in dependence of Cu/(Zn+Ge).

Any G- and F-type contribution goes along with the formation of Zn_i^{2+} defects, which can therefore be found in the vast majority of samples that extend from moderately Cu-poor conditions far into the Cu-rich region, although the energy required to form Zn_i^{2+} defects is comparably high owing to its divalent state. Information on interstitial defects cannot be directly inferred from structure refinement, albeit the structural model applied for the Rietveld refinement can basically be manipulated in a way that allows consideration of interstitial positions. This, however, will lead to more independent and fragile parameters that result in an even more reduced robustness. Hence, the possible occupation of interstitial positions is inferred indirectly by taking the difference of the number of cations obtained from WDX results and the number of cations necessary to fill up all structural sites. In the region spanning from B – G- to F – I-type the material is highly populated with Zn_i^{2+} defects, whose concentration starts to decrease significantly as soon as the I-type fraction becomes dominating, otherwise in case of lower Zn/Ge (Figure 3-43).

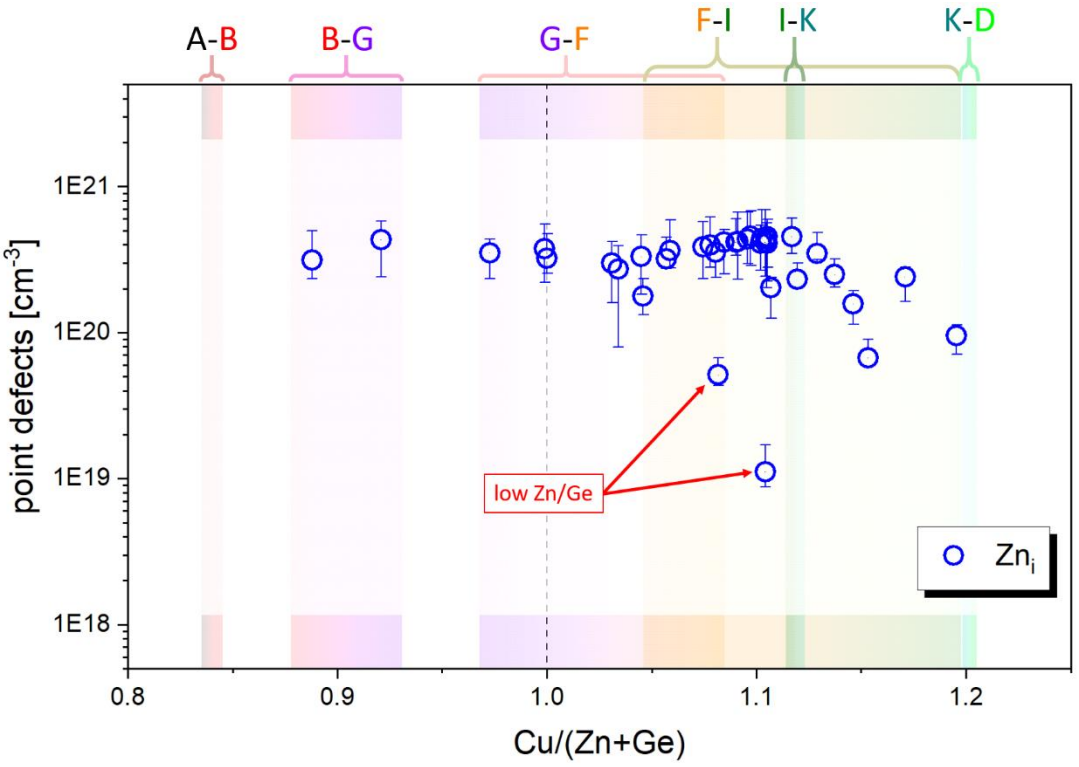

Figure 3-43 Point defect concentration of Zn_i^{2+} in dependence of Cu/(Zn+Ge).

The existence of Zn_i^{2+} deep donor defects in solar cell absorbers worsens the electronic properties through annihilation of charge carriers and by creating intermediate states in the band gap. The composition typically chosen for kesterite-type absorbers, however, does not lead to the formation of normative Zn_i^{2+} defects and even a minor formation of electronically active defects can be expected to be additionally impeded due to its high formation energy.

In spite of the lower formation energy of Cu_i^+ as compared to Zn_i^{2+}, those atoms on interstitial positions are ever more unfavorable in general. Antisite defects involving copper, in fact, have a considerably lower formation energy and copper is therefore primarily consumed for Cu_{Zn}^- and Cu_{Ge}^{3-}, respectively. Nonetheless do Cu_i^+ defects appear as soon as the composition becomes partly F-type and its concentration steeply increases by about one order of magnitude between Cu/(Zn+Ge) = 0.97 (i.e. the least F-type contribution) and Cu/(Zn+Ge) = 1. With increasing Cu-content (Cu/(Zn+Ge) > 1), eventually, the concentration of the Cu_i^+ defect rises fairly linearly as the increasing number of copper-related antisite defects require more Cu_i^+ in

order to compensate for the negative excess charges and to distribute the available copper entirely (Figure 3-44).

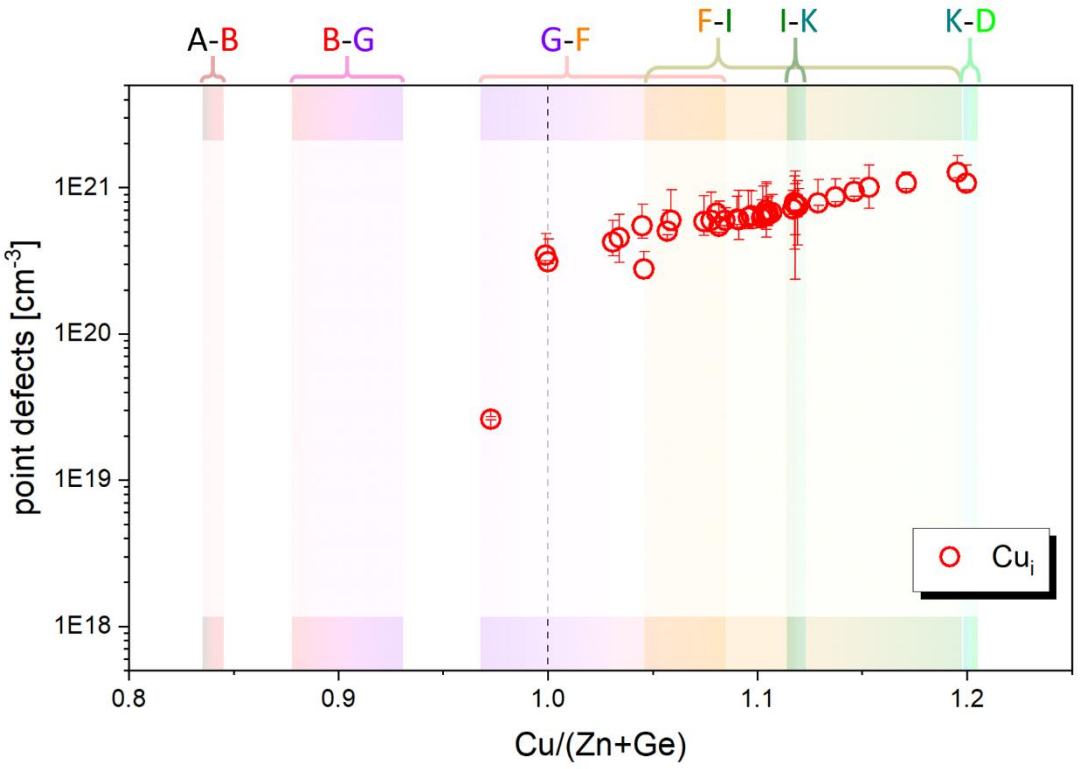

Figure 3-44 Point defect concentration of Cu_i^+ in dependence of Cu/(Zn+Ge).

A considerable occurrence of Cu_i^+ defects seems unlikely to happen for the Cu-poor regime, and even if so, its impact on electronic structure was shown to be weak and is thus attributed to the group of benign defects [85, 86].

3.5.5 Microstrain vs. point defect density

Microstructure parameters do include microstrain, ε, and the volume-averaged domain size, $D_{\langle V \rangle}$, though, the latter will not be reported for two reasons: (1) The domain sizes are too large to be resolvable by conventional XRD (i.e. well above ~120 nm) and (2) the domain sizes are artificially modified by the ball milling applied after the solid-state reaction and would therefore not reflect the actual domain sizes developed during synthesis. The microstrain, on the other hand, can

indeed be expected to be not (much) impacted by the ball milling process but the peak broadening attributed to microstrain is actually a consequence of two superposing effects: (1) By microstrain itself that is induced by lattice strain due to various kinds of lattice defects and (2) by chemical inhomogeneities which do result in a broader distribution of lattice plane distances. Since the extent of inhomogeneity does differ among the samples a random effect on peak broadening is introduced that is difficult to separate from the actual microstructure effect.

Nonetheless will a possible dependency attempted to be elucidated in the following. Asymmetric strain broadening (cf. section 2.2.2.3) is examined to account for potentially dissimilar magnitudes of lattice distortions along different directions within the unit cell. The microstructural response can be expected not only to be caused by the dissimilar ionic radii taking effect through antisite defects but also by the direction-dependent strength of the electrostatic field in the vicinity of a point defect. Depending on the local structural environment and the resulting electrostatic interactions a specific point defect may experience a stronger displacement towards a certain direction. Consequently, the impact on the concerned interplanar distances becomes more pronounced (e.g. along [100]) whereas lattice planes perpendicular to them might be less affected (e.g. along [001]. A stronger deviation from the unstrained lattice plane distance results in a broader distribution of interplanar distances for the given lattice plane which directly translates to a broader (Gaussian) distribution of intensity for the corresponding Bragg peak. However, a distribution of interplanar distances is also caused by compositional inhomogeneities that do bias the determination of the microstrain.

The extensive grain statistics established upon WDX measurements not only provide a more robust quantification of the composition but also allow to simulate the effects chemical inhomogeneities do have on the peak shape. Figure 3-45 shows the histograms of a Cu-poor and a Cu-rich sample, respectively, that represent the compositional distribution in general and the frequency of each data bin (bin size = 0.005) in particular, with each data bin being eventually treated as an individual CZGSe phase and corresponding associated lattice parameters.

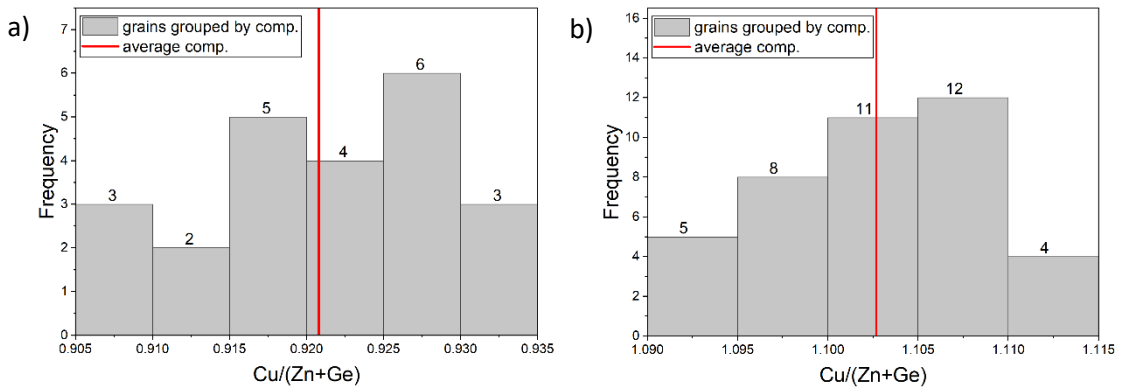

Figure 3-45 Histograms of the composition (frequency vs. Cu/(Zn+Ge)) of a) a Cu-poor and b) a Cu-rich CZGSe sample, respectively. The average composition (i.e. the one considered to be the actual composition) is indicated by red solid lines.

The impact of compositional inhomogeneity on peak shape depends on the compositional distribution, the frequency of each data bin (i.e. 'number' of CZGSe phases) and its distribution, and the compositional regime. From the Cu/(Zn+Ge) of each data bin (CZGSe phase) the corresponding lattice parameters are obtained by interpolating on a third-order polynomial fit of the refined lattice parameters. Figure 3-46 shows the refined lattice parameters *a* and *c* in dependence of Cu/(Zn+Ge) together with the compositional distribution of, respectively, those Cu-poor (A0125-2) and Cu-rich (D0010-1) sample introduced in Figure 3-45.

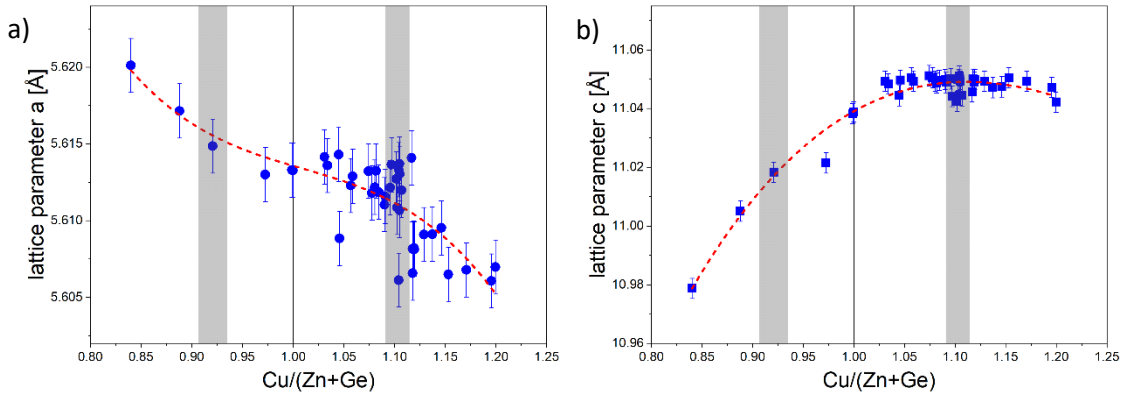

Figure 3-46 Lattice parameters *a* and *c* of all CZGSe samples as obtained from structure refinement of XRD data (cf. Figure 3-20 & Figure 3-22). The grey-shaded area reflects the compositional distribution of the aforementioned samples. A third-order polynomial fit (red dashed line) is taken to interpolate the lattice parameters for any given composition within the covered range.

Although a broader compositional distribution can generally be expected to cause a stronger variation in lattice parameters does the compositional regime play a huge

role too. In fact, a broader distribution of lattice parameters for a given compositional spreading results for Cu-poor samples due to the steeper slopes obtained for the lattice parameters in this region. XRD patterns are calculated for every sample that include as many CZGSe phases as data bins are contained in the respective histograms. The Cu/(Zn+Ge) at each bin center is taken to interpolate the corresponding lattice parameters and the frequency is applied to the scale factor in XRD pattern calculations. The effect is generally strongest for Cu-poor samples and particularly for 00l reflections owing to the larger absolute changes over Cu/(Zn+Ge) exhibited by lattice parameter *c* (Figure 3-47).

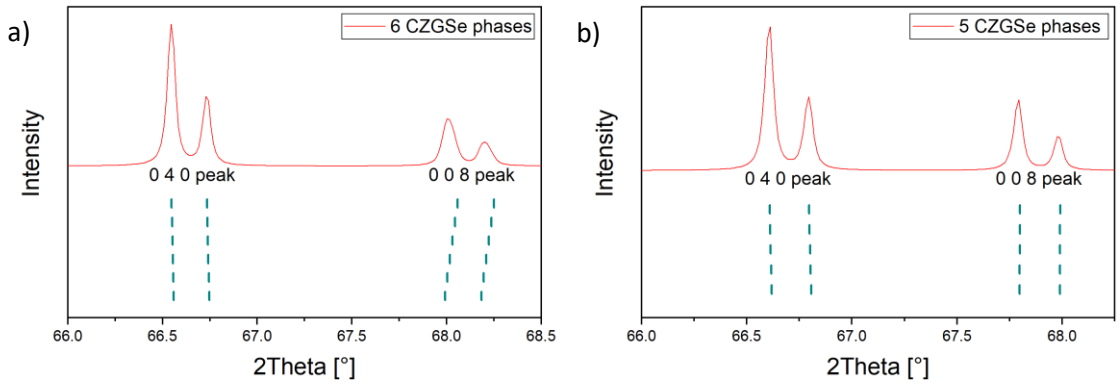

Figure 3-47 Detail view of the calculated 040 and 008 peaks for a) the Cu-poor sample and b) the Cu-rich sample demonstrating the peak broadening caused by the inhomogeneity effect. While all peaks are subject to broadening through compositional inhomogeneity is the impact largest for the 008 peak of the Cu-poor sample. The phases included in the calculation and the resulting 2Theta positions of the 040 and 008 peaks are indicated by green dashes ($K_{\alpha 1+2}$).

Figure 3-48 provides a comparison between the peak widths obtained from the multi-phase approach with the calculated peak widths of a single distinctively composed CZGSe phase. The 040 peak of the Cu-poor sample (Figure 3-48a) is only little affected by inhomogeneity whereas the 008 peak (Figure 3-48c) is greatly broadened (red curve) compared to the hypothetical situation of only one well-defined composition (blue curve). For the Cu-rich sample, on the other hand, only subtle differences exist between the two cases (Figure 3-48b & d).

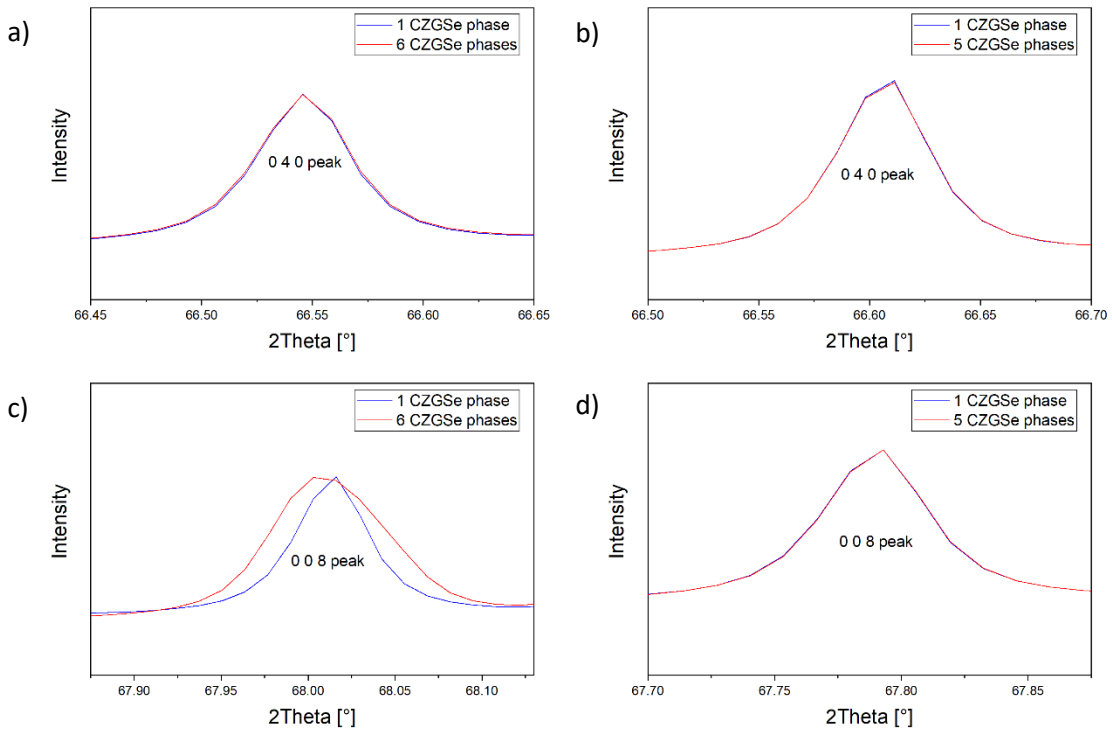

Figure 3-48 Calculated profiles of CZGSe 040 (upper panels) and 008 (lower panels) peaks for a single well-defined composition (blue curves) and for a set of differing compositions (red curves). The latter leads to various peak positions that are shifted among each other and eventually convolutes to a broadened peak through superposition.

The amount of peak broadening of the calculated XRD patterns for multiple CZGSe phases is eventually subtracted from the peak broadening determined for the experimental XRD patterns and, that way, the microstrain can be supposed to be at least roughly corrected for the inhomogeneity effect. Figure 3-49 shows the corrected microstrain values obtained for the [100] direction (i.e. extractable from h00/0k0 Bragg peaks).

In spite of the challenges linked to microstructure analysis pointed out previously does the trend shown by the microstrain along [100] direction imply a relationship with the point defect density. The highest values of microstrain are obtained for those samples containing the lowest number of point defects per unit cell, and tend to decrease as the density of point defects increases.

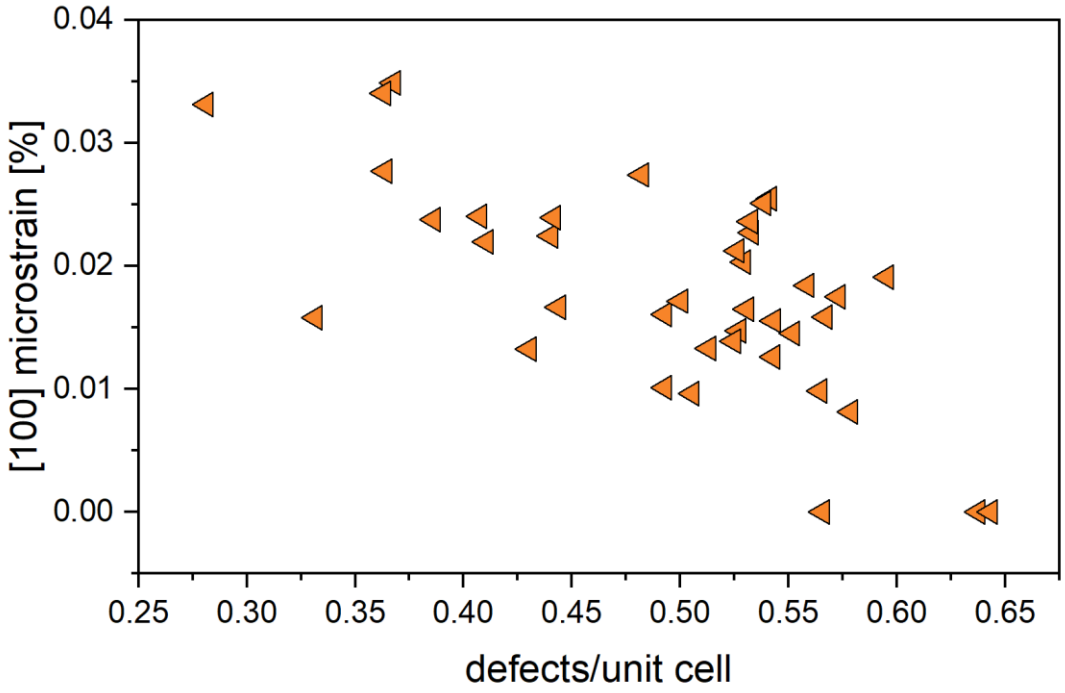

Figure 3-49 Inhomogeneity-corrected microstrain along [100] direction in dependence of total point defect density as established from structure refinement of neutron diffraction data in conjunction with EPMA data. The microstrain along the [100] direction is highest for lower point defect concentrations and tends to decrease with increasing point defect density.

Although it appears counterintuitively can a higher point defect density be expected to reduce the lattice strain through enhanced relaxation; microstrain and the corresponding peak broadening result from deviations from the 'average' structure (metrics) which become more pronounced in case of lower defect densities. As the defect density increases, the 'average' metrics and the one altered by defects can be expected to become more and more similar, which would lead to a diminishment of peak broadening (microstrain). Conversely, a reduction in microstrain should also be happening towards lower defect concentrations, yet remains in the area of speculation owing to the lack in data coverage between 0 and ~0.25 defects/unit cell. This reduction in microstrain is however suggested by the behavior of the microstrain along [001] direction. The microstrain tends to gently increase from lower defect concentration until reaching its culmination point at around 0.5 defects/unit cell from where it then steeply decreases as the defect concentration further increases (Figure 3-50).

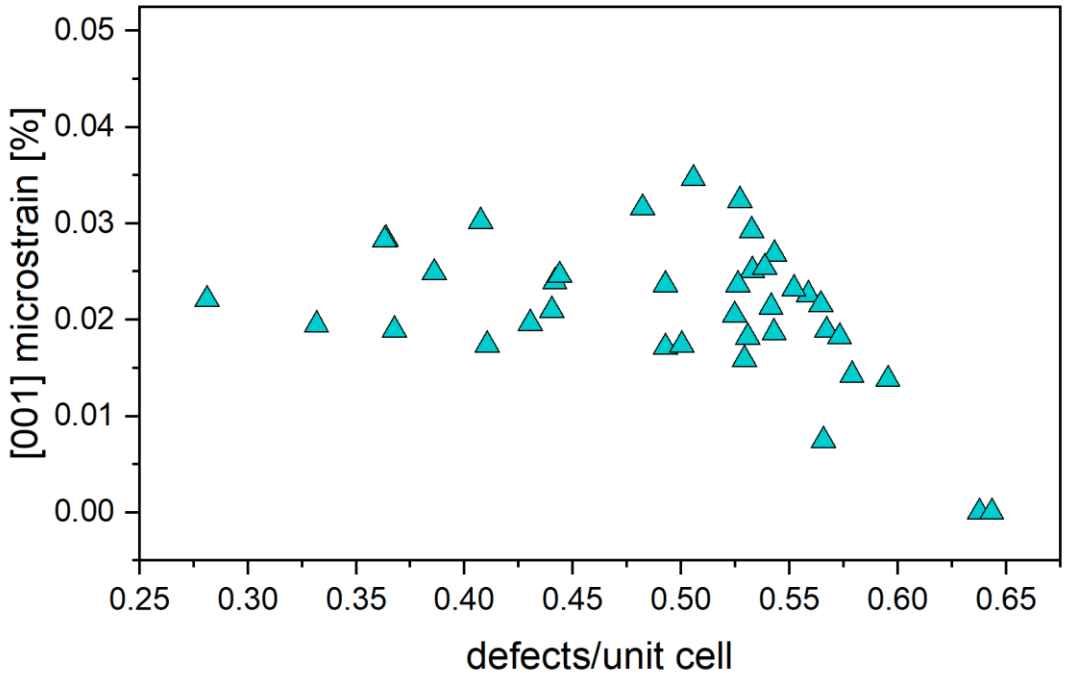

Figure 3-50 Inhomogeneity-corrected microstrain along [001] direction in dependence of total point defect density as established from structure refinement of neutron diffraction data in conjunction with EPMA data. A plateau-like region implying a gentle increase in microstrain with increasing point defect density is followed by a steep drop in microstrain as the point defect density further increases.

3.5.6 Conclusions of the structural characterization

Comparison of the quality factors resulting from structure refinements as well as the values obtained for site occupancy factors determined from neutron diffraction data clearly favor the kesterite-type structure (s.g. $I\bar{4}$) for CZGSe. The dissimilar cation distribution in the stannite-type structure (s.g. $I\bar{4}2m$) would cause differences in relative peak intensities that are already noticeable in XRD data. In addition does the employment of the stannite-type structure as structural starting model in the Rietveld refinements lead to unreasonable site occupancy factors, eventually proofing its inapplicability for this material. In the ordered and partially disordered state, hence, CZGSe adopts the kesterite-type structure with space group $I\bar{4}$. For an equal distribution of Cu and Zn among the 2c and 2d positions the symmetry increases, with those two cation positions becoming the 4d position and the previous 8g anion position (x, y, z) changing to 8i position (x, x, z). The resulting crystal structure is described by space group $I\bar{4}2m$ and is referred to as disordered

kesterite. Apart from the crystal structure itself does the distribution of cations, in conjunction with the deviation from stoichiometry, determine the behavior of the unit cell metrics in multifaceted ways. Dissimilarities both in ionic radii as well as valence states do influence bond lengths, bond angles and anion position as soon as cations get distributed differently. On the next-larger scale do these changes, in general, allometrically feedback onto the unit cell dimensions. For instance, a dependency between unit cell volume and effective concentration of defect species assumed to have an overall shrinking impact on the unit cell could be demonstrated (c.f. Figure 3-19). Likewise, a fairly straightforward relationship was obtained between cation ratios and tetragonal deformation, which was found to generally decrease from Cu-poor towards Cu-rich conditions and to increase from Ge-rich to Ge-poor conditions. The changes in tetragonal deformation are most pronounced in the Cu-poor and Ge-rich region, respectively (c.f. Figure 3-24). This trend results from the disctinctively different behavior of lattice parameters *a* and *c*, with the former being more responsive to any changes in composition and the latter only being modestly or virtually not at all affected over a wide compositional range. Whose rather complex trends (c.f. Figure 3-20 to Figure 3-23) result from a variety of point defects species and concentrations, respectively, that not only induce various changes with different magnitudes and potentially along different directions each for themselves, but which do also influence, intensify, and/or counteract each other. This complexity, eventually, is also reflected by poorly developed trends for the anion positions and tetragonal distortion as well as for bond distances and angles, respectively. The large errors connected to those parameters additionally hindered a more thoroughly evaluation.

Sufficient chemical homogeneity was achieved for the vast majority of the samples that allowed for a meaningful analysis of the cation distribution by means of the average neutron scattering length method [8, 9] as well as by considering the corresponding defect complexes [2, 3, 89-91] and the proportionalities of the associated defect species. The densities of the resulting point defect species were obtained from the modeled cation distributions, the unit cell volumes, and the chemical compositions. The point defect species identified for the investigated off-stoichiometry regimes demonstrate the importance of achieving Cu-poor and Zn-rich A – B-type composition when aiming at best possible PV devices as this off-

stoichiometry type exclusively exhibits defects causing little impact on the electronic structure (A – B-type: V_{Cu}^{-}, Zn_{Cu}^{+}, Zn_{Ge}^{+}). Although also Cu-poor and Zn-rich, a deterioration of PV performance will already result for the B – G-type composition owing to the emergence of detrimental Zn_i^{2+} defects. A high concentration of the rather harmless Zn_{Ge}^{2-} antisite defect was found for the entire Cu-poor region, which then drops quite rapidly towards more Cu-rich conditions and eventually vanishes for Cu/(Zn+Ge) > 1.1. The Cu-rich regime is characterized by defects particularly deteriorating the PV performance: the detrimental Cu_{Ge}^{3-} antisite defect becomes increasingly favored over Zn_{Ge}^{2-}, which is concomitant with the enhanced formation of similarly detrimental Zn_i^{2+} defects. A common feature that is essentially independent of the composition is the Cu-Zn disorder, which is known to cause both band gap fluctuations and the open-circuit voltage to decrease [106]. The Cu-Zn disorder, however, was not explicitly investigated but only displayed in the cation distribution models because its extent is solely determined by the thermal history a sample has experienced, and its quantity would have only been relevant for correlation with PV performance (specifically open-circuit voltage).

Microstructure analysis was performed to evaluate domain sizes and microstrain. The domain sizes turned out to be too large to cause an evaluable (Lorentzian) peak broadening whereas the small but yet existing chemical inhomogeneities led to a biased microstrain determination. A stronger impact of chemical inhomogeneity on resulting peak breadths was found for Cu-poor samples. The corresponding overrepresentation of microstrain could approximately accounted for by means of a robust statistic of WDX data and XRD pattern simulations. A larger microstrain along [100] direction was found for low defect concentrations, which decreases towards higher defect concentrations. The microstrain along [001] direction, on the contrary, remains fairly constant for low to intermediate defect concentrations but likewise decreases as soon as defect concentrations become larger. This decrease in microstrain is attributed to a diminishing deviation between average structure (or rather d_{hkl}) and locally distorted structure (Δd_{hkl}) with increasing defect density. Regarding the correction for inhomogeneity effects it must however be noted that the histograms and the data bins therein assume that the WDX results are precise enough to allow for this approach. Also, the discrete (and artificial) grouping of

compositions within the range offered by the compositional distributions likely represents an over-simplification as the spreading is rather made up by a continuous distribution of compositions (i.e. Δd_{hkl}). Apart from that does the complex interplay between the different kinds of point defects and their local structural environment potentially lead to a mutual diminishment or enhancement of the peak broadening that additionally frustrates its direct correlation with point defect density. Consequently, unambiguous trends for microstrain are difficult to obtain and the results elaborated are to be taken with care.

3.6 Optical band gap

The reflectance spectra recorded for all samples are converted to pseudo-absorption spectra *F(R)* by means of the Kubelka-Munk function [5] (Eq. 2.26). The band gap is inferred by extrapolating from the linear region of the $(F(R)h\nu)^2$ vs. $h\nu$ curve to the intercept of the abscissa. Figure 3-51 exemplarily shows the Tauc plot [180] of a highly Cu-poor and Zn-rich sample for which a satisfactorily pseudo-absorption spectrum is obtained that allows for reasonable extraction of the band gap energy. Evaluable curves are obtained for samples that are Cu-poor and Zn-rich, or rather when the ratio Cu/(Zn+Ge) : Zn/Ge is below ~0.94. A higher value for the rationed cation ratios essentially results in pseudo-absorption spectra being unsuitable for the purpose of band gap determination. A ratio of 0.92 and above coincides well with the emergence and increasing population of the deep Cu_{Ge}^{3-} defect, eventually leading to unevaluable pseudo-absorption spectra owing to additional electronic transitions in the band gap (Figure 3-52).

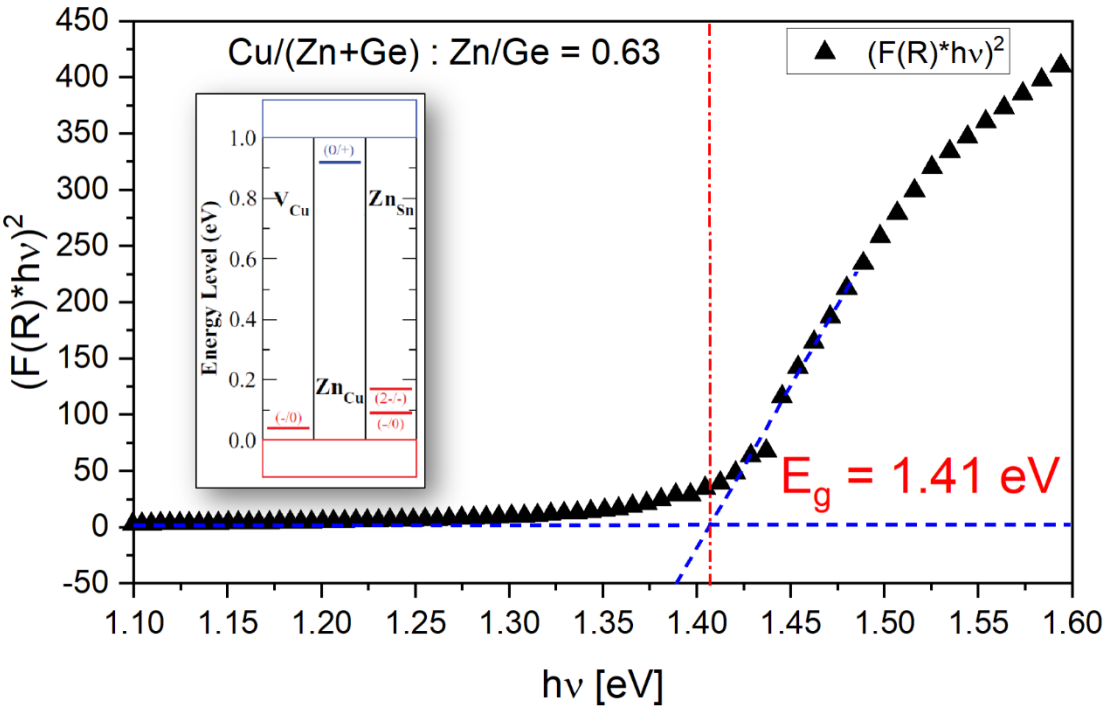

Figure 3-51 Estimation of the band gap energy of a Cu-poor and Zn-rich sample by means of the Tauc plot [180] and the extrapolation method. The inset depicts the ionization levels of the point defects in CZTS (modified after [86]) that are considered applicable for this CZGSe sample. All those defects create shallow states without impacting the electronic structure noteworthily.

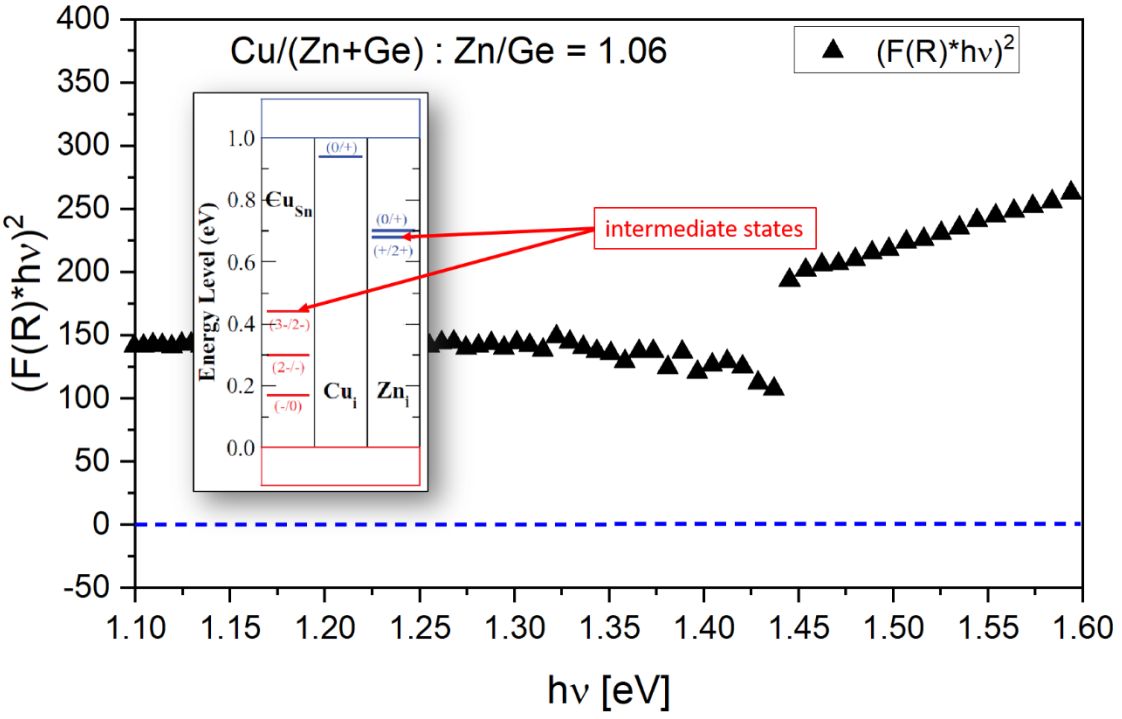

Figure 3-52 Pseudo-absorption spectrum of a Cu-rich and Zn-rich sample. The inset depicts the ionization levels of the point defects in CZTS (modified after [86]) that are considered applicable for this CZGSe sample. As the population of $Cu_{Sn}^{3-}/Cu_{Ge}^{3-}$ (and Zn_i^{2+}) defects increases, the deep intermediate states thereby introduced in the band gap become significant which eventually frustrates band gap determination.

Although the uncertainties of the extractable band gap energies are relatively large, a dependency on Cu/(Zn+Ge) can still be observed (Figure 3-53). In agreement with findings made on CZTSe thin film solar cells [185] the band gap energy tends to increase as the Cu-content decreases which, in turn, affects the unit cell metrics too.

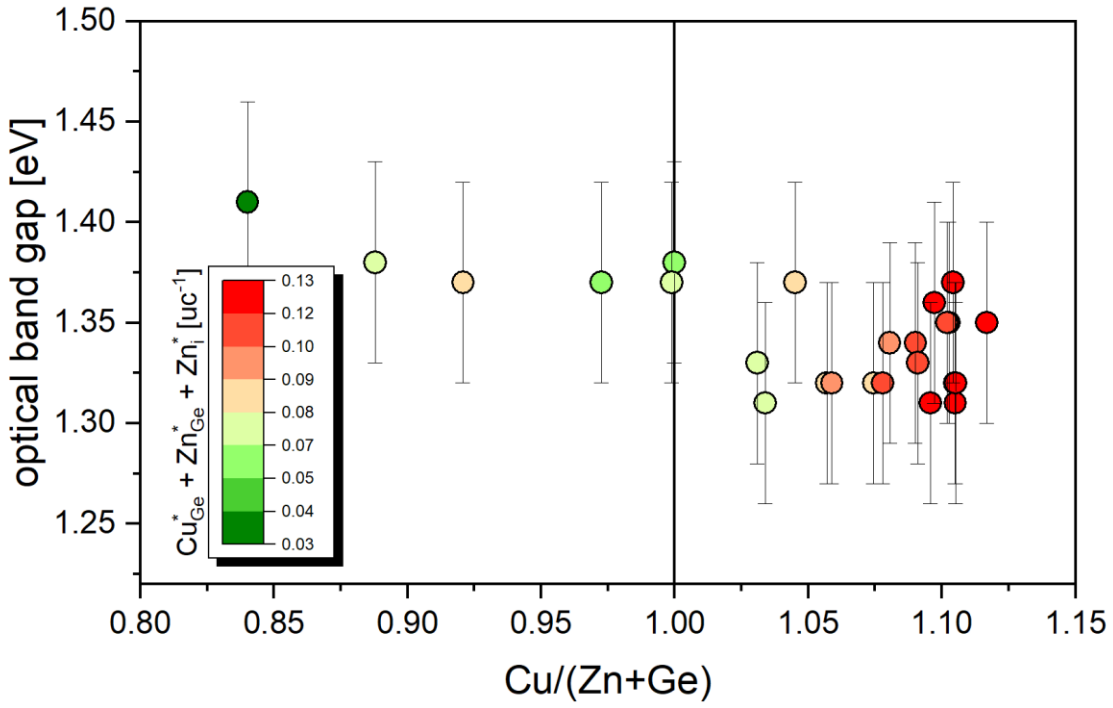

Figure 3-53 Band gap energy in dependence of Cu/(Zn+Ge). The colormap represents the weighted (marked with *) concentratrion of point defects potentially leading to decreasing band gap energy.

A shift in band gap energy can generally be attributed to changing unit cell metrics (Figure 3-54a) that affects the electronic structure and which essentially also cause the differences in the fundamental band gap energies among the various kesterite-type end-members (Figure 3-54b). In addition, certain point defects creating additional electronic transitions in the band gap do also influence the band gap energy. In Figure 3-53 & Figure 3-54 the concentration of defects believed to potentially downgrade the fundamental band gap energy is included using colormaps. The concentration of each of those defects is weighted according to the respective ionization levels to roughly account for their dissimilar impact on band gap energy.

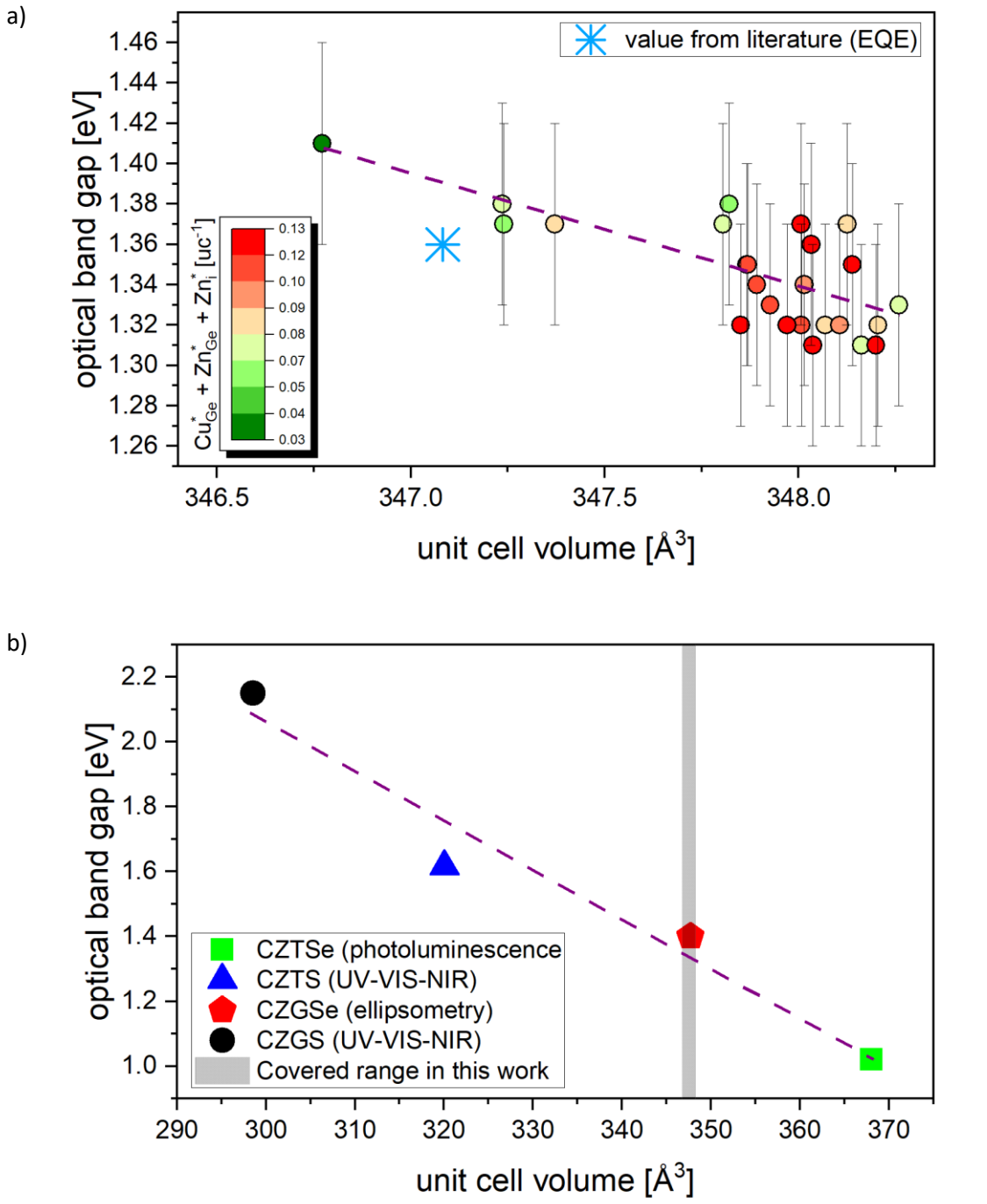

Figure 3-54 a) Band gap energy in dependence of unit cell volume. A reference value [186] obtained from EQE spectra is included for the sake of comparison. The colormap represents the weighted (marked with *) concentratrion of point defects potentially leading to a narrowing of the fundamental band gap. b) Large-scale impact of unit cell volume [110, 111, 117, 187] on band gap energy [115, 117, 188, 189] for four kesterite-type end-members.

In conclusion, the band gap energy seems particularly responding both to point defects creating intermediate states deep in the band gap as well as to the unit cell metrics with the latter being particularly accountable for the fundamental band gap.

Among the end-members shown in (Figure 3-54b) the band gap averagely decreases by ~15 meV per every 1 Å^3 unit cell volume increase whereas for the CZGSe samples investigated here the decrease occurs more rapidly (about -55 meV/Å^3), although a steady linear behavior might not thoroughly be realized among the end-members. It must also be noticed that the method applied is subject to some limitations as, for instance, its primary application area is originally dedicated to amorphous materials including the assumption of localized energy states, which is not met in case of crystalline material [190]. Apart from that do the poor coverage of data, the rather small differences in unit cell volumes and the large errors make an estimation of robust trends and predictions beyond the covered region a vague affair. Nonetheless does this method offer a facile mean to estimate the band gap energies of bulky samples with a satisfactorily reliability, as is confirmed by comparable bang gap energy values found in literature that were obtained using dissimilar techniques (i.a. [115, 186]).

4 Conclusion

This work was aiming at unravelling the cation distribution in off-stoichiometric CZGSe compounds as well as the identification of the point defect species and their densities related to various compositions. In addition, the question regarding the actual crystal structure CZGSe does adopt is to be answered conclusively, which is eventually key to make the aforementioned aims properly addressable in the first place.

Solid-state synthesis has proven appropriate in producing off-stoichiometric powder samples [2, 3, 89-91] both of high enough quantity as well as with sufficient chemical homogeneity on a whole, albeit with considerably different post-synthesis composition that resulted in the formation of mixed off-stoichiometry types. Two approaches were tested to evaluate the impact of grain size of the germanium metal precursor on phase purity and chemical homogeneity. No noticeable differences could be observed between sample series with differently sized germanium pieces, although the compositional deviation of the obtained CZGSe phases appears slightly more systematic when pre-milled germanium was used. The total weight synthesized (ranging from 4 g to 8 g), however, does not seem to have noteworthy effects. A particular susceptibility to form several CZGSe phases (i.e. strong chemical inhomogeneities) was found for as-weighed Cu-rich and especially Ge-rich (=C-type) composition. A repition of the homogenization step led to successful recovery only of a few samples, indicating that a reasonable chemical homogeneity becomes even more difficult to achieve once a sample has developed inhomogeneities after the regular synthesis process. Upon potential future investigations, hence, this issue might probably be better addressable by applying different temperature profiles which were kept the same during this study. On the other hand, readily and commonly forming ZnSe as well as systematic removal of germanium from the actual specimen upon thermal treatment were identified as to be the most hindering mechanisms for achieving phase purity and aimed composition. The issue of driven off germanium may promote the formation of secondary phases like ZnSe in the first

place, yet can poorly be addressed for the given synthesis just by changing temperature conditions.

Structural analysis has been perfomed applying the Rietveld method [6, 7] both on p-XRD and p-ND data. By means of relative peak intensities, refinement's quality factors as well as refined neutron scattering lengths it was demonstrated that CZGSe does not adopt the stannite-type structure (s.g. $I\bar{4}2m$) but the kesterite-type structure (s.g. $I\bar{4}$), and is generally characterized by some Cu-Zn disorder among the 2c and 2d Wyckoff position, respectively. Cation distribution models were established for the 41 off-stoichiometric CZGSe phases covering a variety of off-stoichiometry type mixtures, from which the density of normatively associated point defect species could be derived. For the least off-stoichiometric CZGSe phases a total point defect density of around $6 \cdot 10^{20}$ cm^{-3} was obtained and is up to three times higher for the CZGSe phases exhibiting strongest off-stoichiometry, specifically those belonging to the high-grade Cu-rich regime. The Cu-poor/Zn-rich region is mainly characterized by benign point defect species, though, detrimental Zn_i^{2+} defects are introduced as soon as the composition gets any G-type contribution. A high density of detrimental defects is found throughout the Cu-rich regime, hence ultimately leaving a rather small compositional region suitable for PV application (namely A – B-type region). A correlation was found between the unit cell volume of the respective CZGSe phase and the effective amount of point defects causing overall enlargement of unit cell dimensions whereas the remaining unit cell metrics (i.e. lattice parameter, anion parameter, bond angles, and bond distances) do reflect the complex interactions resulting from the various compositions and corresponding kinds of point defects. The lattice parameter *a* is generally more sensitively responding to any change in composition while the lattice parameter *c* shows stronger absolute changes, which yet are restricted to the Cu-poor and highly Ge-rich regime. Over a wide compositional range the lattice parameter *c* indeed remains fairly constant.

Anisotropic peak broadening was considered upon p-XRD data refinement to seek for a possible correlation between microstrain and point defect density. Depending on the compositional regime and the corresponding variability of lattice parameters a considerable impact even for only slight chemical inhomogeneities was found that

eventually leads to an overestimation of microstrain. A comprehensive frequency analysis over the compositional distribution was performed to account for peak broadening caused by chemical inhomogeneity. Absolute values obtained for microstrain are thus to be taken with care, though, relative differences and the resulting trends are believed to reflect at least its general behavior.

Band gap energies were obtained for the majority of the CZGSe phases using UV-Vis spectroscopy measurements to which the Kubelka-Munk method [5] was applied. The band gap energy tends to decrease with increasing unit cell volume (and likewise with increasing Cu/(Zn+Ge)) which generally agrees with the trend obtained for the end-members, yet the experimental error of the band gap values is quite large. High concentrations of point defects creating deep states in the band gap did not deliver reflectance spectra suitable for band gap energy determination, thus no band gap energies could be estimated for highly Cu-rich/Zn-poor composition as it facilitates the enhanced formation of Cu_{Ge}^{3-} antisite defects. Individual consideration of the cation ratios is therefore inappropriate due to the insufficient dimensionality, but a dependency can rather be found if the proportion between Cu/(Zn+Ge) and Zn/Ge is taken. In fact, reflectance spectra were unsuitable for band gap energy determination as soon as Cu/(Zn+Ge) : Zn/Ge > 0.94 which is associated with the emergence and increasing concentration of Cu_{Ge}^{3-} defects.

This study not only has confirmed the crystal structure of CZGSe to be kesterite-type $I\bar{4}$ but also signifies the importance of well-adjusted compositions for photovoltaic applications in order to suppress the formation of point defects being detrimental to the optoelectronic properties. Controlling of germanium incorporation in the CZGSe phase has been identified as a major obstacle in achieving the composition of desire and, thus, likely requires carefully tuned synthesis conditions when CZGSe is to be considered for real applications.

References

1. Shockley, W. and H.J. Queisser, *Detailed balance limit of efficiency of p-n junction solar cells.* Journal of applied physics, 1961. **32**(3): p. 510-519.
2. Lafond, A., et al., *Crystal structures of photovoltaic chalcogenides, an intricate puzzle to solve: the cases of CIGSe and CZTS materials.* Zeitschrift für anorganische und allgemeine Chemie, 2012. **638**(15): p. 2571-2577.
3. Rios, L.E.V., et al., *Existence of off-stoichiometric single phase kesterite.* Journal of Alloys and Compounds, 2016. **657**: p. 408-413.
4. Choubrac, L., et al., *The stability domain of the selenide kesterite photovoltaic materials and NMR investigation of the Cu/Zn disorder in Cu 2 ZnSnSe 4 (CZTSe).* Physical Chemistry Chemical Physics, 2015. **17**(23): p. 15088-15092.
5. Kubelka, P. and F. Munk, *An article on optics of paint layers.* Z. Tech. Phys, 1931. **12**(593-601): p. 259-274.
6. Rietveld, H.M., *Line profiles of neutron powder-diffraction peaks for structure refinement.* Acta Crystallographica, 1967. **22**(1): p. 151-152.
7. Rietveld, H.M., *A profile refinement method for nuclear and magnetic structures.* Journal of Applied Crystallography, 1969. **2**(2): p. 65-71.
8. Schorr, S., *Structural aspects of adamantine like multinary chalcogenides.* Thin Solid Films, 2007. **515**(15): p. 5985-5991.
9. Schorr, S., H.-J. Hoebler, and M. Tovar, *A neutron diffraction study of the stannite-kesterite solid solution series.* European Journal of Mineralogy, 2007. **19**(1): p. 65-73.
10. Becquerel, E., *On electric effects under the influence of solar radiation.* Compt. Rend., 1839. **9**: p. 561.
11. Fritts, C.E., *On a new form of selenium cell, and some electrical discoveries made by its use.* American Journal of Science, 1883(156): p. 465-472.
12. Einstein, A., *On a heuristic point of view concerning the production and transformation of light.* Annalen der Physik, 1905: p. 1-18.
13. Small, E.E., *The Earth System: An Introduction to Earth Systems Science.* Eos, Transactions American Geophysical Union, 1999. **80**(48): p. 577-577.
14. Hoffmann, W., *Fallout from the Chernobyl nuclear disaster and congenital malformations in Europe.* Archives of Environmental Health: An International Journal, 2001. **56**(6): p. 478-484.
15. Holt, M., R.J. Campbell, and M.B. Nikitin, *Fukushima nuclear disaster*. 2012: Congressional Research Service.
16. Loarte, A., et al., *High confinement/high radiated power H-mode experiments in Alcator C-Mod and consequences for International Thermonuclear Experimental Reactor (ITER) QDT= 10 operation.* Physics of Plasmas, 2011. **18**(5): p. 056105.
17. Klinger, T., et al., *Performance and properties of the first plasmas of Wendelstein 7-X.* Plasma Physics and Controlled Fusion, 2016. **59**(1): p. 014018.
18. Hoffert, M.I., et al., *Energy implications of future stabilization of atmospheric CO 2 content.* Nature, 1998. **395**(6705): p. 881-884.
19. Lewis, N.S., et al., *Basic Research Needs for Solar Energy Utilization. Report of the Basic Energy Sciences Workshop on Solar Energy Utilization, April 18-21, 2005*. 2005, DOESC (USDOE Office of Science (SC)).
20. Smith, E. and H. Klick. *Explaining NIMBY opposition to wind power*. in *Annual Meeting of the American Political Science Association*. 2007.

21. Molderink, A., et al. *Domestic energy management methodology for optimizing efficiency in smart grids*. in *2009 IEEE Bucharest PowerTech*. 2009. IEEE.
22. Schmietendorf, K., J. Peinke, and O. Kamps, *The impact of turbulent renewable energy production on power grid stability and quality.* The European Physical Journal B, 2017. **90**(11): p. 222.
23. Chapin, D.M., C. Fuller, and G. Pearson, *A new silicon p-n junction photocell for converting solar radiation into electrical power.* Journal of Applied Physics, 1954. **25**(5): p. 676-677.
24. Goodman, C. and R. Douglas, *New semiconducting compounds of diamond type structure.* Physica, 1954. **20**(7-12): p. 1107-1109.
25. Jenny, D.A. and R.H. Bube, *Semiconducting cadmium telluride.* Physical Review, 1954. **96**(5): p. 1190.
26. Goodman, C., *The prediction of semiconducting properties in inorganic compounds.* Journal of Physics and Chemistry of Solids, 1958. **6**(4): p. 305-314.
27. *NREL Efficiency Chart*. 2020.
28. Rühle, S., *Tabulated values of the Shockley–Queisser limit for single junction solar cells.* Solar Energy, 2016. **130**: p. 139-147.
29. Dharmadasa, I., *Advances in thin-film solar cells*. 2018: CRC Press.
30. Grenet, L., et al., *Analysis of Failure Modes in Kesterite Solar Cells.* ACS Applied Energy Materials, 2018. **1**(5): p. 2103-2113.
31. Hahsim, E.T. and A.A. Abbood, *Temperature Effect on Power Drop of Different Photovoltaic Modules.* Journal of Engineering, 2016. **22**(5): p. 129-143.
32. Green, M.A., *Self-consistent optical parameters of intrinsic silicon at 300 K including temperature coefficients.* Solar Energy Materials and Solar Cells, 2008. **92**(11): p. 1305-1310.
33. Sze, S.M. and K.K. Ng, *Physics of semiconductor devices*. 2006: John wiley & sons.
34. Low, J.J., et al., *Band gap energy in silicon.* Am. J. Undergrad. Res., 2008. **7**(1): p. 27-32.
35. Prabahar, S., et al., *Optical properties of copper indium diselenide thin films.* Chalcogenide letters, 2010. **7**(1): p. 49-58.
36. Ito, K. and T. Nakazawa, *Electrical and optical properties of stannite-type quaternary semiconductor thin films.* Japanese Journal of Applied Physics, 1988. **27**(11R): p. 2094.
37. Behnam, A., et al., *Highlights in Applied Mineralogy*. 2017: Walter de Gruyter GmbH & Co KG.
38. Ravi, K., *The growth of EFG silicon ribbons.* Journal of Crystal Growth, 1977. **39**(1): p. 1-16.
39. Woodall, J. and H. Hovel, *An isothermal etchback-regrowth method for high-efficiency Ga1− x Al x As-GaAs solar cells.* Applied Physics Letters, 1977. **30**(9): p. 492-493.
40. de Wild-Scholten, M.M., *Energy payback time and carbon footprint of commercial photovoltaic systems.* Solar Energy Materials and Solar Cells, 2013. **119**: p. 296-305.
41. Release, F.S.P., *First Solar achieves yet another cell conversion efficiency world record.* 2016.
42. Yaroshevsky, A., *Abundances of chemical elements in the Earth's crust.* Geochemistry International, 2006. **44**(1): p. 48-55.
43. Nakamura, M., et al., *Cd-free Cu (In, Ga)(Se, S) 2 thin-film solar cell with record efficiency of 23.35%.* IEEE Journal of Photovoltaics, 2019. **9**(6): p. 1863-1867.
44. ENTR, D., *Report on critical raw materials for the EU.* Ares (2015), 2014. **1819503**.
45. *Deutsche Rohstoffagentur, Bundesanstalt für Geowissenschaften und Rohstoffe.* Preismonitor, 2019.
46. *China Petroleum & Chemical Industry Association: Petrochemical Price: Inorganic: Chemical Material.* 2020.
47. *Shanghai Metals Market.* 2020.

48. Pamplin, B., *A systematic method of deriving new semiconducting compounds by structural analogy.* Journal of Physics and Chemistry of Solids, 1964. **25**(7): p. 675-684.
49. Walsh, A., et al., *Kesterite thin-film solar cells: Advances in materials modelling of Cu2ZnSnS4.* Advanced Energy Materials, 2012. **2**(4): p. 400-409.
50. Chen, S., et al., *Crystal and electronic band structure of Cu 2 ZnSn X 4 (X= S and Se) photovoltaic absorbers: First-principles insights.* Applied Physics Letters, 2009. **94**(4): p. 041903.
51. Jimbo, K., et al., *Cu2ZnSnS4-type thin film solar cells using abundant materials.* Thin Solid Films, 2007. **515**(15): p. 5997-5999.
52. Paier, J., et al., *Cu 2 ZnSnS 4 as a potential photovoltaic material: a hybrid Hartree-Fock density functional theory study.* Physical Review B, 2009. **79**(11): p. 115126.
53. Wagner, S. and P. Bridenbaugh, *Multicomponent tetrahedral compounds for solar cells.* Journal of Crystal Growth, 1977. **39**(1): p. 151-159.
54. Pamplin, B., *The adamantine family of compounds.* Progress in Crystal Growth and Characterization, 1980. **3**(2): p. 179-192.
55. Nakayama, N. and K. Ito, *Sprayed films of stannite Cu2ZnSnS4.* Applied Surface Science, 1996. **92**: p. 171-175.
56. Katagiri, H., et al., *Preparation and evaluation of Cu2ZnSnS4 thin films by sulfurization of E-B evaporated precursors.* Solar Energy Materials and Solar Cells, 1997. **49**(1-4): p. 407-414.
57. Katagiri, H., *Cu2ZnSnS4 thin film solar cells.* Thin Solid Films, 2005. **480**: p. 426-432.
58. Katagiri, H., et al., *Enhanced conversion efficiencies of Cu2ZnSnS4-based thin film solar cells by using preferential etching technique.* Applied physics express, 2008. **1**(4): p. 041201.
59. Wang, K., et al., *Thermally evaporated Cu 2 ZnSnS 4 solar cells.* Applied Physics Letters, 2010. **97**(14): p. 143508.
60. Guo, Q., et al., *Fabrication of 7.2% efficient CZTSSe solar cells using CZTS nanocrystals.* Journal of the American Chemical Society, 2010. **132**(49): p. 17384-17386.
61. Todorov, T.K., K.B. Reuter, and D.B. Mitzi, *High-efficiency solar cell with earth-abundant liquid-processed absorber.* Advanced materials, 2010. **22**(20): p. E156-E159.
62. Barkhouse, D.A.R., et al., *Device characteristics of a 10.1% hydrazine-processed Cu2ZnSn(Se,S)4 solar cell.* Progress in Photovoltaics: Research and Applications, 2012. **20**(1): p. 6-11.
63. Wang, W., et al., *Device characteristics of CZTSSe thin-film solar cells with 12.6% efficiency.* Advanced Energy Materials, 2014. **4**(7).
64. Dullweber, T., et al., *Study of the effect of gallium grading in Cu (In, Ga) Se2.* Thin Solid Films, 2000. **361**: p. 478-481.
65. Dullweber, T., U. Rau, and H. Schock, *A new approach to high-efficiency solar cells by band gap grading in Cu (In, Ga) Se2 chalcopyrite semiconductors.* Solar Energy Materials and Solar Cells, 2001. **67**(1-4): p. 145-150.
66. Li, J., et al., *Cation Substitution in Earth-Abundant Kesterite Photovoltaic Materials.* Advanced Science, 2018. **5**(4): p. 1700744.
67. Simya, O., A. Mahaboobbatcha, and K. Balachander, *Compositional grading of CZTSSe alloy using exponential and uniform grading laws in SCAPS-ID simulation.* Superlattices and Microstructures, 2016. **92**: p. 285-293.
68. Fairbrother, A., et al., *Compositional paradigms in multinary compound systems for photovoltaic applications: a case study of kesterites.* Journal of Materials Chemistry A, 2015. **3**(18): p. 9451-9455.
69. Márquez, J., et al., *Chemistry and Dynamics of Ge in Kesterite: Toward Band-Gap-Graded Absorbers.* Chemistry of Materials, 2017.

70. Giraldo, S., et al., *How small amounts of Ge modify the formation pathways and crystallization of kesterites.* Energy & Environmental Science, 2018. **11**(3): p. 582-593.
71. Platzer-Björkman, C., et al., *Back and front contacts in kesterite solar cells: state-of-the-art and open questions.* Journal of Physics: Energy, 2019. **1**(4): p. 044005.
72. Garcia-Llamas, E., et al., *Cu2ZnSnS4 thin film solar cells grown by fast thermal evaporation and thermal treatment.* Solar Energy, 2017. **141**: p. 236-241.
73. Li, X., et al., *8.6% Efficiency CZTSSe solar cell with atomic layer deposited Zn-Sn-O buffer layer.* Solar Energy Materials and Solar Cells, 2016. **157**: p. 101-107.
74. Stolt, L., et al., *ZnO/CdS/CuInSe2 thin-film solar cells with improved performance.* Applied Physics Letters, 1993. **62**(6): p. 597-599.
75. Holz, J., F. Karg, and H.v. Philipsborn. *The effect of substrate impurities on the electronic conductivity in CIS thin films*. in *Proceedings of the 12th european photovoltaic solar energy conference*. 1994.
76. Nicoara, N., et al., *Direct evidence for grain boundary passivation in Cu (In, Ga) Se 2 solar cells through alkali-fluoride post-deposition treatments.* Nature communications, 2019. **10**(1): p. 1-8.
77. Mule, A., et al., *Effect of different alkali (Li, Na, K, Rb, Cs) metals on Cu2ZnSnSe4 solar cells.* Thin Solid Films, 2017. **633**: p. 156-161.
78. Hsieh, Y.T., et al., *Efficiency enhancement of Cu2ZnSn (S, Se) 4 solar cells via alkali metals doping.* Advanced Energy Materials, 2016. **6**(7): p. 1502386.
79. Altamura, G., M. Wang, and K.-L. Choy, *Influence of alkali metals (Na, Li, Rb) on the performance of electrostatic spray-assisted vapor deposited Cu 2 ZnSn (S, Se) 4 solar cells.* Scientific reports, 2016. **6**: p. 22109.
80. López-Marino, S., et al., *Alkali doping strategies for flexible and light-weight Cu 2 ZnSnSe 4 solar cells.* Journal of Materials Chemistry A, 2016. **4**(5): p. 1895-1907.
81. Haass, S.G., et al., *Complex interplay between absorber composition and alkali doping in high-efficiency kesterite solar cells.* Advanced Energy Materials, 2018. **8**(4): p. 1701760.
82. Zhou, J., et al., *Regulating crystal growth via organic lithium salt additive for efficient Kesterite solar cells.* Nano Energy, 2021. **89**: p. 106405.
83. Xu, X., et al., *Efficient and Composition-Tolerant Kesterite Cu2ZnSn (S, Se) 4 Solar Cells Derived From an In Situ Formed Multifunctional Carbon Framework.* Advanced Energy Materials, 2021: p. 2102298.
84. Gong, Y., et al., *Identifying the origin of the V oc deficit of kesterite solar cells from the two grain growth mechanisms induced by Sn 2+ and Sn 4+ precursors in DMSO solution.* Energy & Environmental Science, 2021. **14**(4): p. 2369-2380.
85. Chen, S., et al., *Intrinsic point defects and complexes in the quaternary kesterite semiconductor Cu_2ZnSnS_4.* Physical Review B (Condensed Matter and Materials Physics), 2010. **81**(24): p. 245204---245204.
86. Chen, S., et al., *Classification of lattice defects in the kesterite Cu2ZnSnS4 and Cu2ZnSnSe4 earth-abundant solar cell absorbers.* Advanced Materials, 2013. **25**(11): p. 1522-1539.
87. Noufi, R., et al., *Electronic properties versus composition of thin films of CuInSe2.* Applied Physics Letters, 1984. **45**(6): p. 668-670.
88. Polizzotti, A., et al., *The state and future prospects of kesterite photovoltaics.* Energy & Environmental Science, 2013. **6**(11): p. 3171-3182.
89. Gunder, R., et al., *Structural characterization of off-stoichiometric kesterite-type Cu 2 ZnGeSe 4 compound semiconductors: from cation distribution to intrinsic point defect density.* CrystEngComm, 2018. **20**(11): p. 1491-1498.

90. Schöppe, P., et al., *Discrepancy between integral and local composition in off-stoichiometric Cu2ZnSnSe4 kesterites: A pitfall for classification.* Applied Physics Letters, 2017. **110**(4): p. 043901.
91. Gurieva, G., et al., *Intrinsic point defects in off-stoichiometric Cu2ZnSnSe4: A neutron diffraction study.* Journal of Applied Physics, 2018. **123**(16): p. 161519.
92. Dudchak, I. and L. Piskach, *Phase equilibria in the Cu2SnSe3–SnSe2–ZnSe system.* Journal of alloys and compounds, 2003. **351**(1-2): p. 145-150.
93. Olekseyuk, I.D., I.V. Dudchak, and L.V. Piskach, *Phase equilibria in the Cu_2S-ZnS-SnS_2 system.* Journal of Alloys and Compounds, 2004. **368**(12): p. 135-143.
94. Romanyuk, Y.E. and O. Parasyuk, *Phase equilibria in the quasi-ternary Cu2Se–ZnSe–GeSe2 system.* Journal of alloys and compounds, 2003. **348**(1-2): p. 195-202.
95. Platzer-Björkman, C., et al., *Influence of precursor sulfur content on film formation and compositional changes in Cu2ZnSnS4 films and solar cells.* Solar Energy Materials and Solar Cells, 2012. **98**: p. 110-117.
96. Siebentritt, S. and S. Schorr, *Kesterites - a challenging material for solar cells.* Progress in Photovoltaics: Research and Applications, 2012. **20**(5): p. 512-519.
97. Nam, D., et al., *Solar conversion efficiency and distribution of ZnS secondary phase in Cu2ZnSnS4 solar cells.* Solar Energy Materials and Solar Cells, 2016. **149**: p. 226-231.
98. Hsu, W.-C., et al., *The effect of Zn excess on kesterite solar cells.* Solar Energy Materials and Solar Cells, 2013. **113**(0): p. 160-164.
99. Delbos, S., *Kësterite thin films for photovoltaics : a review.* EPJ Photovolt., 2012. **3**: p. 35004.
100. Li, W., et al., *The effect of ZnS segregation on Zn-rich CZTS thin film solar cells.* Journal of Alloys and Compounds, 2015. **632**: p. 178-184.
101. Wang, W., et al., *The effects of SnS 2 secondary phases on Cu 2 ZnSnS 4 solar cells: a promising mechanical exfoliation method for its removal.* Journal of Materials Chemistry A, 2018. **6**(7): p. 2995-3004.
102. Chen, G., et al., *Formation mechanism of secondary phases in Cu2ZnSnS4 growth under different copper content.* Materials Letters, 2017. **186**: p. 98-101.
103. Scragg, J.J., et al., *A detrimental reaction at the molybdenum back contact in Cu2ZnSn (S, Se) 4 thin-film solar cells.* Journal of the American Chemical Society, 2012. **134**(47): p. 19330-19333.
104. Li, W., et al., *Inhibiting MoS2 formation by introducing a ZnO intermediate layer for Cu2ZnSnS4 solar cells.* Materials Letters, 2014. **130**: p. 87-90.
105. Chelvanathan, P., et al., *Effects of transition metal dichalcogenide molybdenum disulfide layer formation in copper–zinc–tin–sulfur solar cells from numerical analysis.* Japanese Journal of Applied Physics, 2012. **51**(10S): p. 10NC32.
106. Scragg, J.J., et al., *Cu–Zn disorder and band gap fluctuations in Cu2ZnSn (S, Se) 4: Theoretical and experimental investigations.* physica status solidi (b), 2016. **253**(2): p. 247-254.
107. Bishop, D.M., et al., *Modification of defects and potential fluctuations in slow-cooled and quenched Cu2ZnSnSe4 single crystals.* Journal of Applied Physics, 2017. **121**(6): p. 065704.
108. Valakh, M.Y., et al., *Raman scattering and disorder effect in Cu2ZnSnS4.* physica status solidi (RRL)–Rapid Research Letters, 2013. **7**(4): p. 258-261.
109. Scragg, J.J., et al., *A low-temperature order-disorder transition in Cu2ZnSnS4 thin films.* Applied Physics Letters, 2014. **104**(4): p. 041911.
110. Többens, D.M., et al., *Temperature dependency of Cu/Zn ordering in CZTSe kesterites determined by anomalous diffraction.* physica status solidi (b), 2016. **253**(10): p. 1890-1897.

111. Gurieva, G., et al., *Cu-Zn disorder in Cu2ZnGeSe4: A complementary neutron diffraction and Raman spectroscopy study.* Journal of Physics and Chemistry of Solids, 2016. **99**: p. 100-104.
112. Giraldo, S., et al., *Large efficiency improvement in Cu2ZnSnSe4 solar cells by introducing a superficial Ge nanolayer.* Advanced Energy Materials, 2015. **5**(21): p. 1501070.
113. Collord, A. and H. Hillhouse, *Germanium alloyed kesterite solar cells with low voltage deficits.* Chemistry of Materials, 2016. **28**(7): p. 2067-2073.
114. Bhaskar, P.U., et al., *Preparation and characterization of co-evaporated Cu2ZnGeSe4 thin films.* Thin Solid Films, 2013. **534**: p. 249-254.
115. León, M., et al., *Spectroscopic ellipsometry study of Cu2ZnGeSe4 and Cu2ZnSiSe4 poly-crystals.* Materials Chemistry and Physics, 2013. **141**(1): p. 58-62.
116. León, M., et al., *Optical constants of Cu 2 ZnGeS 4 bulk crystals.* Journal of Applied Physics, 2010. **108**(9): p. 093502.
117. Tsuji, K., T. Maeda, and T. Wada, *Optical properties and electronic structures of Cu2ZnSnS4, Cu2ZnGeS4, and Cu2Zn (Ge, Sn) S4 and Cu2Zn (Ge, Sn) Se4 solid solutions.* Japanese Journal of Applied Physics, 2018. **57**(8S3): p. 08RC21.
118. Geisz, J.F., et al., *Six-junction III–V solar cells with 47.1% conversion efficiency under 143 Suns concentration.* Nature Energy, 2020. **5**(4): p. 326-335.
119. Yang, H., et al., *Nontoxic and abundant copper zinc tin sulfide nanocrystals for potential high-temperature thermoelectric energy harvesting.* Nano letters, 2012. **12**(2): p. 540-545.
120. Fan, F.J., et al., *Large-Scale Colloidal Synthesis of Non-Stoichiometric Cu2ZnSnSe4 Nanocrystals for Thermoelectric Applications.* Advanced Materials, 2012. **24**(46): p. 6158-6163.
121. Ibáñez, M., et al., *Cu2ZnGeSe4 nanocrystals: synthesis and thermoelectric properties.* Journal of the American Chemical Society, 2012. **134**(9): p. 4060-4063.
122. Seebeck, T.J., *Ueber die magnetische Polarisation der Metalle und Erze durch Temperaturdifferenz.* Annalen der Physik, 1826. **82**(3): p. 253-286.
123. Peltier, J.C., *Nouvelles expériences sur la caloricité des courants électrique.* Ann. Chim. Phys, 1834. **56**(371): p. 371-386.
124. Gupta, M.P., et al., *Ultrathin thermoelectric devices for on-chip Peltier cooling.* IEEE Transactions on Components, Packaging and Manufacturing Technology, 2011. **1**(9): p. 1395-1405.
125. Hisatomi, T., J. Kubota, and K. Domen, *Recent advances in semiconductors for photocatalytic and photoelectrochemical water splitting.* Chemical Society Reviews, 2014. **43**(22): p. 7520-7535.
126. Roberts, G.G., S. Tutihasi, and R.C. Keezer, *Optical absorption edge of trigonal selenium.* Physical Review, 1968. **166**(3): p. 637.
127. Stearns, R.I., *Band Gap of Boron Phosphide.* Journal of Applied Physics, 1965. **36**(1): p. 330-331.
128. Mead, C. and W. Spitzer, *Conduction band minima in AlAs and AlSb.* Physical Review Letters, 1963. **11**(8): p. 358.
129. Lorenz, M., G. Pettit, and R. Taylor, *Band gap of gallium phosphide from 0 to 900 K and light emission from diodes at high temperatures.* Physical Review, 1968. **171**(3): p. 876.
130. Larach, S., R. Shrader, and C. Stocker, *Anomalous variation of band gap with composition in zinc sulfo-and seleno-tellurides.* Physical Review, 1957. **108**(3): p. 587.
131. Rao, K.P., et al., *Characterization of two-source evaporated cadmium zinc telluride thin films.* Optical Materials, 1996. **5**(1-2): p. 63-68.

132. El Allali, M., et al., *Experimental determination of the GaAs and Ga 1− x Al x As band-gap energy dependence on temperature and aluminum mole fraction in the direct band-gap region.* Physical Review B, 1993. **48**(7): p. 4398.
133. White, A., et al., *Applications of photoluminescence excitation spectroscopy to the study of indium gallium phosphide alloys.* Journal of Physics D: Applied Physics, 1970. **3**(9): p. 1322.
134. Hinzer, K., et al., *Room temperature operation of AlInAs/AlGaAs quantum dot lasers.* Physica E: Low-dimensional Systems and Nanostructures, 1998. **2**(1-4): p. 729-733.
135. Matsushita, H., et al., *Thermal analysis and synthesis from the melts of Cu-based quaternary compounds Cu–III–IV–VI4 and Cu2–II–IV–VI4 (II= Zn, Cd; III= Ga, In; IV= Ge, Sn; VI= Se).* Journal of Crystal Growth, 2000. **208**(1-4): p. 416-422.
136. Parasyuk, O., et al., *Phase diagram of the Cu2GeSe3–ZnSe system and crystal structure of the Cu2ZnGeSe4 compound.* Journal of alloys and compounds, 2001. **329**(1-2): p. 202-207.
137. Olekseyuk, I., I. Dudchak, and L. Piskach, *Phase equilibria in the Cu2S–ZnS–SnS2 system.* Journal of alloys and compounds, 2004. **368**(1-2): p. 135-143.
138. Moh, G.H., *Tin-containing mineral systems, part II: phase relations and mineral assemblages in the Cu-Fe-Zn-Sn-S system.* Chem. Erde, 1975. **34**: p. 1-61.
139. Hall, S.R., J.T. Szymanski, and J.M. Stewart, *Kesterite, $Cu_2(Zn,Fe)SnS_4$, and stannite, $Cu_2(Fe,Zn)SnS_4$, structurally similar but distinct minerals.* The Canadian Mineralogist, 1978. **16**(2): p. 131-137.
140. Brockway, L., *The crystal structure of stannite, Cu2FeSnS4.* Zeitschrift für Kristallographie-Crystalline Materials, 1934. **89**(1-6): p. 434-441.
141. Olekseyuk, I., et al., *Single crystal preparation and crystal structure of the Cu2Zn/Cd, Hg/SnSe4 compounds.* Journal of Alloys and Compounds, 2002. **340**(1-2): p. 141-145.
142. Hahn, H. and H. Schulze, *Über quaternäre chalkogenide des germaniums und zinns.* Naturwissenschaften, 1965. **52**(14): p. 426-426.
143. Nitsche, R., D. Sargent, and P. Wild, *Crystal growth of quaternary 122464 chalcogenides by iodine vapor transport.* Journal of Crystal Growth, 1967. **1**(1): p. 52-53.
144. Schorr, S., *The crystal structure of kesterite type compounds: A neutron and X-ray diffraction study.* Solar Energy Materials and Solar Cells, 2011. **95**(6): p. 1482-1488.
145. Chen, S., et al., *Electronic structure and stability of quaternary chalcogenide semiconductors derived from cation cross-substitution of II-VI and I-III-VI 2 compounds.* Physical Review B, 2009. **79**(16): p. 165211.
146. Shannon, R., *Bond distances in sulfides and a preliminary table of sulfide crystal radii.* Structure and bonding in crystals, 1981. **2**: p. 53-70.
147. Rey, G., et al., *The band gap of Cu2ZnSnSe4: Effect of order-disorder.* Applied Physics Letters, 2014. **105**(11): p. 112106.
148. Többens, D.M., et al., *Quantitative anomalous powder diffraction analysis of cation disorder in kesterite semiconductors.* Powder Diffraction, 2016. **31**(3): p. 168-175.
149. Schorr, S. and G. Gonzalez-Aviles, *In-situ investigation of the structural phase transition in kesterite.* Physica Status Solidi A, 2009. **206**(5): p. 1054-1058.
150. Kühn, G. and H. Neumann, *AIBIIICVI2-Halbleiter mit Chalcopyritstruktur.* Zeitschrift für Chemie, 1987. **27**(6): p. 197-206.
151. Hull, W. and W. Bragg, *Structure of some Crystals.* Proc. R. Soc. London Ser. A, 1913. **33**: p. 277-277.
152. Gerlach, W.v., *Das K α Dublett, nebst einer Neube-stimmung der Gitterckonstanten einiger Kristalle.* Phys. Zeit. XXIII, 1922: p. 114-129.

153. Aminoff, G., *XI. Untersuchungen über die Kristallstrukturen von Wurtzit und Rotnickelkies.* Zeitschrift für Kristallographie-Crystalline Materials, 1923. **58**(1-6): p. 203-219.
154. Sachanyuk, V., I. Olekseyuk, and O. Parasyuk, *X-ray powder diffraction study of the Cu2Cd1–xMnxSnSe4 alloys.* physica status solidi (a), 2006. **203**(3): p. 459-465.
155. Gulay, L., O. Nazarchuk, and I. Olekseyuk, *Crystal structures of the compounds Cu2CoSi (Ge, Sn) S4 and Cu2CoGe (Sn) Se4.* Journal of alloys and compounds, 2004. **377**(1-2): p. 306-311.
156. Bragg, W.L. and E.J. Williams, *The Effect of Thermal Agitation on Atomic Arrangement in Alloys.* Proceedings of the Royal Society of London. Series A, 1934. **145**(855): p. 699-730.
157. Stephan, C., et al., *Comprehensive insights into point defect and defect cluster formation in CuInSe 2.* Applied Physics Letters, 2011. **98**(9): p. 091906.
158. Nishihara, H., T. Maeda, and T. Wada, *First-principles study of defect formation in a photovoltaic semiconductor Cu2ZnGeSe4.* Japanese Journal of Applied Physics, 2018. **57**(2S2): p. 02CE06.
159. Reed, S.J.B., *Electron microprobe analysis and scanning electron microscopy in geology*. 2005: Cambridge university press.
160. Brentano, J., *Focussing method of crystal powder analysis by X-rays.* Proceedings of the Physical Society of London, 1924. **37**(1): p. 184.
161. Friedrich, W., P. Knipping, and M. Laue, *Interferenzerscheinungen bei roentgenstrahlen.* Annalen der Physik, 1913. **346**(10): p. 971-988.
162. Bragg, W.H. and W.L. Bragg, *The reflection of X-rays by crystals.* Proceedings of the Royal Society of London. Series A, Containing Papers of a Mathematical and Physical Character, 1913. **88**(605): p. 428-438.
163. Spieß, L., et al., *Moderne Röntgenbeugung: Röntgendiffraktometrie für Materialwissenschaftler, Physiker und Chemiker*. 2009: Vieweg+Teubner Verlag. 564-564.
164. Debye, P., *Interferenz von röntgenstrahlen und wärmebewegung.* Annalen der Physik, 1913. **348**(1): p. 49-92.
165. Waller, I., *Zur frage der einwirkung der wärmebewegung auf die interferenz von röntgenstrahlen.* Zeitschrift für Physik, 1923. **17**(1): p. 398-408.
166. Bryan, R., *International tables for crystallography. Vol. C. Mathematical, physical and chemical tables edited by AJC Wilson*. 1993, International Union of Crystallography.
167. Sears, V.F., *Neutron scattering lengths and cross sections.* Neutron news, 1992. **3**(3): p. 26-37.
168. Franz, A. and A. Hoser, *E9: The Fine Resolution Powder Diffractometer (FIREPOD) at BER II.* Journal of large-scale research facilities JLSRF, 2017. **3**: p. 103.
169. Carvajal, J.R., *Recent developments of the program FULLPROF, in commission on powder diffraction (IUCr).* Newsletter, 2001. **26**: p. 12-19.
170. Rodriguez-Carvajal, J. and T. Roisnel. *WinPLOTR: A windows tool for powder diffraction pattern analysis*. in *Mater. Sci. Forum, ed. R. Delhez, EJ Mittemeijer, Proceedings of the Seventh European Powder Diffraction Conference, Barcelona, Spain*. 2000.
171. Young, R.A., *The Rietveld Method*. 1995: Oxford University Press.
172. Caglioti, G., A. Paoletti, and F.P. Ricci, *Choice of collimators for a crystal spectrometer for neutron diffraction.* Nuclear Instruments, 1958. **3**(4): p. 223-228.
173. Thompson, P., D. Cox, and J. Hastings, *Rietveld refinement of Debye-Scherrer synchrotron X-ray data from Al2O3.* Journal of Applied Crystallography, 1987. **20**(2): p. 79-83.
174. Stokes, A. and A. Wilson, *The diffraction of X rays by distorted crystal aggregates-I.* Proceedings of the Physical Society, 1944. **56**(3): p. 174.

175. Rodriguez-Carvajal, J., M. Fernandez-Diaz, and J. Martinez, *Neutron diffraction study on structural and magnetic properties of La2NiO4.* Journal of Physics: Condensed Matter, 1991. **3**(19): p. 3215.
176. Stephens, P.W., *Phenomenological model of anisotropic peak broadening in powder diffraction.* Journal of Applied Crystallography, 1999. **32**(2): p. 281-289.
177. Scherrer, P., *Estimation of the size and internal structure of colloidal particles using X-rays.* Nachr. Ges. Wiss. Göttingen, 1918. **2**: p. 96-100.
178. Finger, L.W., D.E. Cox, and A.P. Jephcoat, *A correction for powder diffraction peak asymmetry due to axial divergence.* Journal of Applied Crystallography, 1994. **27**(6): p. 892-900.
179. Dollase, W., *Correction of intensities for preferred orientation in powder diffractometry: application of the March model.* Journal of Applied Crystallography, 1986. **19**(4): p. 267-272.
180. Tauc, J., *Optical properties and electronic structure of amorphous Ge and Si.* Materials Research Bulletin, 1968. **3**(1): p. 37-46.
181. Ross, L. and M. Bourgon, *The germanium–selenium phase diagram.* Canadian Journal of Chemistry, 1969. **47**(14): p. 2555-2559.
182. Redinger, A., et al., *The consequences of kesterite equilibria for efficient solar cells.* Journal of the American Chemical Society, 2011. **133**(10): p. 3320-3323.
183. Scragg, J.J., et al., *Chemical insights into the instability of Cu2ZnSnS4 films during annealing.* Chemistry of Materials, 2011. **23**(20): p. 4625-4633.
184. Chen, S., et al., *Classification of Lattice Defects in the Kesterite Cu2ZnSnS4 and Cu2ZnSnSe4 Earth-Abundant Solar Cell Absorbers.* Advanced Materials, 2013. **25**(11): p. 1522-1539.
185. Márquez, J., et al., *Systematic compositional changes and their influence on lattice and optoelectronic properties of Cu 2 ZnSnSe 4 kesterite solar cells.* Solar Energy Materials and Solar Cells, 2016. **144**: p. 579-585.
186. Choubrac, L., et al., *7.6% CZGSe solar cells thanks to optimized CdS chemical bath deposition.* physica status solidi (a), 2018. **215**(13): p. 1800043.
187. Ritscher, A., M. Hoelzel, and M. Lerch, *The order-disorder transition in Cu2ZnSnS4–A neutron scattering investigation.* Journal of Solid State Chemistry, 2016. **238**: p. 68-73.
188. Grossberg, M., et al., *Radiative recombination in Cu2ZnSnSe4 monograins studied by photoluminescence spectroscopy.* Thin Solid Films, 2009. **517**(7): p. 2489-2492.
189. Malerba, C., et al., *CZTS stoichiometry effects on the band gap energy.* Journal of alloys and compounds, 2014. **582**: p. 528-534.
190. Dolgonos, A., T.O. Mason, and K.R. Poeppelmeier, *Direct optical band gap measurement in polycrystalline semiconductors: A critical look at the Tauc method.* Journal of solid state chemistry, 2016. **240**: p. 43-48.

Acknowledgment

Above all, I would like to express my deep gratitude to my supervisor Prof. Dr. Susan Schorr for her patience, trust and unconditional support through all stages of my academic degrees. Thanks to her strong encouragement this Ph.D. thesis could eventually be successfully conducted and completed. I am particularly grateful for the opportunity to pursue scientific issues hitting the spirit of the time and that are of pressing relevance to society. The high degree of self-determination as well as the professional and well-organized working environment are to be especially acknowledged.

I would also like to thank PD Dr. Ralf Milke who has mainly aroused my enthusiasm for mineralogy and which finally determined the academic path taken by me. Another strong appreciation is devoted to his valuable technical support at the electron probe microanalyzer which was key for my Ph.D. studies. Moreover, I am particularly thankful for his unresting support during my studies and his exceptional commitment regardless of the issue. Lastly, I would like to express my sincere gratitude to him for kindly agreeing to be my second supervisor.

In addition, I want to thank Dr. Moritz Liesegang for also supporting and advising me at the electron probe microanalyzer. A special thank is devoted to Mrs. Christiane Behr for preparing the numerous samples measured with the electron microanalyzer system. Finally, I want to thank all my colleagues in the department Structure and Dynamics of Energy Materials at Helmholtz-Zentrum Berlin for their support, fruitful discussions, and helpful contributions, namely Dr. Alexandra Franz and Dr. Galina Gurieva specifically for their assistance during the neutron diffraction experiments as well as for the valuable and critical scientific discussions, Dr. Daniel M. Toebbens for his all-time willingness to share his knowledge regarding structure refinement and handling of the used refinement program. Further I want to acknowledge the SEM and EDX analysis carried out by Dr. Stefan Zander. Last but not least I would like to thank all my fellow Ph.D. students, particularly Kai, Elisa and Julien, for an enjoyable time and their mutual support.

Appendix

A.1 Rietveld Refinements of Neutron Diffraction Data

Sample A0000-1: $Cu_{2.24}Zn_{1.01}Ge_{0.93}Se_4$

Cu/(Zn+Ge) = 1.153, Zn/Ge = 1.083

29% F-type (0% F(1)/29% F(2)), 71% I-type

Included phases: $Cu_2ZnGeSe_4$ (s.g. $I\bar{4}$), ZnSe (s.g. $F\bar{4}3m$)

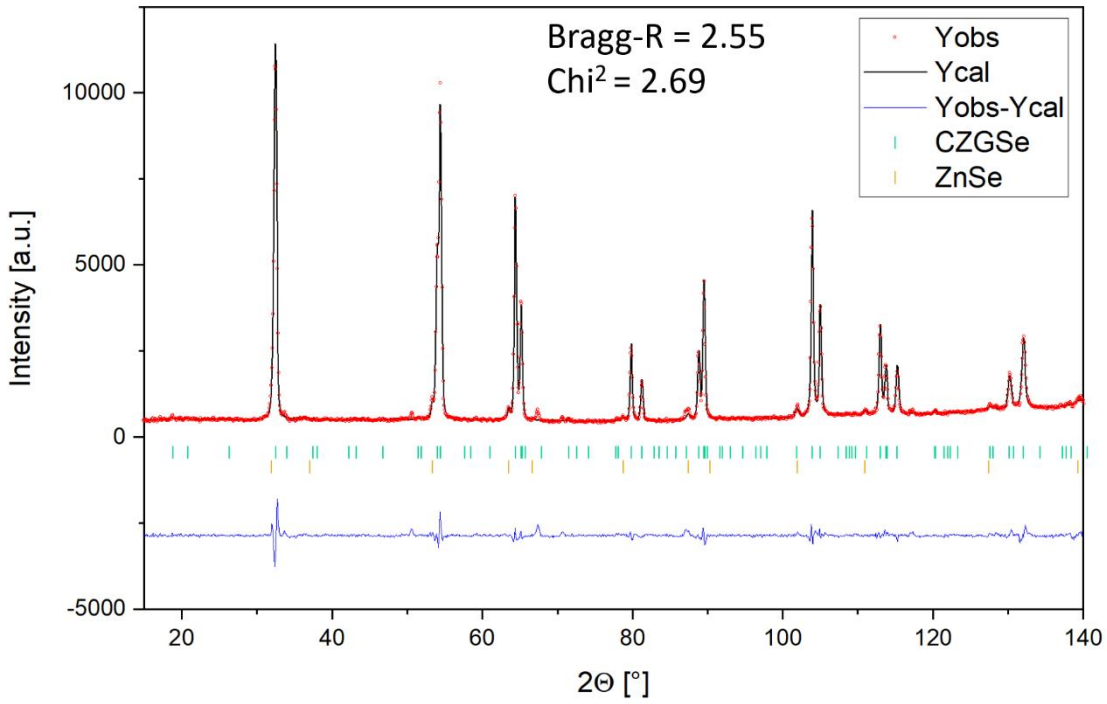

Figure A.1 - 1 Refined profile of neutron diffraction data of sample A0000-1.

Refined OCCs (CZGSe): Cu 2a = 1.014 (37)

Cu 2c = 0.950 (22)

Zn 2d = 1.092 (29)

Ge 2b = 0.997 (30)

Sample A0015-1: $Cu_{2.20}Zn_{1.04}Ge_{0.93}Se_4$

Cu/(Zn+Ge) = 1.120, Zn/Ge = 1.119

71% F-type (0% F(1)/71% F(2)), 29% I-type

Included phases: $Cu_2ZnGeSe_4$ (s.g. $I\bar{4}$), ZnSe (s.g. $F\bar{4}3m$)

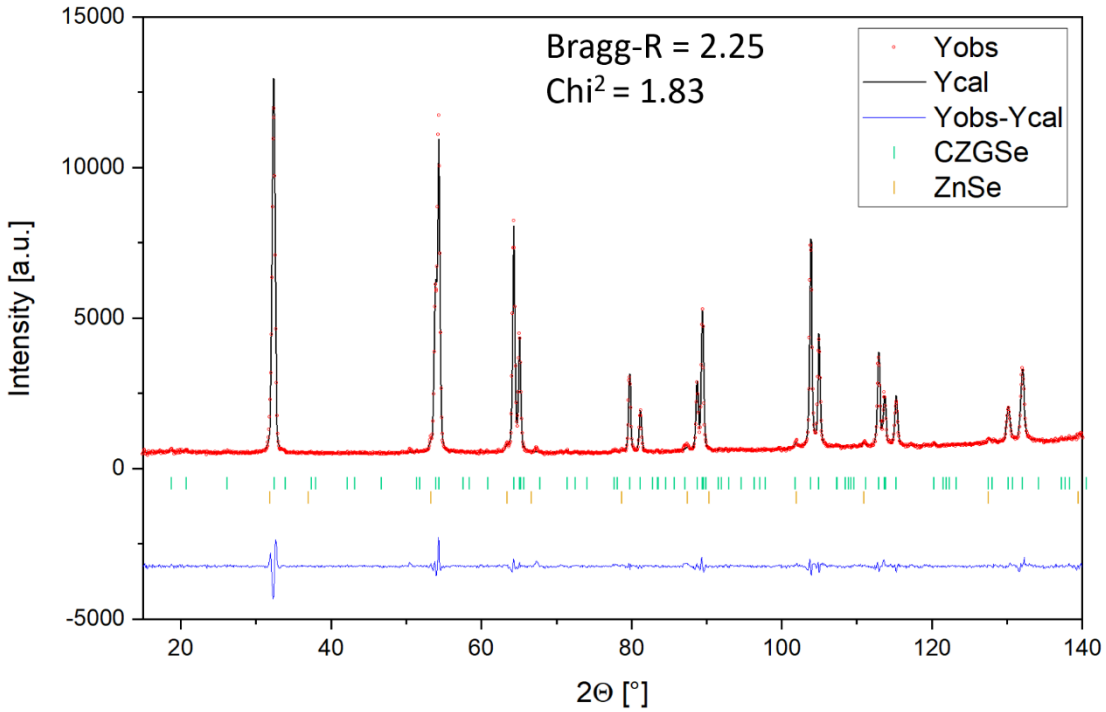

Figure A.1 - 2 Refined profile of neutron diffraction data of sample A0015-1.

Refined OCCs (CZGSe): Cu 2a = 1.011 (24)

Cu 2c = 0.972 (20)

Zn 2d = 1.055 (26)

Ge 2b = 0.995 (16)

Sample A0040-1: $Cu_{2.18}Zn_{1.04}Ge_{0.94}Se_4$

Cu/(Zn+Ge) = 1.107, Zn/Ge = 1.105

72% F-type (0% F(1)/72% F(2)), 28% I-type

Included phases: $Cu_2ZnGeSe_4$ (s.g. $I\bar{4}$), Ge (s.g. $Fd\bar{3}m$)

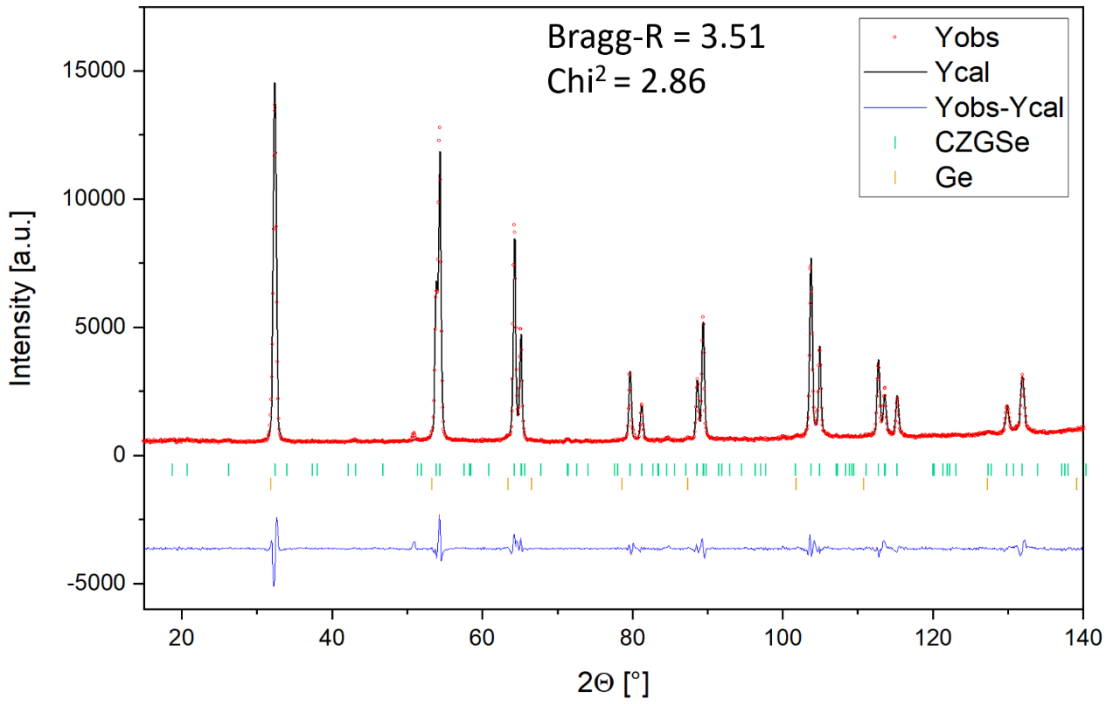

Figure A.1 - 3 Refined profile of neutron diffraction data of sample A0040-1.

Refined OCCs (CZGSe): Cu 2a = 0.990 (28)

Cu 2c = 0.952 (25)

Zn 2d = 1.038 (36)

Ge 2b = 1.007 (24)

Sample A0075-1: $Cu_{2.05}Zn_{1.14}Ge_{0.92}Se_4$

Cu/(Zn+Ge) = 1.000, Zn/Ge = 1.242

25% F-type (25% F(1)/0% F(2)), 75% G-type

Included phases: $Cu_2ZnGeSe_4$ (s.g. $I\bar{4}$), ZnSe (s.g. $F\bar{4}3m$)

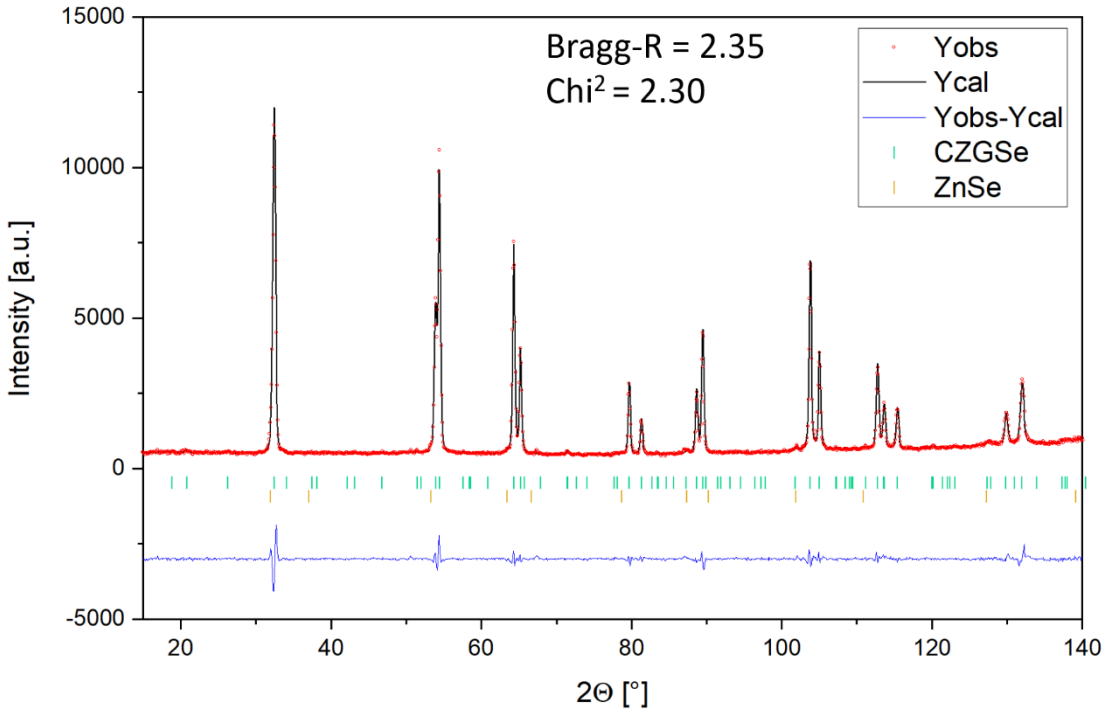

Figure A.1 - 4 Refined profile of neutron diffraction data of sample A0075-1.

Refined OCCs (CZGSe): Cu 2a = 1.019 (34)

Cu 2c = 0.990 (23)

Zn 2d = 1.059 (32)

Ge 2b = 0.974 (24)

Sample A0125-1: $Cu_{2.01}Zn_{1.13}Ge_{0.94}Se_4$

Cu/(Zn+Ge) = 0.973, Zn/Ge = 1.201

2% F-type (2% F(1)/0% F(2)), 98% G-type

Included phases: $Cu_2ZnGeSe_4$ (s.g. $I\bar{4}$)

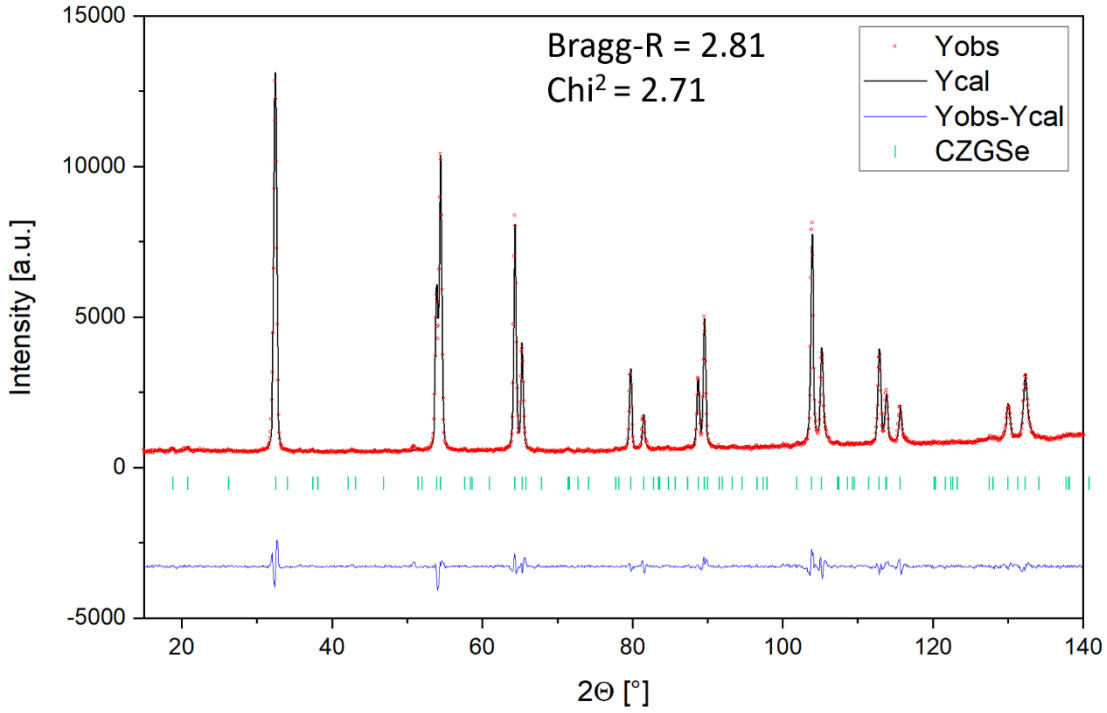

Figure A.1 - 5 Refined profile of neutron diffraction data of sample A0125-1.

Refined OCCs (CZGSe): Cu 2a = 1.020 (25)

Cu 2c = 0.966 (18)

Zn 2d = 1.009 (23)

Ge 2b = 0.993 (16)

Sample A0200-1: $Cu_{1.82}Zn_{1.24}Ge_{0.93}Se_4$

Cu/(Zn+Ge) = 0.840, Zn/Ge = 1.333

6% A-type, 94% B-type

Included phases: $Cu_2ZnGeSe_4$ (s.g. $I\bar{4}$), Ge (s.g. $Fd\bar{3}m$)

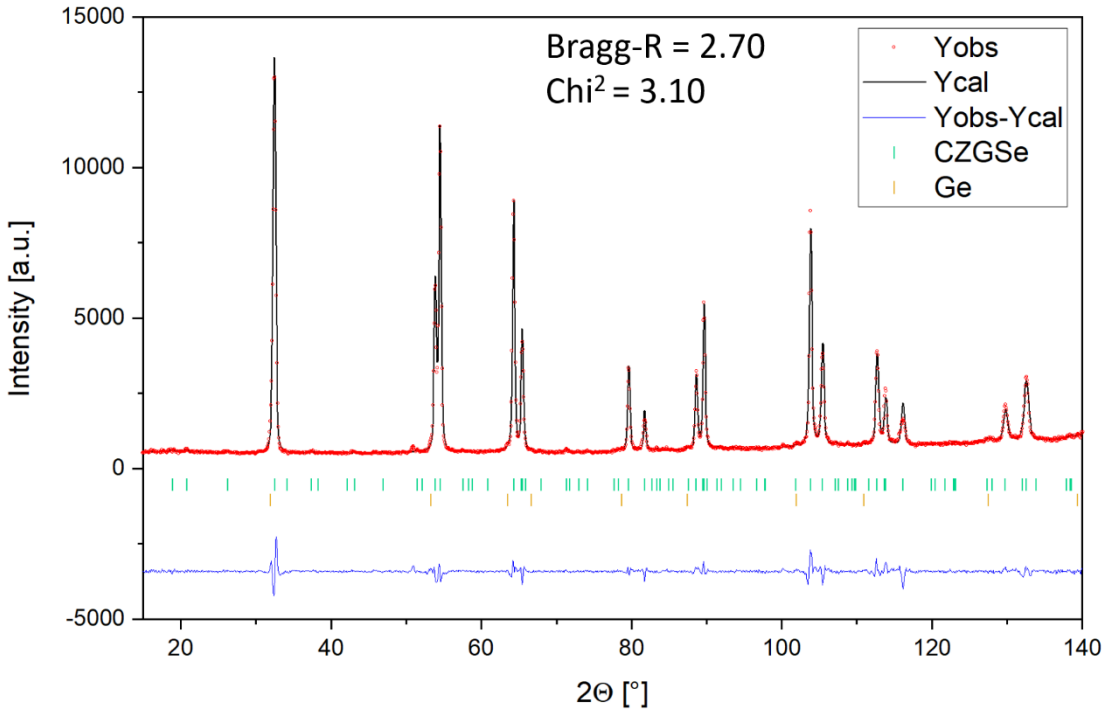

Figure A.1 - 6 Refined profile of neutron diffraction data of sample A0200-1.

Refined OCCs (CZGSe): Cu 2a = 0.944 (40)

Cu 2c = 0.924 (38)

Zn 2d = 0.999 (50)

Ge 2b = 0.981 (29)

Sample A0000-2: $Cu_{2.20}Zn_{1.08}Ge_{0.91}Se_4$

Cu/(Zn+Ge) = 1.105, Zn/Ge = 1.189

95% F-type (7% F(1)/88% F(2)), 5% I-type

Included phases: $Cu_2ZnGeSe_4$ (s.g. $I\bar{4}$), Ge (s.g. $Fd\bar{3}m$), ZnSe (s.g. $F\bar{4}3m$)

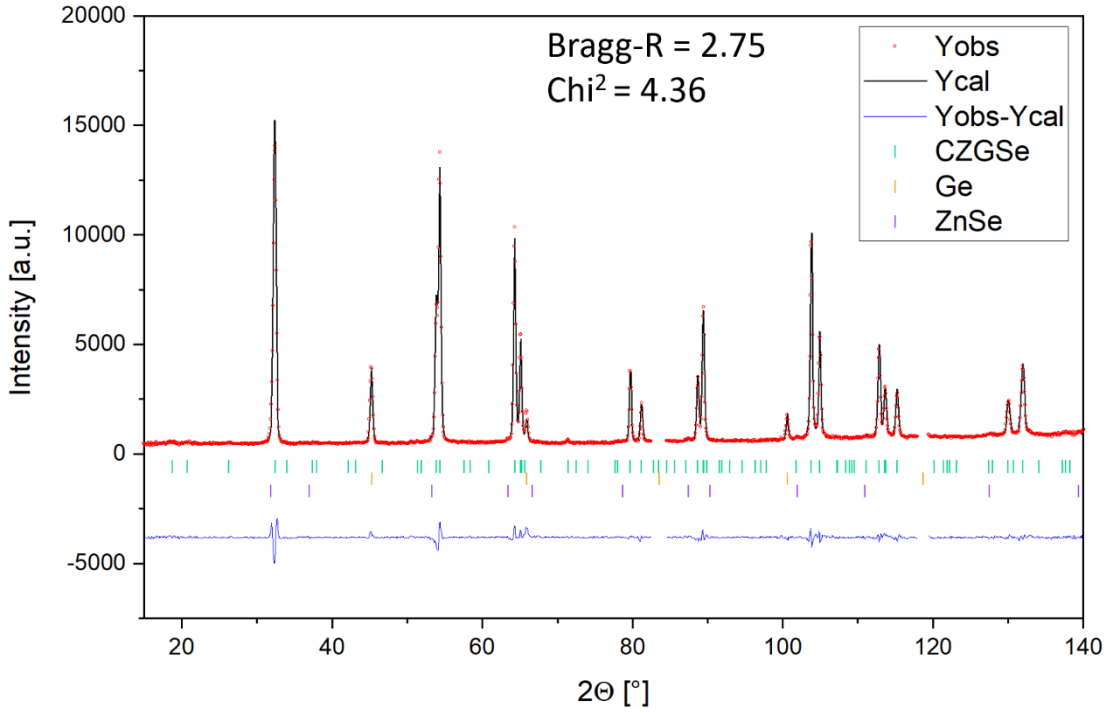

Figure A.1 - 7 Refined profile of neutron diffraction data of sample A0000-2.

Refined OCCs (CZGSe): Cu 2a = 0.992 (28)

Cu 2c = 0.934 (29)

Zn 2d = 1.034 (38)

Ge 2b = 1.008 (20)

Sample A0015-2: $Cu_{2.19}Zn_{1.09}Ge_{0.91}Se_4$

Cu/(Zn+Ge) = 1.096, Zn/Ge = 1.197

98% F-type (14% F(1)/84% F(2)), 2% I-type

Included phases: $Cu_2ZnGeSe_4$ (s.g. $I\bar{4}$), ZnSe (s.g. $F\bar{4}3m$)

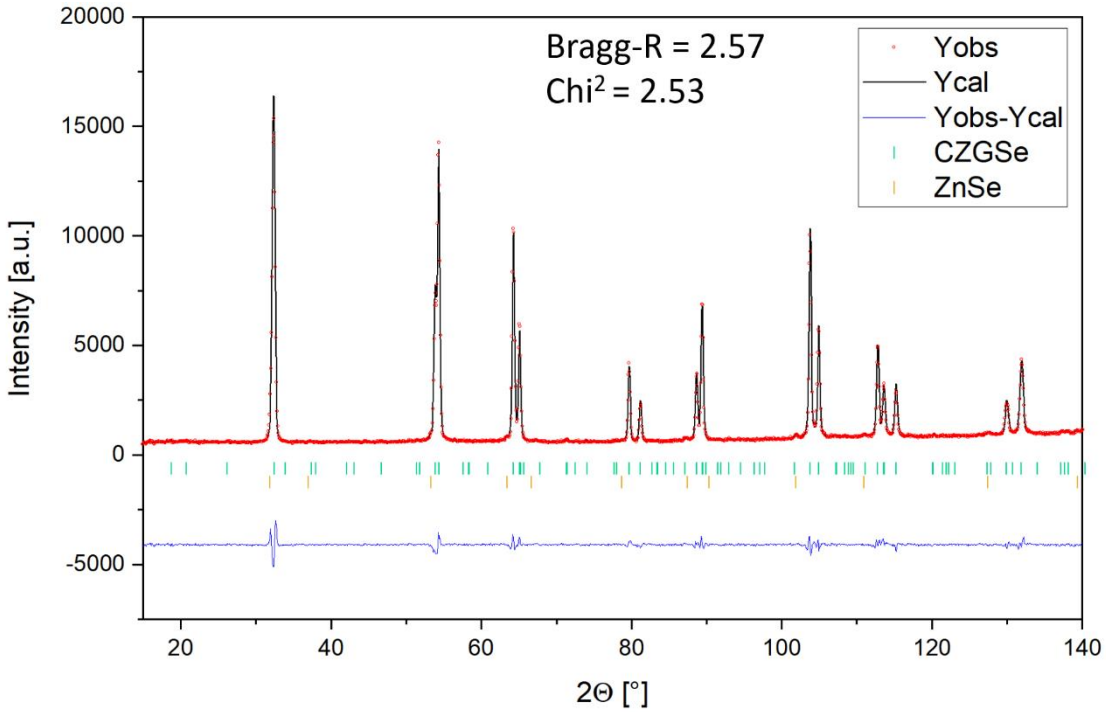

Figure A.1 - 8 Refined profile of neutron diffraction data of sample A0015-2.

Refined OCCs (CZGSe): Cu 2a = 0.987 (32)

Cu 2c = 0.941 (34)

Zn 2d = 1.103 (48)

Ge 2b = 0.998 (23)

Sample A0040-2: $Cu_{2.12}Zn_{1.13}Ge_{0.91}Se_4$

Cu/(Zn+Ge) = 1.045, Zn/Ge = 1.240

56% F-type (29% F(1)/27% F(2)), 44% G-type

Included phases: $Cu_2ZnGeSe_4$ (s.g. $I\bar{4}$), ZnSe (s.g. $F\bar{4}3m$)

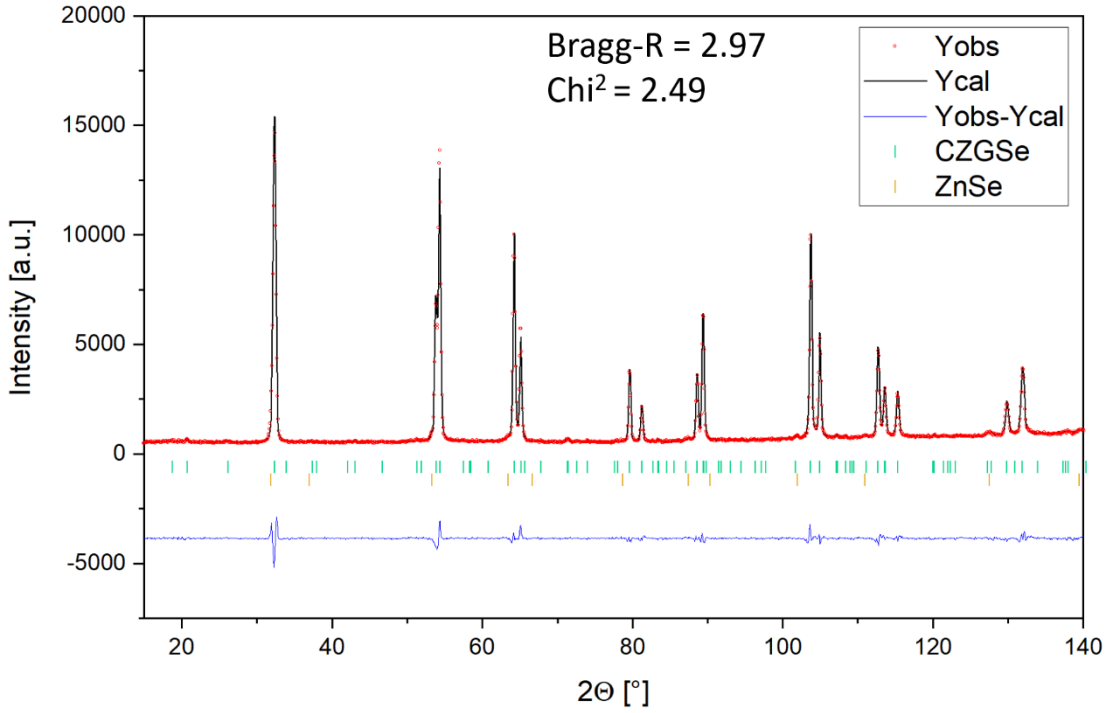

Figure A.1 - 9 Refined profile of neutron diffraction data of sample A0040-2.

Refined OCCs (CZGSe): Cu 2a = 0.981 (29)

Cu 2c = 0.952 (31)

Zn 2d = 1.042 (43)

Ge 2b = 0.990 (27)

Sample A0075-2: $Cu_{2.06}Zn_{1.16}Ge_{0.91}Se_4$

Cu/(Zn+Ge) = 0.999, Zn/Ge = 1.282

24% F-type (24% F(1)/0% F(2)), 76% G-type

Included phases: $Cu_2ZnGeSe_4$ (s.g. $I\bar{4}$), ZnSe (s.g. $F\bar{4}3m$)

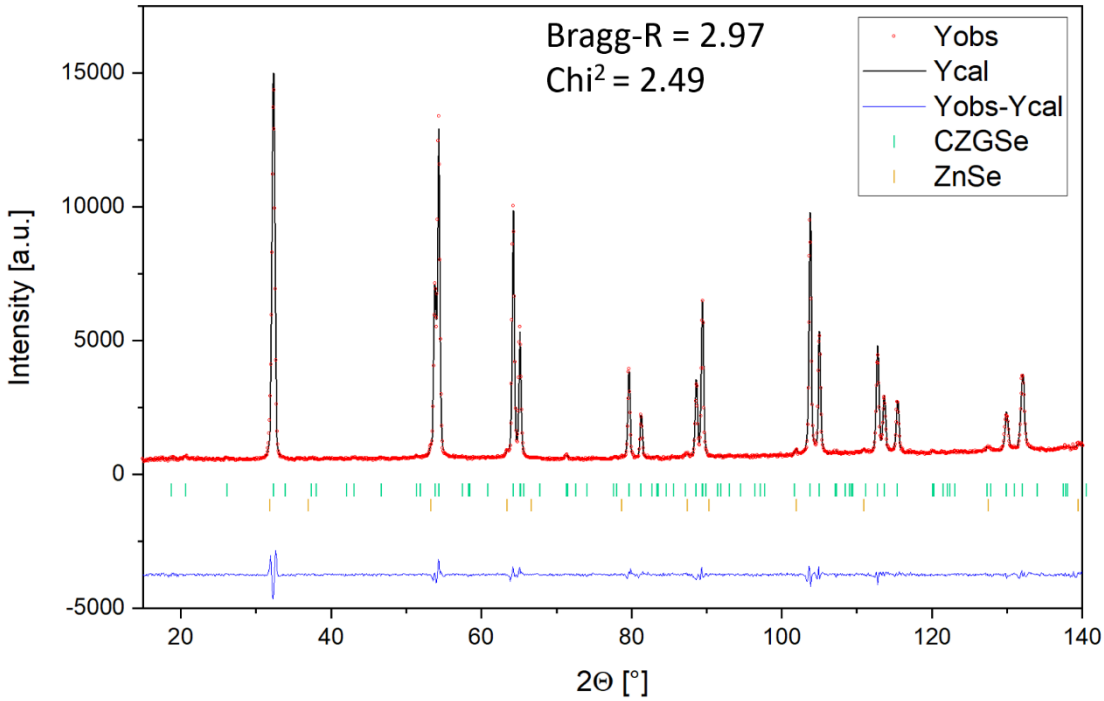

Figure A.1 - 10 Refined profile of neutron diffraction data of sample A0075-2.

Refined OCCs (CZGSe): Cu 2a = 0.997 (40)

Cu 2c = 0.981 (28)

Zn 2d = 1.050 (37)

Ge 2b = 0.965 (37)

Sample A0125-2: $Cu_{1.95}Zn_{1.22}Ge_{0.90}Se_4$

Cu/(Zn+Ge) = 0.921, Zn/Ge = 1.354

29% B-type, 71% G-type

Included phases: $Cu_2ZnGeSe_4$ (s.g. $I\bar{4}$), ZnSe (s.g. $F\bar{4}3m$)

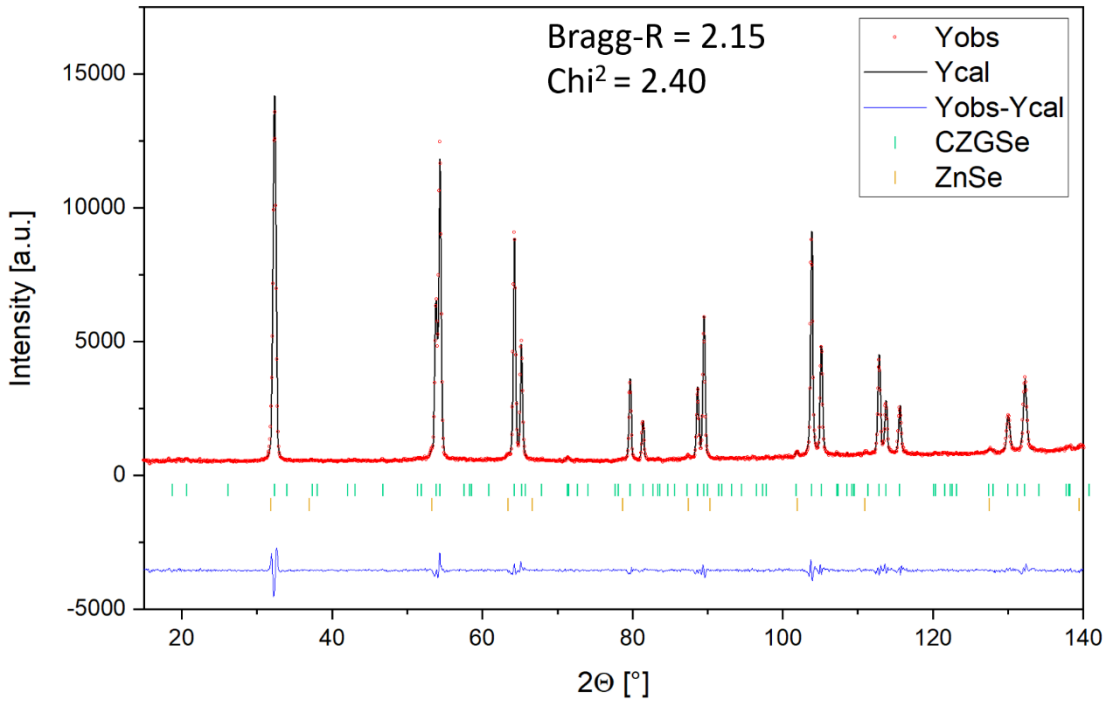

Figure A.1 - 11 Refined profile of neutron diffraction data of sample A0125-2.

Refined OCCs (CZGSe): Cu 2a = 0.978 (28)

Cu 2c = 0.960 (29)

Zn 2d = 1.061 (40)

Ge 2b = 0.950 (25)

Sample A0200-2: $Cu_{1.91}Zn_{1.25}Ge_{0.90}Se_4$

Cu/(Zn+Ge) = 0.888, Zn/Ge = 1.392

53% B-type, 47% G-type

Included phases: $Cu_2ZnGeSe_4$ (s.g. $I\bar{4}$), ZnSe (s.g. $F\bar{4}3m$)

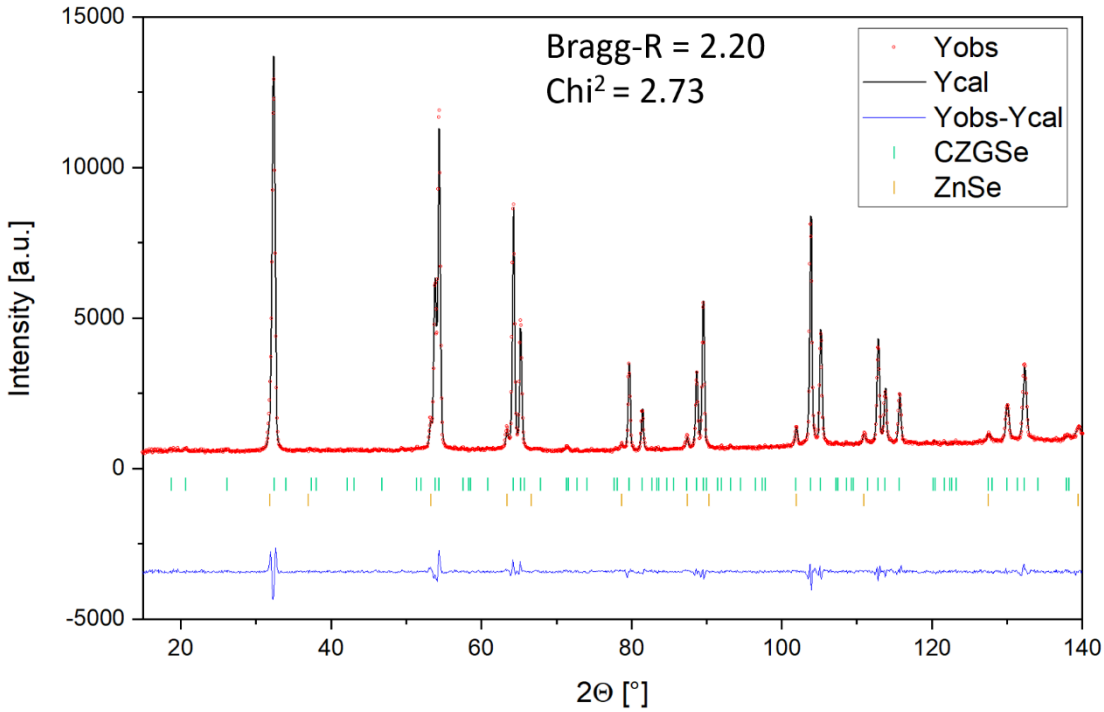

Figure A.1 - 12 Refined profile of neutron diffraction data of sample A0200-2.

Refined OCCs (CZGSe): Cu 2a = 0.984 (28)

Cu 2c = 0.959 (33)

Zn 2d = 1.057 (46)

Ge 2b = 0.995 (24)

Sample B0000-1: $Cu_{2.18}Zn_{1.09}Ge_{0.91}Se_4$

Cu/(Zn+Ge) = 1.090, Zn/Ge = 1.193

99% F-type (17% F(1)/82% F(2)), 1% I-type

Included phases: $Cu_2ZnGeSe_4$ (s.g. $I\bar{4}$)

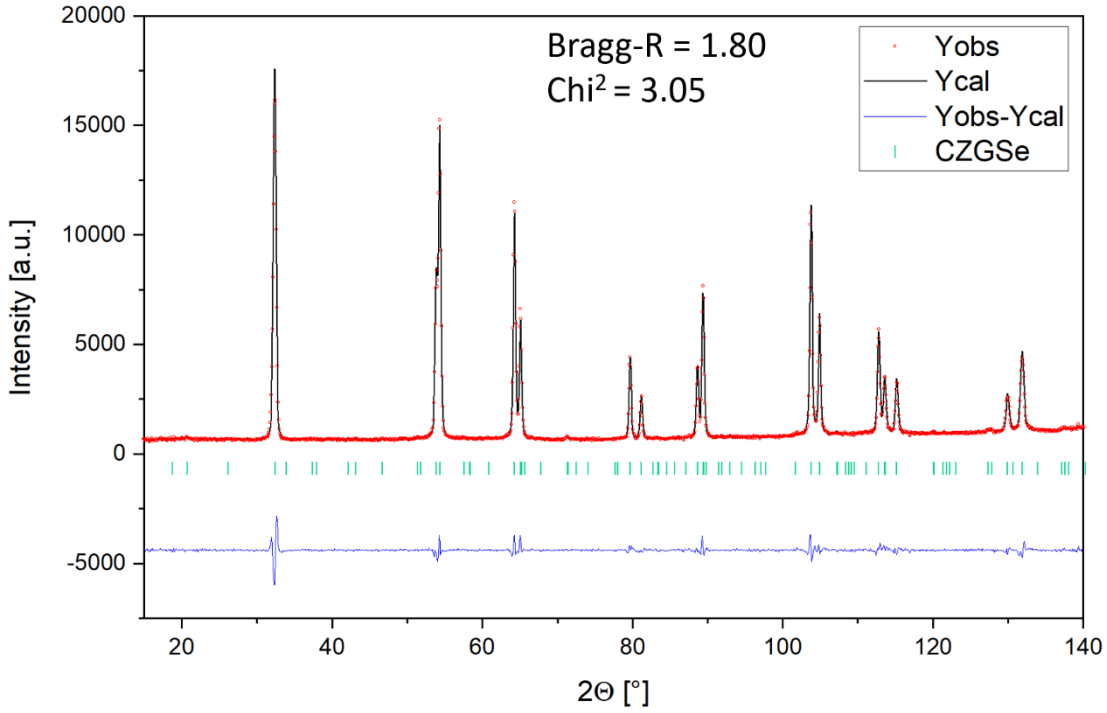

Figure A.1 - 13 Refined profile of neutron diffraction data of sample B0000-1.

Refined OCCs (CZGSe): Cu 2a = 0.994 (35)

Cu 2c = 0.960 (20)

Zn 2d = 1.081 (27)

Ge 2b = 1.000 (27)

Sample B0010-1A: $Cu_{2.16}Zn_{1.10}Ge_{0.91}Se_4$

Cu/(Zn+Ge) = 1.074, Zn/Ge = 1.208

84% F-type (21% F(1)/63% F(2)), 16% G-type

Included phases: $Cu_2ZnGeSe_4$ (s.g. $I\bar{4}$), Ge (s.g. $Fd\bar{3}m$), ZnSe (s.g. $F\bar{4}3m$)

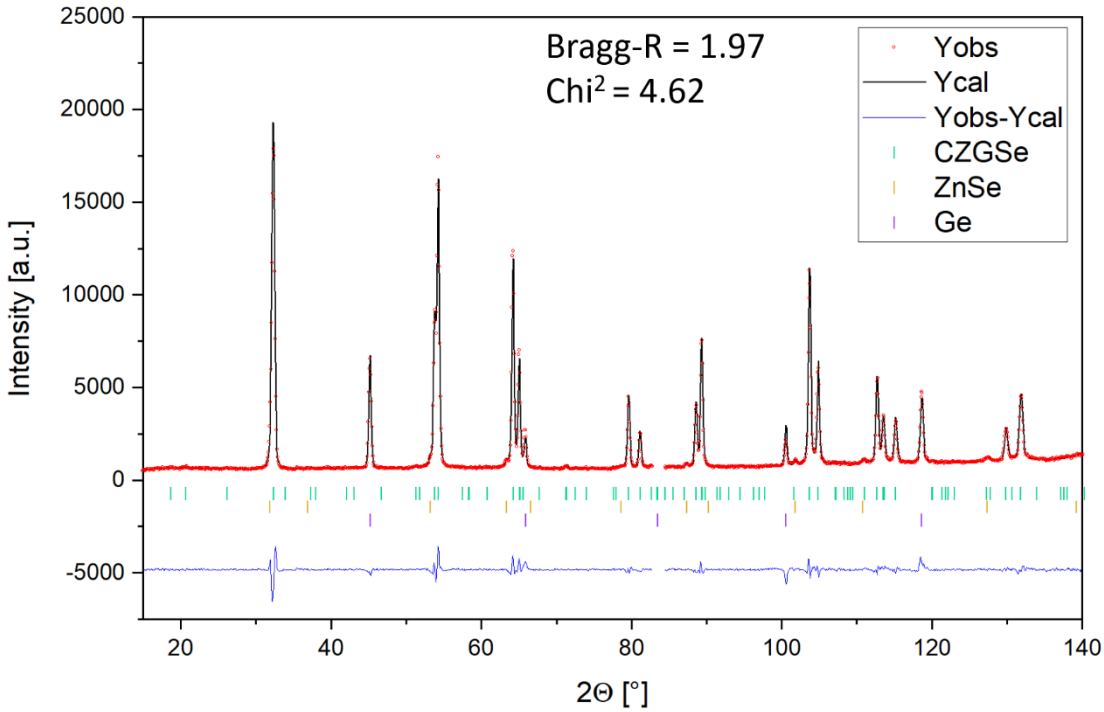

Figure A.1 - 14 Refined profile of neutron diffraction data of sample B0010-1A.

Refined OCCs (CZGSe): Cu 2a = 0.999 (51)

Cu 2c = 0.959 (26)

Zn 2d = 1.068 (39)

Ge 2b = 0.990 (40)

Sample B0010-1B: $Cu_{2.18}Zn_{1.09}Ge_{0.91}Se_4$

Cu/(Zn+Ge) = 1.091, Zn/Ge = 1.191

99% F-type (15% F(1)/84% F(2)), 1% I-type

Included phases: $Cu_2ZnGeSe_4$ (s.g. $I\bar{4}$)

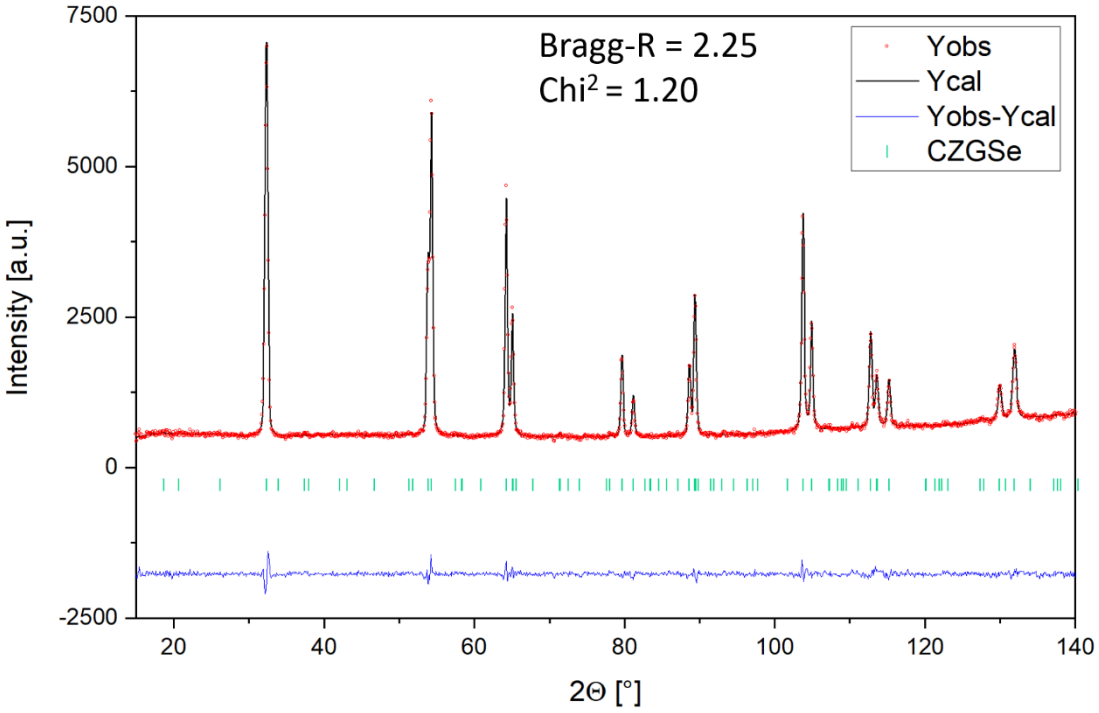

Figure A.1 - 15 Refined profile of neutron diffraction data of sample B0010-1B.

Refined OCCs (CZGSe): Cu 2a = 0.998 (30)

Cu 2c = 0.936 (46)

Zn 2d = 1.113 (58)

Ge 2b = 0.984 (21)

Sample B0020-1: $Cu_{2.16}Zn_{1.10}Ge_{0.91}Se_4$

Cu/(Zn+Ge) = 1.078, Zn/Ge = 1.209

87% F-type (20% F(1)/67% F(2)), 13% G-type

Included phases: $Cu_2ZnGeSe_4$ (s.g. $I\bar{4}$), ZnSe (s.g. $F\bar{4}3m$)

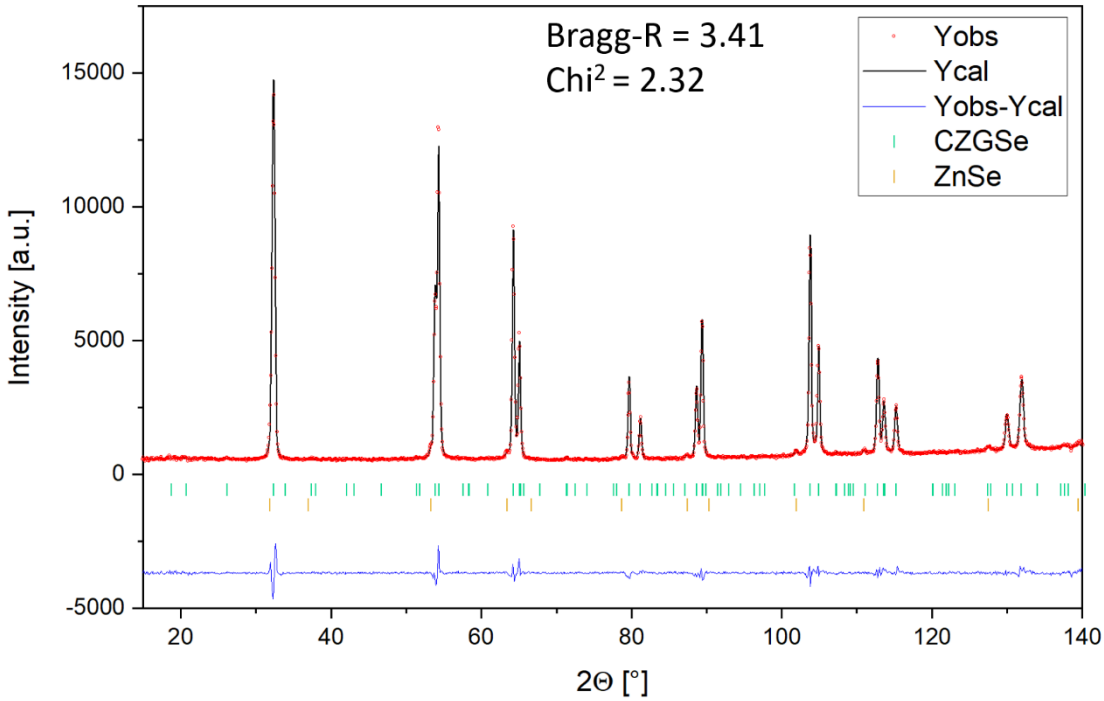

Figure A.1 - 16 Refined profile of neutron diffraction data of sample B0020-1.

Refined OCCs (CZGSe): Cu 2a = 1.004 (23)

Cu 2c = 0.968 (30)

Zn 2d = 1.101 (39)

Ge 2b = 0.977 (24)

Sample B0075-1: $Cu_{2.13}Zn_{1.09}Ge_{0.92}Se_4$

Cu/(Zn+Ge) = 1.057, Zn/Ge = 1.188

75% F-type (23% F(1)/52% F(2)), 25% G-type

Included phases: $Cu_2ZnGeSe_4$ (s.g. $I\bar{4}$), ZnSe (s.g. $F\bar{4}3m$)

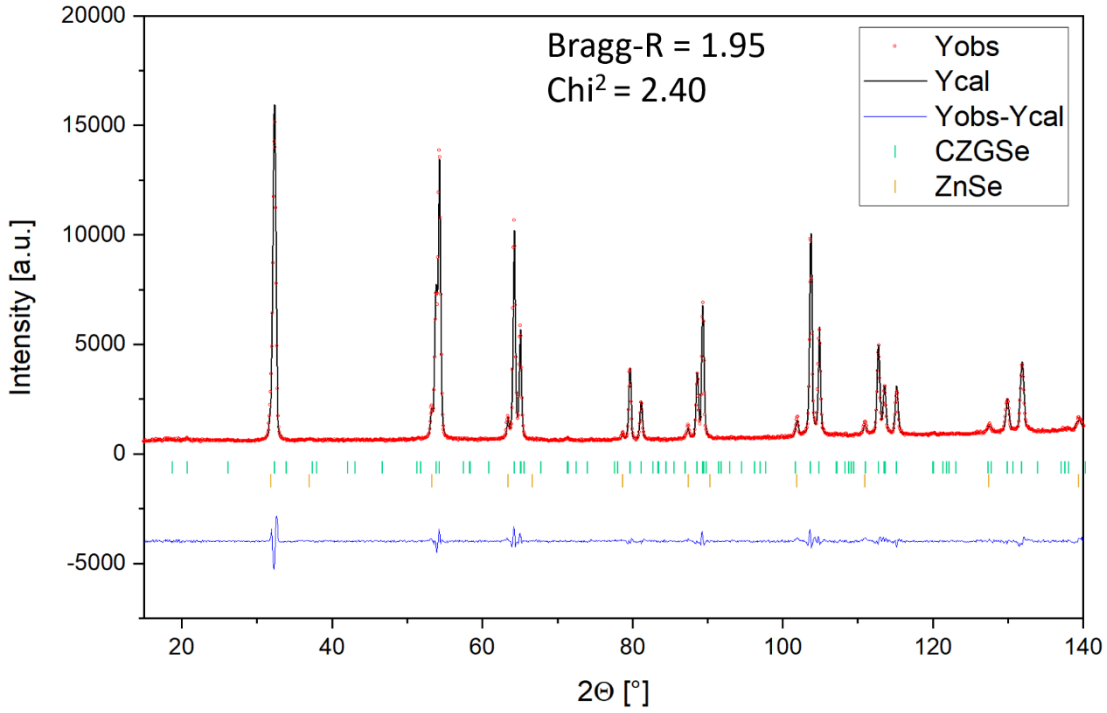

Figure A.1 - 17 Refined profile of neutron diffraction data of sample B0075-1.

Refined OCCs (CZGSe): Cu 2a = 0.993 (25)

Cu 2c = 0.957 (21)

Zn 2d = 1.092 (28)

Ge 2b = 0.990 (17)

Sample B0100-1A: $Cu_{2.10}Zn_{1.11}Ge_{0.92}Se_4$

Cu/(Zn+Ge) = 1.034, Zn/Ge = 1.200

53% F-type (30% F(1)/23% F(2)), 47% G-type

Included phases: $Cu_2ZnGeSe_4$ (s.g. $I\bar{4}$), ZnSe (s.g. $F\bar{4}3m$)

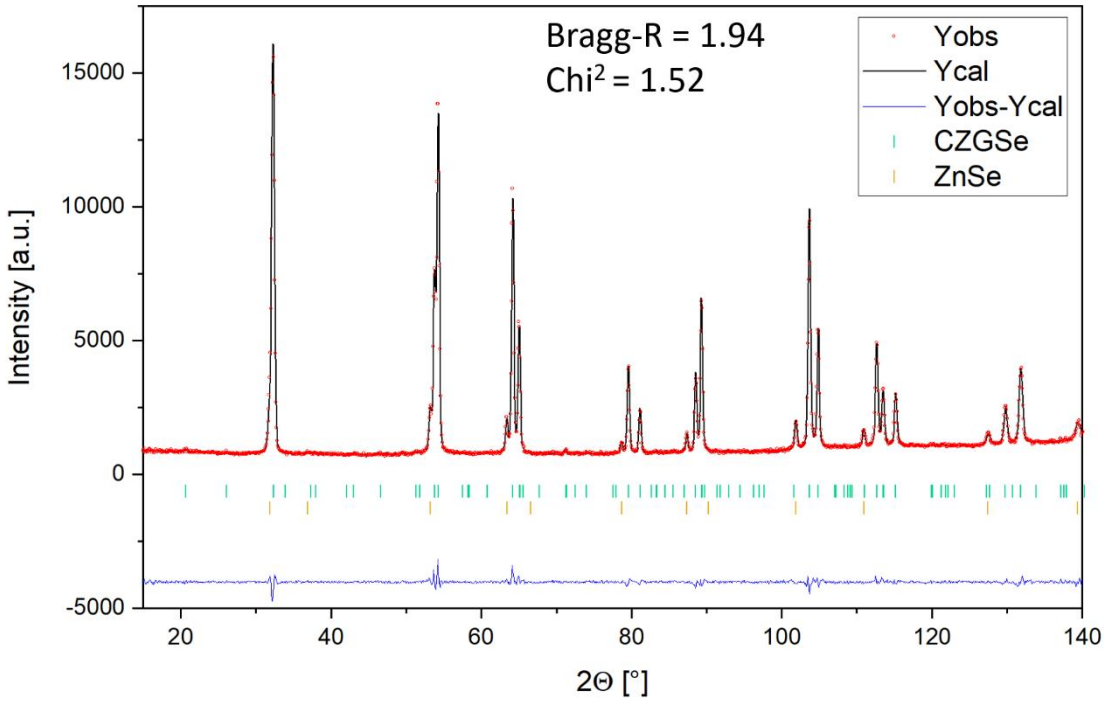

Figure A.1 - 18 Refined profile of neutron diffraction data of sample B0100-1A.

Refined OCCs (CZGSe): Cu 2a = 1.048 (47)

Cu 2c = 0.979 (30)

Zn 2d = 1.055 (43)

Ge 2b = 0.946 (47)

Sample B0100-1B: $Cu_{2.09}Zn_{1.11}Ge_{0.92}Se_4$

Cu/(Zn+Ge) = 1.031, Zn/Ge = 1.208

50% F-type (25% F(1)/25% F(2)), 50% G-type

Included phases: $Cu_2ZnGeSe_4$ (s.g. $I\bar{4}$)

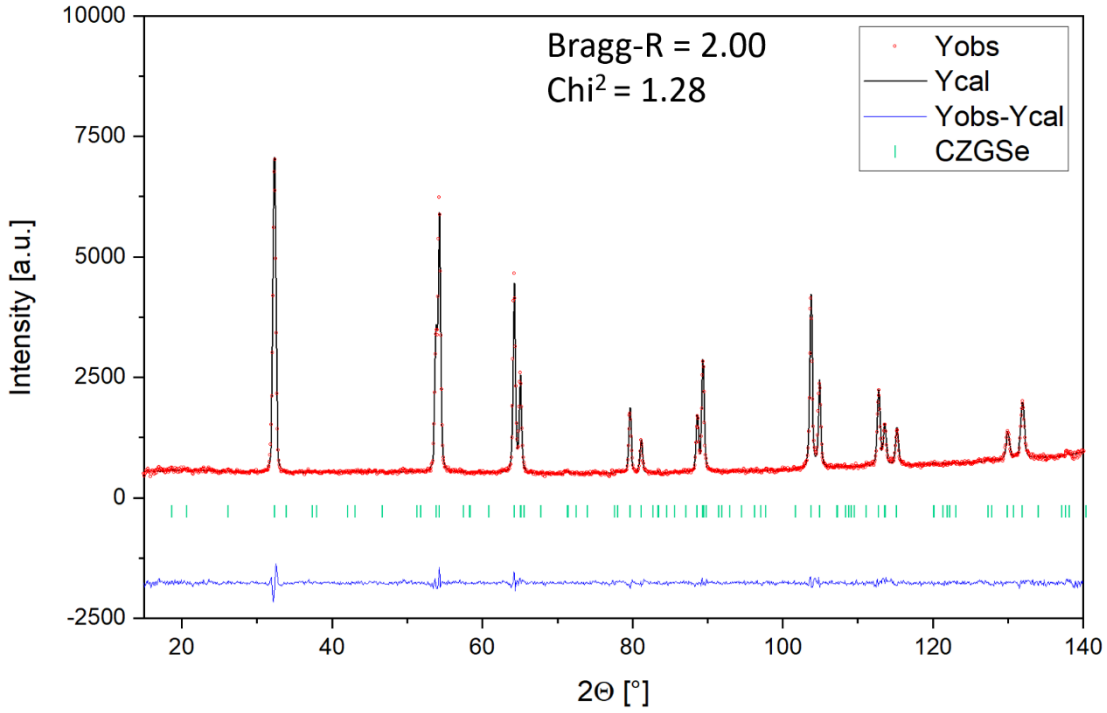

Figure A.1 - 19 Refined profile of neutron diffraction data of sample B0100-1B.

Refined OCCs (CZGSe): Cu 2a = 1.009 (28)

Cu 2c = 0.937 (35)

Zn 2d = 1.061 (44)

Ge 2b = 1.000 (18)

Sample B0125-1: $Cu_{2.14}Zn_{1.12}Ge_{0.90}Se_4$

Cu/(Zn+Ge) = 1.059, Zn/Ge = 1.243

66% F-type (26% F(1)/40% F(2)), 34% G-type

Included phases: $Cu_2ZnGeSe_4$ (s.g. $I\bar{4}$), ZnSe (s.g. $F\bar{4}3m$)

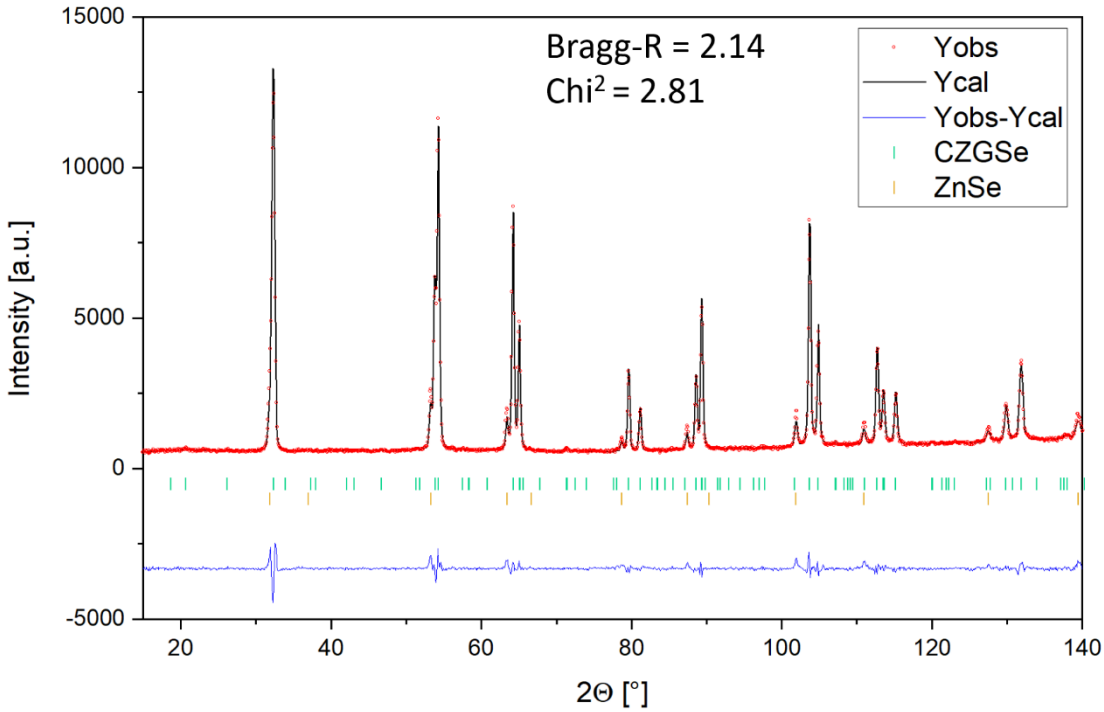

Figure A.1 - 20 Refined profile of neutron diffraction data of sample B0125-1.

Refined OCCs (CZGSe): Cu 2a = 1.007 (38)

Cu 2c = 0.975 (29)

Zn 2d = 1.090 (41)

Ge 2b = 0.984 (31)

Sample C0025-1R: $Cu_{2.24}Zn_{1.03}Ge_{0.93}Se_4$

Cu/(Zn+Ge) = 1.146, Zn/Ge = 1.108

54% F-type (0% F(1)/54% F(2)), 46% I-type

Included phases: $Cu_2ZnGeSe_4$ (s.g. $I\bar{4}$)

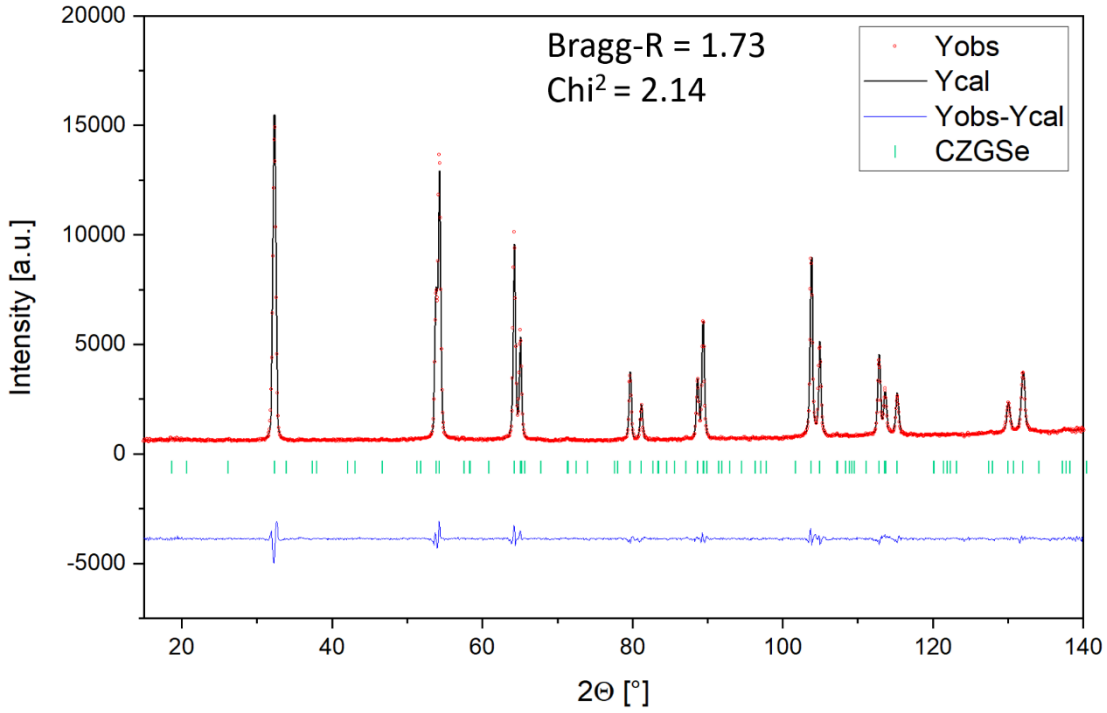

Figure A.1 - 21 Refined profile of neutron diffraction data of sample C0025-1R.

Refined OCCs (CZGSe): Cu 2a = 0.997 (18)

Cu 2c = 0.947 (24)

Zn 2d = 1.065 (30)

Ge 2b = 0.991 (11)

Sample C0000-2R: $Cu_{2.17}Zn_{1.09}Ge_{0.91}Se_4$

Cu/(Zn+Ge) = 1.085, Zn/Ge = 1.202

94% F-type (18% F(1)/76% F(2)), 6% G-type

Included phases: $Cu_2ZnGeSe_4$ (s.g. $I\bar{4}$)

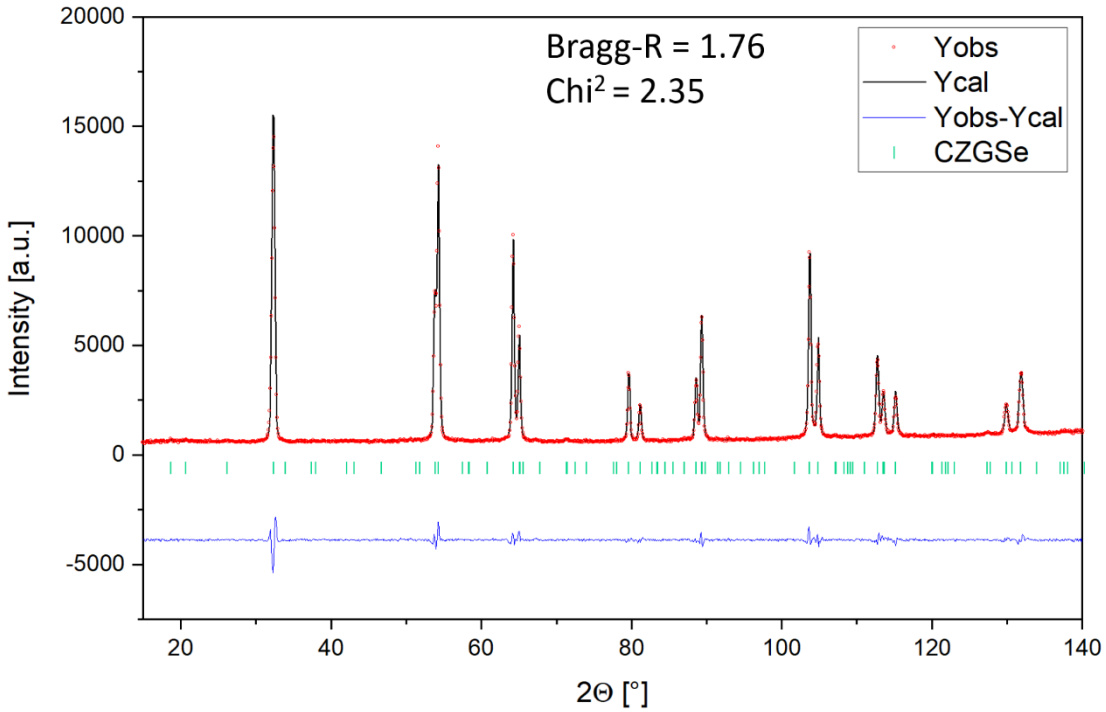

Figure A.1 - 22 Refined profile of neutron diffraction data of sample C0000-2R.

Refined OCCs (CZGSe): Cu 2a = 0.999 (26)

Cu 2c = 0.939 (24)

Zn 2d = 1.069 (33)

Ge 2b = 0.980 (18)

Sample C0025-2: $Cu_{2.23}Zn_{1.04}Ge_{0.92}Se_4$

Cu/(Zn+Ge) = 1.137, Zn/Ge = 1.132

70% F-type (0% F(1)/70% F(2)), 30% I-type

Included phases: $Cu_2ZnGeSe_4$ (s.g. $I\bar{4}$), Ge (s.g. $Fd\bar{3}m$)

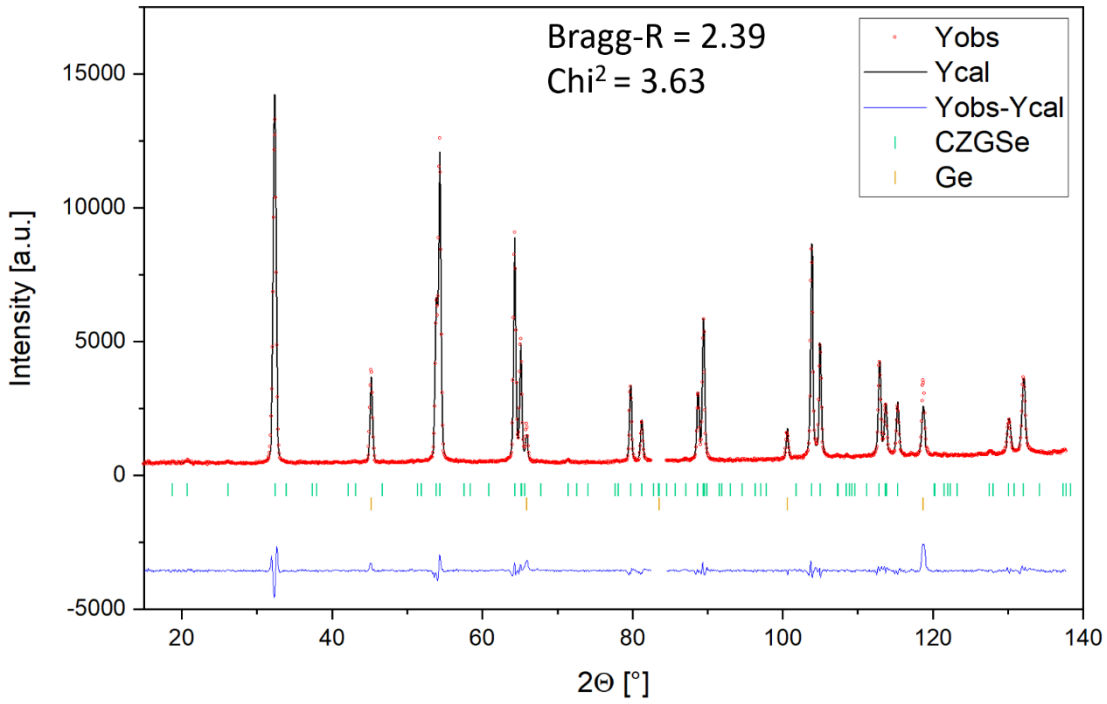

Figure A.1 - 23 Refined profile of neutron diffraction data of sample C0025-2.

Refined OCCs (CZGSe): Cu 2a = 0.999 (25)

Cu 2c = 0.981 (22)

Zn 2d = 1.039 (27)

Ge 2b = 0.999 (17)

Sample C0050-2R: $Cu_{2.28}Zn_{0.95}Ge_{0.96}Se_4$

Cu/(Zn+Ge) = 1.200, Zn/Ge = 0.992

7% D-type, 93% K-type

Included phases: $Cu_2ZnGeSe_4$ (s.g. $I\bar{4}$)

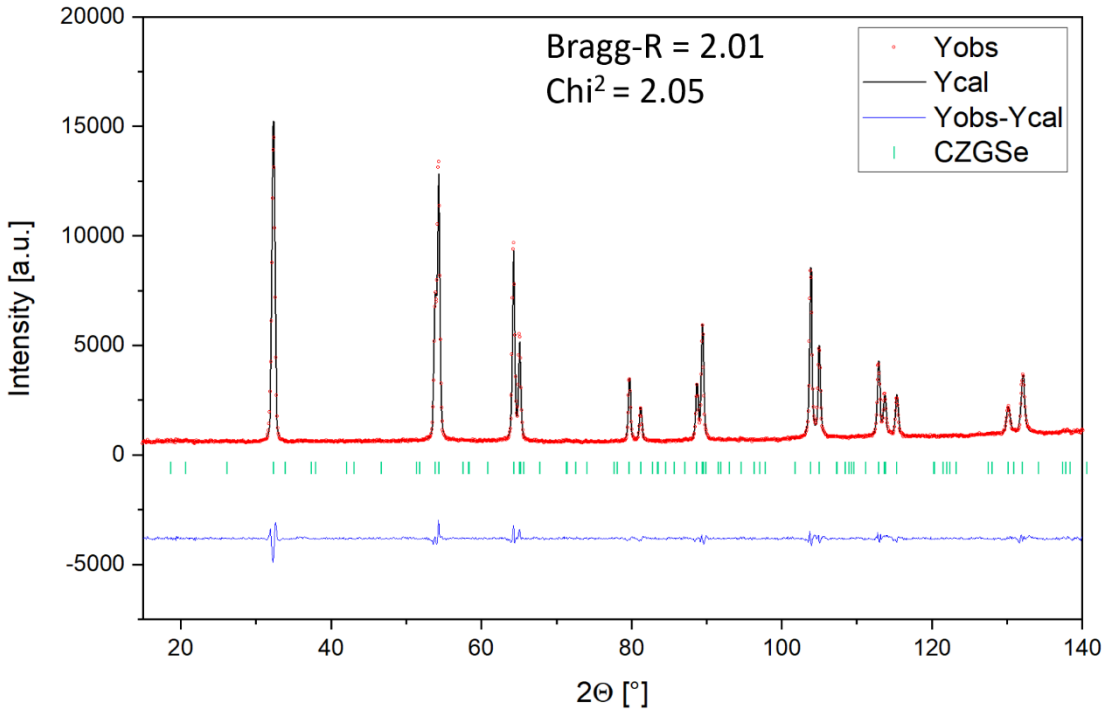

Figure A.1 - 24 Refined profile of neutron diffraction data of sample C0050-2R.

Refined OCCs (CZGSe): Cu 2a = 0.991 (21)

Cu 2c = 0.951 (23)

Zn 2d = 1.105 (28)

Ge 2b = 0.986 (16)

Sample D0000-1: $Cu_{2.17}Zn_{1.10}Ge_{0.91}Se_4$

Cu/(Zn+Ge) = 1.081, Zn/Ge = 1.216

87% F-type (30% F(1)/57% F(2)), 13% G-type

Included phases: $Cu_2ZnGeSe_4$ (s.g. $I\bar{4}$)

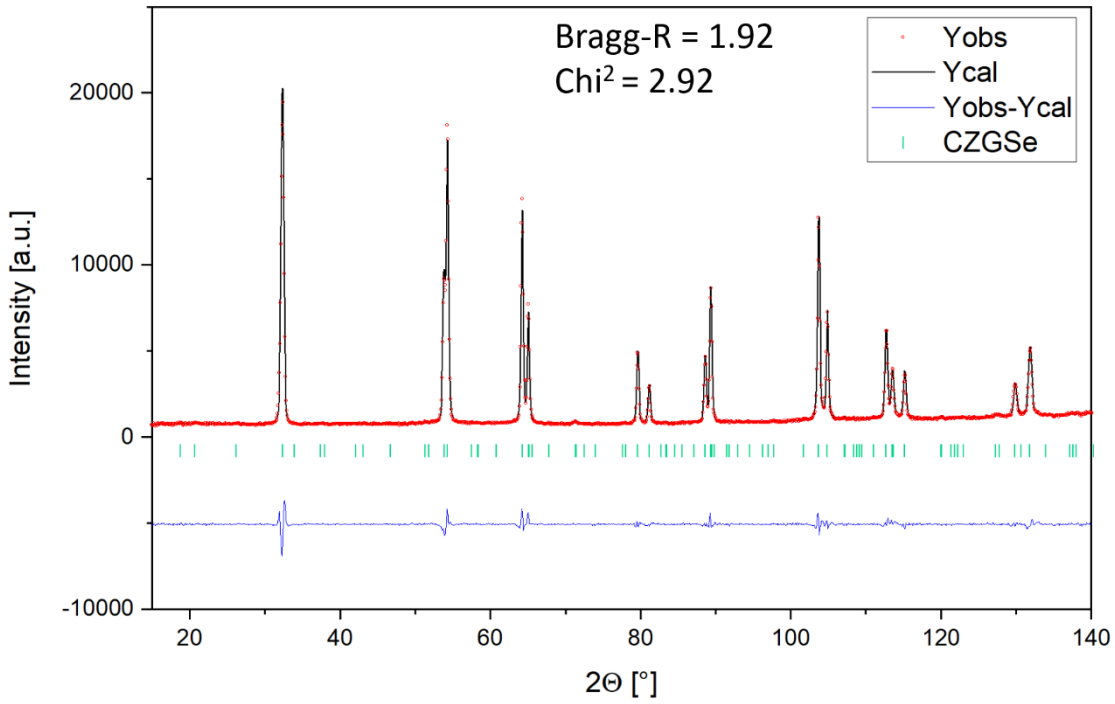

Figure A.1 - 25 Refined profile of neutron diffraction data of sample D0000-1.

Refined OCCs (CZGSe): Cu 2a = 1.005 (33)

Cu 2c = 0.927 (21)

Zn 2d = 1.076 (29)

Ge 2b = 0.959 (27)

Sample D0010-1: $Cu_{2.20}Zn_{1.09}Ge_{0.91}Se_4$

Cu/(Zn+Ge) = 1.103, Zn/Ge = 1.196

96% F-type (10% F(1)/86% F(2)), 4% I-type

Included phases: $Cu_2ZnGeSe_4$ (s.g. $I\bar{4}$)

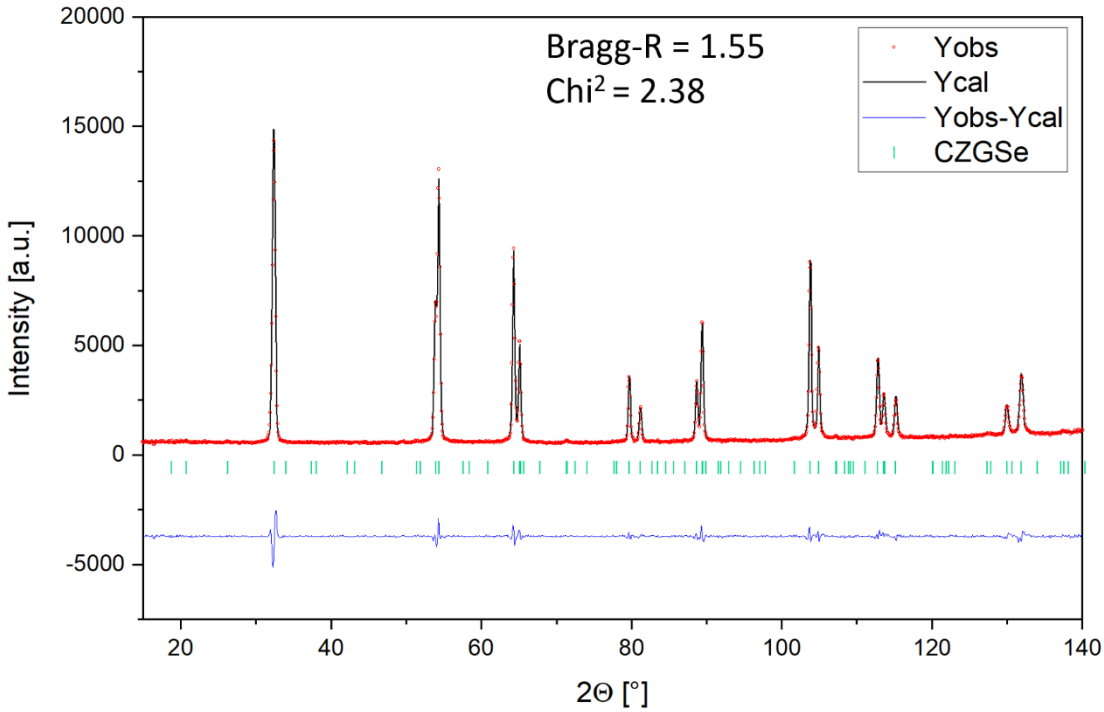

Figure A.1 - 26 Refined profile of neutron diffraction data of sample D0010-1.

Refined OCCs (CZGSe): Cu 2a = 0.994 (28)

Cu 2c = 0.974 (29)

Zn 2d = 1.085 (37)

Ge 2b = 1.001 (22)

Sample D0025-1: $Cu_{2.22}Zn_{1.06}Ge_{0.91}Se_4$

Cu/(Zn+Ge) = 1.129, Zn/Ge = 1.160

82% F-type (0% F(1)/82% F(2)), 18% I-type

Included phases: $Cu_2ZnGeSe_4$ (s.g. $I\bar{4}$)

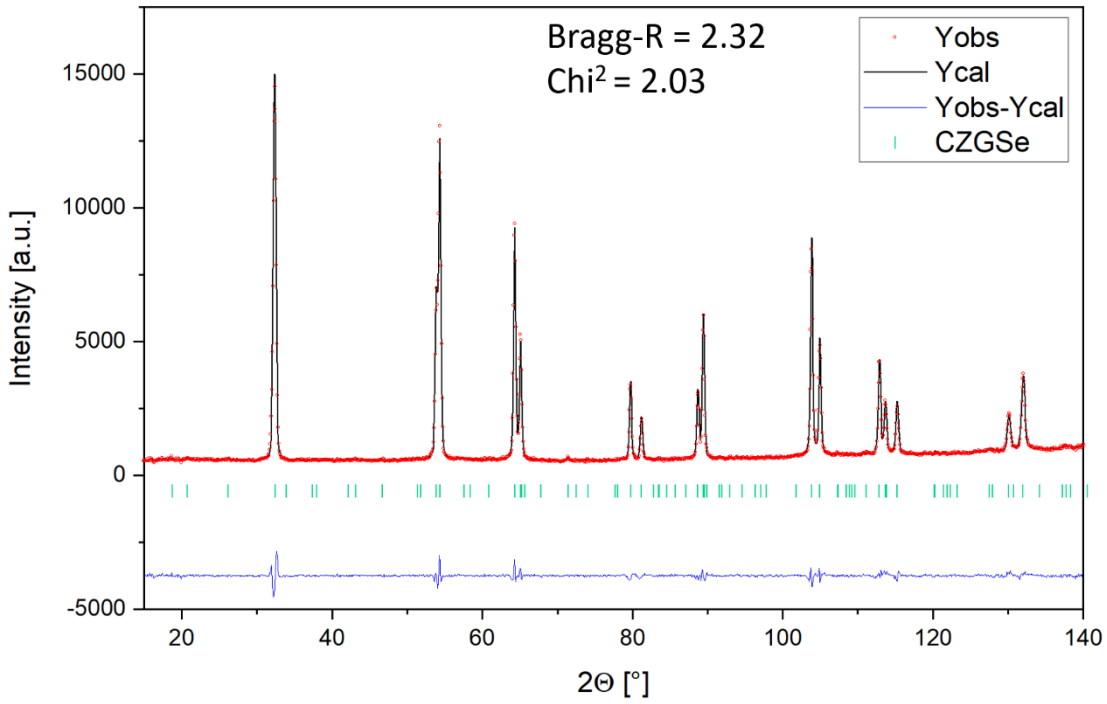

Figure A.1 - 27 Refined profile of neutron diffraction data of sample D0025-1.

Refined OCCs (CZGSe): Cu 2a = 0.997 (19)

Cu 2c = 0.969 (24)

Zn 2d = 1.080 (28)

Ge 2b = 1.006 (14)

Sample D0040-1: $Cu_{2.28}Zn_{1.04}Ge_{0.91}Se_4$

Cu/(Zn+Ge) = 1.171, Zn/Ge = 1.145

62% F-type (0% F(1)/62% F(2)), 38% I-type

Included phases: $Cu_2ZnGeSe_4$ (s.g. $I\bar{4}$)

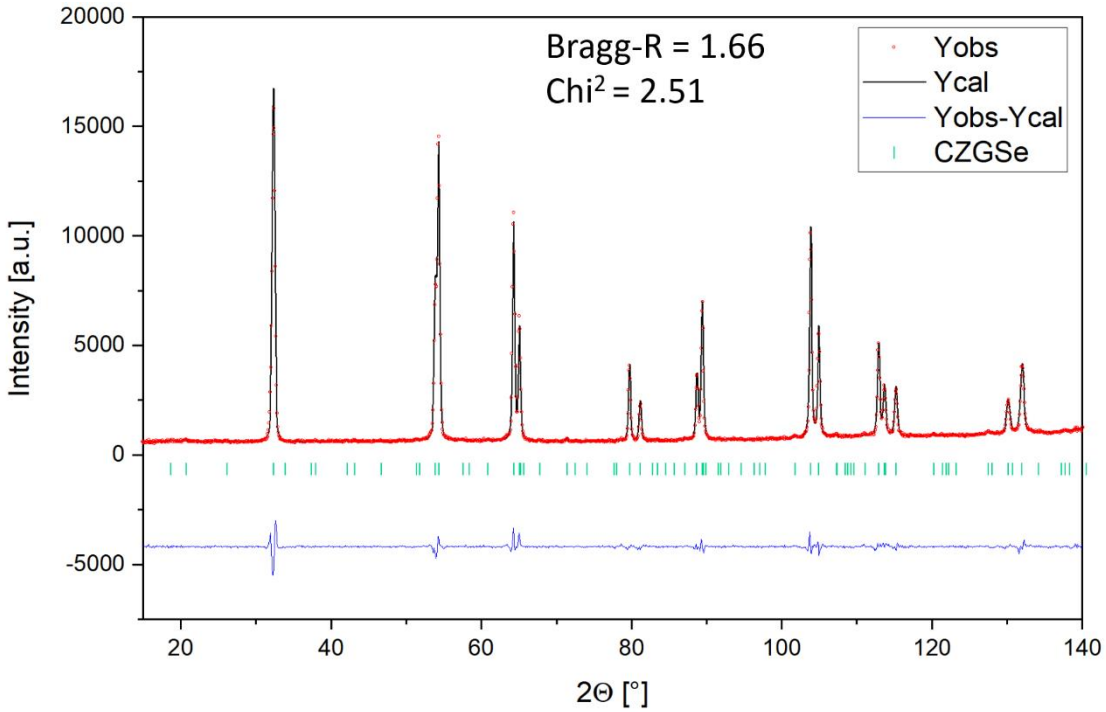

Figure A.1 - 28 Refined profile of neutron diffraction data of sample D0040-1.

Refined OCCs (CZGSe): Cu 2a = 1.006 (32)

Cu 2c = 0.949 (22)

Zn 2d = 1.051 (31)

Ge 2b = 0.975 (25)

Sample D0075-1: $Cu_{2.31}Zn_{1.02}Ge_{0.92}Se_4$

Cu/(Zn+Ge) = 1.196, Zn/Ge = 1.110

32% F-type (0% F(1)/32% F(2)), 68% I-type

Included phases: $Cu_2ZnGeSe_4$ (s.g. $I\bar{4}$)

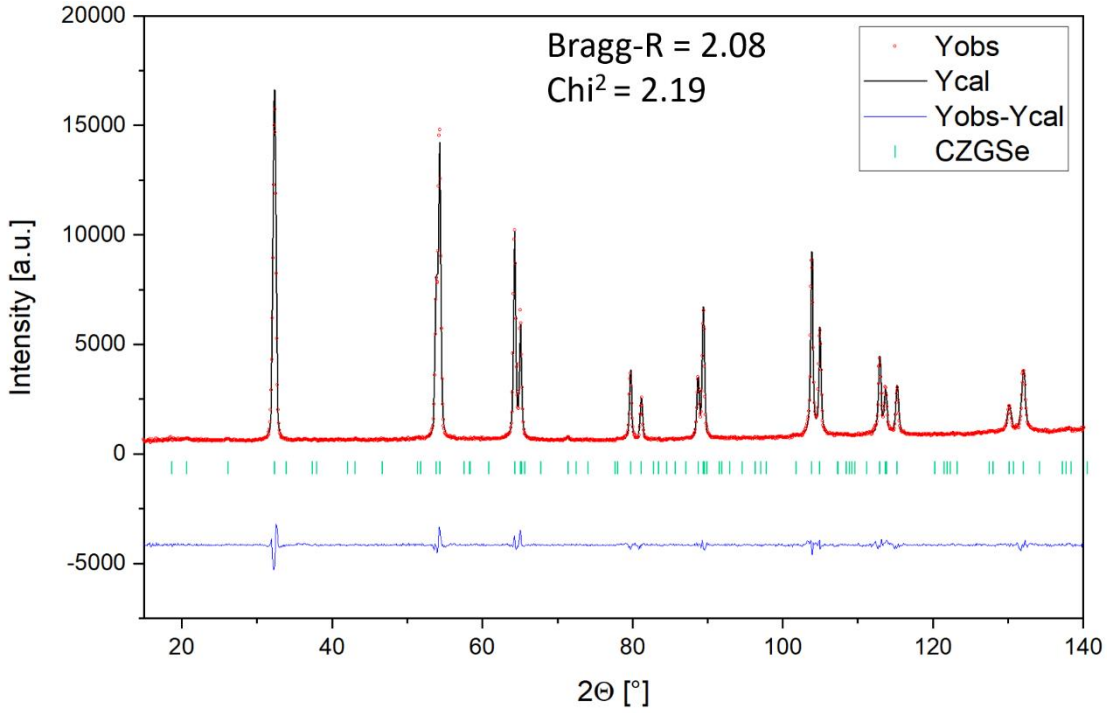

Figure A.1 - 29 Refined profile of neutron diffraction data of sample D0075-1.

Refined OCCs (CZGSe): Cu 2a = 1.005 (23)

Cu 2c = 0.973 (21)

Zn 2d = 1.028 (27)

Ge 2b = 1.007 (17)

Sample E0000-1: $Cu_{2.20}Zn_{1.08}Ge_{0.91}Se_4$

Cu/(Zn+Ge) = 1.105, Zn/Ge = 1.178

93% F-type (6% F(1)/87% F(2)), 7% I-type

Included phases: $Cu_2ZnGeSe_4$ (s.g. $I\bar{4}$)

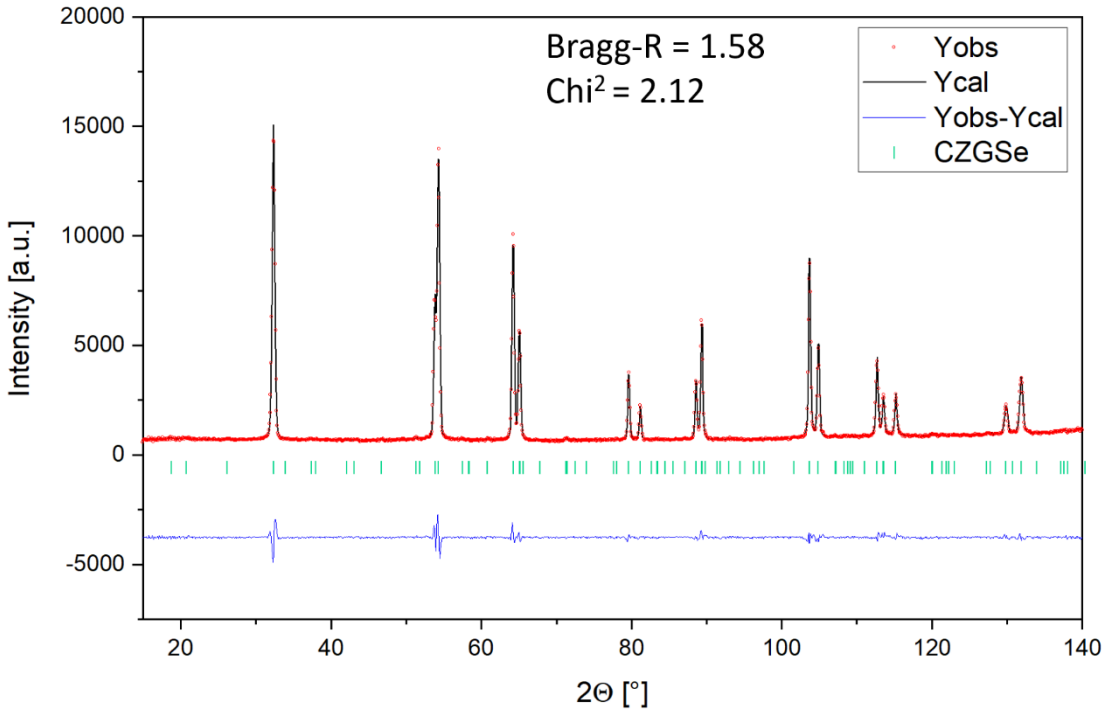

Figure A.1 - 30 Refined profile of neutron diffraction data of sample E0000-1.

Refined OCCs (CZGSe): Cu 2a = 1.009 (30)

Cu 2c = 0.946 (16)

Zn 2d = 1.063 (22)

Ge 2b = 0.973 (27)

Sample E0010-1: $Cu_{2.22}Zn_{1.08}Ge_{0.91}Se_4$

Cu/(Zn+Ge) = 1.117, Zn/Ge = 1.196

92% F-type (4% F(1)/88% F(2)), 8% I-type

Included phases: $Cu_2ZnGeSe_4$ (s.g. $I\bar{4}$)

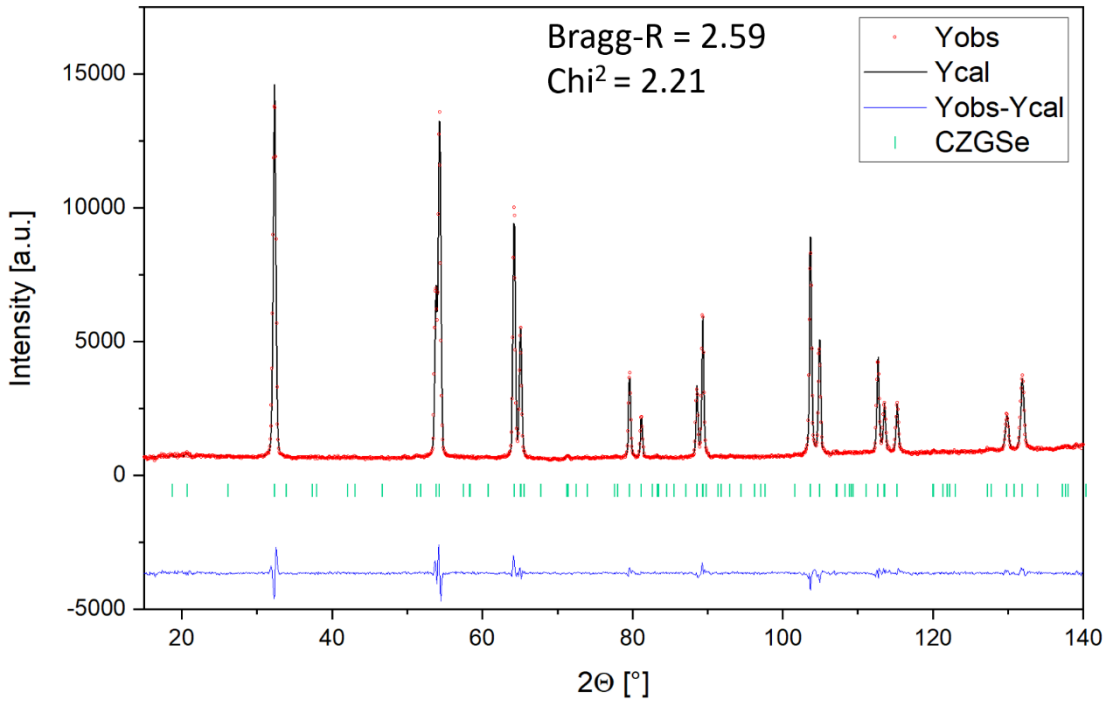

Figure A.1 - 31 Refined profile of neutron diffraction data of sample E0010-1.

Refined OCCs (CZGSe): Cu 2a = 1.011 (32)

Cu 2c = 0.992 (15)

Zn 2d = 1.022 (19)

Ge 2b = 0.998 (29)

Sample E0030-1: $Cu_{2.20}Zn_{1.09}Ge_{0.91}Se_4$

Cu/(Zn+Ge) = 1.105, Zn/Ge = 1.202

96% F-type (9% F(1)/87% F(2)), 4% I-type

Included phases: $Cu_2ZnGeSe_4$ (s.g. $I\bar{4}$)

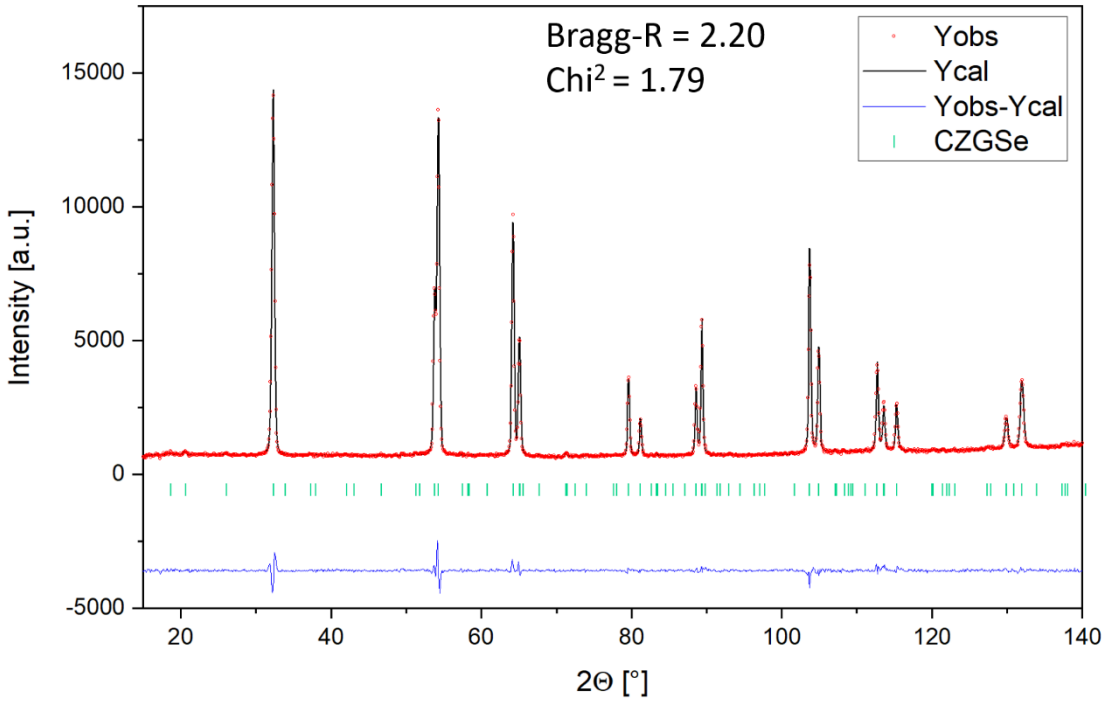

Figure A.1 - 32 Refined profile of neutron diffraction data of sample E0030-1.

Refined OCCs (CZGSe): Cu 2a = 1.021 (28)

Cu 2c = 0.968 (20)

Zn 2d = 1.011 (26)

Ge 2b = 1.000 (29)

Sample E0050-1: $Cu_{2.19}Zn_{1.07}Ge_{0.92}Se_4$

Cu/(Zn+Ge) = 1.102, Zn/Ge = 1.172

93% F-type (3% F(1)/90% F(2)), 7% I-type

Included phases: $Cu_2ZnGeSe_4$ (s.g. $I\bar{4}$)

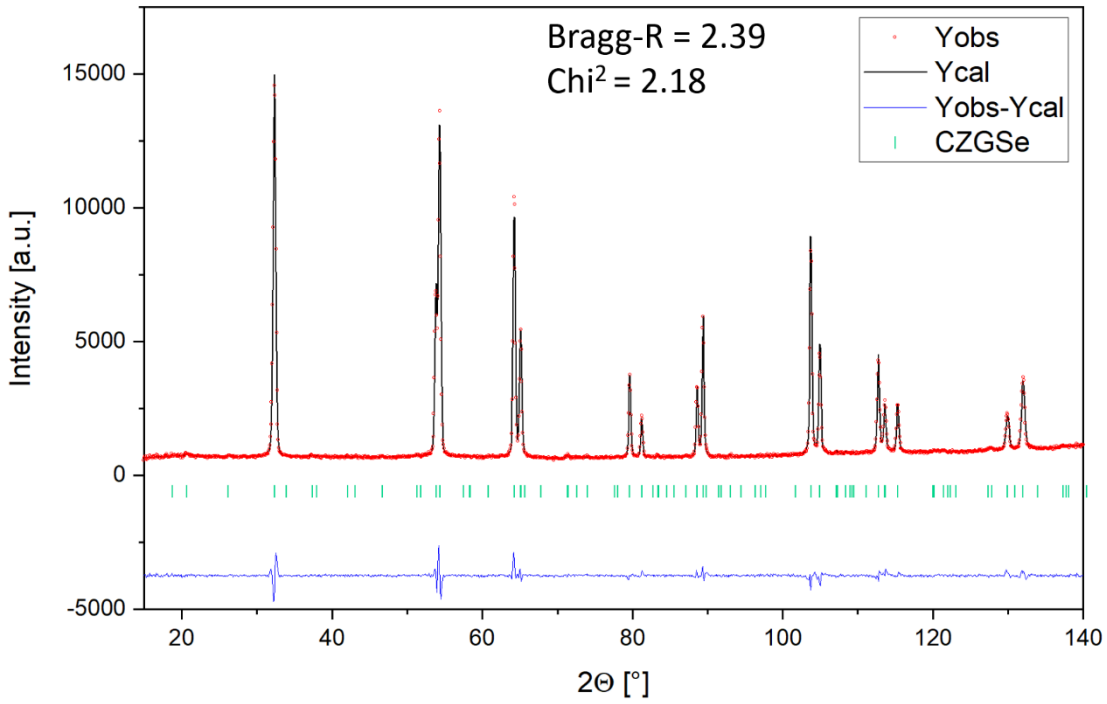

Figure A.1 - 33 Refined profile of neutron diffraction data of sample E0050-1.

Refined OCCs (CZGSe): Cu 2a = 1.008 (29)

Cu 2c = 0.994 (23)

Zn 2d = 1.012 (28)

Ge 2b = 0.991 (29)

Sample E0070-1: $Cu_{2.19}Zn_{1.09}Ge_{0.91}Se_4$

Cu/(Zn+Ge) = 1.097, Zn/Ge = 1.209

99% F-type (15% F(1)/84% F(2)), 1% I-type

Included phases: $Cu_2ZnGeSe_4$ (s.g. $I\bar{4}$)

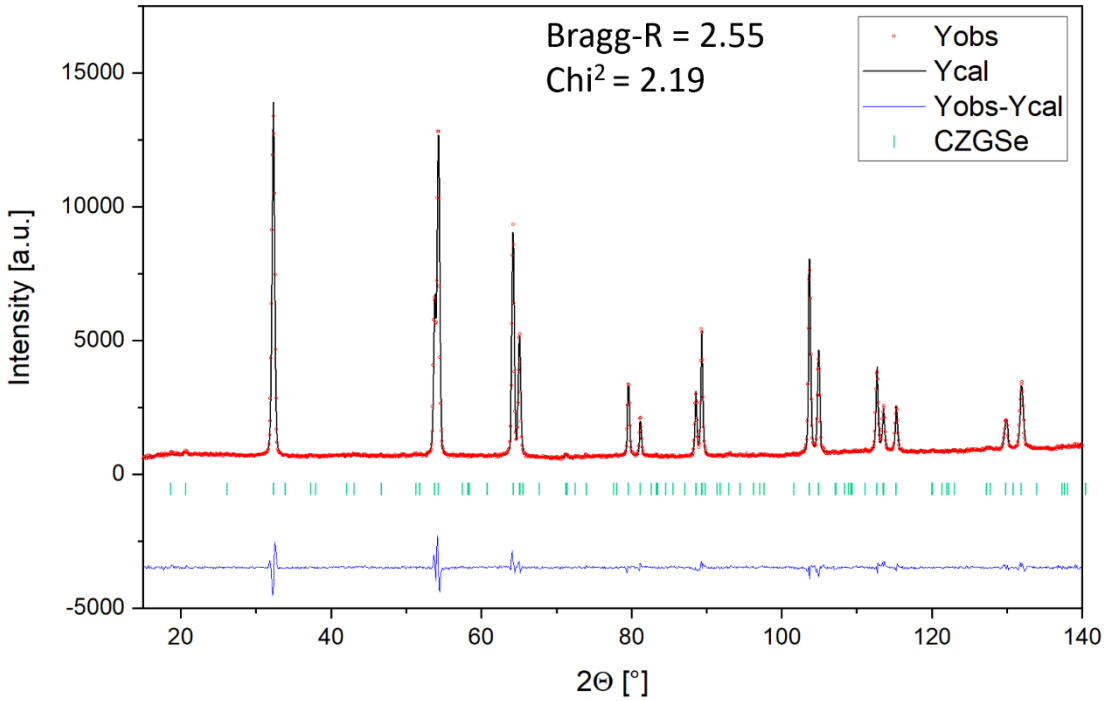

Figure A.1 - 34 Refined profile of neutron diffraction data of sample E0070-1.

Refined OCCs (CZGSe): Cu 2a = 0.994 (32)

Cu 2c = 0.983 (33)

Zn 2d = 1.035 (39)

Ge 2b = 0.995 (32)

Sample E0090-1: $Cu_{2.19}Zn_{1.08}Ge_{0.91}Se_4$

Cu/(Zn+Ge) = 1.104, Zn/Ge = 1.177

93% F-type (4% F(1)/89% F(2)), 7% I-type

Included phases: $Cu_2ZnGeSe_4$ (s.g. $I\bar{4}$)

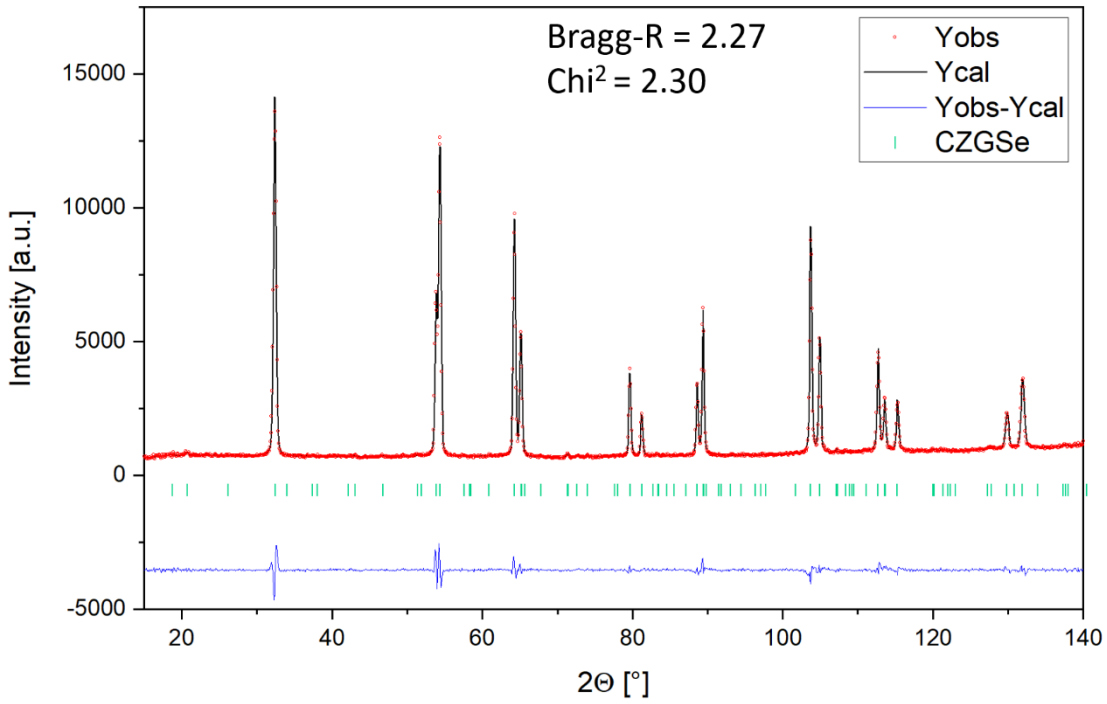

Figure A.1 - 35 Refined profile of neutron diffraction data of sample E0090-1.

Refined OCCs (CZGSe): Cu 2a = 0.991 (47)

Cu 2c = 0.981 (36)

Zn 2d = 1.050 (51)

Ge 2b = 1.005 (45)

Sample F0000-1: $Cu_{2.13}Zn_{1.01}Ge_{0.96}Se_4$

Cu/(Zn+Ge) = 1.082, Zn/Ge = 1.048

38% F-type (0% F(1)/38% F(2)), 62% I-type

Included phases: $Cu_2ZnGeSe_4$ (s.g. $I\bar{4}$)

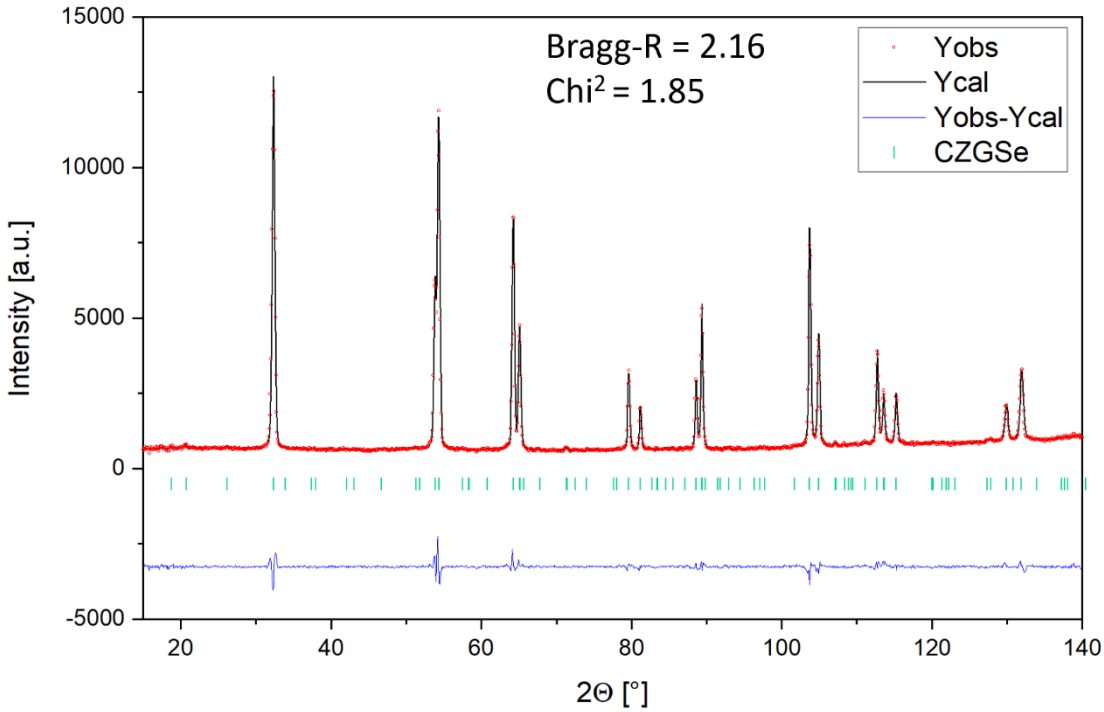

Figure A.1 - 36 Refined profile of neutron diffraction data of sample F0000-1.

Refined OCCs (CZGSe): Cu 2a = 1.018 (28)

Cu 2c = 1.002 (22)

Zn 2d = 1.017 (26)

Ge 2b = 1.015 (29)

Sample F0015-1: $Cu_{2.09}Zn_{1.03}Ge_{0.96}Se_4$

Cu/(Zn+Ge) = 1.046, Zn/Ge = 1.070

91% F-type (0% F(1)/91% F(2)), 9% I-type

Included phases: $Cu_2ZnGeSe_4$ (s.g. $I\bar{4}$), ZnSe (s.g. $F\bar{4}3m$)

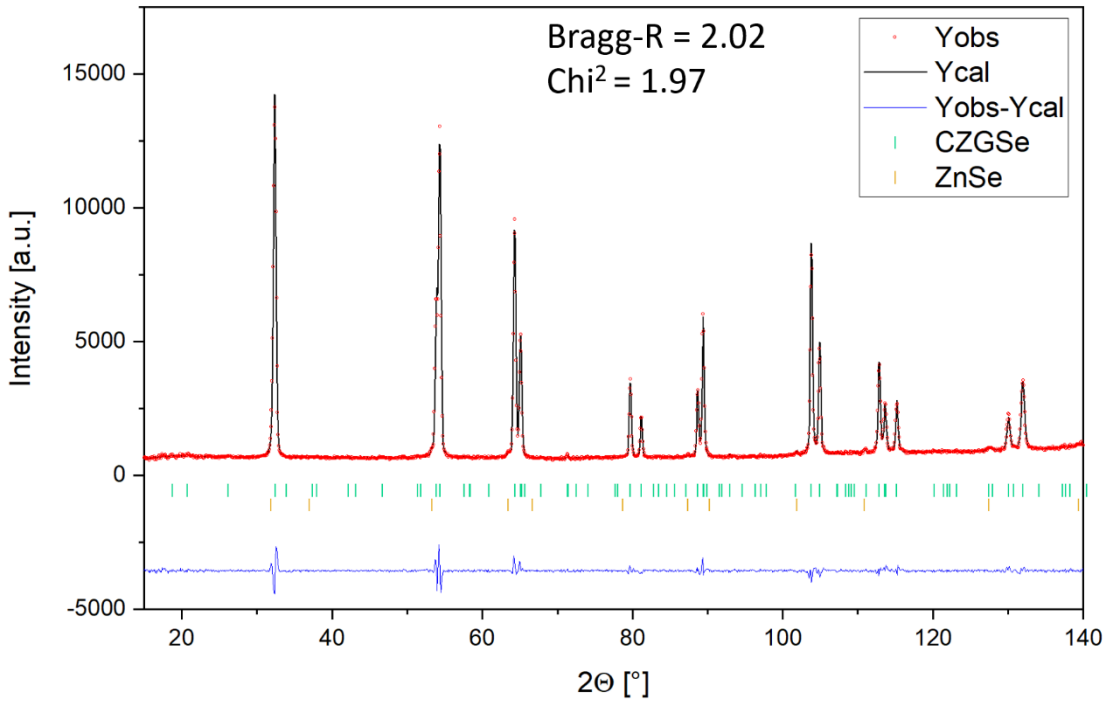

Figure A.1 - 37 Refined profile of neutron diffraction data of sample F0015-1.

Refined OCCs (CZGSe): Cu 2a = 1.020 (23)

Cu 2c = 0.928 (26)

Zn 2d = 1.105 (34)

Ge 2b = 0.979 (26)

Sample F0030-1: $Cu_{2.16}Zn_{1.00}Ge_{0.96}Se_4$

Cu/(Zn+Ge) = 1.104, Zn/Ge = 1.046

9% F-type (0% F(1)/9% F(2)), 91% I-type

Included phases: $Cu_2ZnGeSe_4$ (s.g. $I\bar{4}$), ZnSe (s.g. $F\bar{4}3m$)

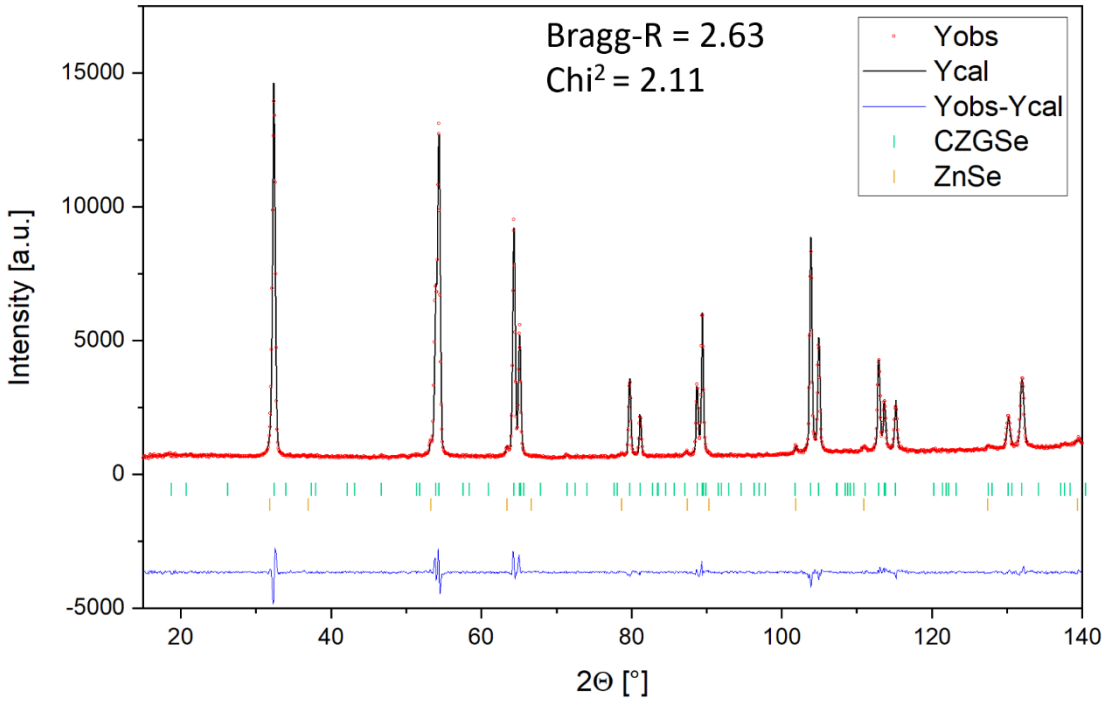

Figure A.1 - 38 Refined profile of neutron diffraction data of sample F0030-1.

Refined OCCs (CZGSe): Cu 2a = 1.026 (37)

Cu 2c = 0.932 (33)

Zn 2d = 1.132 (47)

Ge 2b = 0.955 (37)

Sample F0050-1: $Cu_{2.18}Zn_{0.99}Ge_{0.96}Se_4$

Cu/(Zn+Ge) = 1.119, Zn/Ge = 1.033

67% I-type, 33% K-type

Included phases: $Cu_2ZnGeSe_4$ (s.g. $I\bar{4}$), ZnSe (s.g. $F\bar{4}3m$)

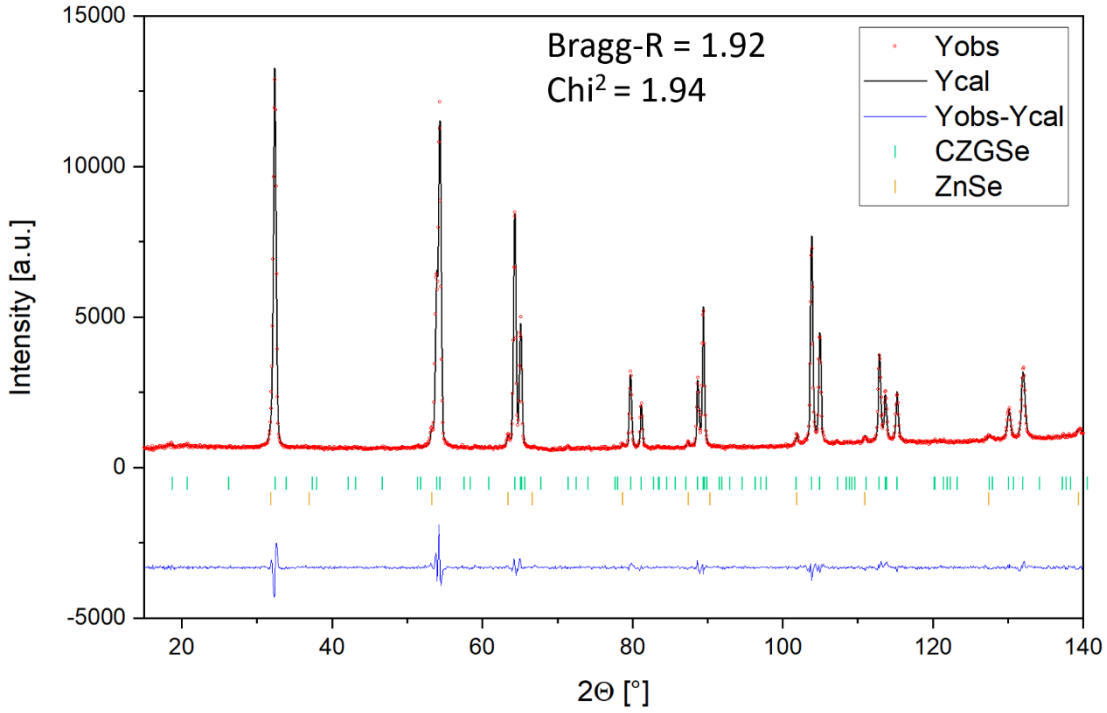

Figure A.1 - 39 Refined profile of neutron diffraction data of sample F0050-1.

Refined OCCs (CZGSe): Cu 2a = 1.009 (29)

Cu 2c = 0.966 (27)

Zn 2d = 1.085 (33)

Ge 2b = 0.989 (32)

Sample F0075-1: $Cu_{2.18}Zn_{1.00}Ge_{0.95}Se_4$

Cu/(Zn+Ge) = 1.118, Zn/Ge = 1.047

98% I-type, 2% K-type

Included phases: $Cu_2ZnGeSe_4$ (s.g. $I\bar{4}$), ZnSe (s.g. $F\bar{4}3m$)

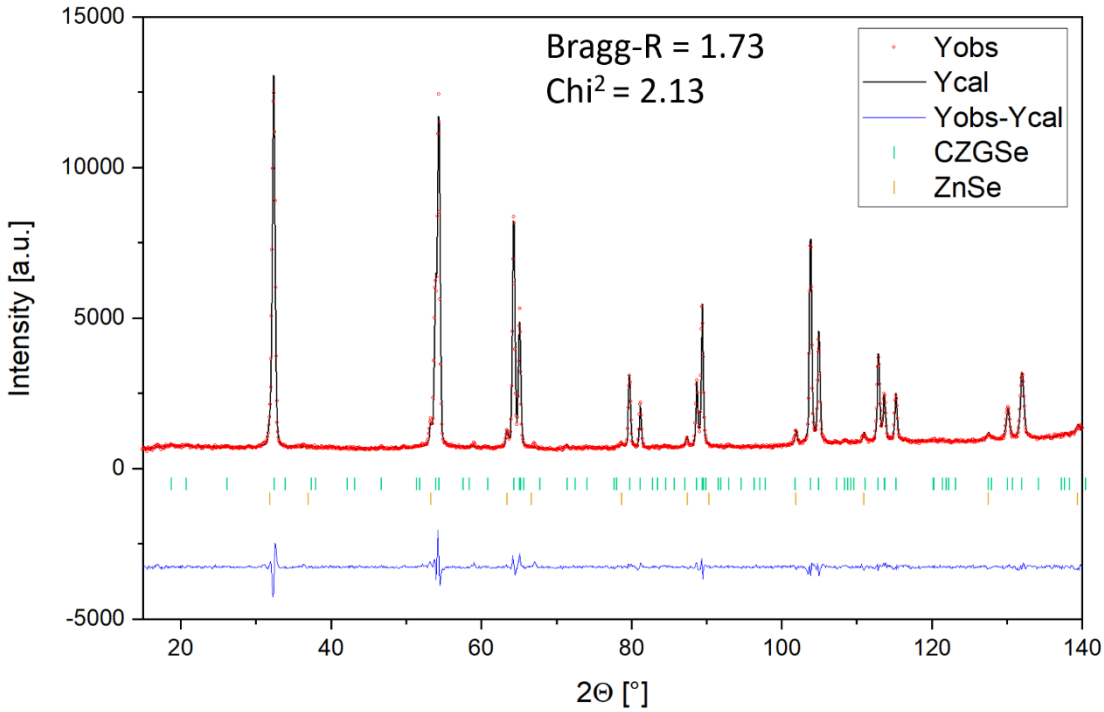

Figure A.1 - 40 Refined profile of neutron diffraction data of sample F0075-1.

Refined OCCs (CZGSe): Cu 2a = 1.021 (32)

Cu 2c = 0.956 (34)

Zn 2d = 1.074 (40)

Ge 2b = 1.001 (37)

Sample F0100-1: $Cu_{2.18}Zn_{0.99}Ge_{0.96}Se_4$

Cu/(Zn+Ge) = 1.118, Zn/Ge = 1.038

78% I-type, 22% K-type

Included phases: $Cu_2ZnGeSe_4$ (s.g. $I\bar{4}$), ZnSe (s.g. $F\bar{4}3m$)

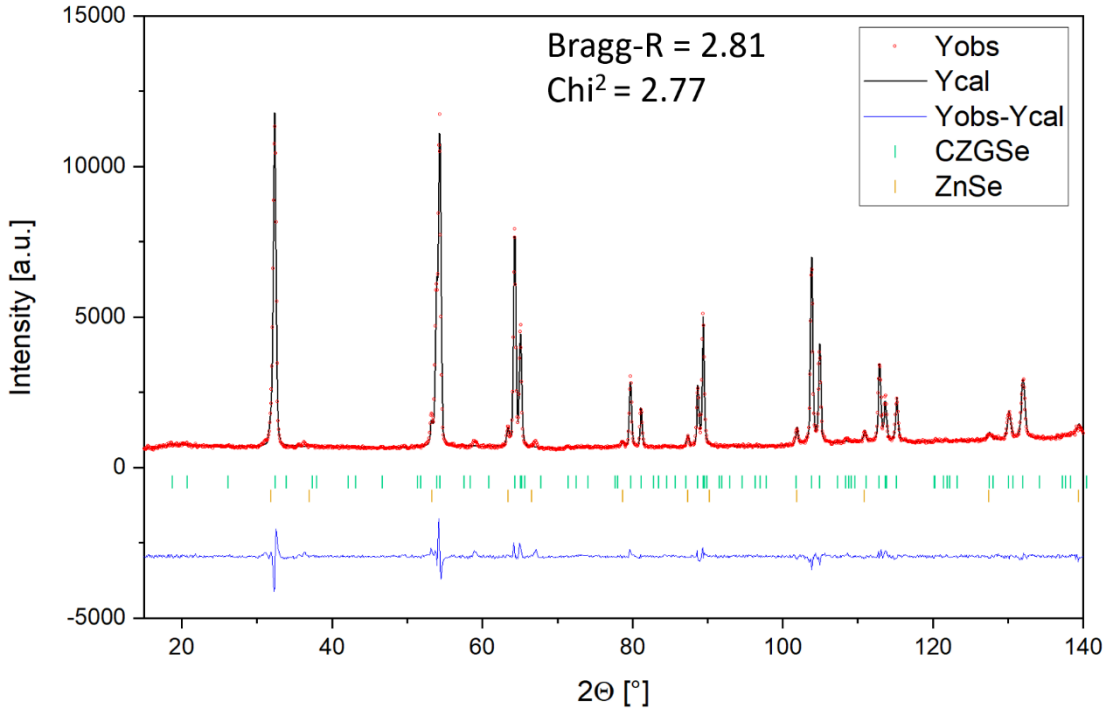

Figure A.1 - 41 Refined profile of neutron diffraction data of sample F0100-1.

Refined OCCs (CZGSe): Cu 2a = 1.016 (52)

Cu 2c = 0.960 (39)

Zn 2d = 1.107 (47)

Ge 2b = 0.987 (52)

A.2 Tabulated Summary of Results

Table A.2 - 1: Overview of results from compositional analysis.

labeling		cation ratios				off-stoichiometry types					stoichiometric coefficients								
No.	sample	Cu/(Zn+Ge)	err	Zn/Ge	err	type/percentage		type/percentage		err	Cu	err	Zn	err	Ge	err	Se	Σ cations	err
1	A0000-1	1.153	0.012	1.083	0.010	F	29%	I	71%	3.6%	2.241	0.060	1.012	0.027	0.934	0.025	4	4.187	0.112
2	A0015-1	1.120	0.011	1.119	0.011	F	72%	I	28%	4.0%	2.200	0.070	1.040	0.034	0.930	0.031	4	4.171	0.135
3	A0040-1	1.107	0.011	1.105	0.011	F	71%	I	29%	4.0%	2.180	0.069	1.035	0.034	0.937	0.031	4	4.153	0.133
4	A0075-1	1.000	0.01	1.242	0.012	F	25%	G	75%	2.3%	2.054	0.036	1.139	0.021	0.917	0.017	4	4.110	0.074
5	A0125-1	0.973	0.01	1.201	0.012	F	2%	G	98%	2.5%	2.005	0.044	1.125	0.025	0.937	0.021	4	4.066	0.089
6	A0200-1	0.8402	0.008	1.333	0.013	A	6%	B	94%	3.2%	1.816	0.058	1.237	0.039	0.928	0.029	4	3.980	0.125
7	A0000-2	1.105	0.011	1.189	0.012	F	5%	I	95%	4.2%	2.198	0.089	1.082	0.045	0.910	0.038	4	4.189	0.172
8	A0015-2	1.096	0.011	1.197	0.012	F	98%	I	2%	4.2%	2.188	0.093	1.088	0.046	0.909	0.039	4	4.185	0.178
9	A0040-2	1.045	0.010	1.240	0.012	F	56%	G	44%	2.4%	2.121	0.038	1.125	0.020	0.907	0.016	4	4.154	0.073
10	A0075-2	0.999	0.010	1.282	0.013	F	24%	G	76%	2.3%	2.060	0.037	1.160	0.021	0.905	0.016	4	4.125	0.074
11	A0125-2	0.921	0.009	1.355	0.014	B	29%	G	71%	3.1%	1.953	0.046	1.221	0.029	0.901	0.021	4	4.075	0.096
12	A0200-1	0.888	0.009	1.392	0.014	B	53%	G	47%	3.2%	1.906	0.043	1.250	0.028	0.898	0.020	4	4.055	0.091
13	B0000-1	1.090	0.011	1.193	0.012	F	99%	I	1%	4.1%	2.179	0.094	1.088	0.047	0.911	0.040	4	4.178	0.180
14	B0010-1A	1.074	0.011	1.208	0.012	F	84%	G	16%	2.4%	2.159	0.048	1.100	0.024	0.910	0.020	4	4.169	0.093
15	B0010-1B	1.091	0.011	1.191	0.012	F	99%	I	1%	4.2%	2.179	0.093	1.086	0.046	0.912	0.039	4	4.178	0.179
16	B0020-1	1.078	0.011	1.209	0.012	F	87%	G	13%	2.4%	2.164	0.049	1.099	0.025	0.909	0.021	4	4.173	0.095
17	B0075-1	1.057	0.011	1.188	0.012	F	75%	G	25%	2.4%	2.128	0.044	1.094	0.022	0.921	0.019	4	4.143	0.084
18	B0100-1A	1.034	0.010	1.201	0.012	F	53%	G	47%	2.3%	2.096	0.037	1.107	0.019	0.922	0.016	4	4.126	0.072
19	B0100-1B	1.031	0.010	1.208	0.012	F	50%	G	50%	2.3%	2.093	0.036	1.112	0.019	0.921	0.016	4	4.126	0.071
20	B0125-1	1.059	0.011	1.243	0.012	F	66%	G	34%	2.4%	2.142	0.041	1.122	0.021	0.903	0.017	4	4.168	0.078

Table A.2 - 1: (Continued).

No.	sample	Cu/(Zn+Ge)	err	Zn/Ge	err	type/percentage		type/percentage		err	Cu	err	Zn	err	Ge	err	Se	Σ cations	err
21	C0025-1R	1.146	0.011	1.108	0.011	F	54%	I	46%	3.8%	2.236	0.061	1.027	0.029	0.927	0.026	4	4.191	0.116
22	C0000-2R	1.085	0.011	1.202	0.012	F	94%	G	6%	2.4%	2.173	0.053	1.094	0.027	0.910	0.026	4	4.176	0.103
23	C0025-2	1.137	0.011	1.132	0.011	F	70%	I	30%	4.0%	2.228	0.069	1.043	0.034	0.921	0.030	4	4.193	0.132
24	C0050-2R	1.200	0.012	0.992	0.010	D	7%	K	93%	3.6%	2.283	0.077	0.947	0.032	0.956	0.032	4	4.186	0.142
25	D0000-1	1.081	0.011	1.216	0.012	F	87%	G	13%	2.4%	2.169	0.050	1.102	0.025	0.907	0.021	4	4.178	0.096
26	D0010-1	1.103	0.011	1.196	0.012	F	96%	I	4%	4.2%	2.196	0.091	1.086	0.045	0.908	0.038	4	4.190	0.174
27	D0025-1	1.129	0.011	1.160	0.012	F	82%	I	18%	4.1%	2.223	0.077	1.061	0.038	0.914	0.033	4	4.198	0.149
28	D0040-1	1.171	0.012	1.145	0.011	F	62%	I	38%	3.9%	2.277	0.065	1.042	0.031	0.910	0.027	4	4.229	0.124
29	D0075-1	1.196	0.012	1.110	0.011	F	32%	I	68%	3.6%	2.305	0.062	1.017	0.027	0.915	0.024	4	4.237	0.113
30	E0000-1	1.105	0.011	1.178	0.012	F	93%	I	7%	4.2%	2.195	0.087	1.076	0.044	0.913	0.037	4	4.184	0.168
31	E0010-1	1.117	0.011	1.196	0.012	F	92%	I	8%	4.2%	2.215	0.087	1.082	0.044	0.905	0.037	4	4.203	0.167
32	E0030-1	1.105	0.011	1.202	0.012	F	96%	I	4%	4.2%	2.201	0.091	1.088	0.045	0.906	0.038	4	4.195	0.175
33	E0050-1	1.102	0.011	1.172	0.012	F	93%	I	7%	4.2%	2.189	0.087	1.073	0.043	0.916	0.037	4	4.178	0.167
34	E0070-1	1.097	0.011	1.209	0.012	F	99%	I	1%	4.2%	2.193	0.094	1.094	0.047	0.905	0.039	4	4.191	0.180
35	E0090-1	1.104	0.011	1.177	0.012	F	93%	I	7%	4.2%	2.194	0.087	1.076	0.044	0.914	0.037	4	4.183	0.168
36	F0000-1	1.082	0.011	1.048	0.010	F	38%	I	62%	3.7%	2.132	0.056	1.009	0.027	0.963	0.025	4	4.103	0.108
37	F0015-1	1.046	0.010	1.070	0.011	F	91%	I	9%	4.2%	2.085	0.082	1.031	0.041	0.963	0.039	4	4.079	0.162
38	F0030-1	1.104	0.011	1.046	0.010	F	9%	I	91%	3.4%	2.164	0.066	1.002	0.031	0.958	0.029	4	4.124	0.126
39	F0050-1	1.119	0.011	1.033	0.010	I	67%	K	33%	5.7%	2.182	0.096	0.990	0.044	0.959	0.050	4	4.132	0.190
40	F0075-1	1.118	0.011	1.047	0.010	I	98%	K	2%	6.1%	2.184	0.130	0.999	0.060	0.954	0.082	4	4.138	0.272
41	F0100-1	1.118	0.011	1.038	0.010	I	78%	K	22%	5.8%	2.182	0.106	0.994	0.049	0.958	0.059	4	4.133	0.215

Table A.2 - 2: Overview of results from structural analysis (p-XRD).

labeling		lattice parameters				microstrain (as-refined/corrected)			secondary phases			
No.	sample	a [Å]	c [Å]	V_{UC} [Å^3]	c/2a	$\varepsilon_{[100]}$ [%]	$\varepsilon_{[001]}$ [%]	$\varepsilon_{\varnothing}$ [%]	CuSe [wt%]	ZnSe [wt%]	$GeSe_2$ [wt%]	Ge [wt%]
1	A0000-1	5.607	11.050	347.4	0.9855	0.0248/0.0096	0.0356/0.0347	0.0223/0.0150	5	5	3	—
2	A0015-1	5.608	11.050	347.5	0.9852	0.0287/0.0274	0.0316/0.0316	0.0231/0.0224	—	3	1	—
3	A0040-1	5.612	11.044	347.8	0.9840	0.0218/0.0132	0.0196/0.0196	0.0163/0.0121	—	1	—	—
4	A0075-1	5.613	11.039	347.8	0.9833	0.0237/0.0237	0.0266/0.0249	0.0192/0.0187	—	2	2	—
5	A0125-1	5.613	11.021	347.2	0.9818	0.0547/0.0546	0.1075/0.087	0.0576/0.0516	—	1	1	—
6	A0200-1	5.620	10.979	346.8	0.9767	0.0160/0.0133	0.0916/0.0671	0.0361/0.0269	—	2	—	—
7	A0000-2	5.611	11.050	347.9	0.9847	0.0210/0.0184	0.0226/0.0226	0.0167/0.0154	—	2	—	9
8	A0015-2	5.612	11.050	348.0	0.9845	0.0166/0.0145	0.0233/0.0233	0.0147/0.0137	—	1	1	—
9	A0040-2	5.614	11.044	348.1	0.9836	0.0168/0.0161	0.0199/0.0171	0.0139/0.0127	—	2	—	—
10	A0075-2	5.613	11.038	347.8	0.9832	0.0241/0.0224	0.0316/0.0210	0.0208/0.0170	—	2	—	—
11	A0125-2	5.615	11.018	347.4	0.9812	0.0239/0.0239	0.0357/0.0239	0.0219/0.0140	—	3	—	—
12	A0200-2	5.617	11.005	347.2	0.9796	0.0174/0.0171	0.0292/0.0174	0.0168/0.0100	—	10	—	—
13	B0000-1	5.611	11.050	347.9	0.9847	0.0236/0.0227	0.0251/0.0251	0.0187/0.0183	—	1	—	—
14	B0010-1A	5.613	11.051	348.2	0.9844	0.0122/0.0101	0.0236/0.0236	0.0127/0.0118	—	2	—	12
15	B0010-1B	5.612	11.049	347.9	0.9844	0.0179/0.0165	0.0182/0.0182	0.0140/0.0133	—	—	—	—
16	B0020-1	5.612	11.051	348.0	0.9846	0.0171/0.0147	0.0327/0.0324	0.0177/0.0165	—	3	—	—
17	B0075-1	5.612	11.051	348.1	0.9845	0.0174/0.0166	0.0254/0.0246	0.0157/0.0151	—	9	—	—
18	B0100-1A	5.614	11.048	348.2	0.9841	0.0244/0.0240	0.0327/0.0302	0.0212/0.0203	—	11	—	—
19	B0100-1B	5.614	11.049	348.3	0.9841	0.0227/0.0220	0.0245/0.0174	0.0181/0.0158	—	11	—	—
20	B0125-1	5.613	11.049	348.1	0.9843	0.0209/0.0203	0.0168/0.0159	0.0151/0.0146	—	16	—	—

Table A.2 - 2: (Continued).

No.	sample	a [Å]	c [Å]	V_{UC} [Å^3]	c/2a	$\varepsilon_{[100]}$ [%]	$\varepsilon_{[001]}$ [%]	$\varepsilon_{\varnothing}$ [%]	CuSe [wt%]	ZnSe [wt%]	$GeSe_2$ [wt%]	Ge [wt%]
21	C0025-1R	5.610	11.047	347.6	0.9847	0.0232/0.0212	0.0236/0.0236	0.0181/0.0171	—	—	—	—
22	C0000-2R	5.612	11.050	348.0	0.9845	0.0245/0.0236	0.0293/0.0293	0.0203/0.0199	—	—	—	—
23	C0025-2	5.609	11.047	347.6	0.9848	0.0172/0.0156	0.0268/0.0268	0.0160/0.0153	—	1	—	8
24	C0050-2R	5.607	11.042	347.1	0.9847	0.0168/—	0.0152/0.0075	0.0126/—	—	—	—	—
25	D0000-1	5.612	11.049	348.0	0.9844	0.0144/0.0126	0.0186/0.0186	0.0124/0.0115	—	—	—	—
26	D0010-1	5.611	11.050	347.9	0.9847	0.0116/0.0098	0.0215/0.0215	0.0118/0.0110	—	—	—	—
27	D0025-1	5.609	11.049	347.6	0.9850	0.0200/0.0159	0.0189/0.0189	0.0152/0.0131	—	1	—	—
28	D0040-1	5.607	11.049	347.3	0.9854	0.0047/—	0.0129/—	0.0061/—	—	1	—	—
29	D0075-1	5.606	11.047	347.2	0.9853	0.0160/—	0.0070/—	0.0106/—	—	1	1	—
30	E0000-1	5.614	11.049	348.2	0.9841	0.0276/0.0255	0.0213/0.0213	0.0198/0.0187	—	—	—	—
31	E0010-1	5.614	11.046	348.1	0.9838	0.0215/0.0191	0.0138/0.0138	0.0146/0.0134	—	—	—	—
32	E0030-1	5.613	11.044	348.0	0.9838	0.0107/0.0081	0.0142/0.0142	0.0093/0.0081	—	—	—	—
33	E0050-1	5.613	11.042	347.9	0.9837	0.0155/0.0139	0.0204/0.0204	0.0134/0.0126	—	—	—	—
34	E0070-1	5.614	11.044	348.0	0.9837	0.0195/0.0175	0.0182/0.0182	0.0148/0.0138	—	—	—	—
35	E0090-1	5.613	11.045	348.0	0.9838	0.0261/0.0251	0.0254/0.0254	0.0201/0.0196	—	—	—	—
36	F0000-1	5.613	11.049	348.1	0.9842	0.0338/0.0331	0.0221/0.0221	0.0232/0.0228	—	—	—	—
37	F0015-1	5.609	11.050	347.6	0.9850	0.0108/—	0.0173/—	0.0102/—	—	2	—	—
38	F0030-1	5.606	11.051	347.3	0.9856	0.0183/0.0158	0.0195/0.0195	0.0142/0.0133	—	3	—	—
39	F0050-1	5.608	11.049	347.5	0.9851	0.0301/0.0277	0.0284/0.0284	0.0229/0.0217	—	6	—	—
40	F0075-1	5.608	11.050	347.5	0.9852	0.0378/0.0349	0.0189/0.0189	0.0246/0.0230	5	8	—	—
41	F0100-1	5.607	11.050	347.3	0.9855	0.0369/0.0340	0.0283/0.0283	0.0263/0.0249	8	7	—	—

Table A.2 - 3: Overview of site occupancy factors, isotropic temperature factors, anion positions (p-ND).

labeling		site occupancy factors								isotr. temperature factors					anion coordinates					
No.	sample	2a	err	2c	err	2d	err	2b	err	2a [Å²]	2c [Å²]	2d [Å²]	2b [Å²]	8g [Å²]	x	err	y	err	z	err
1	A0000-1	1.014	0.037	0.950	0.022	1.092	0.029	0.997	0.030	1.577	1.2474	1.5440	0.6022	1.3683	0.24259	0.01083	0.24159	0.00162	0.12182	0.00049
2	A0015-1	1.011	0.024	0.972	0.020	1.055	0.026	0.995	0.016	2.277	1.9724	1.1379	0.2039	1.0913	0.24192	0.00080	0.25080	0.00187	0.12257	0.00042
3	A0040-1	0.990	0.028	0.952	0.025	1.038	0.036	1.007	0.024	2.1068	1.6777	2.2999	1.7999	1.1304	0.24219	0.00080	0.25080	0.00187	0.12257	0.00042
4	A0075-1	1.019	0.034	0.990	0.023	1.059	0.032	0.974	0.024	1.7297	2.3232	1.1868	0.3852	1.1354	0.24427	0.00269	0.25739	0.00217	0.12236	0.00044
5	A0125-1	1.020	0.025	0.966	0.018	1.009	0.023	.0993	0.016	3.6306	1.8905	0.9122	0.4355	0.9936	0.24383	0.00240	0.25739	0.00217	0.12236	0.00072
6	A0200-1	0.943	0.040	0.924	0.038	0.999	0.051	0.981	0.030	3.7691	0.6305	1.0474	0.5514	0.8221	0.24202	0.00235	0.25613	0.00277	0.12375	0.00058
7	A0000-2	0.991	0.033	0.934	0.034	1.035	0.044	1.010	0.023	2.3042	1.5276	0.7360	0.4357	0.7240	0.25244	0.00434	0.25881	0.00121	0.12361	0.00052
8	A0015-2	0.987	0.033	0.940	0.034	1.104	0.049	0.999	0.024	2.4236	1.3517	1.5349	0.5677	0.7164	0.25166	0.00561	0.25814	0.00127	0.12286	0.00036
9	A0040-2	0.981	0.030	0.952	0.032	1.042	0.044	0.990	0.027	1.4236	2.0820	1.5196	0.6060	0.7225	0.25026	0.00521	0.26008	0.00052	0.12356	0.00045
10	A0075-2	0.998	0.041	0.981	0.028	1.050	0.038	0.965	0.037	1.3750	1.8367	1.4000	0.8064	0.6997	0.24853	0.00452	0.25977	0.00102	0.12342	0.00071
11	A0125-2	0.978	0.029	0.960	0.030	1.061	0.040	0.950	0.025	1.4610	2.0011	1.5847	0.3052	0.8888	0.24953	0.00457	0.25992	0.00068	0.12238	0.00035
12	A0200-2	0.984	0.028	0.959	0.033	1.056	0.046	0.994	0.024	1.8804	2.7265	1.7690	0.4933	0.7461	0.25016	0.00571	0.25857	0.00068	0.12177	0.12177
13	B0000-1	0.994	0.035	0.960	0.020	1.081	0.028	1.000	0.028	1.9218	1.3729	1.5611	0.7704	0.6183	0.24342	0.00242	0.25673	0.00222	0.12374	0.00053
14	B0010-1A	0.999	0.051	0.959	0.026	1.068	0.039	0.990	0.040	1.7544	1.3455	1.9602	0.6170	1.0113	0.24576	0.00724	0.25923	0.00343	0.12374	0.00070
15	B0010-1B	0.998	0.030	0.936	0.047	1.114	0.059	0.983	0.021	3.0042	2.1753	0.7295	0.7161	0.9645	0.24761	0.01213	0.25872	0.00344	0.12387	0.00086
16	B0020-1	1.004	0.023	0.969	0.030	1.101	0.040	0.978	0.024	0.4560	2.9220	1.4238	1.7971	0.8644	0.24357	0.00204	0.25473	0.00205	0.12299	0.00042
17	B0075-1	0.993	0.026	0.957	0.022	1.092	0.029	0.990	0.018	2.2932	1.7268	0.9007	0.5297	0.7466	0.24374	0.00219	0.25575	0.00218	0.12311	0.00043
18	B0100-1A	1.049	0.047	0.979	0.030	1.055	0.043	0.946	0.047	0.9694	1.3790	1.6449	1.9317	0.9467	0.24723	0.00382	0.25756	0.00174	0.12370	0.00048
19	B0100-1B	1.009	0.028	0.937	0.035	1.061	0.044	1.000	0.018	2.6857	2.0486	0.6208	0.3932	1.1426	0.24537	0.00849	0.25848	0.00465	0.12287	0.00064
20	B0125-1	1.006	0.041	0.974	0.032	1.090	0.044	0.984	0.034	2.0432	1.7936	1.5627	0.3101	0.8447	0.24620	0.00735	0.25814	0.00292	0.12326	0.00050

Table A.2 - 3: (Continued).

No.	sample	2a	err	2c	err	2d	err	2b	err	2a [Å²]	2c [Å²]	2d [Å²]	2b [Å²]	8g [Å²]	x	err	y	err	z	err
21	C0025-1R	0.996	0.018	0.947	0.025	1.065	0.031	0.992	0.011	2.8694	2.4568	0.5469	0.2630	1.0576	0.24290	0.00172	0.25472	0.00214	0.12305	0.00042
22	C0000-2R	0.999	0.027	0.939	0.024	1.069	0.034	0.980	0.018	2.5244	1.4597	1.4065	0.4340	0.9857	0.24744	0.00789	0.25838	0.00241	0.12289	0.00042
23	C0025-2	0.997	0.029	0.981	0.026	1.039	0.032	1.001	0.020	2.3863	2.7043	0.4525	0.7628	0.8221	0.24349	0.00248	0.25685	0.00196	0.12407	0.00063
24	C0050-2R	0.990	0.022	0.951	0.023	1.106	0.028	0.986	0.016	2.3005	2.6922	0.5546	0.8302	1.1089	0.24463	0.00256	0.25469	0.00230	0.12385	0.00057
25	D0000-1	1.005	0.033	0.927	0.021	1.076	0.030	0.959	0.028	1.9769	1.1248	1.6868	0.5200	0.7652	0.24401	0.00467	0.25778	0.00314	0.12327	0.00043
26	D0010-1	0.994	0.028	0.975	0.030	1.085	0.038	1.001	0.022	2.4960	2.2209	0.6405	0.4955	0.9987	0.24562	0.00423	0.25754	0.00244	0.12401	0.00061
27	D0025-1	0.997	0.019	0.969	0.024	1.080	0.028	1.006	0.014	2.0011	3.4414	0.8039	0.8288	0.8961	0.24501	0.00287	0.25580	0.00205	0.12293	0.00037
28	D0040-1	1.006	0.032	0.949	0.023	1.051	0.031	0.975	0.026	2.1471	1.6145	1.6090	0.5434	0.8660	0.24533	0.00606	0.25763	0.00322	0.12343	0.00046
29	D0075-1	1.004	0.024	0.973	0.021	1.028	0.028	1.007	0.017	2.2505	1.8985	0.8209	0.7048	1.2276	0.24980	0.00538	0.25709	0.00109	0.12322	0.00044
30	E0000-1	1.009	0.030	0.946	0.016	1.063	0.022	0.973	0.027	1.7547	1.5124	2.5791	1.4491	1.1458	0.24265	0.00209	0.25717	0.00219	0.12309	0.00042
31	E0010-1	1.012	0.032	0.992	0.015	1.022	0.019	0.998	0.029	1.9559	1.8045	1.9851	1.6420	0.9682	0.24017	0.00081	0.25254	0.00172	0.12327	0.00045
32	E0030-1	1.021	0.028	0.968	0.020	1.011	0.026	1.000	0.029	1.3875	2.3212	2.2241	2.6463	1.0479	0.25207	0.00690	0.26030	0.00140	0.12345	0.00043
33	E0050-1	1.009	0.029	0.993	0.023	1.012	0.028	0.990	0.029	1.3056	2.3328	0.6543	3.5248	1.0793	0.25346	0.00418	0.25922	0.00158	0.12308	0.00045
34	E0070-1	0.993	0.032	0.983	0.033	1.036	0.039	0.995	0.032	3.2379	1.6159	0.6693	1.8220	1.3387	0.24151	0.00095	0.25115	0.00171	0.12274	0.00042
35	E0090-1	0.991	0.047	0.980	0.036	1.050	0.051	1.005	0.045	1.7358	1.8294	1.1260	1.2220	0.8087	0.24172	0.00143	0.25525	0.00177	0.12423	0.00064
36	F0000-1	1.018	0.028	1.002	0.022	1.017	0.026	1.015	0.029	1.2510	2.2220	1.0815	2.6647	0.9293	0.24170	0.00149	0.25501	0.00197	0.12335	0.00047
37	F0015-1	1.020	0.023	0.927	0.026	1.105	0.034	0.979	0.026	0.5308	2.1874	1.4942	3.1902	1.0695	0.24879	0.00751	0.25990	0.00110	0.12337	0.00047
38	F0030-1	1.026	0.037	0.932	0.033	1.132	0.047	0.954	0.037	1.0534	1.8335	1.2140	2.4330	0.9601	0.24682	0.00576	0.25828	0.00228	0.12314	0.00048
39	F0050-1	1.009	0.029	0.965	0.027	1.086	0.033	0.989	0.032	0.8078	1.8545	1.0564	3.5777	1.2042	0.24222	0.00214	0.25561	0.00285	0.12386	0.00065
40	F0075-1	11.02 1	0.032	0.956	0.034	1.074	0.040	1.002	0.037	0.5583	1.6050	0.8070	3.3283	1.3485	0.25304	0.00453	0.25895	0.00157	0.12346	0.00061
41	F0100-1	1.016	0.052	0.960	0.039	1.108	0.047	0.987	0.052	1.1022	1.1946	1.5115	3.2274	1.3223	0.24464	0.00462	0.25500	0.00361	0.12382	0.00086

Table A.2 - 4: Overview of calculated and refined bond distances (p-ND).

labeling		bond distances (calculated) [Å]								bond distances (refined) [Å]							
No.	sample	2a – 8g	err	2c – 8g	err	2d – 8g	err	2b – 8g	err	2a – 8g	err	2c – 8g	err	2d – 8g	err	2b – 8g	err
1	A0000-1	2.4750	0.0916	2.4761	0.0578	2.4789	0.0666	2.3583	0.0686	2.3770	0.0117	2.4048	0.0114	2.4719	0.0114	2.419	0.0115
2	A0015-1	2.4750	0.0594	2.4757	0.0513	2.4794	0.0616	2.3588	0.0355	2.3783	0.0073	2.4037	0.0072	2.4613	0.0071	2.4261	0.0071
3	A0040-1	2.4750	0.0668	2.4758	0.0644	2.4793	0.0823	2.3578	0.0568	2.4006	0.0127	2.3868	0.0125	2.4712	0.0126	2.4202	0.0125
4	A0075-1	2.4750	0.0817	2.4755	0.0586	2.4795	0.0741	2.3607	0.0581	2.4067	0.0120	2.3938	0.0119	2.4780	0.0120	2.4002	0.0122
5	A0125-1	2.4750	0.0619	2.4754	0.0454	2.4796	0.0531	2.3582	0.0385	2.4000	0.0098	2.3950	0.0098	2.4663	0.0098	2.4065	0.0099
6	A0200-1	2.4624	0.1015	2.4758	0.0988	2.4800	0.1218	2.3595	0.0700	2.4011	0.0125	2.3767	0.0123	2.4678	0.0124	2.4142	0.0123
7	A0000-2	2.4750	0.0693	2.4759	0.0752	2.4792	0.0888	2.3616	0.0475	2.4449	0.0139	2.4054	0.0141	2.4495	0.0137	2.3743	0.0141
8	A0015-2	2.4750	0.0792	2.4763	0.0903	2.4787	0.1090	2.3618	0.0548	2.4385	0.0202	2.4124	0.0203	2.4519	0.0198	2.3724	0.0204
9	A0040-2	2.4750	0.0718	2.4758	0.0799	2.4793	0.1012	2.3619	0.0652	2.4433	0.0165	2.3951	0.0168	2.4607	0.0164	2.3772	0.0170
10	A0075-2	2.4750	0.0990	2.4755	0.0712	2.4795	0.0886	2.3622	0.0900	2.4366	0.0170	2.3929	0.0173	2.4630	0.0170	2.3790	0.0175
11	A0125-2	2.4752	0.0699	2.4758	0.0750	2.4793	0.0943	2.3628	0.0609	2.4326	0.0165	2.4008	0.0167	2.4648	0.0163	2.3676	0.0170
12	A0200-2	2.4752	0.0700	2.4759	0.0857	2.4794	0.1093	2.3637	0.0585	2.4239	0.0197	2.4081	0.0198	2.4637	0.0194	2.3674	0.0202
13	B0000-1	2.4750	0.0866	2.4759	0.0521	2.4791	0.0628	2.3615	0.0643	2.4115	0.0098	2.3820	0.0097	2.4730	0.0098	2.4115	0.0098
14	B0010-1A	2.4750	0.1262	2.4759	0.0675	2.4791	0.0910	2.3615	0.0957	2.4274	0.0248	2.3849	0.0251	2.4694	0.0252	2.3947	0.0257
15	B0010-1B	2.4750	0.0743	2.4764	0.1230	2.4786	0.1306	2.3613	0.0500	2.4347	0.0402	2.3898	0.0408	2.4613	0.0404	2.3889	0.0414
16	B0020-1	2.4750	0.0569	2.4760	0.0785	2.4790	0.0901	2.3617	0.0574	2.4027	0.0096	2.3954	0.0095	2.4667	0.0096	2.4093	0.0096
17	B0075-1	2.4750	0.0619	2.4761	0.0550	2.4790	0.0646	2.3601	0.0407	2.4076	0.0096	2.3923	0.0095	2.4702	0.0096	2.4076	0.0096
18	B0100-1A	2.4750	0.1163	2.4756	0.0766	2.4794	0.1024	2.3600	0.1131	2.4255	0.0144	2.3922	0.0145	2.4611	0.0145	2.3954	0.0147
19	B0100-1B	2.4750	0.0693	2.4760	0.0916	2.4790	0.1016	2.3601	0.0433	2.4155	0.0308	2.3898	0.0306	2.4740	0.0310	2.3959	0.0314
20	B0125-1	2.4750	0.0941	2.4759	0.0752	2.4792	0.0958	2.3624	0.0747	2.4217	0.0248	2.3909	0.0249	2.4687	0.0250	2.3955	0.0255

Table A.2 - 4: (Continued).

No.	sample	2a – 8g	err	2c – 8g	err	2d – 8g	err	2b – 8g	err	2a – 8g	err	2c – 8g	err	2d – 8g	err	2b – 8g	err
21	C0025-1R	2.4750	0.0941	2.4759	0.0752	2.4791	0.0958	2.3591	0.0747	2.3985	0.0090	2.3911	0.0088	2.4695	0.0089	2.4122	0.0089
22	C0000-2R	2.4750	0.0644	2.4760	0.0628	2.4790	0.0762	2.3616	0.0430	2.4225	0.0267	2.3968	0.0269	2.4681	0.0268	2.3898	0.0276
23	C0025-2	2.4750	0.0619	2.4755	0.0558	2.4796	0.0649	2.3598	0.0403	2.4113	0.0100	2.3781	0.0099	2.4677	0.0100	2.4126	0.0100
24	C0050-2R	2.4750	0.0520	2.4759	0.0597	2.4789	0.0641	2.3556	0.0378	2.4090	0.0123	2.3915	0.0122	2.4563	0.0124	2.4090	0.0124
25	D0000-1	2.4750	0.0817	2.4762	0.0555	2.4788	0.0662	2.3620	0.0648	2.4155	0.0190	2.3845	0.0190	2.4754	0.0192	2.4024	0.0195
26	D0010-1	2.4750	0.0693	2.4759	0.0752	2.4792	0.0864	2.3619	0.0524	2.4261	0.0149	2.3865	0.0150	2.4644	0.0151	2.4000	0.0153
27	D0025-1	2.4750	0.0470	2.4759	0.0622	2.4792	0.0654	2.3608	0.0332	2.4078	0.0120	2.3952	0.0119	2.4664	0.0120	2.4012	0.0122
28	D0040-1	2.4750	0.0792	2.4758	0.0569	2.4792	0.0726	2.3613	0.0593	2.4174	0.0218	2.3854	0.0219	2.4696	0.0221	2.3978	0.0224
29	D0075-1	2.4750	0.0569	2.4755	0.0532	2.4796	0.0649	2.3606	0.0403	2.4288	0.0168	2.4053	0.0169	2.4513	0.0166	2.3824	0.0171
30	E0000-1	2.4750	0.0743	2.4760	0.0417	2.4791	0.0511	2.3611	0.0642	2.4054	0.0096	2.3836	0.0094	2.4743	0.0096	2.4054	0.0096
31	E0010-1	2.4750	0.0792	2.4752	0.0376	2.4798	0.0464	2.3621	0.0689	2.3827	0.0069	2.3879	0.0069	2.4677	0.0068	2.4305	0.0068
32	E0030-1	2.4750	0.0693	2.4754	0.0505	2.4796	0.0628	2.3621	0.0690	2.4478	0.0233	2.3997	0.0237	2.4536	0.0229	2.3673	0.0237
33	E0050-1	2.4750	0.0718	2.4752	0.0574	2.4798	0.0686	2.3607	0.0688	2.4442	0.0144	2.4084	0.0145	2.4486	0.0141	2.3644	0.0145
34	E0070-1	2.4750	0.0792	2.4754	0.0833	2.4796	0.0942	2.3623	0.0763	2.3779	0.0070	2.3999	0.0069	2.4621	0.0069	2.4263	0.0069
35	E0090-1	2.4750	0.1163	2.4755	0.0915	2.4795	0.1221	2.3610	0.0708	2.4022	0.0084	2.3781	0.0083	2.4659	0.0083	2.4224	0.0083
36	F0000-1	2.4750	0.0693	2.4752	0.0550	2.4798	0.0636	2.3547	0.0684	2.3953	0.0088	2.3841	0.0087	2.4703	0.0087	2.4169	0.0087
37	F0015-1	2.4750	0.0569	2.4763	0.0691	2.4787	0.0771	2.3547	0.0613	2.4360	0.0262	2.3917	0.0266	2.4624	0.0261	2.3778	0.0270
38	F0030-1	2.4750	0.0916	2.4766	0.0890	2.4785	0.1048	2.3552	0.0874	2.421	0.0206	2.3929	0.0207	2.4641	0.0207	2.3883	0.0212
39	F0050-1	2.4750	0.0718	2.4759	0.0702	2.4791	0.0766	2.3557	0.0755	2.4033	0.0127	2.3779	0.0125	2.4687	0.0126	2.4163	0.0124
40	F0075-1	2.4750	0.0792	2.4759	0.0886	2.4791	0.0928	2.3551	0.0874	2.4458	0.0175	2.4070	0.0177	2.4453	0.0172	2.3681	0.0176
41	F0100-1	2.4750	0.1287	2.4761	0.1025	2.4789	0.1078	2.3553	0.1228	2.4087	0.0216	2.3912	0.0214	2.4560	0.0216	2.4087	0.0217

Table A.2 - 5: Overview of tetrahedral bond angles obtained from structure refinements (p-ND).

labeling		tetrahedral bond angles (refined) [°]											
No.	sample	2a – 8g – 2c	err	2a – 8g – 2d	err	2a – 8g – 2b	err	2c – 8g – 2d	err	2c – 8g – 2b	err	2d – 8g – 2b	err
1	A0000-1	110.9	0.4	108.6	0.4	111.6	0.4	108.9	0.4	109.5	0.4	107.3	0.4
2	A0015-1	110.8	0.2	108.9	0.2	111.3	0.2	109.2	0.2	109.2	0.2	107.3	0.2
3	A0040-1	110.8	0.4	107.9	0.4	110.9	0.4	109.7	0.4	110.1	0.4	107.3	0.4
4	A0075-1	110.3	0.4	107.5	0.4	111.5	0.4	109.2	0.4	110.5	0.4	107.7	0.4
5	A0125-1	110.3	0.3	107.9	0.3	111.4	0.3	109.5	0.3	110.1	0.3	107.7	0.3
6	A0200-1	110.6	0.4	107.6	0.4	111.1	0.4	110.1	0.4	110.2	0.4	107.2	0.4
7	A0000-2	108.6	0.5	107.2	0.5	110.9	0.5	109.7	0.5	111.0	0.5	109.5	0.5
8	A0015-2	108.6	0.7	107.3	0.7	111.2	0.7	109.4	0.7	110.8	0.7	109.5	0.7
9	A0040-2	109.0	0.6	106.9	0.5	110.9	0.6	109.7	0.6	111.2	0.6	109.0	0.6
10	A0075-2	109.2	0.6	106.9	0.6	111.0	0.6	109.7	0.6	111.2	0.6	108.8	0.6
11	A0125-2	109.0	0.6	106.9	0.5	111.5	0.6	109.3	0.6	111.2	0.6	109.0	0.6
12	A0200-2	108.9	0.7	107.1	0.6	111.8	0.7	109.1	0.7	110.9	0.7	109.0	0.7
13	B0000-1	110.6	0.3	107.5	0.3	110.8	0.3	109.7	0.3	110.6	0.3	107.5	0.3
14	B0010-1A	109.9	0.8	107.1	0.8	110.8	0.9	109.7	0.8	111.0	0.9	108.2	0.8
15	B0010-1B	109.5	1.4	107.1	1.3	110.8	1.4	109.8	1.4	111.0	1.4	108.6	1.4
16	B0020-1	110.3	0.3	108.0	0.3	111.1	0.3	109.4	0.3	110.1	0.3	107.8	0.3
17	B0075-1	110.3	0.3	107.8	0.3	111.1	0.3	109.5	0.3	110.3	0.3	107.8	0.3
18	B0100-1A	109.7	0.5	107.4	0.5	110.9	0.5	109.8	0.5	110.7	0.5	108.4	0.5
19	B0100-1B	110.1	1.0	107.3	1.0	111.2	1.0	109.4	1.0	110.8	1.0	108.0	1.0
20	B0125-1	109.9	0.8	107.3	0.8	111.0	0.8	109.6	0.8	110.8	0.9	108.2	0.8

Table A.2 - 5: (Continued).

No.	sample	2a – 8g – 2c	err	2a – 8g – 2d	err	2a – 8g – 2b	err	2c – 8g – 2d	err	2c – 8g – 2b	err	2d – 8g – 2b	err
21	C0025-1R	110.6	0.3	108.0	0.3	111.1	0.3	109.4	0.3	110.1	0.3	107.5	0.3
22	C0000-2R	109.7	0.9	107.3	0.9	111.2	0.9	109.4	0.9	110.8	0.9	108.4	0.9
23	C0025-2	110.6	0.3	107.6	0.3	110.6	0.3	109.9	0.3	110.5	0.3	107.5	0.3
24	C0050-2R	110.1	0.4	108.0	0.4	110.8	0.4	109.8	0.4	110.1	0.4	108.0	0.4
25	D0000-1	110.3	0.6	107.3	0.6	111.0	0.6	109.6	0.6	110.8	0.7	107.7	0.6
26	D0010-1	109.9	0.5	107.3	0.5	110.7	0.5	109.8	0.5	110.8	0.5	108.2	0.5
27	D0025-1	110.1	0.4	107.8	0.4	111.2	0.4	109.4	0.4	110.4	0.4	108.0	0.4
28	D0040-1	110.1	0.7	107.4	0.7	110.9	0.7	109.6	0.7	110.8	0.8	108.0	0.7
29	D0075-1	109.0	0.6	107.5	0.6	111.0	0.6	109.5	0.6	110.6	0.6	109.1	0.6
30	E0000-1	110.5	0.3	107.5	0.3	111.1	0.3	109.5	0.3	110.5	0.3	107.5	0.3
31	E0010-1	111.2	0.2	108.5	0.2	111.0	0.2	109.6	0.2	109.5	0.2	106.9	0.2
32	E0030-1	108.6	0.8	106.8	0.8	111.0	0.8	109.7	0.8	111.3	0.8	109.4	0.8
33	E0050-1	108.3	0.5	107.1	0.5	111.1	0.5	109.5	0.5	111.0	0.5	109.7	0.5
34	E0070-1	110.9	0.2	108.8	0.2	111.3	0.2	109.3	0.2	109.2	0.2	107.2	0.2
35	E0090-1	110.8	0.3	107.9	0.3	110.7	0.3	110.0	0.3	110.1	0.3	107.2	0.3
36	F0000-1	110.8	0.3	107.9	0.3	111.0	0.3	109.6	0.3	110.1	0.3	107.3	0.3
37	F0015-1	109.2	0.9	106.9	0.9	110.9	0.9	109.6	0.9	111.2	0.9	108.8	0.9
38	F0030-1	109.7	0.7	107.4	0.7	111.0	0.7	109.4	0.7	110.8	0.7	108.4	0.7
39	F0050-1	110.8	0.4	107.8	0.4	110.7	0.4	109.8	0.4	110.4	0.4	107.3	0.4
40	F0075-1	108.4	0.6	107.2	0.6	110.9	0.6	109.6	0.6	111.0	0.6	109.7	0.6
41	F0100-1	110.2	0.7	108.0	0.7	110.8	0.7	109.7	0.7	110.2	0.7	108.0	0.7

Table A.2 - 6: Overview of point defect concentrations (Pt. 1).

labeling		V_{Cu} (1), Cu_{Zn} (2)			Zn_{Cu}			Zn_{Ge}		
No.	sample	n [cm^{-3}]	err (upper)	err (lower)	n [cm^{-3}]	err (upper)	err (lower)	n [cm^{-3}]	err (upper)	err (lower)
1	A0000-1	—	—	—	—	—	—	—	—	—
2	A0015-1	—	—	—	—	—	—	—	—	—
3	A0040-1	—	—	—	—	—	—	—	—	—
4	A0075-1	—	—	—	—	—	—	4.78E+20	9.16E+19	9.61E+19
5	A0125-1	—	—	—	—	—	—	3.66E+20	8.51E+19	1.07E+19
6	A0200-1	1.15E+20 (1)	1.16E+19 (1)	5.95E+19 (1)	9.48E+20	1.77E+20	1.03E+20	4.17E+20	1.10E+20	8.83E+19
7	A0000-2	—	—	—	—	—	—	3.44E+19	9.76E+18	1.51E+18
8	A0015-2	—	—	—	—	—	—	7.21E+19	1.73E+19	9.84E+18
9	A0040-2	—	—	—	—	—	—	3.86E+20	1.23E+20	4.73E+19
10	A0075-2	—	—	—	—	—	—	5.47E+20	1.39E+20	1.92E+20
11	A0125-2	—	—	—	2.71E+20	9.30E+19	2.29E+19	5.68E+20	2.42E+19	2.08E+20
12	A0200-2	—	—	—	5.41E+20	2.25E+20	5.70E+19	5.85E+20	2.40E+20	1.00E+19
13	B0000-1	—	—	—	—	—	—	8.60E+19	2.52E+19	1.28E+19
14	B0010-1A	—	—	—	—	—	—	1.901E+20	6.75E+19	5.70E+19
15	B0010-1B	—	—	—	—	—	—	7.49E+19	8.12E+18	1.76E+19
16	B0020-1	—	—	—	—	—	—	1.73E+20	1.94E+19	4.87E+19
17	B0075-1	—	—	—	—	—	—	2.20E+20	3.78E+19	2.33E+19
18	B0100-1A	—	—	—	—	—	—	3.45E+20	3.50E+19	2.31E+20
19	B0100-1B	—	—	—	—	—	—	3.42E+20	1.05E+20	3.79E+18
20	B0125-1	—	—	—	—	—	—	3.37E+20	9.67E+19	7.41E+19

Table A.2 - 6: (Continued).

No.	sample	n [cm^{-3}]	err (upper)	err (lower)	n [cm^{-3}]	err (upper)	err (lower)	n [cm^{-3}]	err (upper)	err (lower)
21	C0025-1R	—	—	—	—	—	—	—	—	—
22	C0000-2R	—	—	—	—	—	—	1.23E+20	8.48E+18	2.77E+19
23	C0025-2	—	—	—	—	—	—	—	—	—
24	C0050-2R	1.33E+21 (2)	3.80E+20 (2)	4.16E+19 (2)	—	—	—	—	—	—
25	D0000-1	—	—	—	—	—	—	2.33E+20	2.72E+18	1.00E+20
26	D0010-1	—	—	—	—	—	—	5.09E+19	1.27E+19	5.65E+18
27	D0025-1	—	—	—	—	—	—	—	—	—
28	D0040-1	—	—	—	—	—	—	—	—	—
29	D0075-1	—	—	—	—	—	—	—	—	—
30	E0000-1	—	—	—	—	—	—	2.77E+19	1.39E+18	1.09E+19
31	E0010-1	—	—	—	—	—	—	2.02E+18	5.49E+18	4.08E+18
32	E0030-1	—	—	—	—	—	—	5.22E+19	1.57E+19	9.13E+18
33	E0050-1	—	—	—	—	—	—	1.34E+19	2.79E+18	3.58E+18
34	E0070-1	—	—	—	—	—	—	8.14E+19	2.40E+19	1.87E+19
35	E0090-1	—	—	—	—	—	—	1.84E+19	8.26E+18	5.33E+18
36	F0000-1	—	—	—	—	—	—	—	—	—
37	F0015-1	—	—	—	—	—	—	—	—	—
38	F0030-1	—	—	—	—	—	—	—	—	—
39	F0050-1	5.52E+19 (2)	2.33E+19 (2)	3.22E+18 (2)	—	—	—	—	—	—
40	F0075-1	3.22E+18 (2)	1.30E+18 (2)	3.78E+17 (2)	—	—	—	—	—	—
41	F0100-1	3.62E+19 (2)	2.19E+19 (2)	4.42E+18 (2)	—	—	—	—	—	—

Table A.2 - 7: Overview of point defect concentrations (Pt. 2).

labeling		Zn_i			Cu_i			Cu_{Ge}		
No.	sample	n [cm^{-3}]	err (upper)	err (lower)	n [cm^{-3}]	err (upper)	err (lower)	n [cm^{-3}]	err (upper)	err (lower)
1	A0000-1	6.72E+19	2.27E+19	9.19E+18	1.01E+21	4.10E+20	2.85E+20	3.81E+20	8.65E+19	9.42E+19
2	A0015-1	2.33E+20	6.77E+19	3.16E+19	7.50E+20	2.31E+20	4.62E+19	4.05E+20	3.98E+19	5.96E+19
3	A0040-1	2.03E+20	3.49E+19	7.78E+19	6.74E+20	2.23E+20	8.89E+19	3.60E+20	1.02E+20	3.96E+19
4	A0075-1	3.22E+20	1.53E+20	6.85E+19	3.10E+20	1.34E+20	9.18E+18	—	—	—
5	A0125-1	3.53E+20	8.31E+19	1.19E+20	2.61E+19	9.77E+17	3.29E+17	—	—	—
6	A0200-1	—	—	—	—	—	—	—	—	—
7	A0000-2	4.36E+20	1.29E+20	2.34E+20	6.51E+20	1.93E+20	1.04E+20	4.85E+20	1.37E+20	2.13E+19
8	A0015-2	4.36E+20	2.30E+20	1.38E+20	6.27E+20	3.31E+20	1.05E+20	4.51E+20	1.08E+20	6.16E+19
9	A0040-2	3.33E+20	1.35E+20	1.51E+20	5.49E+20	2.22E+20	1.00E+20	1.48E+20	4.72E+19	1.81E+19
10	A0075-2	3.74E+20	1.77E+20	1.52E+20	3.46E+20	1.38E+20	2.83E+19	—	—	—
11	A0125-2	4.32E+20	1.49E+20	1.91E+20	—	—	—	—	—	—
12	A0200-2	3.15E+20	1.83E+20	8.00E+19	—	—	—	—	—	—
13	B0000-1	4.17E+20	1.83E+20	7.76E+19	6.06E+20	2.65E+20	4.93E+19	4.23E+20	1.24E+20	6.31E+19
14	B0010-1A	3.84E+20	1.91E+20	1.50E+20	5.87E+20	2.92E+20	1.14E+20	3.25E+20	1.15E+20	9.76E+19
15	B0010-1B	4.20E+20	2.51E+20	1.87E+20	6.01E+20	3.60E+20	1.61E+20	4.30E+20	4.67E+19	1.01E+20
16	B0020-1	3.98E+20	2.24E+20	1.17E+20	5.95E+20	3.35E+20	9.87E+19	3.48E+20	3.90E+19	9.77E+19
17	B0075-1	3.19E+20	1.28E+20	4.49E+19	5.03E+20	2.01E+20	2.83E+19	2.34E+20	4.03E+19	2.49E+19
18	B0100-1A	2.71E+20	1.23E+20	1.92E+20	4.53E+20	2.06E+20	1.45E+20	1.02E+20	1.03E+19	6.79E+19
19	B0100-1B	3.00E+20	1.22E+20	1.40E+20	4.23E+20	1.73E+20	8.05E+19	1.13E+20	3.46E+19	1.25E+18
20	B0125-1	3.66E+20	2.27E+20	8.83E+19	5.98E+20	3.70E+20	8.92E+19	2.19E+20	6.30E+19	4.83E+19

Table A.2 - 7: (Continued).

No.	sample	n [cm^{-3}]	err (upper)	err (lower)	n [cm^{-3}]	err (upper)	err (lower)	n [cm^{-3}]	err (upper)	err (lower)
21	C0025-1R	1.58E+20	3.53E+19	4.44E+19	9.38E+20	2.15E+20	6.65E+19	4.18E+20	2.10E+19	5.42E+19
22	C0000-2R	4.16E+20	9.14E+19	1.63E+20	5.97E+20	1.31E+20	5.14E+19	3.94E+20	2.73E+19	8.90E+19
23	C0025-2	2.49E+20	7.02E+19	4.39E+19	8.60E+20	2.82E+20	5.86E+19	4.53E+20	7.60E+19	5.01E+19
24	C0050-2R	—	—	—	1.07E+21	3.54E+20	1.06E+20	2.56E+20	9.48E+18	5.75E+19
25	D0000-1	3.54E+20	4.90E+19	1.15E+20	6.70E+20	9.32E+19	5.02E+19	3.04E+20	3.54E+18	1.31E+20
26	D0010-1	4.43E+20	2.50E+20	6.84E+19	6.51E+20	3.68E+20	5.67E+19	4.78E+20	1.19E+20	5.30E+19
27	D0025-1	3.48E+20	1.38E+20	3.25E+19	7.88E+20	3.51E+20	3.39E+19	4.95E+20	1.01E+20	1.25E+19
28	D0040-1	2.40E+20	4.12E+19	7.63E+19	1.08E+21	1.90E+20	9.24E+19	5.19E+20	2.18E+19	1.91E+20
29	D0075-1	9.52E+19	1.79E+19	2.46E+19	1.27E+21	3.84E+20	1.00E+20	4.87E+20	1.15E+20	2.06E+19
30	E0000-1	4.08E+20	5.84E+19	1.83E+20	6.50E+20	9.30E+19	4.16E+19	4.70E+20	2.36E+19	1.84E+20
31	E0010-1	4.53E+20	1.54E+20	1.05E+20	7.11E+20	2.42E+20	5.61E+19	5.26E+20	1.43E+20	1.06E+20
32	E0030-1	4.54E+20	1.42E+20	1.74E+20	6.67E+20	2.08E+20	7.96E+19	4.90E+20	1.47E+20	8.57E+19
33	E0050-1	4.08E+20	1.34E+20	1.42E+20	6.18E+20	2.04E+20	7.08E+19	4.69E+20	9.74E+19	1.25E+20
34	E0070-1	4.58E+20	2.22E+20	1.70E+20	6.42E+20	3.11E+20	1.15E+20	4.65E+20	1.37E+20	1.07E+20
35	E0090-1	4.17E+20	2.80E+20	1.75E+20	6.35E+20	4.26E+20	1.79E+20	4.77E+20	2.14E+20	1.38E+20
36	F0000-1	5.13E+19	1.60E+19	7.76E+18	5.42E+20	2.66E+20	4.77E+19	2.15E+20	8.11E+19	2.09E+19
37	F0015-1	1.78E+20	5.59E+19	4.63E+19	2.78E+20	8.84E+19	3.98E+19	2.12E+20	1.23E+19	7.78E+19
38	F0030-1	1.11E+19	5.87E+18	2.33E+18	7.02E+20	3.95E+20	1.83E+20	2.41E+20	4.62E+19	1.00E+20
39	F0050-1	—	—	—	7.57E+20	3.51E+20	1.27E+20	2.34E+20	4.67E+19	7.79E+19
40	F0075-1	—	—	—	7.92E+20	4.14E+20	1.65E+20	2.63E+20	8.74E+19	7.19E+19
41	F0100-1	—	—	—	7.66E+20	5.31E+20	2.92E+20	2.43E+20	8.25E+19	1.25E+20

Table A.2 - 8: Overview of obtained optical band gaps.

No.	sample	Cu/(Zn+Ge)	Zn/Ge	$\frac{Cu/(Zn+Ge)}{Zn/Ge}$	V_{UC} [Å^3]	E_g [eV]
1	A0000-1	1.153	1.083	1.065	347.3	—
2	A0015-1	1.120	1.119	1.000	347.5	—
3	A0040-1	1.107	1.105	1.002	347.8	—
4	A0075-1	1.000	1.242	0.805	347.8	1.38 (1)
5	A0125-1	0.973	1.201	0.810	347.2	1.37 (1)
6	A0200-1	0.840	1.333	0.630	346.8	1.41 (1)
7	A0000-2	1.105	1.189	0.929	347.9	1.32 (1)
8	A0015-2	1.096	1.197	0.915	348.0	1.31 (1)
9	A0040-2	1.045	1.240	0.842	348.1	1.37 (1)
10	A0075-2	0.999	1.282	0.779	347.8	1.37 (1)
11	A0125-2	0.921	1.355	0.680	347.4	1.37 (1)
12	A0200-2	0.888	1.392	0.638	347.2	1.38 (1)
13	B0000-1	1.090	1.193	0.914	347.9	1.34 (1)
14	B0010-1A	1.074	1.208	0.889	348.2	1.32 (1)
15	B0010-1B	1.091	1.191	0.916	347.9	1.33 (1)
16	B0020-1	1.078	1.209	0.891	348.0	1.32 (1)
17	B0075-1	1.057	1.188	0.890	348.1	1.32 (1)
18	B0100-1A	1.034	1.201	0.861	348.2	1.31 (1)
19	B0100-1B	1.031	1.208	0.854	348.3	1.33 (1)
20	B0125-1	1.059	1.243	0.852	348.1	1.32 (1)
21	C0025-1R	1.146	1.108	1.035	347.6	—
22	C0000-2R	1.085	1.202	0.902	348.0	—
23	C0025-2	1.137	1.132	1.004	347.6	—
24	C0050-2R	1.200	0.992	1.210	347.1	—
25	D0000-1	1.081	1.216	0.889	348.0	1.34 (1)
26	D0010-1	1.103	1.196	0.922	347.9	1.35 (1)
27	D0025-1	1.129	1.160	0.973	347.6	—
28	D0040-1	1.171	1.145	1.023	347.3	—
29	D0075-1	1.196	1.110	1.077	347.2	—
30	E0000-1	1.105	1.178	0.938	348.2	1.31 (1)
31	E0010-1	1.117	1.196	0.934	348.1	1.35 (1)
32	E0030-1	1.105	1.202	0.920	348.0	1.32 (1)
33	E0050-1	1.102	1.172	0.941	347.9	1.35 (1)

Table A.2 - 8: (Continued).

No.	sample	Cu/(Zn+Ge)	Zn/Ge	$\frac{Cu/(Zn+Ge)}{Zn/Ge}$	V_{UC} [Å^3]	E_g [eV]
34	E0070-1	1.097	1.209	0.908	348.0	1.36 (1)
35	E0090-1	1.104	1.177	0.938	348.0	1.37 (1)
36	F0000-1	1.082	1.048	1.032	348.1	—
37	F0015-1	1.046	1.070	0.977	347.6	—
38	F0030-1	1.104	1.046	1.056	347.3	—
39	F0050-1	1.119	1.033	1.084	347.5	—
40	F0075-1	1.118	1.047	1.067	347.5	—
41	F0100-1	1.118	1.038	1.077	347.3	—

Eidestattliche Erklärung

Ich erkläre hiermit, dass ich die vorgelegte Dissertation mit dem Titel

Structural Trends in Off-stoichiometric $Cu_2ZnGeSe_4$ Kesterite-type Compound Semiconductors

selbständig verfasst und keine anderen als die angegeben Hilfsmittel und Quellen verwendet habe. Ferner wird hiermit erklärt, dass die Dissertation weder in der vorgelegten noch in einer ähnlichen Fassung zu einem früheren Zeitpunkt an der Freien Universität oder einer anderen Hochschule als Dissertation eingereicht worden ist.

Berlin, 13.10.2021

_____

René Gunder